



Skolkovo Institute of Science and Technology

Skolkovo Institute of Science and Technology

SPINOR AND VORTICITY CONTROL IN POLARITON CONDENSATES

Doctoral Thesis

by
Ivan Gnusov

DOCTORAL PROGRAM IN PHYSICS

Supervisor

Professor Pavlos Lagoudakis,

Co-Supervisor

Assistant Professor Sergey Alyatkin

Moscow - 2023

© Ivan Gnusov, 2023.

I hereby declare that the work presented in this thesis was carried out by myself at Skolkovo Institute of Science and Technology, Moscow, except where due acknowledgement is made, and has not been submitted for any other degree.

Ivan Gnusov

Prof. Pavlos G. Lagoudakis

Abstract

This thesis is devoted to the study of exciton-polaritons, which are quasi-particles that emerge in the semiconductor microcavity in the strong coupling regime of excitons and photons. One of the interesting properties of polaritons is their ability to form macroscopic coherent state, known as polariton condensate. The thesis focuses on examining the spin and vorticity of the polariton condensate confined in two types of non-resonant optical traps: static and rotating.

It is revealed that the spin of the condensate in the static annular trap is significantly influenced by the characteristics of the excitation laser (power and polarisation) as well as the size of the optical trap. The process of optical orientation (acquiring the spin state from the excitation) is demonstrated to dictate the spin dynamics for the circular polarisation of the pump laser. Conversely, for linear polarisation, the spin of the condensate is found to be constrained by the in-plane effective magnetic field defined by the excitation position on the sample and induced by strain-related birefringence. However, the stability of the condensate's spin for linear pump polarisation just above the condensation threshold (or with a smaller optical trap) is disrupted by polariton interactions, resulting in stochastic spin flips and a zero integrated degree of polarisation of condensate emission.

In contrast, for the elliptical optical trap, it is shown that the sample birefringent field can be overcome by the interplay of the cavity TE-TM splitting and the elliptical condensate distribution. It results in the condensate adopting a definite linear polarisation directed along the short axis of the ellipse. The all-optical control over the azimuthal angle of linear polarisation of the condensate emission is demonstrated. Furthermore, an investigation of the two coupled elliptical condensates reveals distinctive coupling regimes based on their mutual orientation and separation distance.

Further, a novel approach for rotation of the excitation pattern for polaritons at GHz frequency is introduced. It is achieved by the beating note of two frequency-detuned and shaped laser beams. By recreating the elliptical profile used for the

linear polarisation control and rotating it at GHz frequency, the fundamental regime of the optically driven spin precession previously unseen in polariton condensates is discovered. This spin precession occurs only in resonance with the internal condensate self-induced precession and features a striking coherence of at least 170 ns.

Finally, it is shown that increasing the rotating trap size gives rise to the vortex forming in the condensate for the narrow range of stirring frequencies from 1 to 4 GHz. The winding of the phase in the vortex corotates with the optical trap, akin to the famous "rotating bucket" experiment with conventional superfluids.

Overall, the obtained results demonstrate the vast possibilities of the control on the spin and vortex degree of freedom in polariton condensate and showcase the rich physics of the studied system. These findings could benefit the application of polaritons in analogue and quantum computing and spinoptronics.

Keywords: Polariton, Polariton condensate, Spin, Vortex

Publications

Published as part of this thesis

1. I. Gnusov, H. Sigurdsson, S. Baryshev, T. Ermatov, A. Askitopoulos, and P. G. Lagoudakis, "Optical orientation, polarization pinning, and depolarization dynamics in optically confined polariton condensates," *Phys. Rev. B*, vol. 102, p. 125419, Sep 2020;
2. I. Gnusov, H. Sigurdsson, J. Töpfer, S. Baryshev, S. Alyatkin, and P. Lagoudakis, "All-optical linear-polarization engineering in single and coupled exciton-polariton condensates," *Phys. Rev. Applied*, vol. 16, p. 034014, Sep 2021;
3. I. Gnusov, S. Harrison, S. Alyatkin, K. Sitnik, J. Töpfer, H. Sigurdsson, and P. Lagoudakis, "Quantum vortex formation in the "rotating bucket" experiment with polariton condensates," *Science Advances*, vol. 9, no. 4, p. eadd1299, 2023;
4. I. Gnusov, S. Baryshev, H. Sigurdsson, K. Sitnik, J. Töpfer, S. Alyatkin, and P. G. Lagoudakis, "Optically driven spin precession in polariton condensates," preprint *arXiv 2305.03782*, 2023;
5. I. Gnusov, H. Sigurdsson, S. Baryshev, A. Askitopoulos, and P. G. Lagoudakis, "Pseudo-spin destabilization in optically confined exciton-polariton condensates," in *Frontiers in Optics / Laser Science*, p. FTu2D.4, Optica Publishing Group, 2020; *Proceedings to Frontiers in Optics Conference*;

Other papers with Skoltech affiliation

1. H. Sigurdsson, I. Gnusov, S. Alyatkin, L. Pickup, N. A. Gippius, P. G. Lagoudakis, and A. Askitopoulos, "Persistent self-induced larmor precession evidenced through periodic revivals of coherence," *Phys. Rev. Lett.*, vol. 129, p. 155301, Oct 2022;
2. K. A. Sitnik, S. Alyatkin, J. D. Töpfer, I. Gnusov, T. Cookson, H. Sigurdsson, and P. G. Lagoudakis, "Spontaneous formation of time-periodic vortex cluster in nonlinear fluids of light," *Phys. Rev. Lett.*, vol. 128, p. 237402, Jun 2022;

3. S. Baryshev, A. Zasedatelev, H. Sigurdsson, I. Gnusov, J. D. Töpfer, A. Askitopoulos, and P. G. Lagoudakis, "Engineering photon statistics in a spinor polariton condensate," *Phys. Rev. Lett.*, vol. 128, p. 087402, Feb 2022;
4. T. Ermatov, R. E. Noskov, A. A. Machnev, I. Gnusov, V. Atkin, E. N. Lazareva, S. V. German, S. S. Kosolobov, T. S. Zatsepin, O. V. Sergeeva, J. S. Skibina, P. Ginzburg, V. V. Tuchin, P. G. Lagoudakis, and D. A. Gorin, "Multispectral sensing of biological liquids with hollow-core microstructured optical fibres," *Light: Science and Applications*, vol. 9, Oct. 2020;
5. T. Ermatov, I. Gnusov, J. Skibina, R. E. Noskov, and D. Gorin, "Noncontact characterization of microstructured optical fibers coating in real time," *Optics Letters*, vol. 46, p. 4793, Sept. 2021.

Conferences

1. I. Gnusov, S. Harrison, S. Alyatkin, K. Sitnik., J. Topfer, H. Sigurdsson, P.G. Lagoudakis, "Quantized Vortex Formation in the "Rotating Bucket" Experiment with Nonlinear Fluids of Light", PLMCN 2023. Invited talk;
2. I. Gnusov, S. Harrison, S. Alyatkin, K. Sitnik, J. Topfer, H. Sigurdsson, P.G. Lagoudakis, "Stirring-Induced Vorticity in Nonlinear Fluids of Light", TER-AMETANANO 2022. Invited talk;
3. I. Gnusov, H. Sigurdsson, S. Baryshev, T. Ermatov, A. Askitopoulos, and P. G. Lagoudakis, "Polarization dynamics in optically confined polariton condensates", PLMCN 2020. Poster;
4. I. Gnusov, H. Sigurdsson, S. Baryshev, T. Ermatov, A. Askitopoulos, and P. G. Lagoudakis, "Pseudospin destabilization in optically confined exciton-polariton condensates", *Frontiers in optics + Laser Science* 2020. Oral talk.

Patents

1. I. Gnusov, S. Baryshev, P. G. Lagoudakis, "Method of optical control of linear polarization of the emission", 2023.

Acknowledgements

I would like to express my appreciation and gratitude to all the people who have helped and guided me throughout my PhD journey.

First of all, I am grateful to my supervisor, prof. Pavlos Lagoudakis for giving me the opportunity to work in such a great lab, for his mentorship, advice and support throughout my study.

I thank my co-supervisor Sergey Alyatkin for the guidance in the experiments, for his in-depth knowledge of physics, for the help in alignment, advice on figures design, proofreading of the papers and for injecting a coffee culture to me.

I am grateful to Dr Helgi Sugurdsson for all the numerical simulations and theory he did for our projects, and for his tricky questions on the research, thoroughness, and his invaluable contribution to the papers writing.

I am grateful to Kirill Sitnik for the fruitful discussions on various topics and his assistance and ideas in the experiments.

I am grateful to Stepan Baryshev for all the experiments we did together and for all the discussions of the results.

I am also grateful to Anton Putintsev, Stepan Baryshev, Kirill Sitnik and Sergey Alyatkin for sharing the office and creating a supportive and friendly atmosphere there, and for the coffee breaks and walks.

I appreciate the teaching and insights on polariton physics from Timur Ermatov, Timur Yagafarov, and Alexis Askitopoulos. I am grateful to Tamsin Cookson for the fruitful discussions, and to Dr. Stella Harrison for the simulations for the "Rotating Bucket" experiment, and to all other members of the Hybrid Photonics Labs.

Also, I would like to thank Skoltech for being a wonderful place to study and do research. And finally, I am very grateful to my parents and friends for their constant support.

Glossary

AD Anti-diagonal
AOM Acousto-optic modulator
BEC Bose-Einstein condensate
BS Beamsplitter
CCD Charge-coupled device
D Diagonal
Det. Detector
DOP Degree of polarisation
DLP Degree of linear polarisation
DCP Degree of circular polarisation
FFT Fast Fourier transformation
FWHM Full width at half maximum
GPE Gross-Pitaevskii equation
H Horizontal (polarisation)
HBT Hanbury Brown and Twiss
HWP Half-wave plate
IFFT Inverse Fast Fourier transformation
LP Lower polariton
LPB Lower polariton branch
NA Numerical Aperture
NRMSE Normalised root mean squared error
OAM Orbital Angular Momentum
PBS Polarising Beamsplitter
PL Photoluminescence
SLM Spatial Light modulator
TCSPC Time-correlated Single Photon Counting
QWP Quarter-wave plate
V Vertical
VCSEL Vertical-cavity surface-emitting laser

Contents

1	Introduction	16
2	Physics of Polaritons	21
2.1	Microcavity	21
2.2	Excitons	24
2.3	Strong light-matter coupling regime	25
2.4	Condensation	28
2.4.1	Bose-Einstein Condensates	28
2.4.2	Polariton condensate.	29
2.5	Ballistically propagating vs trapped condensates	32
2.6	Vortices in polariton condensates	35
2.7	Superfluidity of polariton condensates	40
2.8	Polariton spin	41
3	Experimental Setup and Techniques	44
3.1	Excitation part	45
3.1.1	Excitation laser	45
3.1.2	Shaping the excitation beam with spatial light modulator	46
3.1.3	Time-periodic excitation pattern	50
3.2	Sample	51
3.3	Detection part	53
3.3.1	Real-space imaging	53
3.3.2	Spectrum and momentum	54
3.3.3	Phase read-out	55
3.3.4	Phase retrieval: off-axis digital holography	58
3.3.5	Photon statistics measurements	59
3.3.6	Polarisation measurements	61
3.4	Generalised Gross-Pitaevskii Equation	66
4	Spin of Polariton Condensate in the Optical Trap	68
4.1	Introduction	68
4.2	Excitation configuration and optical setup	70
4.3	Spin of polariton condensate under non-resonant excitation: descriptive features	71
4.4	Experimental results	72
4.5	Trap size dependence of the condensate spin.	81
4.6	Theory and Simulations	85

4.7	Self-induced Larmor precession	89
4.8	Conclusions	90
5	All-Optical Linear-Polarisation Engineering in Single and Coupled Polariton Condensates	92
5.1	Introduction	93
5.2	Experimental setting	94
5.3	Elliptical optical trap and linear polarisation	95
5.4	Elliptical condensates excited by different polarisations	96
5.5	All-optical linear polarisation Engineering	99
5.5.1	Elliptical excitation pattern	99
5.5.2	8-point excitation pattern	100
5.6	Compensation for experimental setup optical retardance	101
5.7	Theory of a single condensate in an elliptical trap	104
5.8	Effect of spatial ellipticity	106
5.9	Coupled elliptical condensates	107
5.10	Theory of Coupled condensates	113
5.11	Conclusion	116
6	Driven Spin Precession in Polariton Condensate	117
6.1	Introduction	117
6.2	The quest for the rotating trap realisation	119
6.3	Slow MHz polarisation rotation	124
6.4	Control over spin rotation direction	127
6.5	GHz precession and resonance	128
6.6	Persistence of the precession	132
6.7	Theory	133
6.8	GPE simulations	134
6.9	Conclusion	136
7	Vortices in "Rotating Bucket" Experiment with Polariton Conden- sate	138
7.1	Introduction	139
7.2	Experimental setup	144
7.3	Vortex observation	145
7.4	Frequency dependence	147
7.5	Numerical simulation of 2D Gross-Pitaevskii equation.	154
7.6	Why the second vortex does not appear?	157
7.7	Pump power dependence of the condensate emission	159
7.8	Bigger rotating traps	160
7.9	Conclusions	161

8 Conclusion and Outlook	164
REFERENCES	168

List of Figures

2-1	Distributed Bragg reflector and its reflectivity spectrum.	22
2-2	Semiconductor microcavity: structure and reflectivity.	23
2-3	Dispersion of upper and lower polariton branch at different photon-exciton detunings and corresponding Hopfield coefficients.	28
2-4	Mechanism of polariton condensation	31
2-5	The hallmarks of polariton condensation	33
2-6	Experimentally obtained characteristics of the optically trapped and ballistically expanding condensate.	36
2-7	Vortices in polariton condensates.	37
2-8	Vortices in polariton condensates: chain and lattice.	39
3-1	The sketch of the MBR-110 Ti:Sapphire laser cavity.	46
3-2	Principles of the operation of spatial light modulator.	47
3-3	Principles of the operation of spatial light modulator: example of SLM holograms and generated laser patterns	49
3-4	The excitation part of the experimental setup.	50
3-5	Experimental setup for the rotating excitation pattern generation.	51
3-6	Microcavity Sample: structure, reflection spectrum and polariton dispersion	52
3-7	Detection part of the experimental setup.	54
3-8	Homodyne interferometry setup: interference of the condensate emission with the external resonantly seeded to the condensate reference laser.	56
3-9	The interference of the condensate with the retro-reflected copy of itself and reconstructed phase.	57
3-10	The principles of off-axis digital holography.	60
3-11	Poincare sphere for the representation of polarisation states.	63
3-12	Polarimeter optical setup.	65
4-1	The schematic of the experimental setup for the characterisation of spin of polariton condensate in the optical trap.	70
4-2	The schematic of the lower polariton dispersion illustrating the formation mechanisms of the condensate spinor under non-resonant excitation.	72
4-3	Condensate in the ring confining potential: pump profile, density and dispersion.	73

4-4	Emission intensity, DOP, DLP and S_3 of trapped polariton condensate. The ring trap diameter is $12 \mu\text{m}$.	74
4-5	Simulated dynamics of the condensate spin under linearly polarised excitation.	76
4-6	Experimental evidence of the condensate spin flips under linearly polarised excitation.	77
4-7	S_1 and S_2 components of the condensate emission for two spots on the sample demonstrating the place-dependent birefringence.	78
4-8	Polarisation components of the condensate non-resonantly excited with a slightly elliptically polarised laser.	79
4-9	Stokes vectors of the condensate emission on Poincare sphere.	80
4-10	Spin of polariton condensate in the optical trap for two values of exciton-photon detuning.	81
4-11	Intensity and blueshift of the confined condensate as a function of pump power for different trap sizes.	82
4-12	DLP polarisation maps for the condensate formed in the annular optical traps of different sizes.	83
4-13	Stokes components and DOP of the condensate PL as a function of pump power and QWP angle for different sizes of the annular optical trap.	84
4-14	Condensate polarisation as a function of pump power and incident linear polarisation azimuth angle (for the condensate in the annular optical trap)	85
4-15	Dynamics of the condensate spin for different polarisation of the non-resonant pump retrieved from numerical simulations.	88
4-16	The experimental evidences of self-induced Larmor precession.	90
5-1	Elliptical laser pump profile and correspondent condensate intensity.	95
5-2	Control of the linear polarisation of the condensate PL with the orientation of the non-resonant optical trap.	96
5-3	Condensate Stokes components for different pump powers and directions of linear polarisation of the excitation laser (elliptical optical trap).	97
5-4	Condensate Stokes components for different pump powers and polarisation ellipticity in the units of QWP angle (for the elliptical optical trap).	98
5-5	Rotation of the linear condensate polarisation by all-optical means - by rotation of the excitation laser profile.	100
5-6	Linear polarisation engineering of the condensate emission for the 8-Gaussian excitation profile.	101
5-7	The raw data for the condensate spin measurements.	102
5-8	Energy splitting in elliptical condensate.	104
5-9	Effect of spatial ellipticity on the polarisation of the condensate.	107
5-10	Two coupled horizontally elongated elliptical condensates	108
5-11	Two coupled elliptical condensates at different separation distance: experiment and simulations.	111

5-12	Two coupled elliptical condensates - additional experimental data. . .	112
6-1	Rotating trap profile for the optically driven spin precession of the condensate.	121
6-2	Experimental setup for the realisation of the rotating optical pattern with AOMs used for the laser frequency shift.	121
6-3	Experimental setup for the realisation of the rotating optical pattern with the beating note of two single-mode lasers.	123
6-4	Mutual frequency stability of two excitation lasers.	124
6-5	Optically driven spin precession: schematic of the excitation part of experimental setup and polariton condensate intensity distribution. .	125
6-6	Rotation of polariton condensate polarisation under slow stirring. . .	127
6-7	Control on the direction of the optically driven spin precession. . . .	128
6-8	GHz optically driven spin precession evidenced through the photon correlation measurements.	130
6-9	GHz rotation of the condensate pseudospin appearing in resonance with internal Larmor precession.	131
6-10	Measured $g_{H,V}^{(2)}$ of the condensate emission at big time delay.	133
7-1	The "rotating bucket" experiment with superfluid He.	141
7-2	The "rotating bucket" experiment with atomic Bose-Einstein condensates.	143
7-3	Excitation part of the experimental setup for the realisation of "rotating bucket" experiment with polariton condensates.	144
7-4	Quantised vortex formation in the "rotating bucket" experiment with polariton condensates.	146
7-5	Energy and intensity distribution of the condensate in the static annular optical trap.	147
7-6	Deterministic control of the quantum vortex charge.	148
7-7	Condensate intensity and energy dispersion for different rotation speed. .	149
7-8	Examples of polariton condensate phase distribution under different stirring frequencies.	151
7-9	Frequency dependence of the quantised vortex formation in stirred polariton condensates.	153
7-10	Condensate intensity and phase distribution simulated with 2D generalised Gross-Pitaevskii equation.	156
7-11	Numerically simulated snapshots of the active reservoir intensity distribution for different rotation frequency.	157
7-12	Condensate energy pump power dependence for different stirring frequencies.	158
7-13	Bigger number of vortices in the "rotating bucket" experiment with polaritons.	160
7-14	"Rotating bucket" experiment in different systems.	162

Chapter 1

Introduction

Photonics and solid-state physics are two pivotal fields at the forefront of twenty-first century science and technology. They offer a wide range of applications that have a profound impact on our daily lives. On the one hand, photonics studies the fundamental properties of light and its interactions with matter. Nowadays, photonics plays a crucial role in internet data transmission, medical imaging, environment monitoring, sensing and advanced manufacturing. On the other hand, solid-state physics focuses on the study of the physical properties of condensed matter. These studies have driven rapid progress in semiconductors, nanotechnology, and quantum computing. For instance, semiconductor components, such as transistors, form the foundation of modern electronics and are crucial for computers, smartphones, and other devices.

The development of the scientific knowledge and complexity of the investigated subjects blur the boundaries between different scientific disciplines. This has led to the emergence of combined research directions, such as biophysics, bioinformatics, physical chemistry and many others. The established communication and joint effort of scientists with different specialisations results in state-of-the-art research and advanced technologies [11, 12].

Polaritonics is a great example of the collaborative synergy of photonics and solid-state physics. Combining insights from both fields it forms a separate research direction with remarkable findings and applications. Polaritonics studies exciton-

polaritons (*polaritons* further on), which are bosonic quasi-particles formed as a result of the strong coupling of exciton and photon in the semiconductor microcavity [13]. Being part-light, part-matter, they inherit the properties from both constituents. Namely, the small effective mass, short lifetime and high mobility from the photons, and interactions from excitons. Moreover, polaritons are bosons, so they can occupy the single energy-momentum state, forming a condensate. Thanks to the low effective mass, polaritons feature a much higher critical temperature for condensation than that of the atomic Bose-condensates and can condense even at room temperature [14]. The condensate is formed at the balance of the external laser or electric pump and polariton dissipation. The latter allows non-invasively characterising the polariton state only through conventional optical devices. This makes polaritons a very practical system to investigate and visualise the many-body and quantum phenomena. In fact, since the first condensate observation in 2006 [15] numerous interesting effects have been reported including quantised vortices [16], superfluidity [17], solitons [18] and other [19, 20].

The intriguing direction for polariton research is an investigation of extended arrays of condensates. Different lattice geometries were realised for polaritons with optical imprinting [21, 22, 23] or cavity etching techniques [24]. The condensates in the lattice interact with each other and can synchronise, forming exotic energy states. The flexibility in shaping the energy landscapes for polaritons makes them promising candidates for the analogue simulations [23, 25, 26]. It suggests that by preparing the array of condensates in the required manner, it is possible to emulate the problem which cannot be solved numerically by a conventional computer (like diagonalisation of the Hamiltonian of complex many-body systems or optimisation problems). While the early proposals for the simulator focused on the ballistically propagating condensates, the optically confined condensates could benefit the future device by prolonged condensate coherence time.

The approach for optical confinement was introduced in 2014 [27]. There, the annular laser pattern creates the ring-shaped repulsive potential for polaritons, making them condense inside the trap [28]. The decreased spatial overlap of the condensate and incoherent exciton reservoir diminishes their interactions and leads to an in-

crease in phase and spin coherence times. Similarly to the ballistic condensates [29], the confined ones can also synchronise [30] and form lattices of different geometries [21, 31]. Moreover, confined condensate features well-defined pseudo-spin (or just spin) that can be another degree of freedom for the future simulator [32]. It is worth mentioning that polariton spin itself has remarkable properties. The spin-anisotropic interactions and polariton non-linearity make the spin physics quite rich, and numerous intriguing properties have been reported [33, 34, 35] with the scarce investigation of optically confined condensates [36]. Moreover, the variety of the observed phenomena makes polaritons prominent in another interdisciplinary application - spinoptronics [37]. Spinoptronics combines the best of photonics and spintronics in order to create efficient and effective devices with unique properties. Nevertheless, before these promising applications are possible, it is essential to study the behaviour of the spin at different excitation conditions and develop ways to control it.

In this regard, the *first objective* of this thesis is to carry out the comprehensive study of the spin of polariton condensate in the optical trap. The aim is to investigate the effects of the non-resonant pump polarisation and power, along with the shape and size of the optical trap, on the dynamics of the condensate spin. Given that, we will be able to develop tools for the all-optical deterministic spin control for applications in analogue simulations and spinoptronics.

Regardless of the advances in building spatially periodic lattices of coupled condensates, the time-periodic potentials have remained out of the scope of polariton research. This was primarily due to the ultra-fast modulation frequency required in order to affect the polariton state defined by its short ps- lifetime and nanosecond condensate coherence. Notably, the periodic potentials are actively utilised in the adjacent science fields, for instance, for Floquet engineering [38, 39], and spin manipulation in BEC [40]. The specific case of the time-periodic potential is a rotating one. The rotating potentials, in turn, are also widely studied in BECs [41, 42] and superfluids [43, 44] systems. For example, the famous signature experiment for the superfluid, known as the "Rotating bucket", concerns the dynamics of the superfluid (and later BEC) in the rotating reservoir. Being non-rotational by nature, superfluid

indeed can acquire the external rotation of the container in the form of quantised vortices.

In this regard, *the second aim of this thesis* is to develop a time-periodic rotating potential for polariton condensate and investigate the vorticity in the stirred quantum fluid of light. Moreover, linking to the previous objective, the condensate spin in the time-periodic potentials is to be studied.

The study of vortices in polariton condensate is blooming now [7, 45, 46, 47] driven by the possible application for quantum computing [48] and analogue simulation [31]. So, the means for vortex generation and control are in high demand.

All in all, we have discussed the general motivation for this work. The more focused introduction for each study is given in the corresponding Chapters 3-7. It is worth mentioning that before we arrive at the beautiful applications of polaritons, it is crucial to gain a deep understanding of polariton physics, and this is what was the main driving force for this thesis.

Overall, the thesis is divided into eight chapters. The thesis continues with a brief introduction to the physics of polaritons and polariton condensates (Chapter 2). The main experimental techniques and methods used in this work are discussed in Chapter 3. The foundation of the research part of the thesis is four articles featured with Author - Refs. [1, 2, 3, 4]. In Chapter 4, the experimental results of the study of the condensate spin in the optical trap for various excitation conditions are discussed. Chapter 5 concerns a developed method of all-optical linear polarisation control of the condensate emission by utilising the elliptical optical trap. The Chapter 5 also includes the study of two coupled elliptical condensates and the identification of their distinctive spinor synchronisation regimes. Chapter 6 delves into the methodology of achieving a GHz rotation of the optical trap for polaritons. The Chapter provides a detailed account of the optically driven spin precession triggered by the rotating optical pattern, uncovering its resonance characteristics and remarkable coherence. In Chapter 7, the discussion centres around the formation of a quantised vortex in the stirred polariton condensate, elucidating its frequency dependence analogous to the "rotating bucket" experiment.

Chapter 1 - Introduction : This part of the thesis includes a brief review of the

research field, novelty and motivation.

Chapter 2 - Physics of Polaritons : This part of the thesis includes a review of polaritons and polariton condensates, their superfluidity, spin and vortices.

Chapter 3 - Experimental Setup and Techniques : This part of the thesis describes the main experimental approaches used in the thesis.

Chapter 4 - Spin of Polariton Condensate in the Optical Trap : This part of the thesis concerns the investigation of the spin of optically confined polariton condensate depending on pump power, polarization and the size of the trap.

Chapter 5 - All-Optical Linear-Polarization Engineering in Single and Coupled Exciton-Polariton Condensates : This part of the thesis concerns the study of polarization properties of the condensate in the elliptical trap and achieving control over linear spin projection.

Chapter 6 - Driven Spin Precession in Polariton Condensate : This part of the thesis describes the study of the condensate spin in the rotating trap that revealed the resonance GHz spin precession with striking spin coherence.

Chapter 7 - Vortices in "Rotating Bucket" Experiment with Polariton Condensate: This part of the thesis describes the study of the vorticity in a rotating optical trap that revealed the co-rotating vortex in the condensate in the narrow range of GHz frequencies.

Chapter 8 - Conclusion and Outlook : This part of the thesis includes conclusive remarks and an outlook for future research.

Chapter 2

Physics of Polaritons

Polaritons are the quasi-particles which arise in the strong coupling regime between the microcavity photon and quantum well exciton.

At first glance, this definition could seem unclear and loaded with complex terms. So, in this chapter, the related terms will be introduced consequently. Further, the polariton condensates physics and the recent studies relevant to this thesis will be discussed.

2.1 Microcavity

The microcavity consists of two mirrors closely spaced together so that the distance between them is comparable to the light wavelength. To realise the high reflectivity and avoid the absorbance of the metallic mirrors, the distributed Bragg reflectors (DBRs) are used to build a microcavity [13]. The DBR is a composite structure constructed from the alternating layers of two semiconductor materials with refractive indices n_1 and n_2 (see Figure 2-1(a)). The optical thickness of each layer is chosen to be the quarter of the desired wavelength λ_0 of light to be reflected from the mirror. As a result of the multiple reflections from each layer and the destructive interference of incident light, the DBR structure provides the maximum amount of reflection for the defined part of the spectrum (DBR photonic stop-band). The typical DBR reflectivity spectrum is presented in Figure 2-1(b). Notably, the reflectivity

of the structure in the stop-band could reach high values of more than 99.9%. The width of the stop-band is defined by the layers' refractive indices. The reflectivity R of the structure is usually calculated by the Transfer Matrix method [49], but the middle of the stop-band can be approximated by

$$R = \left(\frac{n_2^{2N} - n_1^{2N}}{n_2^{2N} + n_1^{2N}} \right)^2 \quad (2.1)$$

where N is the number of pairs of low and high refractive index layers in the DBR.

If some media (semiconductor layer or other) with the optical thickness of the several half-wavelength $\lambda_c/2$ of light is sandwiched between two DBRs (see Figure 2-2(a)), they form a microcavity. This results in the formation of a confined optical mode inside the cavity. Figure 2-2(b) depicts the modified reflectivity spectrum and features the reflection minimum in the stop-band at λ_c .

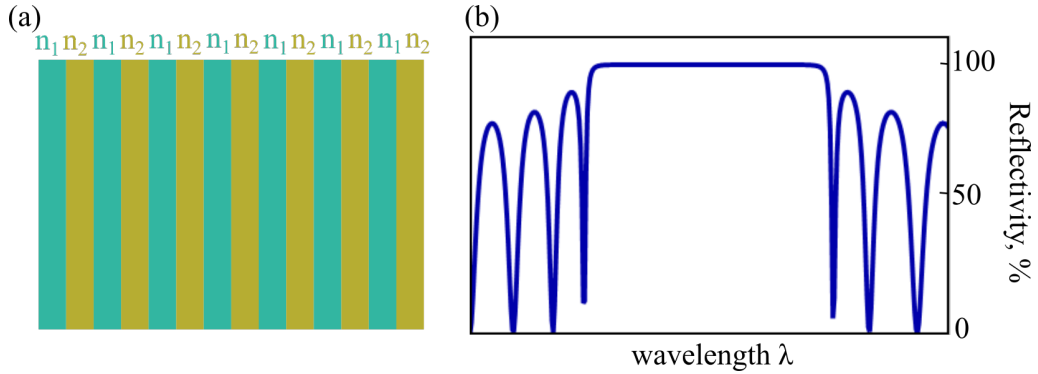


Figure 2-1: (a) The schematic of the Distributed Bragg Reflector (DBR) built of the alternating layers of two semiconductor materials with different refractive indices n_1 and n_2 . (b) The typical reflectivity spectrum of the DBR at a normal incidence.

The quality factor of such micro-resonator is defined by the reflectance R_1 and R_2 of the DBRs and written as [20]

$$Q = \frac{\lambda_c}{\Delta\lambda_c} \simeq \frac{\pi \sqrt[4]{R_1 R_2}}{1 - \sqrt{R_1 R_2}}. \quad (2.2)$$

where $\Delta\lambda_c$ is the width of the resonance. Thanks to the high reflectance of the DBRs, it is possible to produce the microcavity with extremely high Q-factors (10^5 and more). The Q factor defines the number of times that the photon confined in the microcavity is reflected back and forth - the bigger Q, the better the confinement.

The high Q-factor allows for the realisation of the strong coupling regime in the polariton microcavity due to multiple acts of creation and dissociation of photon and exciton. Moreover, the confined resonant light obtains a dramatic increase in the electric field inside the cavity with respect to the free space, which also favours the strong coupling.

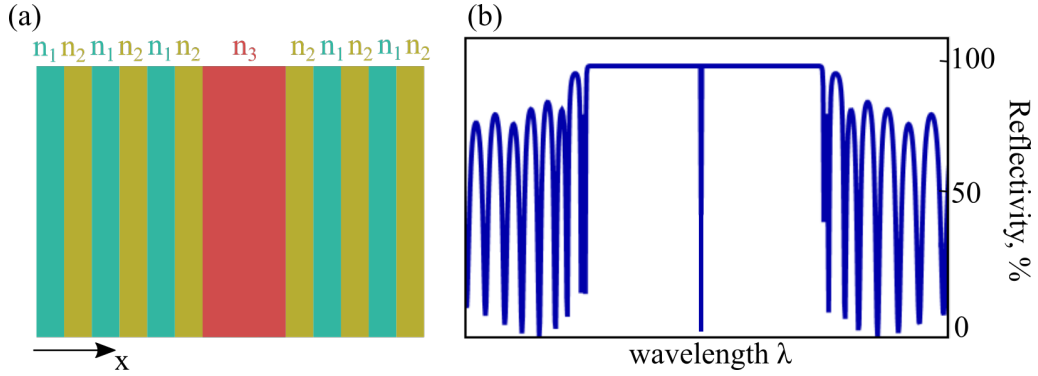


Figure 2-2: (a) The schematic of the microcavity built of DBRs. (b) The typical reflectivity spectrum of the microcavity.

The light passing through the microcavity perpendicularly to the layers (along the x-direction in Figure 2-2(a)) with the wavelength λ_c is confined in only this direction but not in two other in-plane ones. If the incident light is coming at a slight θ angle with respect to the x-axis, then the resonance wavelength is changed to $\lambda_c/\cos(\theta)$. In this regard, the dispersion of the light in the microcavity differs from the linear dispersion of the free propagating light ($E = \hbar ck$). It is more convenient to consider separately the out-of-plane (confined) and in-plane components of the light in the microcavity. The k-vector of the light can be written as $k = \sqrt{k_{\perp}^2 + k_{\parallel}^2}$. So the microcavity dispersion at the small k_{\parallel} appears to be quadratic as a function of k_{\parallel} (reminiscent of the particle with the mass) [13, 20]:

$$E_c(k_{\parallel}) = \frac{\hbar c}{n_c} \sqrt{k_{\perp}^2 + k_{\parallel}^2} \approx \frac{\hbar c}{n_c} k_{\perp} \left(1 + \frac{k_{\parallel}^2}{2k_{\perp}^2} \right) = E_c(0) + \frac{\hbar^2 k_{\parallel}^2}{2m_{ph}} \quad (2.3)$$

As long as the k_{\perp} is quantised in the microcavity $k_{\perp} = n_c(2\pi/\lambda_c) \times n$, where n_c is the cavity refractive index, the photon dispersion in the microcavity is parabolic so that photon acquires an effective mass m_{ph} . The effective mass can be deduced from the dispersion curve as follows:

$$\frac{1}{m_{ph}} = \frac{1}{\hbar^2} \frac{\partial^2 E_c}{\partial k_{||}^2} \quad (2.4)$$

The typical value of the photon effective mass in the microcavity is 10^{-5} of the free electron mass m_e .

2.2 Excitons

The other component of polariton is an exciton. Exciton is a quasi-particle that arises in the semiconductor [50]. The mole of a semiconductor (for example, the mole of silicon has a weight of 28g) consists of 6.022×10^{23} atoms; it is practically impossible to describe the properties of each atom and their behaviour in such a gigantic ensemble. The standard approach in solid-state physics is the description of the matter in terms of its excitation or quasi-particles. For this, the whole solid is thought to be in the stable ground state, while the state of the solid is described by the excitations above this ground state, which interact with each other and define the properties of the semiconductor. When the electron is excited from the valence to the conduction band (by the voltage or photon), it leaves a vacancy in the valence band. This vacancy can be treated as a positively charged quasi-particle called a "hole". Both electron and hole are characterised by the effective mass, which may significantly differ from that of the free electron [13, 20]. In this regard, the exciton is a quasi-particle formed via Coulomb attractive interaction between an excited electron and a hole. The exciton, thus, is a neutral bosonic quasi-particle and has properties similar to that of the hydrogen atom (bound state of nucleus and electron).

There are two types of excitons in semiconductors - Wannier-Mott and Frenkel. The Frenkel [51] excitons are highly bound and localised on the scale of one atom - the typical binding energy and radius are on the order of 1 eV and 1 nm, respectively. However, these excitons are inherent to the molecular structures (e.g. organic molecules [14, 52]) that are out of the scope of this thesis. So further, only Wannier-Mott excitons [53], which form in the semiconductor crystals and have a typical binding energy of 10-100 meV and size of several lattice constants ($\approx 10\text{nm}$) [50, 54]

will be considered. These excitons usually disintegrate at the ambient conditions since their binding energy is less than the room temperature (25 meV), so experiments with inorganic microcavity polaritons are usually carried out at cryogenic temperatures (with the notable exception of perovskite [23] microcavities).

The confinement in 2D can increase the binding energy of the exciton. The semiconductor quantum well (the layered sandwich structure of two thin semiconductors of different band gap energy) is used for this. The dispersion of the confined exciton is also parabolic and written as

$$E_{ex}(k_{\parallel}) = E_g + E_{conf} - \frac{Ry}{(n - \frac{1}{2})^2} + \frac{\hbar^2 k_{\parallel}^2}{2m_{ex}}, n \in \mathbb{N}^+. \quad (2.5)$$

where E_g is the band-gap energy of the semiconductor, E_{conf} is the confinement energy due to quantum well, Ry is the exciton Rydberg energy (analogously to the hydrogen atom), m_{ex} is the exciton mass. The typical exciton mass is $10^{-2}m_e$.

Depending on the spin of constituents, excitons can have different integer-valued spin ($\pm 1, \pm 2$). However, due to spin conservation laws, only excitons with unity spin can interact with light (photon spin is ± 1); such excitons are called "bright". So, for the quantum well inside the microcavity described above, the bright excitons inside the quantum well can be created by illuminating the structure with light. When exciton decays, the photon is born, which can still survive in the microcavity, reflect back to the quantum well and excite another exciton. Thus, matter (exciton) and light (photons) are coupled in the microcavity structure.

2.3 Strong light-matter coupling regime

When the number of absorption and emission events for "the same" photon is significant in the microcavity, it can no longer be described by the bare exciton and cavity photon. In turn, the system is now described by the part light part-matter states - exciton-polaritons. This is a strong coupling regime - the regime when the interaction rate between photon and exciton is higher than their inversed lifetimes in the sample. The photon-exciton interaction is characterised by the Rabi frequency Ω_R , the cavity photon and exciton inverse lifetimes are γ_{ex}, γ_{ph} , so the strong coupling

condition reads as

$$\Omega_R > \gamma_{ex}, \gamma_{ph} \quad (2.6)$$

The Hamiltonian of the interacting photon and exciton can be written as the sum of three terms: bare photon \hat{H}_{ph} , bare exciton \hat{H}_{ex} and their interaction \hat{H}_{int} .

$$\hat{H} = \hat{H}_{ph} + \hat{H}_{ex} + \hat{H}_{int} \quad (2.7)$$

In the second quantization terms, the constituents of the master Hamiltonian are written as [13]:

$$\hat{H}_{ph} = \sum_k E_{ex}(k) \hat{X}_k^\dagger \hat{X}_k \quad (2.8)$$

$$\hat{H}_{ex} = \sum_k E_{ph}(k) \hat{P}_k^\dagger \hat{P}_k \quad (2.9)$$

$$\hat{H}_{int} = \sum_k \hbar\Omega_R (\hat{P}_k^\dagger \hat{X}_k + \hat{X}_k^\dagger \hat{P}_k) \quad (2.10)$$

where \hat{X}_k, \hat{P}_k are annihilation operators for exciton and photon respectively, $\hbar\Omega_R$ is interaction strength.

For simplicity, the Hamiltonian (2.7) can be rewritten in the matrix form $D(k)$:

$$D(K) = \begin{pmatrix} E_{ex}(k) & \hbar\Omega_R \\ \hbar\Omega_R & E_{ph}(k) \end{pmatrix} \quad (2.11)$$

Substituting the expressions for the E_{ex} and E_c from Equations (2.5) and (2.3) respectively and diagonalising the Equation (2.11) one gets two new eigenenergies of the system - lower(LP) and upper(UP) polaritons:

$$E_{UP}(k_{||}) = \frac{E_{ex}(k_{||}) + E_{ph}(k_{||})}{2} + \frac{1}{2} \sqrt{\Delta(k_{||})^2 + 4\hbar^2\Omega_R^2} \quad (2.12)$$

$$E_{LP}(k_{||}) = \frac{E_{ex}(k_{||}) + E_{ph}(k_{||})}{2} - \frac{1}{2} \sqrt{\Delta(k_{||})^2 + 4\hbar^2\Omega_R^2} \quad (2.13)$$

$\Delta(k_{\parallel})$ in (2.12) is energy difference between photonic and excitonic energies ($E_{ph}(k_{\parallel}) - E_{ex}(k_{\parallel})$). $\Delta(0)$ is called exciton-photon detuning, and it is an important quantity for polariton characterisation.

Thus, the polaritons are part-light, part-matter quasi-particles. The fraction of the photonic $|c_{k_{\parallel}}|^2$ and excitonic $|\chi_{k_{\parallel}}|^2$ part in polariton is described by the Hopfield coefficients:

$$|c_{k_{\parallel}}|^2 = 0.5 \left(1 - \frac{\Delta(k_{\parallel})}{\sqrt{\Delta(k_{\parallel})^2 + 4\hbar^2\Omega_R^2}} \right) \quad (2.14)$$

$$|\chi_{k_{\parallel}}|^2 = 0.5 \left(1 + \frac{\Delta(k_{\parallel})}{\sqrt{\Delta(k_{\parallel})^2 + 4\hbar^2\Omega_R^2}} \right) \quad (2.15)$$

Note that the exciton and photon fraction depends on the k_{\parallel} and photon-exciton mode detuning. So for the given exciton media, one can vary the length of the cavity and change the detuning from the positive $\Delta(0) > 0$ (see Figure 2-3(a)) to negative $\Delta(0) < 0$ (see Figure 2-3(c)) through the $\Delta(0) = 0$. During the fabrication process, microcavity usually acquires a wedge between the DBR mirrors, which allows for the detuning adjustment. The amount of exciton and photon fraction in polariton defines its properties such as effective mass, velocity and lifetime. For example, the decay rate (inversely proportional to lifetime) of LP γ_{LP} reads as

$$\gamma_{LP} = |\chi_{k_{\parallel}}|^2 \gamma_{exc} + |c_{k_{\parallel}}|^2 \gamma_{ph} \quad (2.16)$$

The typical lifetime of polaritons is severalps [55]. When polariton decays, the created photon carries all the information about the quasiparticle, the part of which it was - the energy, momentum, spin and phase. Thus, detecting the photons outcoming from the microcavity by conventional optical experimental means discussed further, one can non-invasively read the state of polariton. This makes polaritons very appealing and convenient for experimental investigations.

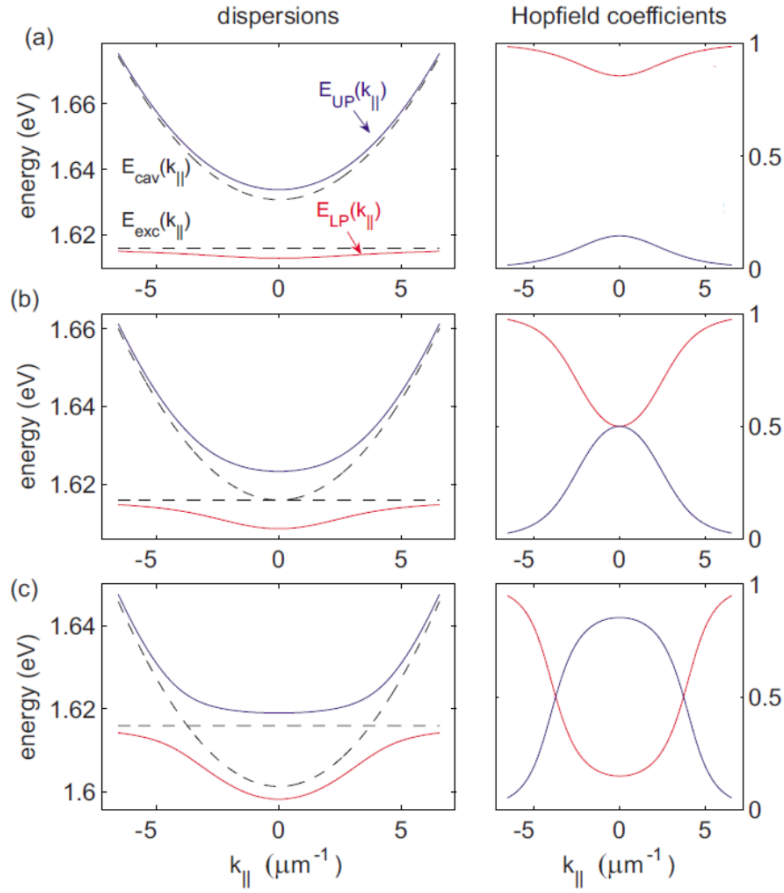


Figure 2-3: The left panels in (a-c) represent the dispersion of upper (purple) and lower (pink) polariton branch at positive (a), zero (b) and negative (c) photon-exciton detunings. The left panels in (a-c) are the corresponding LP Hopfield coefficients $|c_{k_{\parallel}}|^2$ (blue) and $|\chi_{k_{\parallel}}|^2$ (red). Reprinted figure with permission from Ref. [20]. Copyright 2010 by the American Physical Society.

2.4 Condensation

Polaritons are composite bosons (the particles of integer spin) since they are built from two bosonic quasiparticles - photon and exciton. So, under certain conditions, they can occupy a single energy-momentum state, forming the macroscopic coherent state - a condensate.

2.4.1 Bose-Einstein Condensates

The investigation of Bose-Einstein condensates (BECs) began in the 20th century with the works of Bose and Einstein (1924). Bose developed a statistical method to describe the behaviour of bosons. Einstein used this method to predict the

existence of a new state of matter in which a large number of bosons would occupy the same quantum state at low temperatures. However, it was not until the 1990s that experimental techniques were advanced enough to create and study BECs. Then, in 1995, E. Cornell and C. Wieman [56] at the University of Colorado and Wolfgang Ketterle [57] at MIT independently created the first BECs using laser cooling and trapping techniques. The discovery of BECs opened up a new area of research in physics, with potential applications in such fields as quantum computing and precision measurement. Since then, researchers have continued to study the properties and behaviour of BECs in different systems.

The Bose-Einstein statistics reads as follows:

$$n(E) = \frac{1}{\exp\left(\frac{E-\mu}{k_B T}\right) - 1}$$

where n is the number of bosons, E is their energy, μ is chemical potential, k_B is Boltzmann constant, and T is the temperature. In contrast to Fermi-Dirac statistics, the Bose-Einstein one allows for the macroscopic occupation of particles of one energy state. The critical temperature T_c for the Bose-Einstein condensation in 3D reads as

$$T_c = 3.312 \frac{\hbar^2 \rho^{2/3}}{m k_B T}$$

Note that the critical temperature is proportional to the particle density ρ and inversely proportional to the mass m of the particle. For reference, the condensation of Rubidium atoms [56] was achieved at ≈ 100 nK, and realising such low temperatures is quite challenging. In this regard, using particles (or quasiparticles) with smaller masses could increase the condensation temperature and significantly simplify the experimental setup to achieve it.

2.4.2 Polariton condensate.

As discussed above, the polaritons indeed have an extremely low effective mass (due to the photonic part) $\approx 10^{-5} m_e$, which made them very appealing for the studies of condensation. However, polaritons in the quantum well are effectively 2D

quasiparticles, and it is known that a uniform 2D system does not support the BEC transition [58]. The thermal fluctuations destroy the long-range order, preventing condensation. However, that restriction is lifted if the 2D system is subject to the spatially varying potential [59]. The excitonic reservoir forms the repulsive potential for polaritons [13, 27]. There are other ways for the realisation of the trap (for example, by mechanical stress). Moreover, the non-uniformity of the sample or even the finite size of the experimental system makes the condensation of polaritons feasible. Indeed, the polariton condensation has been observed at temperatures of liquid Helium [15] and even at room temperature [14, 23, 52].

In the early stages of polariton research, the non-ideal structure of the sample prevented the observation of the macroscopic polariton occupation. That was why the first works concentrated on the parametric processes where the condensation was seeded with a separate laser in order to trigger the bosonic stimulation [60]. P. Savvidis et al. used a weak probe beam resonant with the LP ground state to induce the stimulated scattering [61] and demonstrate the amplification of polariton emission [62]. However, this experiment required fine-tuning the energy and momentum of the idler and signal beams to satisfy the energy conservation laws. Further, the simulated scattering was shown to occur spontaneously without the seed beam when the excitation laser is tuned at specific energy and angle [63]. These findings made the foundation for the first observation of the polariton condensation (with the pulsed and quasi-nonresonant excitation) [64] in 2002. Finally, the condensation under non-resonant CW excitation was reported for the first time by J. Kasprzak and co-authors in 2006 [15] for CdTe microcavity. This study has created an avalanche of research reports on the condensation in microcavities of different materials (GaAs [55], GaN [65], ZnO [66] etc.) and studies of polariton condensate properties.

The condensation mechanism

The non-resonant excitation removes the necessity for the fine-tuning of the pump laser frequency and diminishes the influence of the pump laser on the condensate. The mechanism of the condensation [19] is schematically depicted in Figure 2-4.

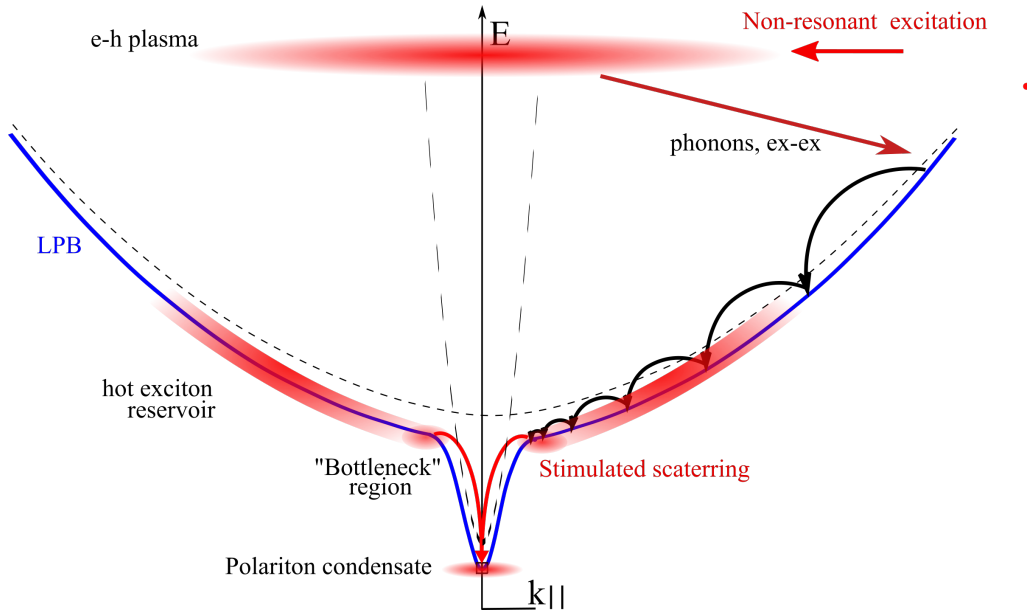


Figure 2-4: Mechanism of polariton condensation under non-resonant excitation.

The excitation laser is tuned to one of the reflection minima of the cavity at an energy higher than the optical stop-band. The laser optically excites the high-energy electron-hole plasma; it relaxes on a picosecond time scale dominantly by the optical phonons. This results in the population of the exciton dispersion at large in-plane momenta (exciton reservoir) [13]. The excitons lose their energy via exciton-exciton and exciton-acoustic phonon interactions. As long as the lifetime of excitons (≈ 1 ns) is much larger than their relaxation time (≈ 10 ps), quasi-thermalisation of the incoherent exciton cloud is possible.

However, the relaxation processes become less efficient once the particles have reached the inflection point on the LP branch. The particles are then accumulated in the so-called "bottleneck" region [67]. For a long time, this effect prohibited condensation in the LP ground state. However, the advances in sample manufacturing helped to overcome this problem and achieve condensation. When the density of polaritons is sufficiently high, they can scatter to the ground state and thus trigger the stimulated scattering process. The ground state population is then growing due to bosonic stimulation and leads to macroscopic occupation and, ergo, condensation. Polariton condensate requires constant laser pumping in order to exist; it forms in the balance of the gain and polariton dissipation. That is why it is usually

non-equilibrium. However, it was shown that if the cavity's quality factor is high enough, the thermodynamic equilibrium with the media (crystal lattice) can indeed be achieved [68].

The hallmarks of polariton condensation

Similarly to the atomic BEC, the power-driven phase transition in polaritons is characterised by the narrowing in both energy and momentum space (see Figure 2-5)(a),(b)). The strong coupling is conventionally proven by the reflectivity measurement and evidence of the anti-crossing of LP and UP branches. The polariton condensation, in turn, is usually distinguished by the following:

- Nonlinear growth of the polariton number (emission intensity) with the pump power due to bosonic stimulation (see Figure 2-5(c)).
- The narrowing of the emission linewidth at condensation threshold (see Figure 2-5(c)).
- The polariton energy blue-shift with the pump power due to polariton-polariton interaction (see Figure 2-5(c)).
- The appearance of the long-range order at the condensation threshold is evidenced usually by the spatial phase coherence $g^{(1)}$ distribution retrieved from the interference of the condensate emission with itself.
- Acquiring the defined projection of the spin at the condensation threshold.

2.5 Ballistically propagating vs trapped condensates

Polaritons are 2D quasiparticles, and the spatially varied potential or interactions are necessary for polaritons to condense. There are several approaches for polariton confinement. For instance, in the first observation of polariton condensate, the trap was induced by the optical disorder [15]. The other approach to polariton trapping

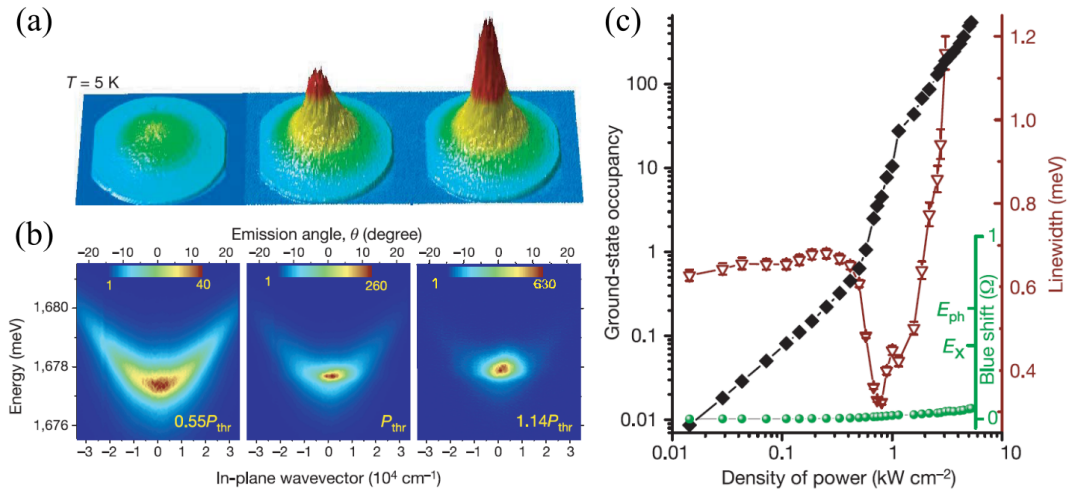


Figure 2-5: Polariton condensation under non-resonant excitation. The narrowing of the distribution and intensity increase in real-space (a) and on the dispersion (b). (c) The power-driven condensation is visible in the nonlinear growth of polariton number, the narrowing of linewidth and energy blueshift. Adapted from Ref. [15]

is the utilisation of the mechanical stress applied to cavity [69, 70]. Usually, a tiny pin squeezes [69] the sample and produces an inhomogeneous strain, acting as a trap for polaritons. The variation of the microcavity width by the mechanical stress also allows for shifting the exciton and cavity modes, thus varying their coupling.

The structure itself could act as a confining potential for polaritons, and there are numerous studies for the realisation of the condensate in the structures of lower dimensionality (e.g. 1D wires [71] or micropillar structures [72, 73, 74]). Such structures provide confinement for polaritons but do not allow the in-situ confining potential modification. In this regard, the utilisation of laser light-induced potentials is a viable alternative.

The nonresonant laser creates a population of hot excitons, which relax to polaritons and interact with them through the coulomb interaction, forming repulsive potential. The focused laser light is shown to modify the potential landscape for polaritons forming the barrier [75, 76]. The light-induced barrier and a wall of the 1D wire formed the confining potential in the study of E Wertz et al. [75]. Interestingly, the optical generation of potential can also be utilised for the control of coupling between two condensates. For instance, the utilisation of a nonresonant optical barrier allowed to drive two condensates from in-phase to out-of-phase coupling

configuration [22]. This approach could be useful for the mutual coupling control in the extended polariton networks for the analogue simulations.

The malleability of the laser beams patterning with the spatial light modulator allowed for the realisation of the purely optical traps for polaritons, which both confine and feed the condensate [27, 77, 78]. The optical trap for polaritons can be implemented both as a combination of Gaussian excitation spots [77] and by ring-shaped laser beams [27, 78].

This thesis concerns the ring optical trapping technique. The different size of the optical trap results in condensation in different spatial and energy modes [27, 28] reminiscent of the harmonic oscillator energy levels. There are numerous publications on the peculiar properties of the trapped condensates in the single [6, 7, 8] and coupled annular traps [30, 79]. Moreover, the spatial separation of the condensate and incoherent reservoir enlarged the condensate's coherence properties, resulting in the nanosecond phase coherence time [80].

With the non-resonant excitation in planar microcavities, the condensate can also be created on top of the pumping spot. When using positive exciton-photon detuning and large laser excitation spots, polariton ground state condensation is typically favoured. On the contrary, negative detuning and tightly focused excitation lasers tend to facilitate non-ground state condensation with finite in-plane momentum [81, 82] (ballistically propagating polaritons). This is because the locally injected exciton reservoir introduces an anti-trapping potential for polaritons [83, 84]. The repulsive potential $V(r)$ felt by polaritons can be expressed as

$$V(r) = \hat{g}n_R(r) + g|\Psi(r)|^2 \quad (2.17)$$

where $\Psi(r)$ is the condensate wave function, $n_R(r)$ is the exciton reservoir population. \hat{g} and g are the exciton-polariton and polariton polariton interactions respectively. Condensed polaritons are created with non-zero in-plane momentum at the pump spot location, which coincides with the maximum of $V(r)$.

Figure 2-6 depicts the characteristic dependencies of polariton intensity and momentum on the excitation power for the two cases of nonresonant optical excitation of the condensate. This data has been retrieved by the Author for the sample, which

is used in all experiments described in the scope of this thesis. The experimental techniques for data retrieval will be introduced in the next Chapter. Figure 2-6 allows one to grasp the main differences between two excitation techniques - with Gaussian spot or annular ring.

The exciton-photon mode detuning is -3meV . The left column in Figure 2-6 corresponds to the incoherent excitation of polariton condensate with the tightly focused ($\text{FWHM} = 3\mu\text{m}$) Gaussian spot, the right one - to the ring excitation with $10\mu\text{m}$ diameter. The condensate is observed for both configurations, which is evident from the narrowing of the condensate wave function in the real (see Figures 2-6 (a,b)) and reciprocal (see Figures 2-6 (c,d)) space. Note that for the case of the Gaussian excitation, the condensate is formed on top of the pumping spot, while for the case of the ring excitation, the condensate forms in the minimum of the intensity pattern (in the optical trap). Moreover, the ballistically propagating condensate occupies a narrow ring in the k-space (see Figures 2-6 (c)) dictated by the shape of the repulsive potential, whereas the confined condensate acquires the low momenta (see Figure 2-6 (d)). Note also that ballistically coupled condensate dispersion depicted in Figure 2-6 (e) features a significantly higher energy state than that of the trapped condensate presented in Figure 2-6(f). The power-driven condensate phase transition demonstrates an apparent threshold behaviour for both excitation cases (see Figures 2-6(g,h)). However, the nonlinearity and population of the condensate are higher for the trapped condensate due to confinement and reduced overlap with the exciton reservoir. The latter also prolongs the condensate phase coherence, which is evident from the significantly narrower linewidth of the condensate for the trapped case (compare Figures 2-6 (i) and (j)). Overall, the difference in the properties of the confined and ballistically propagating condensate widens the range of possible experiments.

2.6 Vortices in polariton condensates

Polariton condensates demonstrate similar properties with the conventional Bose-Einstein condensates and are described by a macroscopic wave function that fol-

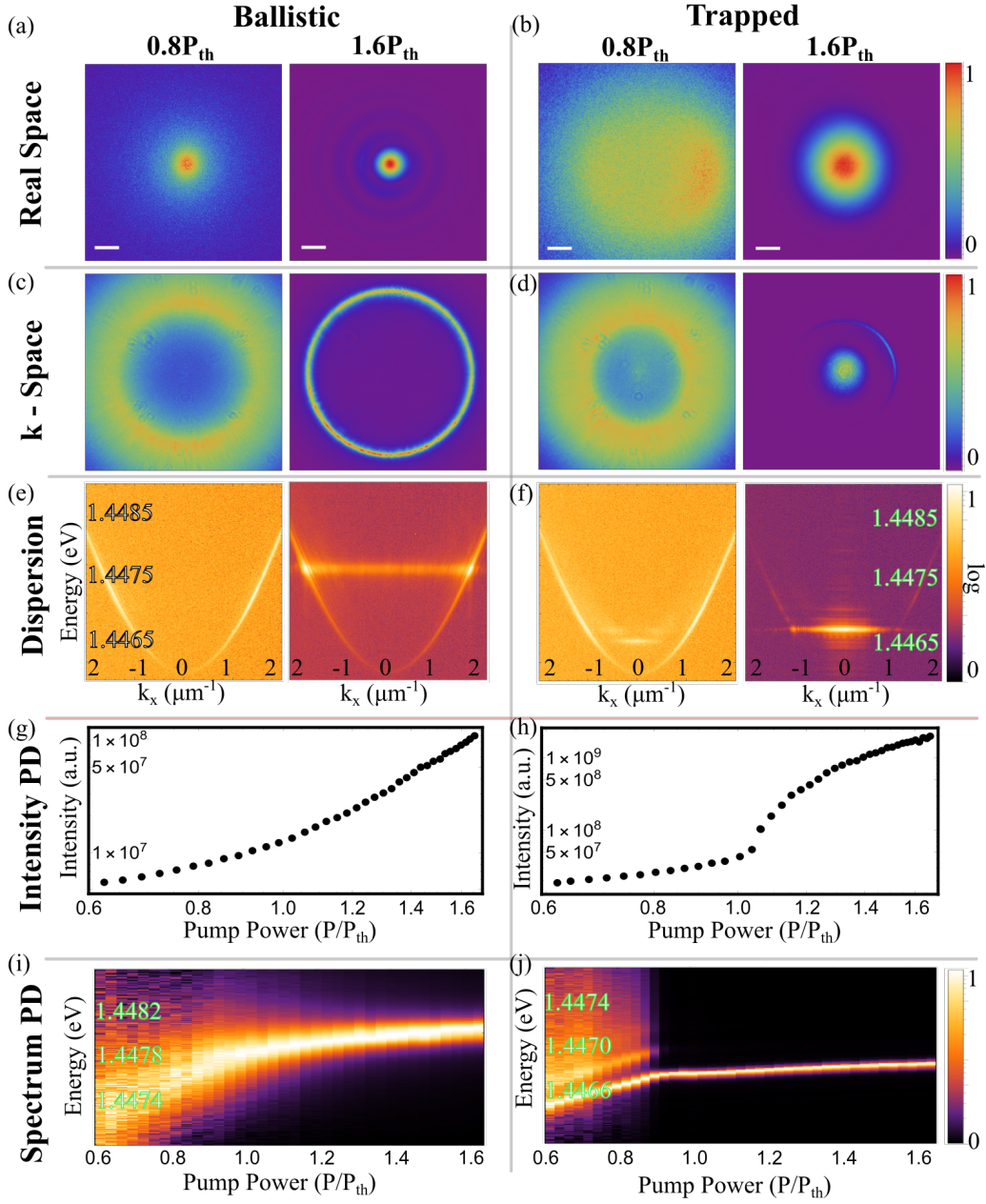


Figure 2-6: Polariton condensation under nonresonant excitation with tightly focused Gaussian spot (left column) and ring (right column). The microcavity sample is described in [55], and the photon-exciton detuning is -3meV . (a,b) The real-space intensity distribution of ballistically expanding and trapped condensate, respectively. The white scale bar corresponds to $2\mu\text{m}$. (c,d) The reciprocal space (k_x, k_y) for ballistically expanding and trapped condensate, respectively. (e,f) The dispersion $E(k_x)$ ballistically expanding and trapped condensate, respectively. The left and right panels in panes (a-f) correspond to the condensate below ($P=0.8P_{th}$) and above ($P=1.6P_{th}$) the condensation threshold, respectively. The intensity (g,h) and energy (i,j) power dependence for ballistically expanding and trapped condensate, respectively.

lows similar equations. The wave function can have phase defects called quantised vortices, which are characterized by a hollow core intensity distribution and quantised phase winding around the core. The vortex states in polariton condensate are demonstrated both experimentally [16] and theoretically [13]. There is considerable interest in studying these states from both fundamental and application points of view. A big part of this thesis is devoted to the generation of the vortex in rotating polariton condensate, so in this section, the current progress in the study of vortices in polariton condensates will be introduced.

The first experimental evidence of quantised vortices was reported by K. Lagoudakis et al. [16] not long after the experimental discovery of polariton condensate [15]. By interfering the condensate emission with a retro-reflected and displaced copy of itself, the authors were able to retrieve a quantised vortex (see Figure 2-7(a,b)) that was pinned on the defect of the microcavity structure.

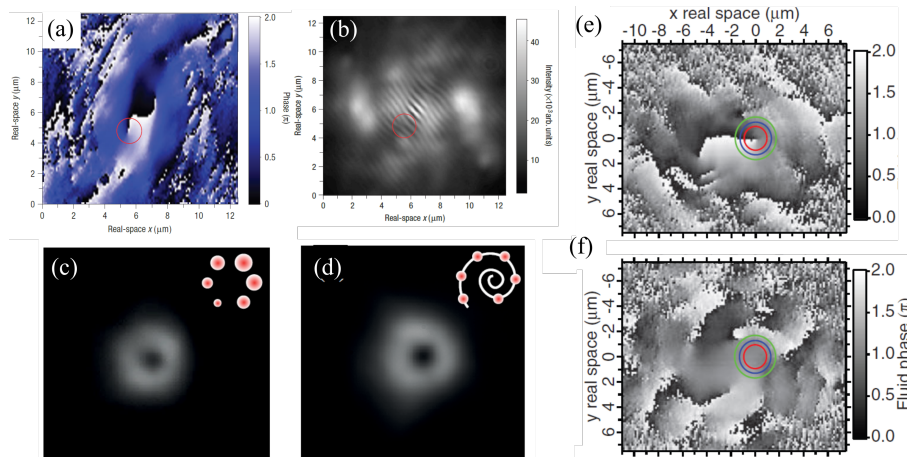


Figure 2-7: (a,b) Adopted from [16], reproduced with permission from Springer Nature. The first demonstration of the quantised vortex in the polariton condensate. Reprinted Panels (c,d) with permission from Ref. [85]. Copyright 2014 by the American Physical Society. The hollow core condensate intensity distribution corresponding to the vortex condensate state formed under the application of chiral nonresonant lens generated by (c) pump spot size (see red dots at the upper right corner) and (d) power. (e,f) Adopted from [35]. Reprinted with permission from AAAS. The observation of the half-quantum vortex manifested in the vortex in right-circular polarisation projection (e), and (f) the flat phase front in the left-circular condensate polarisation emission component.

The approaches used for generating vortices in polariton condensate widely vary and utilise both ballistically propagating and trapped polaritons. For example, the

vortex-antivortex pair was generated with a wide top-flat nonresonant beam [86]. The ballistic flow of polaritons hitting either the structural defect of the microcavity [87] or the one imprinted with the laser [88] had been shown to form multiple vortices in a turbulent flow. On the other hand, the modified trapping potential can force the condensate to form the state with the desired OAM. The nonuniformly pumped polygon formed an optical trap with the condensate occupying the vortex state in the experimental study of Dall et al. [85]. Scientists also showed that their chiral lens for polaritons could be built either with the nonresonant excitation laser power or by altering the pumping spot size (see Figure 2-7(c,d)). Moreover, Kwon et al. demonstrated the direct transfer of OAM to the condensate from the nonresonant excitation laser [89] forming a trap. However, the physical mechanism behind this transfer is still unrevealed.

The dynamics of the vortex formation and interaction between vortices is also investigated. For instance, under uniform nonresonant excitation, vortices in polariton condensate are shown to move on the spiral trajectories defined by the polariton effective mass and pump power [90]. Moreover, two resonantly injected vortices in the condensate interact with each other and experience scattering-like events [47]. The vortex state dynamics is utilised for the control of its OAM in the work of X.Ma et al. [91]. They used a short resonant pulse to manipulate the condensate state in the nonresonant optical trap. As a result, researchers could drive the condensate to the state with the desired phase winding, altering the control pulse length and power.

Polariton condensates possess the spin degree of freedom (see Section 2.8). The vortex which appears only in one spin projection of two-component condensates is called a half-quantum vortex. Half-quantum vortex (see Figure 2-7(e,f)) in the polariton condensate was first observed by K. Lagoudakis et al. [35]. The interplay of the spin and topological properties of the polariton condensate manifested itself in the observation of the spin vortex [92] where the linear polarisation of the emission changes azimuthally around the minimum of the condensate intensity (see Figure 2-8(a)).

The realisation of the vortex lattice could provide means for the utilization of

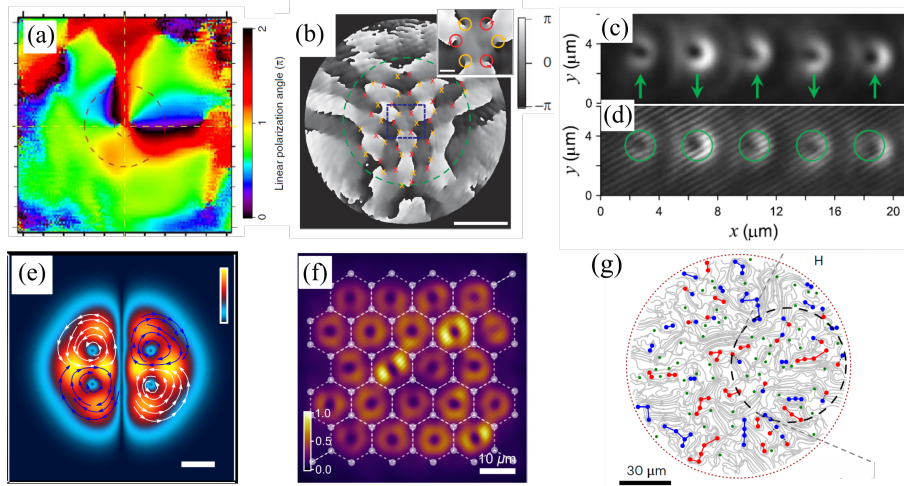


Figure 2-8: (a) Adopted from [92], reproduced with permission from Springer Nature. Panel (a) depicts the experimentally obtained linear polarization angle map, indicating the direction of the linear polarization around the spin vortex core. (b) Adopted from [93], reproduced with permission from Springer Nature. Experimentally measured condensate phase distribution demonstrating vortex lattice marked by red and yellow crosses. Panels (c,d) are reprinted with permission from [94] Copyright 2018 by the American Physical Society. The vortex chain of the condensate intensity (c) and interference pattern (d) obtained by the interference with the flat reference wave (the green circles and arrows depict the position and OAM of the vortices in the chain, respectively). (e) Adopted from [7]. Simulated image of a time-periodic vortex cluster, the white and the blue arrows show the polariton flow around the vortex cores. (f) The lattice of the trapped vortices. Adopted from [31]. (g) Multiple vortex-antivortex pairs (clusters) in a turbulent polariton flow. Adopted from Ref. [95]. Reproduced with permission from Springer Nature.

polariton for data storage and processing. Under resonant polariton injection, interactions modify the imprinted vortex lattice [96]. Geometrically locked vortex lattice with up to 100 elements was achieved by G. Tosi and coauthors [93] under the non-resonant excitation (see Figure 2-8(b)) of equidistant propagating condensates. The vortex chain was experimentally realized in 2018 [94] (see Figure 2-8(c,d)). An etched array of microcavity mesas was illuminated by a non-resonant laser, producing the chain of vortices with the control of respective OAM. On the other hand, the recent study [7] has revealed the possibility of creating the oscillating vortex lattice. Utilizing the annular non-resonant trap K. Sitnik et al. were able to achieve the condensation into two Ince-Gaussian modes - eigenstates of the optical trap. The beating of these modes results in the oscillating vortex cluster (see Figure 2-8(e)) with the flipping of the OAM at 5 GHz frequency. Moreover, the vortex lattice of

trapped condensates (see Figure 2-8(f)) under non-resonant pumping was realised recently [31]. It was shown that vortices in the lattice interact with each other in a way reminiscent of Ising spins, which can be applied to analogue simulation. Furthermore, the study of turbulent flow is also possible with polariton fluids. R. Panico et al. [95] have recently shown the emergence of multiple vortex-antivortex pairs (clusters) (see Figure 2-8(g)) in condensate and studied in details dynamics of its formation.

The studies mentioned above represent only a fraction of the research on vortices in polariton condensate. However, they showcase the significant progress made in this field and highlight the widespread interest in the polaritonics community and outside. Notably, the conventional method of vortex generation through external mechanical rotation, as it is usually done with superfluids [44], was previously unattainable due to the short polariton lifetime. However, this issue has been overcome in a recent experiment that leads to deterministic vortex formation. The details of this experiment will be outlined in detail in Chapter 7. Furthermore, the concept of superfluidity in polariton condensates will be discussed in the next section.

2.7 Superfluidity of polariton condensates

Superfluidity is a fascinating phenomenon that occurs in certain materials, such as liquid helium [43] and ultra-cold atomic gases, when they are cooled to low temperatures. It is characterised by the liquid obtaining the properties to flow with zero viscosity or resistance. The dissipative nature of polariton condensates makes the question of superfluidity there tricky [97] and debatable. However, the experimental evidence, as well as the numerical simulations, support the superfluidity of polaritons. A. Amo et al. in 2009 reported on the frictionless propagation of the polariton fluid through the microcavity defect. They have demonstrated that increasing the power of the non-resonant exciton decreases the amount of Rayleigh scattering on the defect until it disappears almost completely [17]. So, polaritons were moving through the defect without friction. Recently, the same experiment has been imple-

mented with the organic polaritons demonstrating the signatures of superfluidity at room temperature [98].

Another signature of superfluidity is a persistent current observed by Sanvitto and coworkers in 2009 [99]. They resonantly imprinted a vortex with the Laguerre Gaussian beam on top of the condensate. Scientists have shown that the vortex survives in the condensate for a long time and moves in the condensate on the trajectories defined by the potential landscape of the cavity. Moreover, the linear excitation Bogolubov spectra (the hallmark of superfluidity) have also been documented [100].

The other famous manifestation of superfluidity is the generation of quantum vortices in the rotating superfluid [41, 44, 101]. As mentioned earlier, while the vortices in the polariton condensate are well reported, the string-induced ones have not been reported thus far.

2.8 Polariton spin

The polaritons feature angular momentum - pseudospin (or just *spin* hereinafter)-inherent from the constituents photon and exciton. An exciton is a composite boson formed by two fermions (the particle of the half-integer spin) - an electron and a hole. Electron spin is $\mathbf{S} = \frac{1}{2}$. However, the hole in the zinc-blend structured semiconductor (like GaAs) can have the total angular momentum of either $\frac{1}{2}$ or $\frac{3}{2}$. The former is called a light hole, and the latter is a heavy hole. In a bulk semiconductor, the energies of two kinds of holes are usually equal; however, in quantum wells, the energy of the heavy hole is typically smaller than the light one. The bound state of the electron and hole can have the momentum projection of $J_{ex} = \pm 1$ or $J_{ex} = \pm 2$. Taking into account that photon has spin ± 1 , excitons with the momentum of two (dark exciton) cannot be excited optically and do not participate in the formation of the polariton [13, 20]. Thus, polariton is formed by the photon and exciton with equal spins of 1 or -1, which defines the polariton spin. Due to momentum conservation law, the polarisation of the photon emitted when polariton decays is related to the spin of the polariton. And by detecting the polarisation of the cavity PL, one

can characterise the polariton spin state.

In their condensed form, polaritons can be expressed by a spinor order parameter $\Psi = (\psi_+, \psi_-)^T$ with spin-up and spin-down polaritons (ψ_{\pm}) corresponding to right- and left-circularly polarised light respectively. Polariton spin is often conveniently described in the Stokes formalism [102] \mathbf{S} . With the total particle number in the condensate written $S_0 = |\psi_+|^2 + |\psi_-|^2$, the normalized components of the Stokes vector $\mathbf{S} = (S_1, S_2, S_3)^T$ read as

$$\begin{aligned} S_1 &= 2\text{Re}(\psi_-^* \psi_+)/S_0 \\ S_2 &= -2\text{Im}(\psi_-^* \psi_+)/S_0 \\ S_3 &= (|\psi_+|^2 - |\psi_-|^2)/S_0 \end{aligned} \tag{2.18}$$

These parameters can be measured experimentally and tracked on the Poincare sphere (see Section 3.3.6 for details). In his regard, the spin-up polaritons correspond to the right-circular polarisation of the emission and $\mathbf{S} = (0, 0, 1)^T$. The spin-down polaritons are detected as left-circular polarisation ($\mathbf{S} = (0, 0, -1)^T$). The other spin states are the linear combinations of the aforementioned states. Consequently, the representation of the polariton spin measured as PL polarisation on the Poincare sphere is analogous to the classical representation of particle spin on Bloch sphere [103].

Due to the nonlinear nature of polaritons arising because of their interactions, the physics of the condensate spin is very peculiar [37, 104]. Among numerous scientific articles on this subject, there are reports on spin bistability [36, 105, 106] and multistability [107], optical spin Hall effect [108], polarised solitons [109, 110], half-quantised vortices [35, 111], skyrmions [112] and other non-trivial patterns [113, 114, 115].

As long as condensate spin can be operated solely with laser light (non-resonant or resonant), its application for spinoptonics is very appealing. The spinoptonics is a branch of spintronics where the control over spin is planned to be realised by the virtue of light. The spinoptonics combines the study of spin and optical

polarization effects in solids to create quantum optoelectronic devices. It focuses on encoding information carried by photon polarization into spin states of carriers, manipulating them on the nanoscale with light, and retrieving the information as polarized photons [116]. Spinoptronics leverages well-controlled carrier interactions occurring in nanostructures. It also mitigates the challenges of carrier spin relaxation or decoherence, a common limitation in traditional semiconductor-based spintronics. Spinoptronics holds potential for a wide range of applications, including information storage, optical communication, quantum computing, and enhanced sensing technologies. Interestingly, several spinoptronic devices for polaritons have been already realised, for example, polariton spin switch [117], spin memory [118], spin beamsplitter [27], and spin filter [119].

The subject of this thesis is optically confined condensate. The reduced overlap of condensate with the exciton reservoir diminishes detrimental spin-dephasing effects, leading to the well-defined and stable spin just above the condensation threshold for the case of circularly polarised excitation [13]. However, the physics is more complicated for other excitation polarisation and higher pumping powers. The spin properties of the condensate in the optical trap will be discussed in detail in Chapter 4.

Chapter 3

Experimental Setup and Techniques

Just as an astronomer requires a telescope in order to study distant stars, we require the experimental setup and established techniques in order to study polariton condensates. Such a setup was designed and built in the Hybrid Photonics Laboratory in Skoltech by the joined effort of laboratory staff. The setup consists of three main parts - excitation, sample and detection.

The excitation part includes the single-mode laser that is frequency-tuned to the first Bragg minimum of the microcavity sample to realise the nonresonant excitation of polaritons. In addition, the spatial light modulator (SLM) is utilised for the deterministic shaping of the excitation beam. The studies are carried out with the inorganic GaAs semiconductor microcavity. The low binding energy of the Wannier-Mott excitons forming polaritons there renders them unstable at room temperature, so the sample is kept in the cryostat at 4K temperature.

To investigate the state of polaritons, one needs to create experimental equipment and techniques that can detect and analyze the information contained in the photons leaked from the microcavity when polaritons decay. This chapter details the methods and tools used to measure the five main characteristics of a light beam: intensity, phase, polarisation, momentum, and photon statistics.

3.1 Excitation part

The developed setup features a high level of flexibility in the choice of excitation configuration - from non-resonant to resonant and quasi-resonant, from pulsed to CW and time-periodic. However, this thesis is devoted to the non-resonant, CW and time-periodic ones. Therefore, in further discussion, we will omit the parts with pulsed and resonant excitation and related apparatus, concentrating only onto the experimental techniques utilised in the study.

3.1.1 Excitation laser

The light that non-resonantly excites polaritons is generated by single frequency Ti:Sapphire laser MBR-110 by Coherent. This laser offers broad wavelength tunability alongside narrow linewidth and frequency stability. The lasing media is Al_2O_3 (sapphire) crystal doped with Ti ions. The crystal is pumped with a 20W green diode laser (Coherent Verdi or Millennia by Spectra-Physics). The crystal is placed in the monolithic bow-tie ring resonator (see Figure 3-1) with electronic stabilisation. The optical diode composed of the retardation plate and Faraday rotator realises the propagation of the light in the cavity in only one direction. Tuning the birefringent filter allows for the coarse adjustment of the laser emission wavelength, and a thin etalon establishes the fine-tuning as well as a single-frequency operation. This laser system's advantage is the possibility of scanning the emission wavelength with the external voltage source (by rotation of two Brewster Plates). Locking the laser cavity to an in-build high finesse reference cavity makes it possible to achieve a narrow linewidth of less than 75kHz. The maximum output power of the laser system is above 3W. The excitation wavelength in all experiments is around 796 nm.

The laser emission first goes through the Faraday isolator in order to prevent back reflections to the laser cavity and then hits the acousto optic modulator. The modulator is built on the effect of the refractive index alternation by the radio frequency wave. In the experiments, it is used to chop the excitation laser emission to form a few microsecond pulses at a kHz repetition rate. This modulation prevents the heating of the sample by the laser light, which could result in a loss of strong

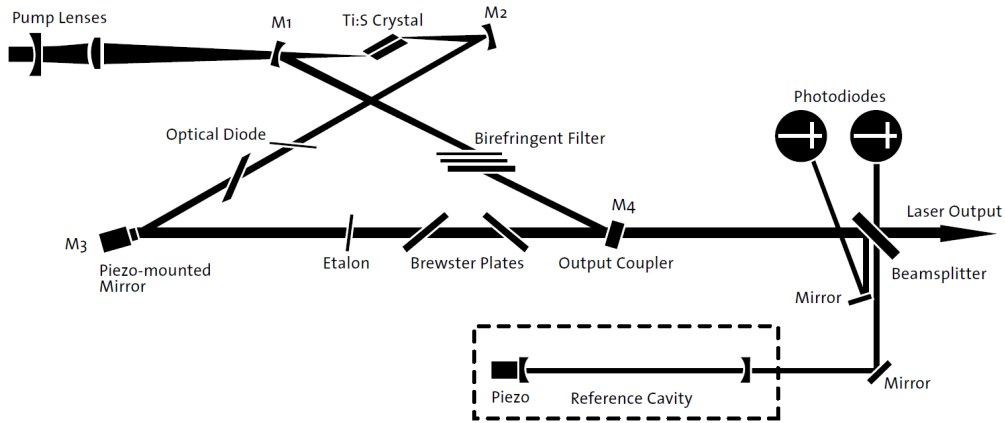


Figure 3-1: The sketch of the MBR-110 Ti:Sapphire laser cavity. The image is taken from the laser manual.

coupling. However, microsecond excitation pulses are still seen as continuous by polaritons due to their short ps- lifetime.

3.1.2 Shaping the excitation beam with spatial light modulator

The time-modulated laser beam is then passed to the phase-only spatial light modulator. This device is utilised in our experiments to shape the excitation laser beam and create various types of repulsive or trapping potentials for polaritons.

For the experiments, the reflective SLMs were utilised. The reflective SLM screen is composed of an array (1272 by 1024) of phase-modulating elements (see Figure 3-2(a)). These elements are optical cells formed by two transparent electrodes and filled with nematic liquid crystals composed of organic molecules. The centres of the molecules are distributed randomly in the cell, whereas all molecules are aligned dominantly in the same direction, giving rise to anisotropy and birefringence (the dependence of the refractive index of the matter on the light propagation direction). Linearly polarised light E_1 passing through the liquid crystal cell at an angle θ with respect to molecules orientation experiences the effective refractive index n_{eff} described by the following equation [49]:

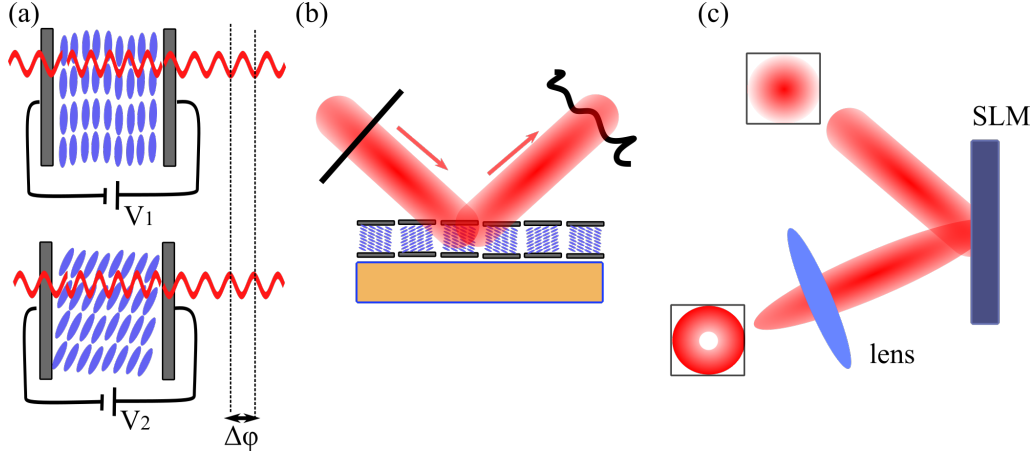


Figure 3-2: (a) The schematic of the pixel of the spatial light modulator under different applied voltage V_1 and V_2 . Alternated with voltage refractive index result into the phase shift $\Delta\phi = \phi(V_1) - \phi(V_2)$ of the transmitted light. (b) The schematic of the change of the wavefront of the incident light by the SLM screen with black lines depicting the phase fronts. (c) Reflective SLM and transformation of the Gaussian beam into the ring-shaped one.

$$\frac{1}{n_{eff}^2(\theta)} = \frac{\cos^2(\theta)}{n_o^2} + \frac{\sin^2(\theta)}{n_e^2} \quad (3.1)$$

where n_e is the refractive index of the material along the long axis of the liquid crystal molecules (the wave travelling along this direction is called extraordinary), and n_o is the refractive index along the two other orthogonal directions (ordinary wave). Applying the voltage to these cells leads to a change in the orientation of the molecules inside and, as a result, an addressable change in the cell's refractive index. The field E_2 escaping the liquid crystal acquires a phase shift ϕ with respect to incident one, which can be written as follows (omitting the losses and scattering inside the cell):

$$E_2 = E_1 e^{i\phi} \quad (3.2)$$

where ϕ is defined by n_{eff} (see Eq. (3.1)), the wavelength of light λ and the length of the cell l as follows: $\phi(\theta) = \pi l n_{eff}(\theta) / \lambda$. The electric field controls the orientation of the liquid crystals in the SLM pixel cell so that the targeted change of the voltage V in each cell allows for the realisation of the needed phase shift. The schematic of the phase shifts induced by two different voltages V_1 and V_2 are

depicted in Figure 3-2 (a). The phase-modulated beam created by the array of cells (see Figure 3-2(b)) produces the target laser intensity pattern in the focal plane of the lens placed after the SLM (see Figure 3-2(c)).

In order to achieve the desired beam profile on the SLM screen, a grayscale pattern or hologram with 8-bit resolution is utilized. This hologram is then converted into an array of voltage values that correspond to each pixel on the SLM screen. Using its corresponding grey level, each pixel is capable of adjusting the phase of the incoming light from 0 to 2π . The phase-only spatial light modulator is the preferred choice for this experiment due to its high efficiency and versatility in creating various optical patterns. Deformable mirrors, which are an alternative for beam shaping, usually have fewer active elements than SLMs, which limits their ability to create optical patterns with many features.

The question now is how to create a proper hologram for a target laser intensity pattern. In general, the field distribution of the light E_{SLM} transformed by SLM is given by the Equation (3.3):

$$E_{SLM} = E_{in}e^{i\Phi_{SLM}(\mathbf{x})} \quad (3.3)$$

where $\Phi_{SLM}(\mathbf{x})$ is a hologram phase distribution (the one imprinted onto SLM), \mathbf{x} is a spatial coordinate. The modified beam distribution is observed in the focal plane of the lens (see Figure 3-2(c)). The lens is performing the spatial Fourier transform \mathbf{F} of the beam, and the target field distribution E_{tar} in the focal plane is written as follows:

$$E_{tar} = \mathbf{F}\{E_{SLM}\} = \mathbf{F}\{E_{in}e^{i\Phi_{SLM}(\mathbf{x})}\} \quad (3.4)$$

And thus, to find the field distribution just after the SLM and a required phase hologram $\Phi_{SLM}(\mathbf{x})$, one should take an inverse Fourier transform \mathbf{F}^{-1} of the target field distribution and retrieve the phase of the resultant wave (see Eq. (3.5)).

$$E_{SLM} = E_{in}e^{i\Phi_{SLM}(\mathbf{x})} = \mathbf{F}^{-1}\{E_{tar}\} \quad (3.5)$$

However, the target field distribution E_{tar} is not always known. Often, the

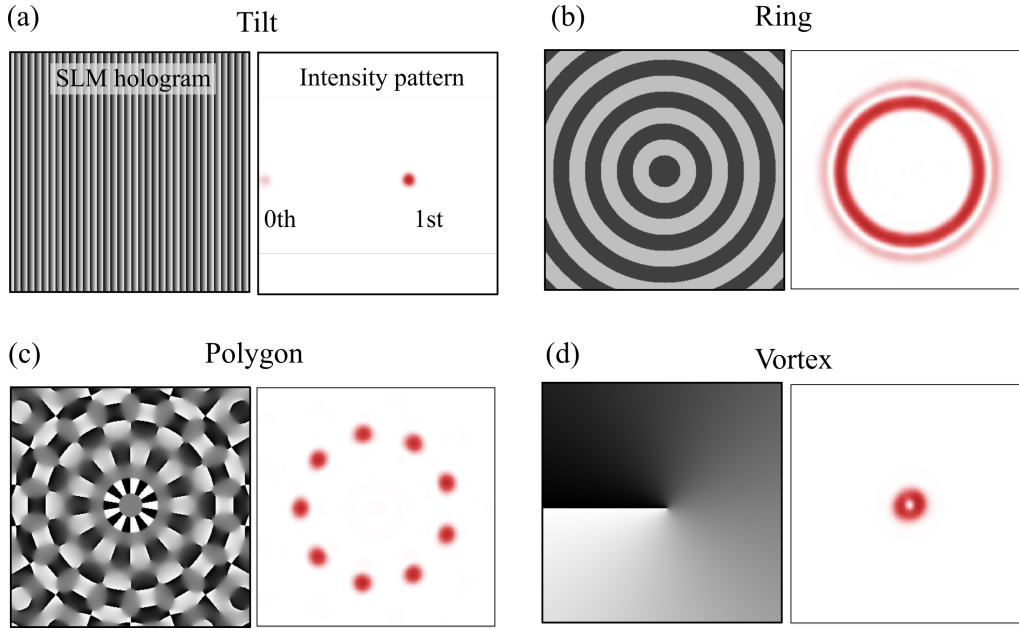


Figure 3-3: The left image in panels (a-d) correspond to the holograms on the SLM for the generation of (a) a tilt to separate the reflection from the SLM (zeroth order) and generated laser pattern, ring pattern (b), a polygon of 9 Gaussian spots (c) and optical vortex (d). The right panels in (a-d) represent the corresponding intensity patterns.

experimental task is to produce the complicated intensity pattern $|E_{tar}|^2$, omitting the phase of the shaped beam. This makes seeking the proper hologram quite challenging, but numerous analytical and numerical [120, 121] approaches are used to overcome this challenge.

For most experiments discussed in this thesis, the holograms for SLM, for example, for creating a ring pattern or vortex, were calculated analytically using (3.5). The examples of the holograms and respective generated intensity patterns are presented in Figure 3-3. To separate the reflection from the SLM and shaped intensity pattern, the hologram is usually superimposed with the blazed grating (see Figure 3-3 (a)). As a result, the target pattern is formed in the first diffraction order of this grating.

The SLM is incorporated into the excitation part of the experimental setup depicted in Figure 3-4. There, the laser beam is reflected from the SLM and transferred to the excitation objective with the conjugated telescope (lenses L_1 and L_2). The iris in the focal plane of lens L_1 is used to cut the zeroth diffraction order from SLM.

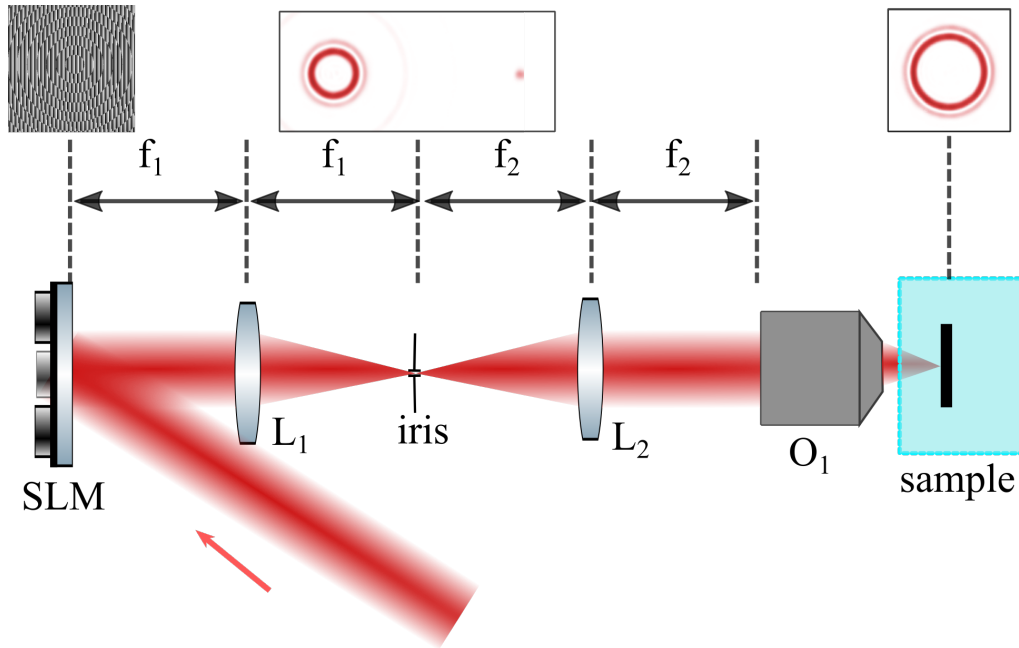


Figure 3-4: The excitation part of the experimental setup: the laser emission is reflected from the SLM and transferred to the excitation objective with the conjugated telescope (lenses L_1 and L_2). The iris diaphragm is used to cut the zeroth diffraction order in the real-space plane. The target excitation pattern shaped with SLM forms in the focal plane of the objective on the sample.

3.1.3 Time-periodic excitation pattern

Two Chapters of this thesis are devoted to the polariton condensates in the time-periodic rotating potentials. In this Section, we will briefly introduce the technique for realising the rotating pattern; however, a more detailed description can be found in Section 6.2.

We utilise two frequency-detuned and externally wavelength-stabilised (f_1 and f_2) Ti: Sapphire MBR 110 lasers and shape each of them using two spatial light modulators. We imprint the so-called "perfect vortex" mask [122] on both SLMs. The resultant beam profiles are annular with orbital angular momenta (OAM) l_1 and l_2 of 1 and -1, respectively, or vice versa. Overlapping two laser beams and projecting their beating note onto the microcavity sample (see Figure 3-5), we obtain a rotating dumbbell excitation pattern depicted at the top of Figure 3-5. The relative difference of both frequencies and OAMs of the excitation lasers dictates the rotation frequency f and direction.

It is worth noting that this all-optical technique allows the achievement of high

GHz time-modulation frequency for polaritons and does not require any modifications made for the sample. In contrast, the periodic modulation technique using surface acoustic waves (SAW) previously implemented for polaritons [123, 124], operates at frequencies in the hundreds of MHz range and requires specific samples. Moreover, except for the realisation of the rotating patterns, our setup can generate any beating time-periodic profiles employing the imprinting of different intensity and phase profiles with SLMs.

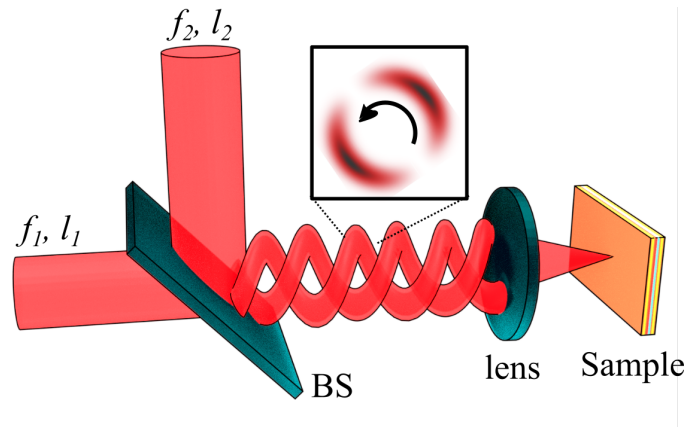


Figure 3-5: Experimental setup for the rotating excitation pattern generation. Two single-mode, frequency stabilised lasers (with frequencies f_1 , f_2 , and OAMs l_1 , l_2 respectively) are overlapped on the beamsplitter (BS). The resulting dumbbell-shaped beating pattern rotates with the frequency and direction defined by two lasers.

3.2 Sample

In the experiments, we use 2λ inorganic semiconductor microcavity with embedded quantum wells. The sample is produced using molecular beam epitaxy technique [55]. The sample structure is presented in Figure 3-6 (a). The bottom DBR consists of 26 pairs of $GaAs$ and $AlAs_{0.98}P_{0.02}$ layers, while the top one is built of 23 pairs [55]. Three pairs of $In_{0.08}Ga_{0.92}As$ quantum wells are placed in the anti-nodes of the field of the $GaAs$ cavity (see Figure 3-6). Two additional quantum wells are placed near the DBRs and used to increase the number of excitons created by laser illumination (see Figure 3-6). This quantity of the quantum wells is chosen to distribute the exciton density and avoid Mott transition [125] (the dissociation of excitons at high densities), increase the Rabi splitting and achieve polariton con-

densation. Insertion [126] of thin 1.1 nm *AlP* layers into the *AlAs* compensates for the mismatch of the DBR layers and lowers the disorder in the sample.

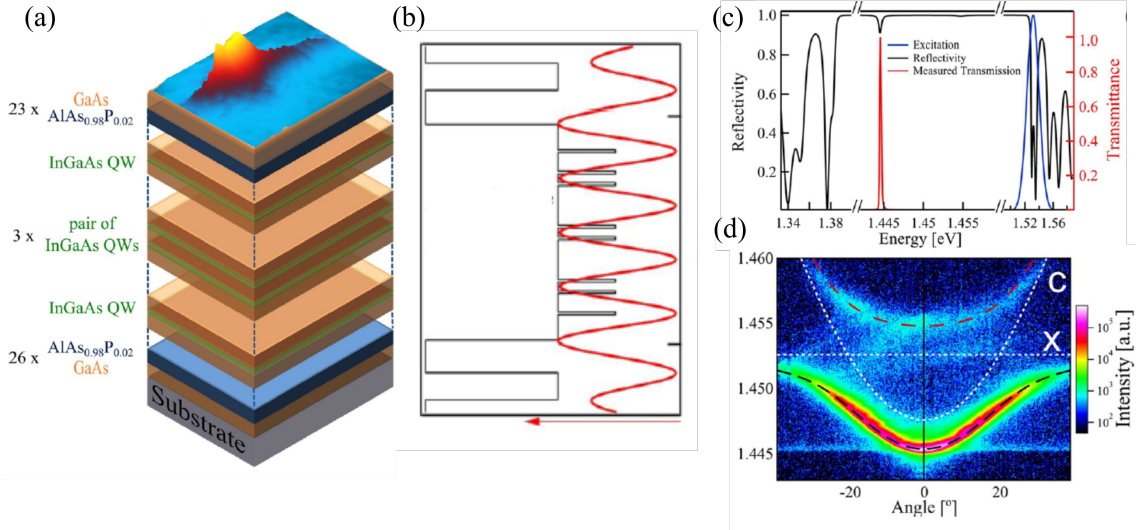


Figure 3-6: The microcavity sample used for experiments. (a) The layered semiconductor structure of the microcavity sample. (b) The refractive index distribution (x-axis) along the cross-section of the microcavity (y-axis). The red line depicts the electric field intensity distribution. (c) The sample's reflectivity (black) and transmittance (red) spectrum. (d) The dispersion of the polariton PL. The image is reprinted from ref. [55], with the permission of AIP Publishing.

The reflectivity and transmission spectra of the sample are presented in Figure 3-6(c); the reflectivity stopband goes from approximately 800 to 900 nm. The exceptional class of the sample's DBRs results in a quality factor Q of 12000 [55]. The sample is shown to possess strong coupling and polariton condensation. The Rabi-splitting is around 8 meV. The polariton lifetime in this sample is estimated to be around 7 ps. Moreover, the wedge between DBR mirrors, which arises in the fabrication process, allows for scanning the photon-exciton detuning in the range from -8 meV to 1 meV by changing the position of the excitation spot on the sample. We usually work with negative detunings of -3 meV, but more precise values of detuning for each experiment will be stated in the corresponding chapters.

This sample has genuinely unique characteristics and purity and is utilised for the numerous studies carried out in our laboratory [7, 8, 22, 31], including the works related to this thesis.

As mentioned above, our experiment's sample is mounted on the cold finger of

a closed-cycle Montana Instruments cryostat at 4K. The closed-cycle cryostat does not require any cooling liquid and operates by the cycle of expansion and cooling of refrigerant gas. The sample is held in the high vacuum chamber in the cryostat and thermally connected to the cooling gas system via the cold finger.

The 50X objective (Mitutoyo M Plan APO NIR B 50X) is used for the excitation of polaritons. It has a depth of field of $1.6 \mu\text{m}$, comparable with the cavity's optical thickness. Thus, only one pair of the quantum wells is positioned in the maximum of the excitation optical field; for the other two, the field intensity is at least twice less. Consequently, condensation occurs only in the one pair of wells for the low pumping power. The PL coming from the other quantum wells is significantly less and poorly collected by the objective, so it does not affect the measurements.

3.3 Detection part

Non-resonant laser excitation creates the exciton-hole plasma in the sample, which then relaxes to excitons and polaritons. The polariton emission is collected with the high 0.42 NA objectives in the transmission and reflection geometry. The objective used for the excitation is also utilised for the polariton photoluminescence (PL) collection in the confocal configuration. Polariton PL is then filtered out from the residual excitation laser with the short-pass dichroic mirror. In the transmission, polariton PL is wavelength-filtered with a long-pass filter. Polariton PL travelling in both directions is identical and is utilised in the setup to study different polariton characteristics. Namely, the intensity and phase distribution are recorded for the transmitted PL and momentum and energy space for the reflected one. The detection part of the setup is schematically depicted in Figure 3-7.

3.3.1 Real-space imaging

The detection part of the experimental setup allows us to record the spatial (or real-space) distribution of the condensate intensity. Condensate PL is focused by the lens L_3 (see the top row in Figure 3-7) onto the screen of the CCD camera. The image formed at the camera sensor corresponds to the intensity distribution of the

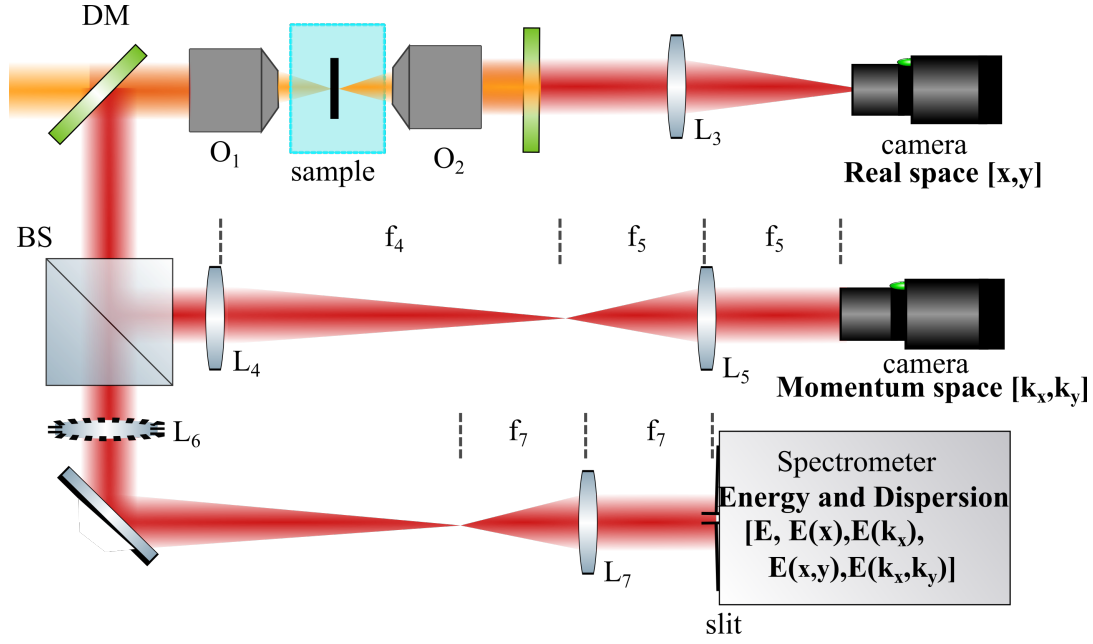


Figure 3-7: Detection part of the experimental setup. The real-space of the polariton emission is recorded in the transmission geometry. The sets of conjugated lenses transfer the k -space distribution both to the CCD camera and the slit of the imaging spectrometer (for dispersion imaging) in the reflection from the sample. The residual excitation laser light is filtered out by the long-pass filter in the transmission and by the dichroic mirror in the reflection. Lens L_6 is placed on the flip mount in order to be able to project either real or k -space onto the spectrometer slit.

condensate wavefunction $|\Psi(x, y)|^2$ and is proportional to the population of polaritons in the condensate. The spatial resolution of the detected condensate image can be increased by shrinking the incident PL beam with the additional telescope put in front of lens L_3 . With the typical camera exposure time of 10 ms, each image retrieved with it is an average of over 50 condensate realisations (50 two-microsecond pulses). However, there is a possibility to fit only one excitation pulse into the camera exposure time. In this scenario, the camera creates a trigger signal for the AOM, which transmits only one excitation laser pulse of the required duration. In this thesis, both detection approaches are used to measure the condensate intensity or phase.

3.3.2 Spectrum and momentum

The lens performs a spatial Fourier transformation of the transmitted light with the result formed in its focal plane [127]. So that by putting the even number

of lenses after the collecting objective in a way that their focal distances overlap (see Figure 3-7), we can detect the momentum (\mathbf{k}) distribution of the condensate $|\Psi(k_x, k_y)|^2$.

Also, by projecting either real-space or \mathbf{k} -space of the condensate on the entrance slit of the imaging spectrometer, the condensate cross-section energy distribution $E(x)$ or polariton dispersion $E(k_x)$ can be retrieved. Moreover, moving the condensate across the entrance slit makes it possible to restore the whole energy dispersion paraboloid $E(k_x, k_y)$.

3.3.3 Phase read-out

The phase of the light wave cannot be directly measured because most of the detectors response is proportional to the light intensity. However, the phase distribution can be deduced from the interference pattern of the studied light wave with the wave of the known phase distribution. The aforementioned statement directly follows from the general considerations on the interference of two electromagnetic waves. Imagine two monochromatic waves at the same energy and polarisation with the complex amplitudes $U_1(\mathbf{r})$ and $U_2(\mathbf{r})$ [49]. When those two waves overlap, the amplitude of the resultant wave would be as follows: $U(\mathbf{r}) = U_1(\mathbf{r}) + U_2(\mathbf{r})$ whereas the intensity I is written as:

$$I = |U|^2 = |U_1 + U_2|^2 = |U_1|^2 + |U_2|^2 + U_1^*U_2 + U_2^*U_1 \quad (3.6)$$

Taking into account that $U_1 = \sqrt{I_1}e^{i\phi_1}$ and $U_2 = \sqrt{I_2}e^{i\phi_2}$ where ϕ_1, I_1, ϕ_2, I_2 are the phases and intensities of the first and the second wave respectively. It results in a well-known interference equation:

$$I = I_1 + I_2 + 2\sqrt{I_1 I_2} \cos(\phi_2 - \phi_1) \quad (3.7)$$

Thus, if the phase distribution of one of the interfering waves is known (the simplest case is the flat wave), it is straightforward from Equation 3.7 to retrieve the phase of the studied wave from the interference intensity pattern (with the accuracy of some constant phase shift).

laser while not affecting the other characteristics of the condensate (phase distribution, energy, number of polaritons etc.). Part of the seed laser is greatly expanded, making a big flat phase front that interferes with polariton emission in a Michelson interferometer (see Figure 3-8). This technique is a great tool for condensate phase extraction and was used in our lab for the phase retrieval of the trapped [7], freely propagating [22] and arrays [21] of the condensates.

Interference of condensate with itself

Even though the homodyne interferometry technique is great, it is not always handy to use it in experiments due to the requirement of the fine adjustment of the reference laser wavelength to that of the condensate. This applies, for example, to the pump power dependencies of the condensate phase when the condensate energy is increasing because of the blueshift. In this regard, another interference technique that allows us to measure the condensate phase features and characterise its spatial and temporal phase coherence was also utilised for phase measurements.

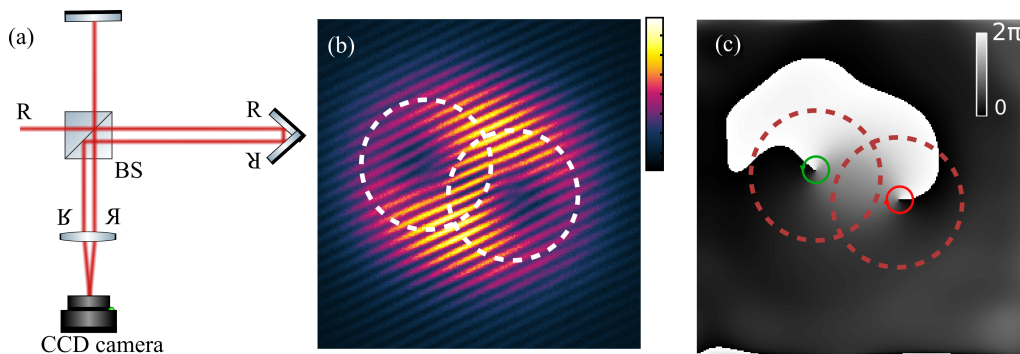


Figure 3-9: The interference of the condensate with the retro-reflected and displaced copy of itself and reconstructed phase - (a) experimental setup (a), (b) the interference pattern, (c) the real-space phase distribution.

In this approach, the condensate interferes with the copy of itself. The condensate PL is sent to the Michelson interferometer depicted in Figure 3-9(a). The condensate emission is split into two parts with the non-polarising beamsplitter. One portion is then reflected back with the mirror; the other is sent to the retro-reflector prism. The prism reflects the PL back while mirroring its orientation along the x and y-axis. Two parts of the PL are then overlapped on the sensor of the CCD

camera. The use of the retroreflector in one arm enables the investigation of the spatial coherence of the condensate and a long-range order [15] since in this configuration, the opposite parts of the condensate interfere with each other. Moreover, the retroreflector is placed on the translation stage used to control the relative optical path of two interferometer arms to measure the temporal decay of the condensate phase coherence [6, 7, 80] (coherence time).

The measurements of the $g^{(1)}$ first-order coherence function require the perfect overlap of the beam coming from two interferometer arms. On the contrary, for the quick characterisation of the condensate phase, we displaced the two interfering beams with respect to each other as shown in Figure 3-9 (b). The retrieved phase reveals two-phase dislocation of the opposite topological charge corresponding to the direct and retro-reflected version of the condensate (see Figure 3-9(c)). A similar approach was used for the first observation of the quantised vortex in polariton condensate by K. Lagoudakis et al. [16]. In this thesis, this method was used for measuring the frequency dependence of the vortex appearance in the stirred polariton condensate.

3.3.4 Phase retrieval: off-axis digital holography

Once the interference pattern is obtained by either of the two aforementioned techniques, one can calculate the phase distribution using the off-axis digital holography technique. The essence of this technique is filtering of 2D spatial Fourier transform of the interference pattern.

For simplicity, let us consider the experimental interference pattern measured with the homodyne approach. Let C and R be the complex amplitudes of the condensate and reference wave, respectively, then the recorded interference pattern depicted in Figure 3-10 (a) would be $|C+R|^2$. Following the equation 3.6, $|C+R|^2 = |C|^2 + |R|^2 + C^*R + R^*C$.

The first step of the off-axis digital holography method is to perform the 2D Fourier transform over the interference pattern. For this, we apply the digital fast Fourier transform (FFT) method [128], and the amplitude of the corresponding FFT image is presented in Figure 3-10(b). It consists of several bright peaks: the

central one corresponds to the Fourier transform of $|C|^2 + |R|^2$ and does not carry any phase information. The two others (at big wave vectors) are $\mathbf{F}C^*R$ and $\mathbf{F}R^*C$. These harmonics have information about the phase of the condensate, so by filtering out one of them (see one harmonics cut in Figure 3-10(c)), one can restore the phase of the condensate. Namely, by performing the inverse Fourier transform (IFFT) over the filtered Fourier space (Figure 3-10(c)) and plotting its amplitude, we obtain the reconstructed intensity distribution of C (see Figure 3-10(d)). Note that the two bright peaks at the first and third quadrants in Figure 3-10(b) correspond to the interference of the PL on the camera window (etaloning) and should not be taken into account.

Then, subtracting from the phase of $\text{IFFT}\{\mathbf{F}\{C^*R\}\}$ the periodic phase pattern depicted in Figure 3-10(e) which appears due to IFFT performed for the off-axis harmonic, we receive the phase distribution of the studied wave C. In the data analysis, the correction phase (Figure 3-10(e)) is obtained as a phase of the IFFT performed over the delta function placed in the centre of mass of the filtered FFT (Figure 3-10(c)). Note that the R wave was not taken into account for the above considerations because it is a plane wave and can induce only a global phase shift to the C wave phase.

3.3.5 Photon statistics measurements

We employ a Hanbury Brown and Twiss (HBT) interferometer coupled with time-correlated single photon counting (TCSPC) technique to measure the second-order cross-correlation function $g_{\mu,\nu}^{(2)}(\tau)$ between two signals μ and ν —which can be different polarisation components of the emitted cavity light—as a function of time delay τ ,

$$g_{\mu,\nu}^{(2)}(\tau) = \frac{\langle a_{\mu}^{\dagger}(t)a_{\nu}^{\dagger}(t+\tau)a_{\nu}(t+\tau)a_{\mu}(t) \rangle}{\langle a_{\mu}^{\dagger}(t)a_{\mu}(t) \rangle \langle a_{\nu}^{\dagger}(t+\tau)a_{\nu}(t+\tau) \rangle}. \quad (3.8)$$

Here, $a_{\mu,\nu}^{\dagger}$ and $a_{\mu,\nu}$ are photon creation and annihilation operators of the emitted cavity light for given polarisations μ, ν , respectively.

In the experiments, we split the polariton emission in the polarisation domain

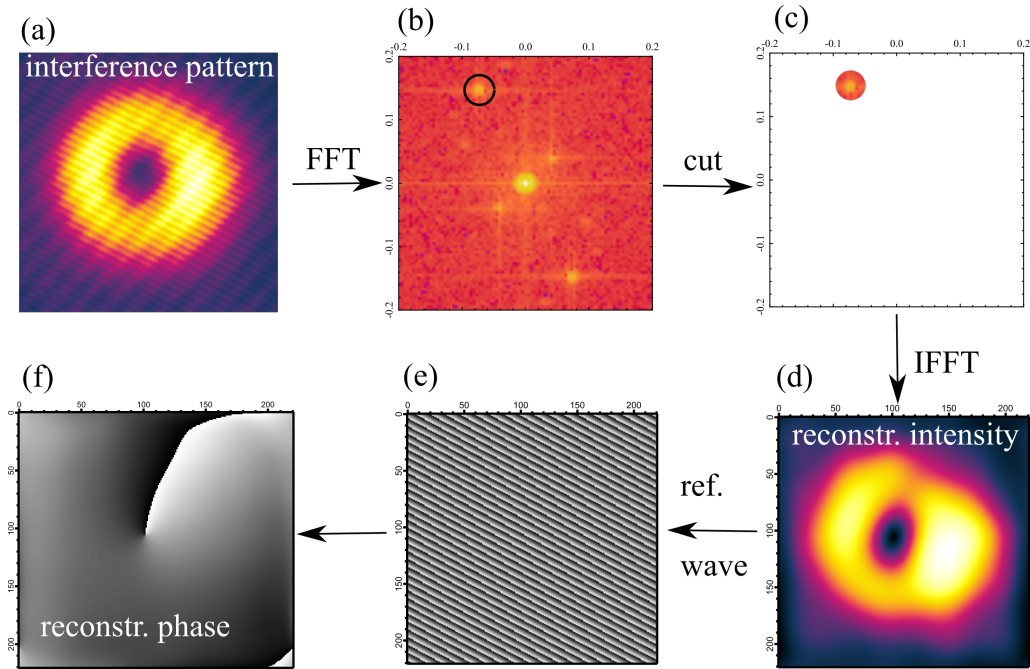


Figure 3-10: 2D FFT is performed on the experimental interference pattern (a), and the resultant image is depicted in (b). The IFFT is performed on the filtered spatial frequency harmonic corresponding to the interference (c). The reconstructed intensity distribution of IFFT intensity is in panel (d). The reconstructed phase corrected on the reference wave (e) is depicted in panel (f).

with the polarising beamsplitter (PBS) and measure the cross-correlation function for the orthogonal linear (horizontal H and vertical V, diagonal D and anti-diagonal AD) and circular polarisation components intensities. As long as the spin of polaritons can be detected as the polarisation of the out-coming cavity photons, the utilisation of the correlation measurements allows us to track the recurrent dynamics of the condensate spin. For instance, the anti-bunching of the cross-correlation H,V polarisation components was reported to be evidence of the instant spin flips occurring in the condensate [8]. Moreover, the oscillations in the intensity cross-correlation function with the local minimum in the zero time-delay manifested the self-induced Larmor precession of the condensate spin [8].

The HBT interferometer is usually utilised for the measurement of the photon statistics of the incoming light. The measurement of the auto-correlation intensity function ($\mu = \nu$ in Equation (3.8)) for the total condensate emission or intensities of separate polarisation components, gives us the correspondent photon statistics. Even though the condensate emission is usually coherent $g^{(2)}(0) = 1$ [8, 129, 130], its

linear polarisation projections could have $g^{(2)}(0) > 1$. Thus, the shape of the auto-correlation function for any spin component allows us to retrieve the characteristic times of the condensate spin dynamics (spin coherence).

The photon detection in the experiment is realised with the avalanche photodiodes. The time delay between the two arms of the interferometer is controlled by the electronics of the TCSPC card or by the optical delay line, depending on the experiment. It is worth mentioning that the intensity (cross-) correlation measurement is the statistical approach. The presented further dependencies of $g_{\mu,\nu}^{(2)}(\tau)$ are the result of the averaging over millions of condensate realisations since it usually takes more than 10 minutes to obtain one set of experimental data.

3.3.6 Polarisation measurements

A big part of this thesis is devoted to the study of the spin of polariton condensate, which is detectable as the polarisation of the out-coming cavity light. This section concerns the experimental techniques used for the polarisation measurements in this work as well as some basic theory of polarisation.

Polarisation is the fundamental property of light, which specifies the behaviour of electric field \mathbf{E} oscillations in the electromagnetic wave. Light can be fully polarised (if there is a certain pattern which strictly describes E-vector behaviour), unpolarised (when amplitude and direction of electric field change stochastically) or partly polarised (a combination of the previous cases).

The conventional description of fully polarised light is built on the decomposition of the electric field to the orthogonal linear polarisations E_x and E_y [131]. Given that light with frequency ω propagates in the z-direction, electric field projections onto the other two axes can be written as follows:

$$E_x = E_{0x} e^{i(\omega t + \phi_x)} \quad (3.9)$$

$$E_y = E_{0y} e^{i(\omega t + \phi_y)} \quad (3.10)$$

where ϕ_x and ϕ_y are the phases of the corresponding electric field projections. If

the phase difference between two orthogonal components is equal to 0 or $\pm\pi$, then the electric field oscillates along one line in xy-plane slanted at angle $\beta = E_y/E_x$ with respect to the x axis. This light is called linearly polarised. Conversely, if $\phi_x - \phi_y = \pm\pi/2$ (and $E_{0x} = E_{0y}$), the electric field vector traces a circle in the xy plane, and the light is circularly polarised. The light is elliptically polarised in all other cases. Depending on the direction of the electric field vector rotation, there are right- (σ_+) and left-circular (σ_-) polarisations.

The representation of polarisation with the orthogonal electric fields (linear or circular polarisation) is quite natural, but it can hardly be measured in the experiment since most of the detectors record the intensity of the field but not its amplitude and phase. Moreover, conventional representation does not describe partially polarised light. In this regard, the alternative approach for the polarisation description was introduced by G.G. Stokes in 1852. In the essence of this approach are 4 Stokes parameters, which fully describe the polarisation state of the light.

Stokes parameters are defined as intensities of studied light passing through different polarisation filters [127]. Namely, the intensities of polarisation projections on horizontal (In_1), diagonal (In_2) and circular polarisers (In_3). So Stokes parameters are written as

$$\begin{aligned}
 S_0 &= 2In_0 \\
 S_1 &= 2In_1 - 2In_0 \\
 S_2 &= 2In_2 - 2In_0 \\
 S_3 &= 2In_3 - 2In_0
 \end{aligned} \tag{3.11}$$

Note that S_0 equals the doubled total light intensity $2In_0$, S_1 is the "tendency" of characterised light to the horizontal (H) polarisation ($S_1 > 0$) or vertical (V) ($S_1 < 0$), S_2 is that of diagonal (D) or anti-diagonal (AD) ones. Finally, S_3 is positive when light has right-handed circular polarisation and negative otherwise.

Taking into account expressions for electric field components in Cartesian coor-

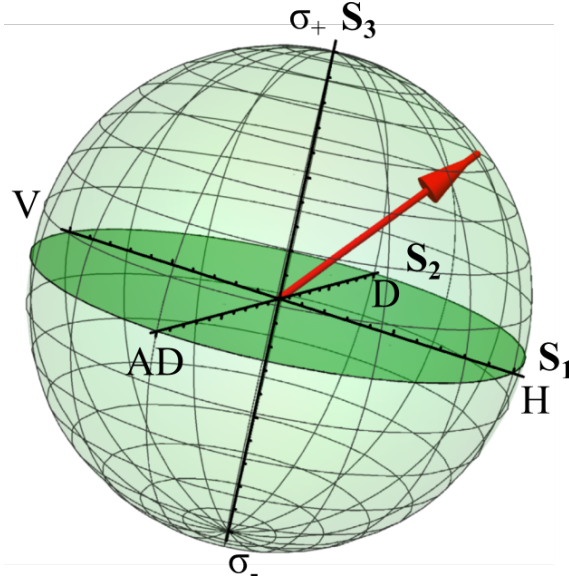


Figure 3-11: Poincare sphere for the representation of polarisation states. The red arrow depicts the polarisation vector. H, V, D, AD σ_+ and σ_- stand for the horizontal, vertical, diagonal, anti-diagonal right- and left-circular polarisation, respectively.

dinates (3.9), one can rewrite (3.11) as follows [127]

$$\begin{aligned}
 S_0 &= |E_x|^2 + |E_y|^2 \\
 S_1 &= |E_x|^2 - |E_y|^2 \\
 S_2 &= 2\text{Re}(E_x E_y^*) \\
 S_3 &= -2\text{Im}(E_x E_y^*)
 \end{aligned} \tag{3.12}$$

In the experiment, it is often handy to operate with the Stokes components normalised on S_0 . So they are three standardised Stokes parameters S_1, S_2, S_3 , which characterise the polarisation of studied light and also build a 3D vector. The full variety of polarisation states then occupies a Poincare sphere with a radius of unity. Fully polarised states lay on the surface of the sphere, while partially polarised ones are inside. The equator of the sphere represents linear polarisation states, and left- and right-circular ones are located at the poles (see Figure 3-11) [132].

In this formalism, the degree of linear polarisation (DLP) [127] of the studied light is written as follows:

$$DLP = \sqrt{S_1^2 + S_2^2} \tag{3.13}$$

The degree of circular polarisation (DCP) reads as

$$DCP = |S_3| \quad (3.14)$$

And finally, the overall degree of polarisation (DOP) is defined as

$$DOP = \sqrt{S_1^2 + S_2^2 + S_3^2} \quad (3.15)$$

While the normalised Stokes components can take any value from -1 to 1, the DLP, DCP and DOP are bound from 0 to 1. Moreover, given the set of Stokes parameters for the studied light, one can calculate the result of its interaction with some polarising elements using Mueller calculus. For this, every element, such as a polariser, QWP, HWP, etc., has a corresponding 4×4 Mueller matrix [127], and by multiplying the initial Stokes vector by this matrix, one deduces the resultant Stokes vector. This method offers an easy way to characterise complex polarisation setups only by multiplying corresponding Mueller matrices.

The representation of polarisation with the Stokes vector is quite handy in experimental research since it operates with the intensities of light, which can be measured with conventional photodetectors. The polarimeter developed by the Author was utilised in the experiments in the scope of this thesis. The device measures the Stokes vector by definition (Eq. (3.11)).

The optical scheme of the polarimeter is depicted in 3-12. A beamsplitter (BS) divides incoming condensate PL light into two equal parts. One of them hits the polarising beamsplitter (PBS), and the intensities of horizontal I_1 and vertical I_2 polarisation components are registered by two photodetectors (Det.1 and Det.2). S_0 and normalised S_1 are calculated by the equation (3.3.6). The other part of the PL is also split with BS. One portion travels through the polariser with the transmission axis at 45 degrees; the transmitted intensity I_3 is recorded with Det.3 and used for the calculation of S_2 (Equation (3.3.6)). The intensity I_4 of the right circular polarisation projection of the remaining light is used to retrieve the S_3 component of the whole characterised PL (see Det. 4 in (3.3.6)). The polarimeter is calibrated to the laser source with a known polarisation state and a wavelength corresponding

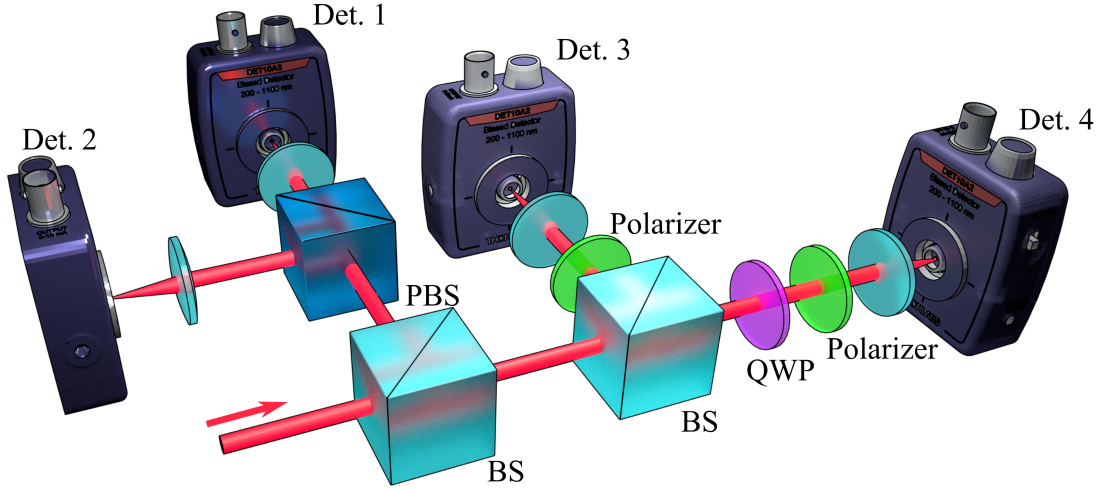


Figure 3-12: The polarimeter optical setup. The intensities of horizontal, vertical, diagonal and circular polarisation projections of the incoming light are measured by Det.1-4, respectively.

to that of the condensate.

$$\begin{aligned}
 S_0 &= 2(I_1 + I_2) \\
 S_1 &= \frac{I_1 - I_2}{I_1 + I_2} \\
 S_2 &= \frac{4I_3 - (I_1 + I_2)}{I_1 + I_2} \\
 S_3 &= \frac{4I_4 - (I_1 + I_2)}{I_1 + I_2}
 \end{aligned} \tag{3.16}$$

To characterise the condensate emission at low excitation powers, we couple the signals from all photodetectors to lock-in amplifiers. Lock-in amplifiers are devices that utilise synchronous detection at a modulation frequency (here the AOM modulation frequency), thus increasing the signal-to-noise ratio. However, the lock-in amplifiers' response time limits the polarimeter's operation speed. The integration time of lock-in is set to 100 ms, so the measured polarisation of condensate PL in experiments is averaged over more than 500 realisations. The polarimeter is built-in into the measurement software of the experimental setup and allows for characterising the condensate PL polarisation while changing excitation parameters (e.g. pump power and polarisation). This polarimeter features high sensitivity and allows char-

acterising the polarisation state in real-time in contrast to the commercially available polarimeters.

For the time-resolved polarisation measurements of the condensate PL, we detect its polarisation projections with high-sensitivity photodiodes. By splitting the condensate emission with PBS we can measure the dynamics of the condensate S_1 during the excitation pulse. In the same manner, characterising the diagonal and circular polarisation projections we measure the S_2 and S_3 components, respectively. More details on this technique are given in the corresponding experimental Chapters.

3.4 Generalised Gross-Pitaevskii Equation

Numerical simulations offer insight into the condensate dynamics that are often hidden in experimental observations. The polariton condensate can be modelled by the generalised Gross-Pitaevskii equation, taking into account the injection, dissipation and interaction of polaritons in the condensate. There are multiple variations of the GPE [13, 133], and the choice of one depends on the task. Here, the general case of GPE is considered an example, whereas the specific simulation equations are described in the corresponding Chapters. The generalised GPE describing the condensate wave-function $\Psi(r, t)$ is written as follows:

$$i\frac{d\Psi(r, t)}{dt} = \left(-\frac{\hbar^2\Delta}{2m} + \frac{i}{2}(R(n_R) - \gamma) + g|\Psi(r, t)|^2 + 2\hat{g}n_R \right) \Psi(r, t) \quad (3.17)$$

where m is the effective mass of polariton, γ is their decay rate, g is polariton-polariton interaction strength and $2\hat{g}$ is the coupling constant of the condensate with the reservoir refining their interaction. $R(n_R)$ is the stimulated scattering rate of polaritons to condensate and is a monotonically growing function of n_R . The exciton reservoir that feeds the condensate is usually described with the rate equation as follows:

$$\frac{dn_R}{dt} = P - \gamma_R n_R - R(n_R)|\Psi(r, t)|^2 + D\Delta n_R \quad (3.18)$$

where P is the laser pumping rate, D is the exciton diffusion rate, and γ_R is reservoir damping.

Chapter 4

Spin of Polariton Condensate in the Optical Trap

Now, we move to the parts of this thesis concerning the experimental and theoretical results obtained by the Author in the course of the PhD study. This particular Chapter is devoted to the experimental study of the spin of polariton condensate in an optical trap depending on the trap size and the excitation laser power and polarisation. These results are published in Physical Review B journal [1].

All experimental results discussed in this Chapter were obtained by the Author if not stated otherwise. All experimental Figures have been produced by the Author and published in Ref. [1] if not stated otherwise. The utilisation of Figures in this Chapter is granted by the American Physical Society (APS) (the publisher of Physical Review B journal) Copyright Policy. The numerical simulations were carried out by Dr. Helgi Sigurdsson. The Figures containing the simulation results were made by Dr. Helgi Sigurdsson and are also published in Ref. [1]. Their usage in the thesis is granted by the APS Copyright Policy.

4.1 Introduction

The information about the polariton spin is encoded in the polarisation of the light emitted from the cavity when polariton decays. The characterisation by conven-

tional polarisation detecting devices in conjunction with nonlinearity inherent to polaritons boosted the research of polariton condensate spin [33, 37]. This has led to numerous studies all over the globe and many remarkable findings. Some polariton spin phenomena are described in Section 2.8. Beyond the fundamental interest of spin studies, there is a search for possible applications. The wide range of discovered properties and spin phenomena in polariton condensates makes them excellent candidates for applications in spinoptronics [37].

Fueled by the promise of developing polariton-based spinoptronic devices, nonresonant excitation schemes are the likely direction for future applications. Such pump configuration is described in detail in Section 2.5. Nonresonant optical excitation builds up a density of incoherent excitons in the cavity, which eventually triggers bosonic stimulated scattering of polaritons with a subsequent buildup of coherence and polarisation, as they condense [15]. This approach eliminates the need to fine-tune an excitation laser's energy, momentum, and phase, thus significantly simplifying the future device operation and widening its application area. Moreover, such a device would likely operate above the condensation threshold in order to efficiently exploit the nonlinear spin dynamics of the polariton fluid. Nonlinearity is the needed ingredient for a device to perform nontrivial tasks [117, 134], but it can also destabilise the spin state of the condensate, affecting said device performance. The way out of this would be the utilisation of the optical traps. The decreased overlap of the condensate with the exciton reservoir will allow to eliminate or at least significantly decrease the destabilisation and decoherence of the spin due to polariton-exciton interactions, thus improving the device stability.

The investigation of the spin of a polariton condensate in the optical trap is ongoing. For instance, in the recent work, Ohadi et al. demonstrated very interesting regimes of polarisation buildup, collapse, inversion, and hysteresis [36] in a condensate created in a pentagon trap. Nevertheless, there are still many unknowns. Namely, a complete characterisation of the spin properties of an optically confined polariton condensate and its stability properties was still lacking.

In this regard, in this Chapter, we introduce the complete characterisation of the polariton condensate in the optical trap. We experimentally and theoretically

investigate the spinor behaviour depending on the trap size, pump polarisation and power. We discover and study several interesting regimes of polariton spin, namely optical orientation, polarisation pinning, depolarisation, and signatures of the self-induced Larmor precession. The details are introduced below.

4.2 Excitation configuration and optical setup

For these experiments, we use the experimental setup described in Chapter 3. The simplified schematic of it is presented in Figure 4-1. We shape the non-resonant laser beam with the SLM to the form of a ring. This ring forms the confining potential for polaritons, which condense and emit light. We characterise the emission in the reflection configuration utilising the polarimeter and detect the Stokes components for the different pumping powers and polarisations (controlled with the quarter-wave plate (QWP) or a half-wave plate (HWP)).

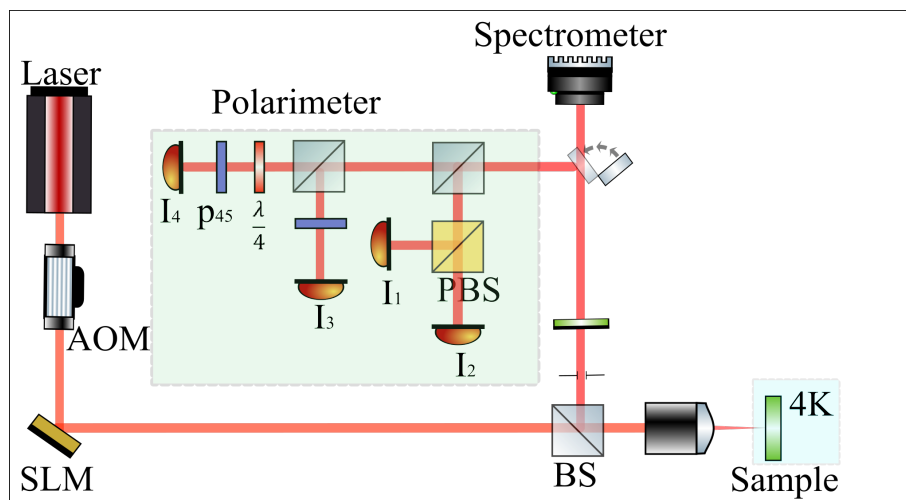


Figure 4-1: The schematic of the experimental setup for study of polariton condensate spin in the optical trap. The condensate is created with the non-resonant laser beam chopped with AOM and shaped with the SLM. The condensate PL is studied in reflection configuration with the polarimeter, real-space camera and spectrometer.

4.3 Spin of polariton condensate under non-resonant excitation: descriptive features

The descriptive features of polariton condensate under non-resonant excitation reported to date are summarised in Figure 4-2. At circular pump polarisation, the condensate polarisation tends to inherit the handedness of the non-resonant excitation due to the optical orientation effect. The essence of this effect is as follows. The circularly polarised light excites the excitons with the same value of spin due to the spin conservation rule. The hot exciton plasma then relaxes to polaritons and excitons, losing the information about the laser photons' spin along the way. However, typical electron spin relaxation times in GaAs-based cavities are much longer than the relaxation time of the excitonic mode [116]. As a result, some of the degree of circular polarisation of the continuous wave beam is transferred to the spin population [13, 135] of the incoherent excitonic reservoir, which feeds polariton condensate. Above the threshold, thus, the reservoir forms the polariton condensate, which is cocircularly polarised with the non-resonant pump. This process is schematically presented in the right part of Figure 4-2.

In the case of linearly polarised excitation, the polarisation of the condensate becomes randomly oriented on the (S_1, S_2) equatorial plane of the Poincaré sphere since no specific condensate phase is adopted from the incoherent reservoir [136, 137, 138]. This is one of the most direct manifestations of spontaneous symmetry breaking due to phase transition occurring when polaritons condense [137]. Thus, both for the linear and circular pump polarisations, the condensate is described by the order parameter (wave function), which can be directly tracked as the degree of polarisation (DOP) of the condensate PL. The increase of DOP is directly related to the increase of the condensate phase coherence [139] (the narrowing of the linewidth).

If the sample structure is anisotropic due to fabrication or structural strains, a fine linear polarisation splitting forms, which pins the condensate polarisation to the defined linear state (see left inset in Figure 4-2) [34, 69, 140, 141, 142]. This effect is called polarisation pinning.

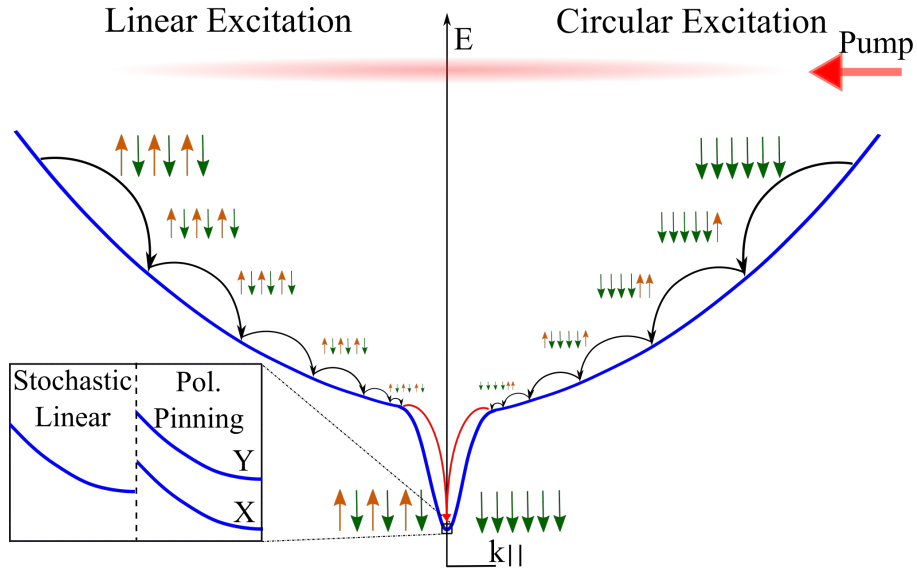


Figure 4-2: Schematic of the lower polariton dispersion (blue curve) illustrating the formation mechanism of the spinor condensate for circular (right side) and linear (left side) polarised non-resonant excitation (red area). The inset: Birefringence splits the degeneracy between X (horizontal) and Y (vertical) polarised modes of the cavity field, leading to the pinning of the condensate pseudospin into the lower energy mode. The figure is adapted from [1].

4.4 Experimental results

We shape the excitation laser in the form of a ring (depicted in Figure 4-3(a)), so it has a $12 \mu\text{m}$ diameter when focused on the sample. The size of the trap is chosen so the condensate always occupies the Gaussian ground energy state presented in Figure 4-3(b,c) for all studied pump powers above the threshold. In order to filter out residual emission from the reservoir and collect only the condensate PL, we perform k -space filtering of wave vectors more than $\pm 1 \mu\text{m}^{-1}$. We do so by the aperture inserted in the input of the polarimeter. The condensate is forming in the ground state of the excitation potential near $k = 0$, so filtering allows us to separate the useful signal from the condensate and the redundant one from the uncondensed polaritons forming at a higher k . We study the time-integrated polarisation from a trapped polariton condensate as a function of both pump power and ellipticity controlled by the rotation of the QWP in the excitation path. The high sensitivity of the polarimeter achieved using the lock-in amplifiers allows us to detect the polarisation state even below the polariton condensation threshold. The results are

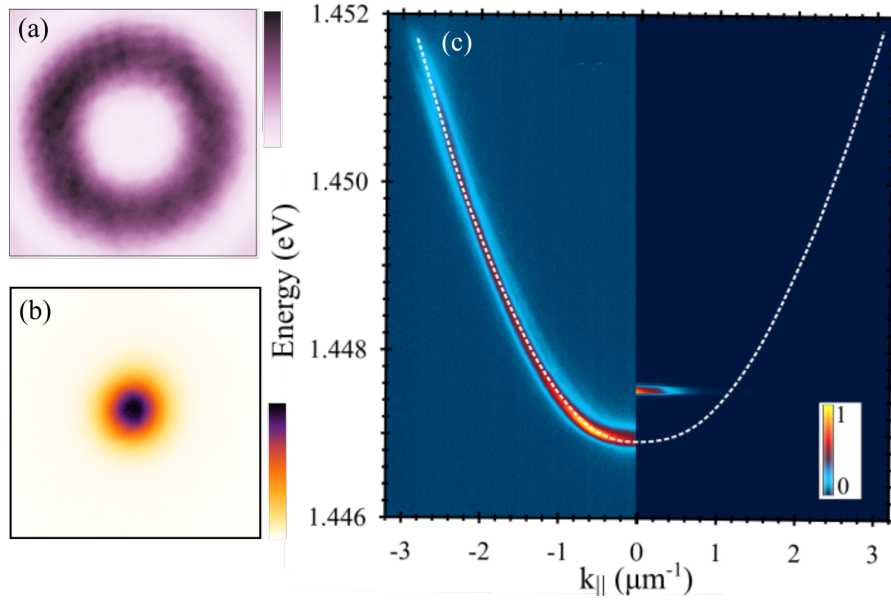


Figure 4-3: (a) The excitation laser profile. The white-to-purple colour scale corresponds to the normalised laser emission intensity. (b) The condensate real-space integrated intensity distribution. (c) The normalised polariton dispersion below (left part) and above (right part) the condensation threshold. The white dashed line is to guide the eye. The colour scales in panels (b) and (c) correspond to the normalised condensate emission intensity.

presented in Figure 4-4.

Here, $\text{QWP} = \mp 45^\circ$, and 0° correspond to right-, left-circular, and linear polarisation of the excitation laser, respectively. Between those values, the pump is elliptically polarised. Figures 4-4(a-d) show the condensate total emission intensity S_0 , degree of linear polarisation $\text{DLP} = \sqrt{S_1^2 + S_2^2}$, total degree of polarisation $\text{DOP} = \sqrt{S_1^2 + S_2^2 + S_3^2}$, and circular S_3 and linear S_2, S_1 polarisation components, respectively.

The total emission intensity (Figure 4-4(a)) is plotted in the logarithmic colour scale. It reveals the non-linear growth of the condensate population with the pump power for each pump polarisation. However, one can notice that condensation threshold power is higher for linear polarisation of the excitation laser (0° of QWP) than that of the circular ones ($\text{QWP} = \mp 45^\circ$). So the x-axis of each measured polarisation map (Figures 4-4(a-f)) is normalised to the threshold pump power P_{th} for the circular polarisation in order to unify the measurements. As a result, we find that the condensation threshold for linearly polarised excitation occurs around $1.18P_{\text{th}}$. The

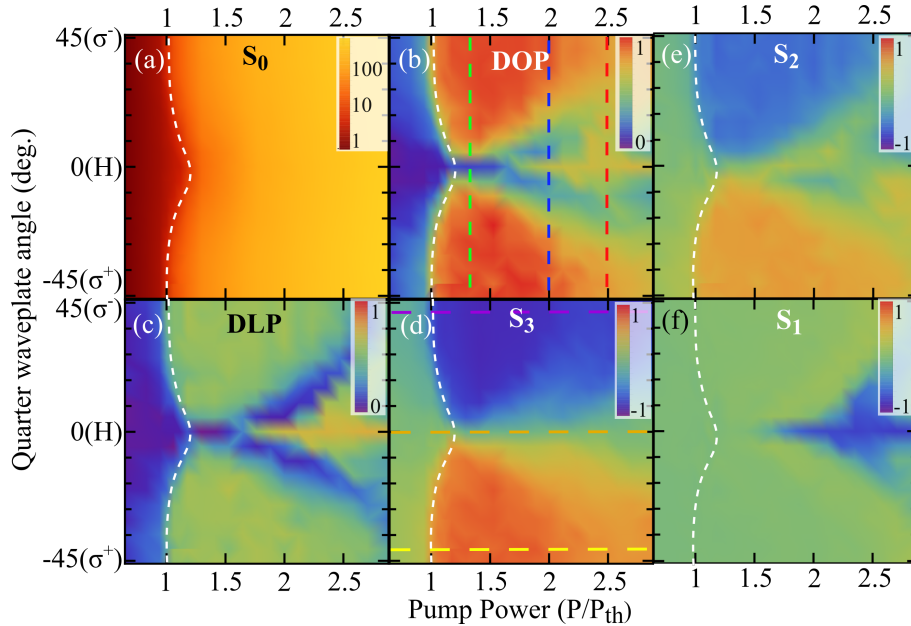


Figure 4-4: (a) Total emission intensity S_0 in arbitrary units, (b) DOP, (c) DLP, (d) S_3 , (e) S_2 and (f) S_1 as a function of pump power P and ellipticity (QWP angle) for a ring excitation geometry with a diameter of $d = 12 \mu\text{m}$. QWP angles $\mp 45^\circ$ and 0° correspond to right-, left-circular, and linear polarised excitation. White dashed lines depict the condensation threshold. Figures are adapted from [1].

larger pump power is required for condensation because of the same-spin Coulomb exchange interactions dominating over opposite-spin interactions [143, 144]. A right (left) circular polarised excitation beam results in a more spin up (down) populated reservoir of incoherent excitons, which will sooner reach threshold density and undergo stimulated scattering into a cocircularly polarised condensate (see Figure 4-4(d)) [61, 145]. On the other hand, the linearly polarised excitation results in an equal population of spin-up and spin-down polaritons, thus requiring a bigger pump power for them to condense.

The simultaneous measurement of three Stokes components gives us access to the total degree of polarisation of the condensate. In Figures 4-4(b), we show that below the threshold, marked by the white dashed line, the absence of stimulation mechanisms results in unpolarised PL emission with DOP close to zero. Above the threshold, a sharp increase in the DOP marks the formation of the condensate order parameter with emission almost fully polarised. The most rapid growth of the DOP corresponds to the case of the circular and elliptical polarisations of the excitation laser (QWP $\mp 45^\circ$ and nearby). The condensate, in this case, is ellipti-

cally polarised, with a significant value of S_3 polarisation component and smaller or absent linear ones (see Figures 4-4(d-f)). Interestingly, due to the process of optical orientation [13, 61, 145] of excitons described above, the handedness of condensate polarisation corresponds to that of the excitation laser. Note that the S_2 polarisation component (see Figure 4-4 (e)) for the elliptically and circularly polarised excitation arises due to the optical retardance of the detection part of the optical setup. The circular polarisation of the condensate emission becomes elliptical while travelling through the optical elements (lenses, mirrors, etc.) in the setup. The value of the corresponding optical retardance is estimated in Section 5.6. This detrimental effect can be corrected by the Soleil-Babinet compensator or by the post-processing rotation of the experimental Stokes vectors. We underline here that this retardance does not affect the conclusions on the spin physics of the condensate made in this Chapter.

The notable exception to the sharp increase of the DOP in Figure 4-4(d-f) is the case of linearly polarised excitation ($\text{QWP} = 0^\circ$), where just above threshold (between $1.18P_{\text{th}}$ and $1.59P_{\text{th}}$) DOP is zero. The reason for this behaviour will be discussed in detail below. At higher pump power, the polarisation of the condensate starts to build up, and condensate PL is linearly polarised, which is manifested by the high values of DLP (see Figure 4-4(c)). Further, we will call this region of high DLP for linearly (and slightly elliptically) polarised pump a linear polarisation "island". We attribute the emergence of this "island" to the in-plane polarisation splitting (due to sample strain/birefringence) leading to the pinning of the condensate pseudospin. The polarisation pinning is inherent to incoherently excited condensate and has been reported elsewhere [34, 69, 140, 141, 142].

While the polarisation pinning is inherent to polariton condensates, the low DOP region before the linear polarisation "island" has not been observed before. Past experiments have shown either the immediate buildup of a pinned polarisation above threshold [141], shot-to-shot stochastic polarisation [135, 137], or S_3 spin flips [146]. We attribute this low DOP regime to the low occupation of the condensate (small non-linearity) at small pump power above the condensation threshold, making its pseudospin weakly pinned. Stochastic noise sets the pseudospin on a random walk

on the Poincaré sphere, resulting in zero average DOP of the condensate PL. In other words, our observation implies that pinning does not occur unless a large enough particle number in the condensate is achieved. The stochastic behaviour of the spinor is confirmed with the numerical simulation performed by Dr. Helgi Sigurdsson and presented in Figure 4-5. Indeed, the flips of S_1 component of the condensate emission are very frequent for the low pump power (Figure 4-5(a)) and become rare (Figure 4-5(b)) until eventually stabilized at linearly polarised (Figure 4-5(c)) state dictated by pinning. The details of the simulation will be introduced in Section 4.6.

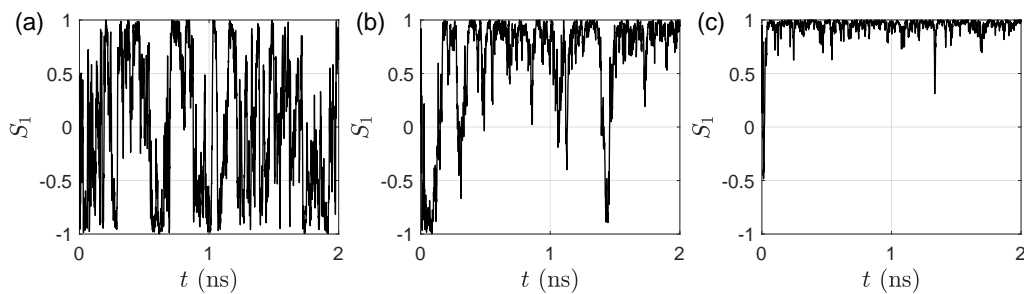


Figure 4-5: Simulated S_1 Stokes component for QWP = 0° showing the onset of pinning with growing pump power. (a) $P = 1.2P_0$. (b) $P = 1.5P_0$. (c) $P = 2P_0$. The figure is adopted from [1].

The stochastic spin flips under linearly polarised excitation have been recently observed experimentally and reported in Ref. [8]. Resolving the H and V condensate PL polarisation projections, Baryshev et al. observed the anti-correlated peaks of intensities at the pump power corresponding to the emergence of the pinning regime. The results are depicted in Figure 4-6(a). The instant anti-correlation peaks observed, for instance, around $0.2 \mu\text{s}$, manifest the flip of the condensate from being pinned vertically to horizontal polarisation. Moreover, the intensity correlation measurement performed in the same study [8] showcased the anti-bunching of H and V (see Figure 4-6(b)) that also evidences the polarisation flips.

Formally, the fine splitting between the polariton pseudospin components can be described by an effective magnetic field

$$\mathbf{\Omega}(\mathbf{r}) = (\Omega_x, \Omega_y, \Omega_z) \quad (4.1)$$

which affects the condensate pseudospin. Here, the z direction is taken along the

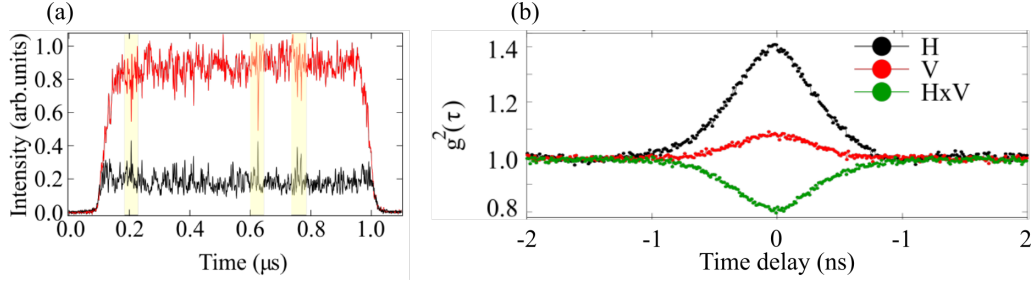


Figure 4-6: (a) Experimentally measured time dynamics of the condensate PL horizontal (black) and vertical (red) polarisation projections. (b) The intensity correlation measurements for the condensate in the optical trap. The black and red dots are the auto-correlation function for horizontal (H) and vertical (V) polarisation projections, respectively. The green dots are the cross-correlation function for H and V polarisation projections. Figures are adopted from [8].

crystal growth axis, normal to the cavity plane. The corresponding Hamiltonian, in the basis of ψ_{\pm} , can be written as $\mathcal{H}_{\Omega}(\mathbf{r}) = \hbar\Omega(\mathbf{r}) \cdot \boldsymbol{\sigma}$, where $\boldsymbol{\sigma}$ is the Pauli matrix vector. The in-plane birefringence induced by mechanical strains in the sample is position-dependent and defined by the local value of birefringence. We confirm it experimentally by measuring the condensate PL polarisation at two different spots on the sample; the results are shown in Figure 4-7.

For the first excitation spot on the sample (see Figure 4-7(a,c)) at high pump powers ($P > 1.4P_{\text{th}}$), we see an increase in the S_2 component, while the S_1 stays close to zero. On the other hand, for the second point (see Figure 4-7(b,d)), both S_1 and S_2 components reach high values for large pump power. In this regard, the (Ω_x, Ω_y) components (in expression (4.1)) of the effective magnetic field are random across the sample, and the total magnetic field is coordinate, \mathbf{r} , dependent. Thus, the polarisation of "island" differs from point to point on the sample.

So far, we have explained the regimes of circular and linear excitation; the elliptical one stayed out of the scope. In general, for the elliptically polarised excitation, the condensate circular polarisation component S_3 follows the handedness of the pump because of the optical orientation [34, 116, 138]. Interestingly, even a very small circular S_3 component (QWP $\approx \pm 2^\circ$) of the optical excitation is enough to set the condensate to circular polarisation (see Figure 4-8 (a)). The tiny imbalance of two different spin reservoirs leads to the condensate having the circular polarisation of the same handedness.

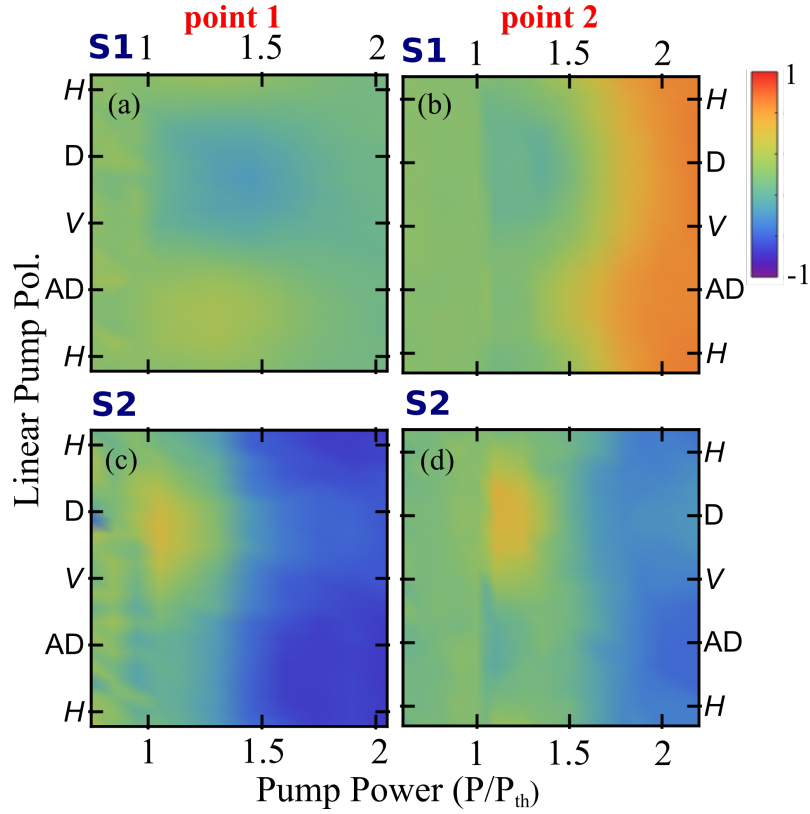


Figure 4-7: (a,b) S_1 and (c,d) S_2 polarisation maps for two different sample positions for varying linear polarisation and power of the excitation laser. H, D, V and AD correspond to horizontal, diagonal, vertical, and anti-diagonal polarisation, respectively. The figure is adopted from [1].

Moreover, the spin-imbalanced condensate and background reservoir of uncondensed polaritons result in an effective out-of-plane magnetic field. This can cause the condensate pseudospin to start precessing around this interaction-induced out-of-plane field (Larmor precession), suppressing the polarisation components in the time-average measurements in Figure 4-4(b). However, for increasing polarisation ellipticity, the condensate starts to become more pinned along the stronger Ω_z magnetic field, observed as an increase in S_3 (see Figure 4-4(d) and Figure 4-8).

Interestingly, the linearly polarised "island" is confined between the two depolarised streaks [see Figure 4-4(b,c)]. These streaks correspond to the interface between the pseudospin being pinned either by the in-plane magnetic field (Ω_x, Ω_y) from birefringence or the interactions-induced magnetic field Ω_z . In between these two pinning regimes, the pseudospin is very sensitive to background white noise, which can stochastically move it from precessing around one field to the other, caus-

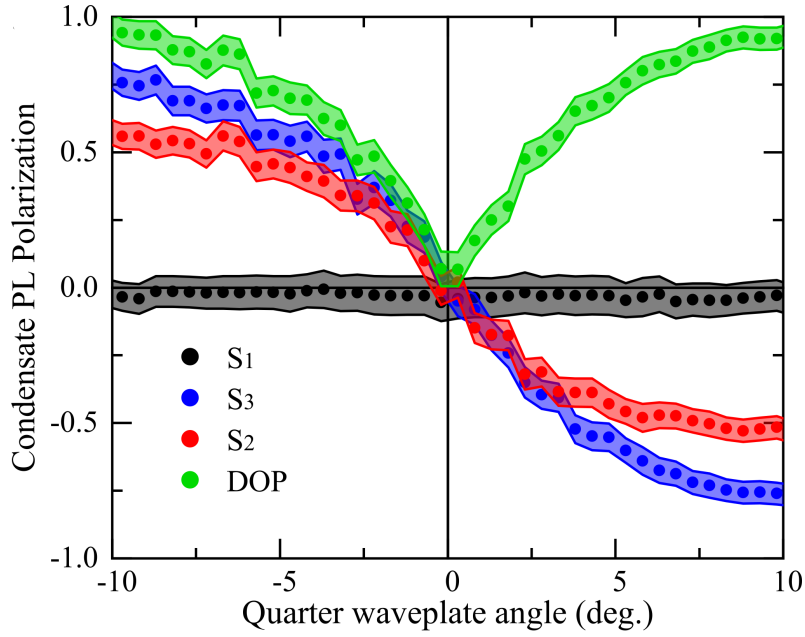


Figure 4-8: S_1 , S_2 , S_3 and DOP for the small pump ellipticity (QWP angle) at $P = 1.23P_{th}$. The figure is adopted from [1].

ing the lowering of the measured degree of polarisation.

To summarise this part and the properties of the condensate created in the ring optical trap with $12 \mu\text{m}$ diameter, we list the main findings described so far below.

1. We have performed the full polarisation analysis of the condensate PL for different pump powers and polarisations.
2. The condensation is accompanied by the growth of the degree of polarisation everywhere except for the linearly polarised pump. For the latter case, the spin is first destabilised by the polariton-polariton interaction, but at higher power, it adopts the defined linear polarisation state dictated by the excitation spot on the sample and birefringence-dependent effective magnetic field.
3. Due to the process of optical orientation, condensate adopts the handedness of the circularly polarised non-resonant pump.
4. Under an elliptically polarised pump, condensate spin precesses around the effective out-of-plane magnetic field.
5. The cross-sections of polarisation maps discussed in Figure 4-4 are plotted on the Poincare sphere in 3D in Figure 4-9. The cross-sections are made for the

fixed pump polarisation (Figure 4-9 (a)) and power (Figure 4-9 (b)). They represent three attractors present in the system for polariton spin. Namely, two cross-circularly polarised states and one linear polarisation state.

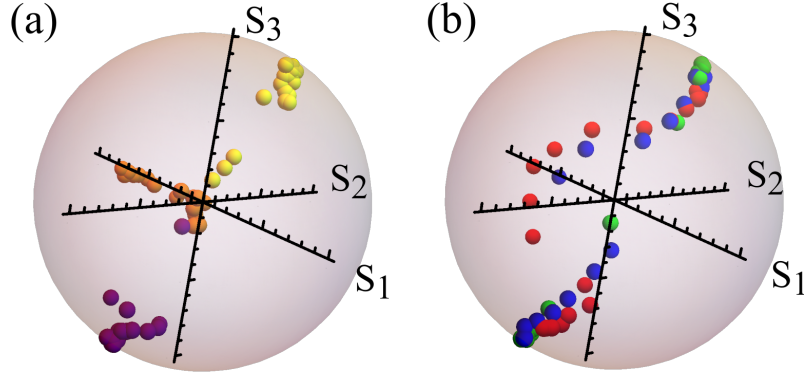


Figure 4-9: (a,b) Three-dimensional representation of the Stokes components with different colours corresponding to the same-colour horizontal and vertical dashed lines in Figures 4-4(b,d). Figures are adapted from [1].

We also note that our results do not depend on the exciton-photon detuning (at least in the range of the latter accessible with our sample). Figure 4-10 showcase the DLP and S_3 for detunings $\Delta = -4$ meV and $\Delta = -2$ meV. Notice that the main polarisation features described above stay unchanged regardless of the detuning value. The slight change of the linear polarisation “island” (see Figure 4-10 (b)) could be connected with the strength of the position-dependent birefringent field. For different positions on the sample, the strain-induced birefringence varies not only in direction but also in the amplitude of the effective magnetic field. That is analogous to the value of the energy splitting between two linear polarisation components – the larger the splitting, the larger the effective magnetic field. In this regard, the shape of the polarisation “island” is defined by the interplay of the self-induced Larmor precession under slightly elliptically polarised excitation and linear polarisation pinning. The change of the “island” shape could also be caused by disorder in the sample.

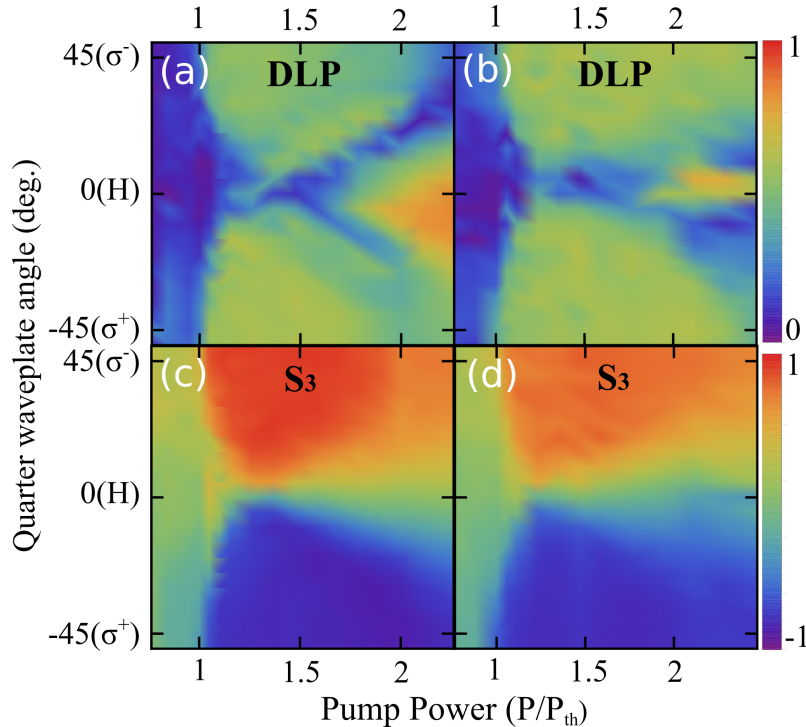


Figure 4-10: Measured DLP (a,b) and S_3 (c,d) for the exciton-photon detuning of $\Delta = -4$ meV (a,c) and $\Delta = -2$ meV (b,d). The figure is adopted from [1].

4.5 Trap size dependence of the condensate spin.

In this section, we study how the size of the annular optical trap affects the spin properties of polariton condensate. We study three different sizes (diameters): $d = 15, 12, 9 \mu\text{m}$. The size of the trap affects the overlap between the exciton reservoir and the condensate - the smaller the trap, the bigger the overlap, and ergo, the bigger their mutual interaction. As an extreme case, we also study the Gaussian excitation, where the condensate is formed atop the pump spot.

In Figure 4-11, we show the characteristic curves measured for three trap sizes. Namely, we measure the intensity of the condensate PL (proportional to the number of polaritons in the condensate) and its energy shift (blueshift due to interactions) depending on the excitation power. Even though the condensate always occupies the ground state of the trap, the characterised properties are indeed affected by the trap size. For example, we observe a more considerable number of polaritons in the condensate formed in a bigger trap, which follows from the decrease in polariton-reservoir interactions. Also, the condensate in the smaller trap has a bigger energy

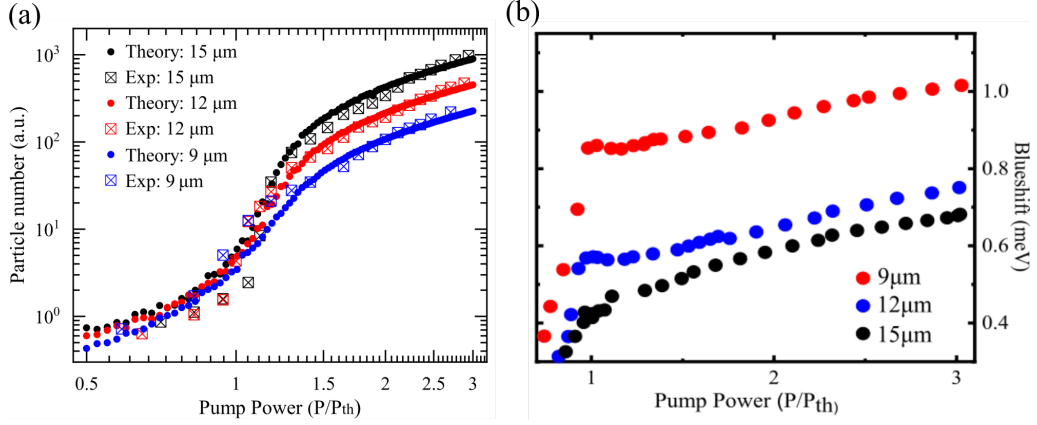


Figure 4-11: (a) Measured (squares) and simulated (circles) number of polaritons in the condensate as a function of pump power in units threshold calculated for $d=12\mu\text{m}$ trap size. (b) Measured blueshift of polariton condensate energy versus pump power for three trap sizes. The blueshift is calculated from the bottom of the lower polariton branch. For both panels, the excitation polarisation is circular. The figure is adopted from [1].

shift, with the condensate occupying higher energy, which is expected due to stronger confinement.

Interestingly, the trap size also influences the condensate's polarisation (or spin) properties. In Figure 4-12, we plot the experimentally and theoretically obtained DLP for different sizes of confined condensate and the one pumped with Gaussian excitation spot (FWHM $4\mu\text{m}$). Note that all excitation configurations for the size dependence are measured on the same spot on the sample.

Interestingly, the linear polarisation "island" in Figure 4-12 experiences a significant transformation for varying trap size. By decreasing the diameter of the excitation ring, we observe that the linear polarisation "island" shrinks (see Figure 4-12(b)) and moves further in pumping power until it vanishes completely (see Figure 4-12(c)). So, for the smallest $9\mu\text{m}$ trap, the condensate is unpolarised (in the integrated measurements) for the whole range of the characterised pump powers. Similarly, when the condensate is excited with a Gaussian excitation spot, the DLP decreases even more (see Figure 4-12(d)). This observation demonstrates that increasing the overlap between the condensate and its background reservoir results in strong depolarisation in the case of the linearly polarised excitation. This finding is supported and explained by numerical simulations below in Section 4.6.

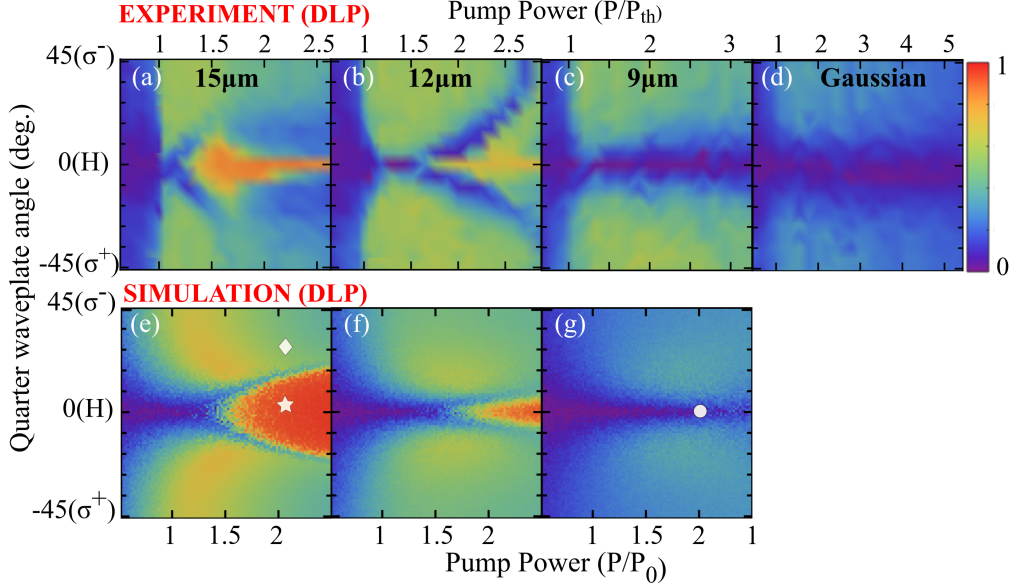


Figure 4-12: DLP polarisation maps as a function of pump power and QWP angle. Panels (a-c) show results for decreasing pump diameter $d = 15, 12, 9 \mu\text{m}$. Panel (d) shows the condensate DLP in the case of a Gaussian spot excitation (no confinement). (e-f) Simulated time-averaged condensate DLP using Eqs. ((4.2)-(4.4)). The star, circle and diamond markers correspond to panels (a-c) in Figure 4-15. The figure is adopted from [1].

To fully understand the condensate spin in traps of different sizes, we plot all three Stokes components and DOP for three studied trap diameters and Gaussian excitation in Figure 4-13.

For all sizes of the excitation ring, as well as for Gaussian excitation, we observe the optical orientation effect and condensate that is co-circularly polarised with the excitation laser (see Figure 4-13(i-l)). The condensate spin depolarisation with increasing pump power is observed for all configurations and is evident in a decrease in DOP. Moreover, the polarisation of the linear polarisation "island" is vertical for both traps where it is present (see Figure 4-13(a,b)). This manifests that the linear polarisation is governed by the local birefringence and does not depend on the size of the symmetric confining potential.

The overlap of the exciton reservoir and polariton condensate in the case of the excitation with the Gaussian spot is significant since the condensate is forming atop the pump spot. In this regard, the spin properties of the condensate for the tight Gaussian excitation are similar to the small optical trap (see Figure 4-13). The major part of the condensate is overlapped with the reservoir, and increased interactions

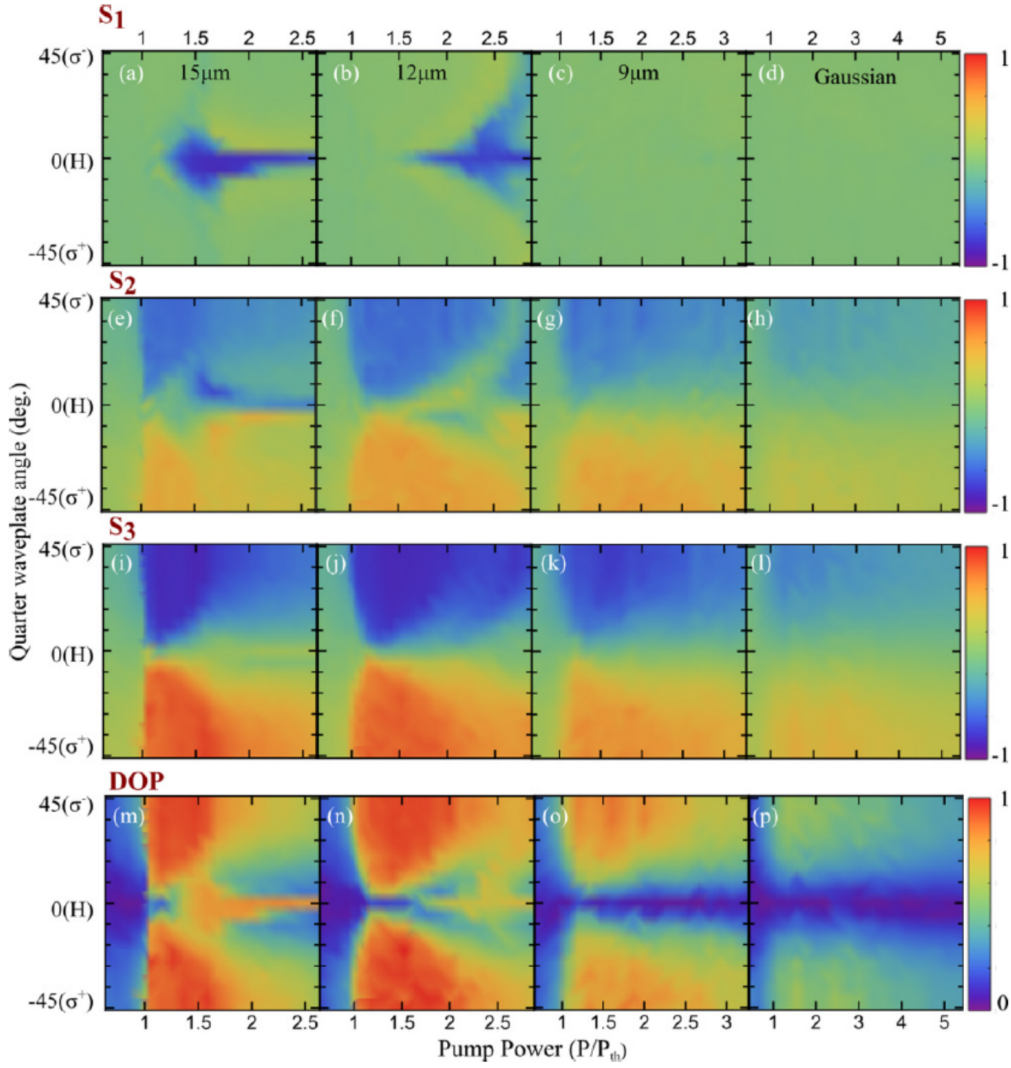


Figure 4-13: S_1 (a-d), S_2 (e-h), S_3 (i-l), and DOP (m-p) for a ring excitation geometry of diameter $d = 15, 12, 9\ \mu\text{m}$ and a Gaussian excitation geometry of FWHM = $4\ \mu\text{m}$, respectively. The figure is adopted from [1].

destabilise the condensate spinor, effectively lowering the integrated DOP (see Figure 4-13(p)) compared to the confined condensate. It should be noted that any light away from the Gaussian excitation spot, possibly adopting nontrivial polarization textures [113], has a negligible contribution to the averaged measurements.

Further, we record the condensate pseudospin when excited with linearly polarised light with different polarisation azimuth angles. The angle there is varied with the HWP in the excitation path. We find that S_3 and DLP of the condensate at high powers are mostly invariant to the linear polarisation azimuth (see Figure 4-14(a,b)). That is in striking contrast to the condensate in organic micro-

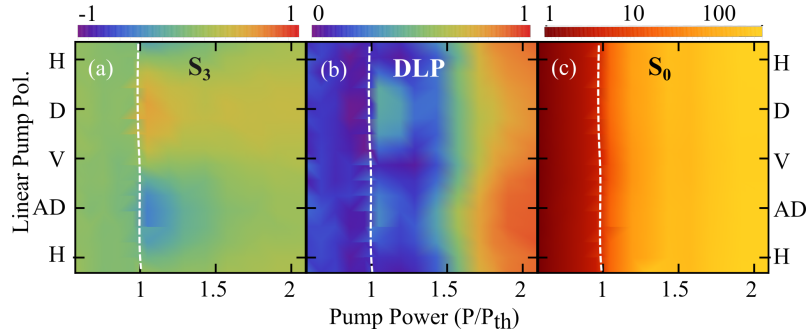


Figure 4-14: Condensate polarisation as a function of pump power and incident linear polarisation angle. (a) S_3 , (b) DLP, and (c) total emitted intensity. The vertical axis denotes the half-waveplate angle and is marked with different linear polarisations. Horizontal (H), vertical (V), diagonal (D), and anti-diagonal (AD). The figure is adopted from [1].

cavities [14, 52], where the linear polarisation is transferred to the condensate from the pump due to the dipole nature of excitons there. Yet, for our inorganic sample, the condensate polarisation is dictated by the local sample birefringence rather than transferred from the pump laser. Note that the condensation threshold is the same for all linear polarisation angles of the excitation (see dashed line in Figure 4-14(c)) because any linear polarisation gives rise to equal populations of polaritons with different spins. We point out that the condensate polarisation varies slightly when excitation switches from diagonal(D) to anti-diagonal(AD). Just above the threshold, we observe a small S_3 component with different signs that vanishes for the bigger pump power (see Figure 4-14(a)). We attribute this to a small pump ellipticity induced by the optical elements in the excitation path, which could introduce the polarisation ellipticity for some linear polarisation azimuth angles.

4.6 Theory and Simulations

Along with the known spin properties inherent for polariton condensates (like optical orientation and polarisation pinning), we also discovered new regimes, for example, polarisation "island", depolarisation, etc. In order to explain these phenomena, the theoretical model based on the Gross-Pitaevskii (GPE) equations was developed by Dr Helgi Sigurdsson, who also performed the numerical simulations described below.

The model includes the set of driven-dissipative stochastic (Langevin-type) GPE

[147] coupled to spin-polarised rate equations describing excitonic reservoirs $X_{\pm} = X_{\pm}^A + X_{\pm}^I$. The mode contains the 0D spin Gross-Pitaevskii equations, which can be derived from Eq. (3.4) by projecting the order parameter on only the lowest trap state (ground state). Then, $\psi_{-\sigma}$ describes polaritons only in the ground state and neglects contribution from higher energy modes. In this regard, the spatial degree of freedom of the condensate is neglected in this simulation, which does not preclude the modelling of spin properties of the condensate.

$$i\dot{\psi}_{\sigma} = \theta_{\sigma}(t) + \frac{1}{2} \left[\alpha |\psi_{\sigma}|^2 + g(1 - \eta P_{\sigma})(X_{\pm}^A + X_{\pm}^I) + i(R(1 - \eta P_{\sigma})X_{\sigma}^A - \Gamma) \right] \psi_{\sigma} - \frac{\Omega_x}{2} \psi_{-\sigma}, \quad (4.2)$$

$$\dot{X}_{\sigma}^A = -(\Gamma_A + R(1 - \eta P_{\sigma})|\psi_{\sigma}|^2) X_{\sigma}^A + \Gamma_s(X_{-\sigma}^A - X_{\sigma}^A) + W X_{\sigma}^I, \quad (4.3)$$

$$\dot{X}_{\sigma}^I = -(\Gamma_I + W) X_{\sigma}^I + \Gamma_s(X_{-\sigma}^I - X_{\sigma}^I) + P_{\sigma}. \quad (4.4)$$

Here, ψ_{σ} is the σ spin component of the condensate wave function. $\sigma = \pm$ and denotes the spin-up and spin-down, respectively. The reservoirs are also spin-polarised and divided into active and inactive ones, $X_{\sigma}^{A,I}$ [34, 45, 148] respectively. R is the spin-conserving rate of stimulated scattering of polaritons into the condensate, Γ is the polariton condensate decay rate, Ω_x represents a birefringence induced effective magnetic field which splits the polariton XY polarisations, $\Gamma_{A,I}$ are the decay rates of active and inactive reservoir excitons, respectively, W is the conversion rate between inactive and active reservoir excitons, Γ_s is a spin-flip rate of excitons in each reservoir, and $P_{\pm} = P_0 \cos^2(\text{QWP} \pm \pi/4)$ is the power of the nonresonant continuous wave pump. The parameter η phenomenologically captures the sublinear dependence of the ground state energy shift and gain with increasing pump power.

The noise is introduced to the equations to reproduce the destabilisation of the condensate spin. The correlators of the background shot noise from the reservoir

$\theta_{\pm}(t)$ are written,

$$\langle d\theta_{\sigma}(t)d\theta_{\sigma'}(t') \rangle = \frac{\Gamma + RX_{\sigma}^A}{2} \delta_{\sigma\sigma'} \delta(t - t'), \quad (4.5)$$

$$\langle d\theta_{\sigma}(t)d\theta_{\sigma'}^*(t') \rangle = 0. \quad (4.6)$$

The threshold in the simulations is defined at pump power when the gain is equal to dissipation $RX_{\pm}^A - \Gamma = 0$. Some parameters are changing with the trap size, namely α, Γ, g, R . The polariton-polariton interaction scales as $\alpha \propto 1/d$ and $g, R \propto 1/d^3$ due to the change of the reservoir condensate overlap (see [1] for the details). The parameters used in the simulations are presented below:

$$T = 10 \text{ ns}, d_0 = 15 \text{ }\mu\text{m}, \alpha = \alpha_0 d_0/d, \alpha_0 = 1.8 \text{ ns}^{-1}, g = g_0(d_0/d)^3, g_0 = 0.36 \text{ ns}^{-1}, R = R_0(d_0/d)^3, R_0 = 3.9 \text{ ns}^{-1}, \Gamma = \Gamma_0(d_0/d)^3, \Gamma_0 = 0.6 \text{ ps}^{-1}, \Gamma_A = 0.78 \text{ ps}^{-1}, \Gamma_I = 0.0026 \text{ ps}^{-1}, \Gamma_s = 0.1 \text{ ps}^{-1}, W = 0.31 \text{ ps}^{-1}, \eta = 0.18/P_0, \Omega_x = 0.18 \text{ ps}^{-1}$$

Simulation results for DLP of the condensate in symmetric traps of different sizes are presented in Figures 4-12(e-g) and reproduce the experimental findings. Pump power in simulation is given in units of $P_0 = 2\Gamma\Gamma_A(\Gamma_I + W)/(RW)$, which is the threshold power for $P_+ = P_-$. For the linearly polarised excitation, simulations showcase the formation of the linear polarisation "island" similar to the experiment. Notably, the "island" disappears for the smaller traps. Evidently, this effect is governed by the interplay between pinning magnetic field Ω_x and polariton-polariton interactions. Indeed, as the trap diameter decreases, the scattering rate $R \propto 1/d^3$ increases proportionally, leading to saturation of the reservoirs X_{σ}^A for smaller particle number \bar{S}_0 . This is supported by the smaller condensate population for smaller trap size observed both in theory and experiment shown in Figure 4-11(a). Note that \bar{S}_0 (see Equation (2.18)) Stokes component is the total emission intensity, which is equal to the total number of polaritons in the condensate.

The simulation allows us to unravel the condensate time dynamics. Figure 4-15 depicts the simulated pseudospin dynamics for three different values of pump power and QWP angles. Figures 4-15(a-c) show the S_1 component corresponding to the star, circle, and diamond markers of Fig. 4-12(e,g), respectively. When the excitation ring diameter is large, the overlap with the reservoir is small, which results

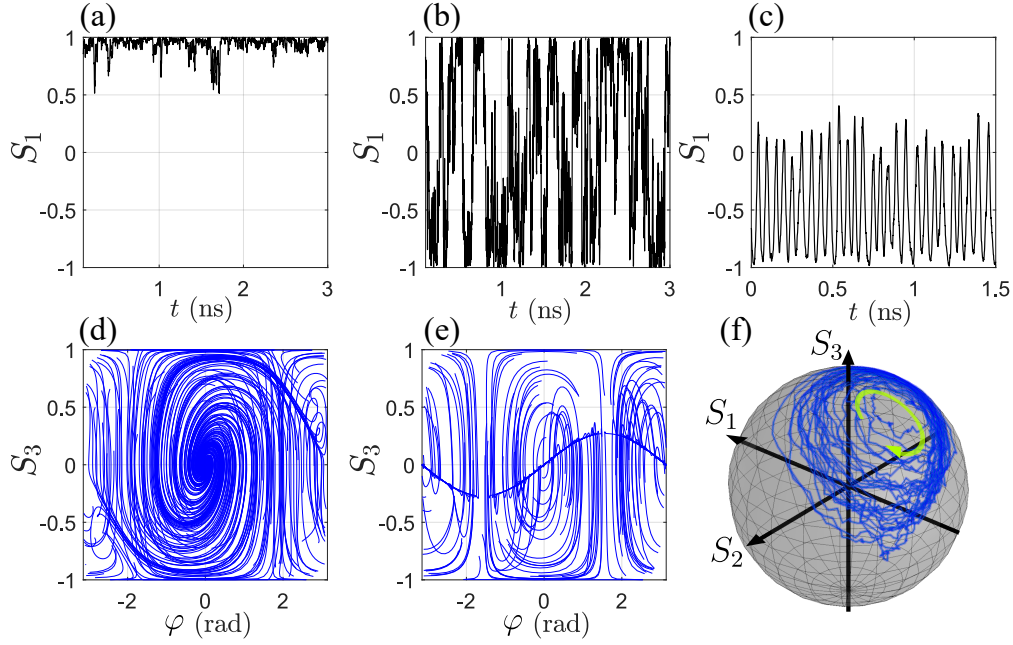


Figure 4-15: (a-c) Dynamics of the normalized S_1 component from the star, circle, and diamond markers in Fig. 4-12, respectively. (a) For large traps, the pseudospin is pinned along the effective magnetic field Ω_x . (b) For smaller pump diameters, the condensate blueshifts and the pseudospin starts destabilizing and fluctuates between $S_1 = \pm 1$. (c) For elliptical excitation, one gets $|\Omega_z| \gtrsim |\Omega_x|$, which can set the condensate into a tilted limit cycle appearing as persistent oscillations in the Stokes components. (d,e) The pseudospin phase space trajectories with $\theta_{\pm}(t) = 0$ but random initial conditions corresponding to the star and circle in Figure 4-12, respectively. φ corresponds to the azimuthal angle of the Poincaré sphere. (f) Representation of the limit cycle (precession) in (c) on the surface of the Poincaré sphere. The figure is adopted from [1].

in strong pinning of the S_1 component along the direction of the in-plane magnetic field (Fig. 4-15(a)). For smaller pump diameter [Fig. 4-15(b)], the overlap between the condensate and reservoir increases, causing the destabilization of the pseudospin, e.g. stochastic fluctuations between $S_1 = \pm 1$. This process of destabilization is plotted in Figure 4-15(d,e) as overlaid phase space trajectories for large and small pump diameters ($d = 15$, and $9 \mu\text{m}$, respectively). Here the $\theta_{\sigma}(t) = 0$, but use random initial conditions for the integration of Eqs. (4.2)-(4.4). For large pump diameters, there exists a dominant phase space attractor at $S_1 = 1$ ($\varphi = 0$, $S_3 = 0$), whereas for smaller diameters, this attractor decreases and a second attractor forms around $S_1 = -1$. Stochastic fluctuations in the dynamics of the pseudospin start shifting the polarisation randomly between $S_1 = \pm 1$, causing the polarisation "island" to vanish in the time-averaged measurements. For an elliptically polarised

pump, the pseudospin undergoes a self-induced Larmor precession (see Figure 4-15(c,f)) overcoming the pinning potential $|\Omega_z| \gtrsim |\Omega_x|$, setting the condensate into a tilted limit cycle which manifests in our measurements as an effective depolarisation.

The phenomenon of the self-induced Larmor precession is highly relevant to this thesis and will be referred to in other Chapters. To explain this phenomenon in more detail, in the next Section, the recent works reporting on the experimental observations of the self-induced Larmor precession in polariton condensates will be discussed.

4.7 Self-induced Larmor precession

Under elliptically polarised excitation, the two spin-polarised exciton reservoirs are imbalanced, leading to the non-zero and non-equal population of spin-up and spin-down polaritons in the condensate. The two populations experience different blueshifts due to interactions leading to the splitting of two cross-circularly polarised states. Alternatively, this splitting can be seen as if some effective magnetic field acts on the system and lifts the degeneracy of the spin-polarised states. The amplitude of the effective Ω_z out-of-plane magnetic field can be written as follows [8]:

$$\Omega_z = \alpha S_3 + g(X_+ - X_-) \quad (4.7)$$

where α and g denote the polariton-polariton and polariton-exciton interaction strengths, respectively, and X_{\pm} are the spin polarised exciton reservoir populations. This field drives the condensate spin into the precession, and the trajectories of such precession on the Poincare sphere are shown in Figure 4-16(a). The self-induced Larmor precession in polariton condensates has been predicted theoretically [33, 149, 150] and recently has been observed experimentally by virtue of the spin-noise measurements [151], and in condensate first [6] and second [8] order coherence functions.

When the condensate spin is set to rotation, both $g^1(\tau)$ and $g_{H-V}^2(\tau)$ correlation functions demonstrate the periodic oscillations (see Figures 4-16(b) and (c)) manifesting the alternation of condensate spin in time. Baryshev et al. [8] also showcased

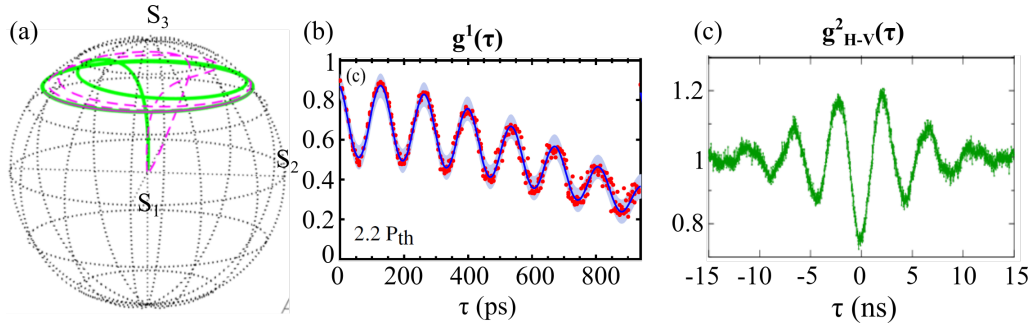


Figure 4-16: (a) The trajectories of the polariton condensate pseudo-spin (green and purple) when in the Larmor precession regime. (b) The Larmor precession is evidenced through the revivals of the first-order coherence function $g^1(\tau)$. Panels (a) and (b) are adapted from [6]. (c) The self-induced Larmor precession of the condensate measured as the oscillations of the second-order intensity cross-correlation function of the H and V polarisation projection of the condensate spin. The panel (c) is adapted from [8].

that the precession frequency is proportional to the pump polarisation ellipticity, and its frequency laying in the GHz range becomes bigger for more circularly polarised excitation. Moreover, the characteristic coherence time of this precession is $\approx 9\text{ns}$, which is three orders of magnitude bigger than polariton lifetime [55].

4.8 Conclusions

All in all, we have experimentally investigated the spinor of a polariton condensate in the annular optical trap depending on the excitation conditions. Alongside the known spin phenomena like polarisation pinning and optical orientation, we have identified new regimes of depolarisation and studied its dependence on the size of the confining potential.

It was confirmed that below the condensation threshold, the condensate is unpolarised. Whereas just above the threshold, condensate is characterised by the well-defined polarisation state only for the case of circularly polarised excitation. In this case, the sharp increase of S_3 polarisation component, governed by the optical orientation, and DOP reaching unity was observed.

For the linearly polarised excitation, the condensate spin is affected by the size of the optical trap. We have observed a transition from pinned linear polarisation (DOP ≈ 1) to depolarised (DOP ≈ 0) state depending on the size of the confining potential and pumping power. The effect is attributed to the interplay between a

location-dependent in-plane polarisation splitting and condensate-reservoir interactions. Shrinking the optical trap leads to the increased overlap and interactions of the condensate and excitonic reservoir. Interactions destabilise the spinor, which is evidenced by the depolarisation of the condensate PL in integrated measurements. Numerical simulations demonstrated that, in this case, interactions weaken the spin phase space attractor (pinning), resulting in stochastic spin fluctuations on the equatorial plane of the Poincare Sphere. These findings are corroborated by the recent experimental work of Baryshev et al. [8]. Moreover, the observed depolarisation of the emission with the excitation power for the elliptically polarised pump indirectly evidenced the spin limit cycles in the condensate. Similar spin effects were observed for the excitation with Gaussian spot. However, the increased polariton-exciton reservoir interactions destabilised the spin and lowered the integrated DOP of the condensate.

The obtained results shed light on the physics of polariton condensate spin, offering ways of controlling it by means of the excitation geometry, excitation laser power and polarisation. This will allow for the on-demand generation of the polariton spin state, which can be utilised for future spinoptronic devices and for generating spin polariton networks. Note that this study was implemented for the condensate in the ground state of the confining potential. The condensate in the excited trap states [28] or expanded condensates [152] could have more intriguing properties and form a subject for further research.

However, the control of the linear polarisation in the optically trapped condensate was so far out of reach. In the next Chapter, we will address this hurdle and propose a way of linear polarisation engineering in polariton condensates.

Chapter 5

All-Optical Linear-Polarisation Engineering in Single and Coupled Polariton Condensates

In the previous Chapter, it was shown that the linear polarisation of an inorganic polariton condensate is often defined by the birefringence of the sample and strongly depends on the location of the excitation spot on the sample. This Chapter is devoted to the development of an experimental approach which provides control over the degree of linear polarisation of the condensate by optical means. These results are published in Physical Review Applied [2].

All experimental results discussed in this Chapter were obtained by the Author if not stated otherwise. The experimental Figures have been produced by the Author, if not stated otherwise, and published in Ref. [2]. The utilisation of Figures in this Chapter is granted by the APS (the publisher) Copyright Policy. The numerical simulations were carried out by Dr. Helgi Sigurdsson. The Figures containing the simulation results were made by Dr. Helgi Sigurdsson and are also published in Ref. [2]. Their usage in the thesis is granted by the APS Copyright Policy. The source of the adopted Figures is stated in the related Figure caption.

5.1 Introduction

Polariton condensates are prominent candidates for future spinoptronic devices. In this regard, establishing all-optical control over polariton spin is a crucial task. This thesis considers condensates confined in a trap created by a non-resonant excitation laser. Above, we have shown that the circular and elliptical polarisation of the condensate PL can be controlled with the polarisation of the non-resonant laser due to the process of optical orientation [1, 36].

The physics is quite different for the non-resonant linearly polarised excitation. The transfer of linear polarisation from the non-resonant excitation to the condensate, or optical alignment, remains elusive for inorganic polaritons. In contrast, this process is dominant for the spin of organic polariton condensates [52]. The Frenkel excitons there have a dipole moment, and linear pump polarisation excites co-aligned dipoles, leading to the same linear polarisation of the condensate [14, 52, 153]. On the contrary, for inorganic polaritons, the linear polarisation of the pump laser leads to a spin-balanced condensate, given the equal relaxation rates of spin-up and spin-down polaritons. In the absence of any cavity strains or birefringence, the condensate builds up random linear polarisation from one realisation to another due to the spontaneous symmetry breaking upon condensation [137, 138].

Nevertheless, as we have shown in the previous Chapter, in most cases, there is some birefringence in the sample due to mechanical strains or the fabrication process, leading to a polarisation pinning effect [1, 69, 140, 141, 142] and a defined place-dependent linear polarisation of the PL. Often, the birefringence is dictated by the sample structure and quality. However, tailoring the birefringence is feasible for elliptically shaped optical micropillar cavities [34, 154, 155, 156]. Such structures can operate both in the weak [155] and strong coupling [34] regimes. The highly developed vertical-cavity surface-emitting lasers [157] (VCSEL) technology also offers numerous approaches to selecting modes with specific linear polarisation. Generally it is achieved by etching [154, 158], heating [159], or applying mechanical stress [160] to the heterostructure. In polaritonics, Klaas et al. [34] showcased that the asymmetric shape of the pillar cavity leads to the splitting of orthogonal linear

polarisation states, which in turn results in the linearly polarised condensate with polarisation parallel to the long axis of the ellipse. Even though those methods offer the possibility to obtain a deterministic linear polarisation state of the condensate, they do not offer in-situ control over the polarisation direction. In order to change the emitted polarisation with respect to the laboratory frame of reference, one has to go through a costly process of making a new sample with new polarisation properties or rotate the cavity, which is hardly convenient in microscale on-chip lasers or spinoptronic circuitry. Overall, all-optical control over the linear polarisation in inorganic polariton condensates was not achieved until the study presented in this Chapter.

Here, we propose a way of engineering the linear polarisation in inorganic polariton condensates in situ and by an all-optical means. By shaping the non-resonant excitation laser profile, we can control the orientation of the condensate spin on the equatorial plane of the Poincaré sphere. The effect is attributed to the interplay between TE-TM splitting [13, 113] of the cavity modes, and the orientation of the optical trap on the sample; the condensate always adopts a high degree of linear polarisation perpendicular to its major axis. We also investigate a dyad of such elliptical condensates and find several exotic polarisation regimes in the coupled system.

5.2 Experimental setting

For this experiment, we use the same experimental apparatus that was utilised in the previous Chapter. In brief, the condensate is excited non-resonantly with a chopped CW laser; the excitation beam is shaped with the SLM in an elliptical form described further. The exciton-cavity mode detuning is -3 meV. The condensate PL is studied in the reflection configuration and characterised in terms of the polarisation (with polarimeter), energy, real and k-space domains (see Chapter 3 for details). In this Chapter, the excitation polarisation is linear if not stated otherwise.

5.3 Elliptical optical trap and linear polarisation

The SLM shapes the transverse profile of the incoming light into the shape of an ellipse (see Figure 5-1(a,b)). Such an excitation profile has a non-uniform intensity distribution, with the maxima along one axis (y -axis on Figures 5-1(a,b)). It creates an elliptical confining potential for polaritons that results in the elliptical condensate (see Figures 5-1(c,d)) occupying the ground state of the optical trap. Polaritons are better confined in one direction, leading to increased tunnelling and leakage of polaritons along the perpendicular one, resulting in the elliptical distribution of the condensate in the reciprocal space, depicted in Figure 5-1(e).

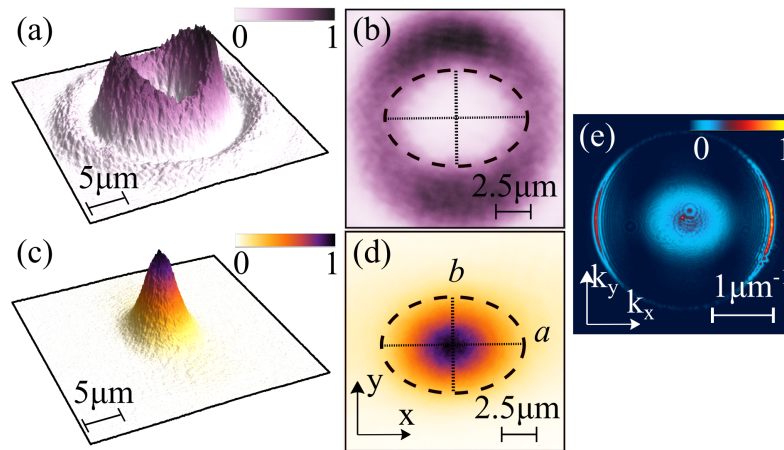


Figure 5-1: Spatial profiles of the (a,b) excitation laser and (c,d) condensate PL. The excitation laser induces a trapping potential with horizontal and vertical radii denoted a, b , respectively. (e) Momentum distribution of the condensate PL. Panels (c,d,e) correspond to a condensate pumped twice above its condensation threshold (i.e., $P = 2P_{th}$). Adopted from [2]

Firstly, we create an annular laser beam profile as we did in the previous Chapter to identify the region on the sample with the smallest structural birefringence. This allows us to separate the effects induced by the elliptical optical trap and the linear polarisation splitting inherent to our sample. Thus, by scanning the excitation position with the ring-shaped laser, we locate a spot on our sample with a small degree of polarisation DOP (see Figure 5-2(a)) of the PL. The small $S_{1,2}$ implies that the trap ground state is spin-degenerate such that from one realisation to another, random linear polarisation builds up, averaging over many shots.

Then, we transform the excitation profile to the elliptical one depicted in Fig-

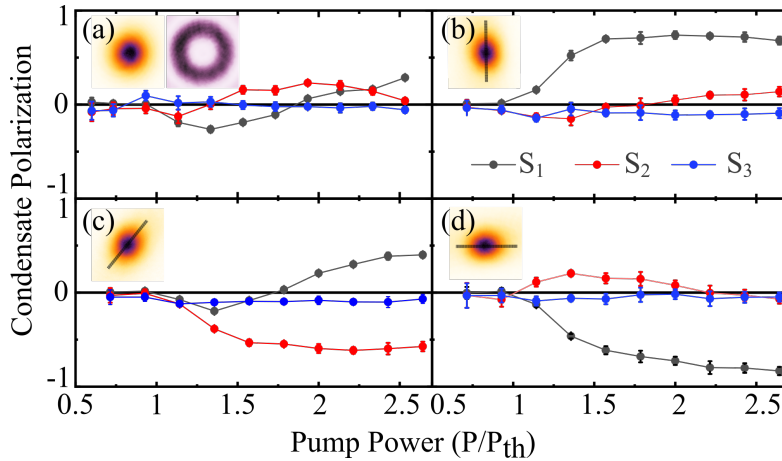


Figure 5-2: (a) Power dependence of the condensate $S_{1,2,3}$ Stokes parameters (black, red, blue markers) for the annular pump with resultant cylindrically symmetric condensate profile (see right and left insets, respectively). (b) Same, but now for a trap/condensate with a major axis orientated at 90° , (c) 45° , and (d) 0° . Insets in (a)-(d) depict the real-space condensate PL with black line showing the orientation of the trap major axis. Adopted from [2]

ures 5-1(a,b). Interestingly, for the elliptical condensate, we observe a massive increase of the condensate’s linear polarisation components above $1.2P_{th}$ for the same spot location. The direction of the linear polarisation is found to follow the trap’s minor axis. Namely, for the vertically elongated condensate in Figure 5-2(b), we observe an increase of the S_1 polarisation component (horizontal polarisation). Similarly, we observe the anti-diagonal and vertical polarisation emerging for the diagonally and horizontally elongated condensates in Figure 5-2(c,d), respectively.

5.4 Elliptical condensates excited by different polarisations

We utilise the horizontally polarised excitation for the elliptical condensates spin measurements presented in Figure 5-2. In order to check the effect of different pump polarisation on the condensate spin, as in the previous Chapter, we put the HWP or QWP into the excitation path to vary the polarisation of the non-resonant excitation laser. First, we alter the linear polarisation of the pump with HWP and record the polarisation maps showcasing the Stokes polarisation components as a function of

linear polarisation angle and pump power. The results for four elliptical traps oriented differently are presented in Figure 5-3. We show the measured condensate PL Stokes components $S_{1,2,3}$ for varying power and linear polarisation angle of the pump laser. The four columns in Figure 5-3 correspond to different spatial orientations of the elliptical pump profile. Figures. 5-3(a-c) correspond to 0° , (d-f) -45° , (g-i) 90° , and (j-l) 45° degrees of the condensate major axis orientation. We observe that, regardless of the linear polarisation angle, the condensate polarisation always dominantly follows the small axis of the trap (see Figure 5-3(a),(e),(g), and (k)). This is in correspondence with our previous study [1] and similar Figure 4-14 obtained for the symmetric condensate.

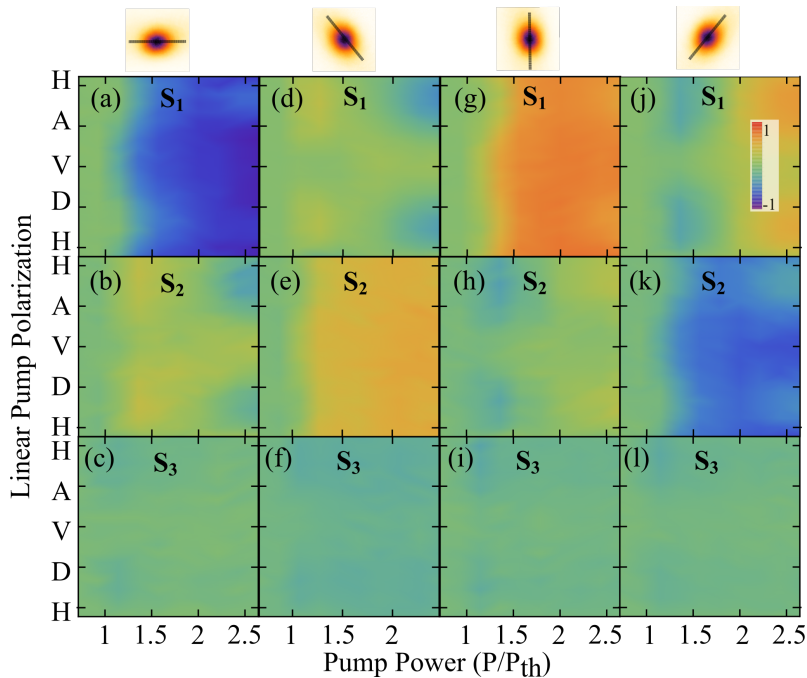


Figure 5-3: Condensate Stokes components for different pump powers and directions of linear polarisation of the excitation laser. The labels H, A, V, and D on the vertical axis denote horizontal, antidiagonal, vertical, and diagonal polarisation, respectively. The condensate PL is depicted on the top row with the black line denoting the trap major axis oriented at (a-c) 0° , (d-f) -45° , (g-i) 90° , and (j-l) 45° degrees with respect to the cavity plane x -axis (horizontal direction). Adopted from [2]

Then, we replace the HWP with the QWP and exert the polarisation ellipticity to the pump. The polarisation maps for different elliptical polarisations of the pump are depicted in Figure 5-4. Similarly to Figure 5-3, the Figure 5-4 depicts the results for four positions of the optical trap and ergo the elliptical condensate oriented at

(a-c) 0° , (d-f) -45° , (g-i) 90° , and (j-l) 45° degrees.

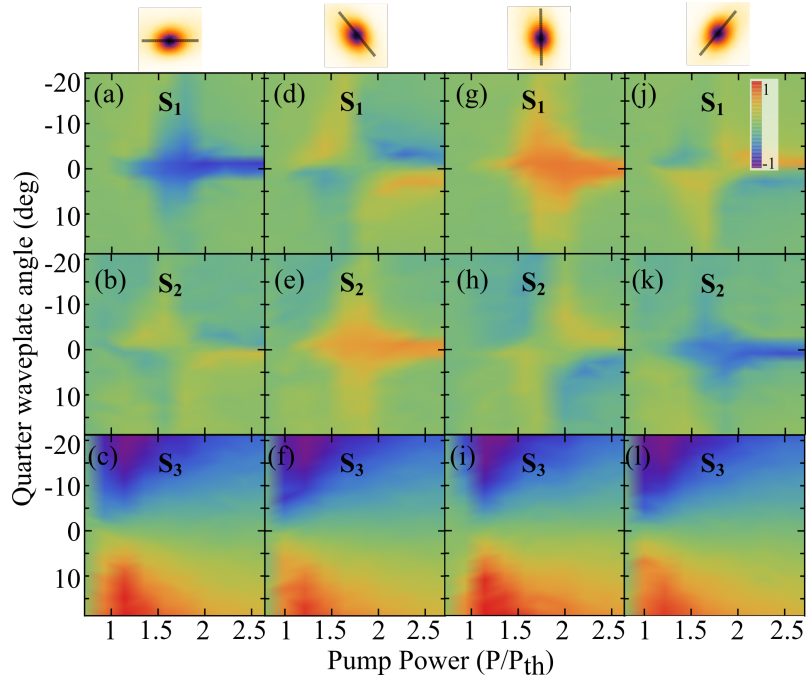


Figure 5-4: Condensate Stokes components for different pump powers and polarisation ellipticity in the units of QWP angle. The circular polarisation component of the pump can be written as $S_3^{\text{pump}} = \sin(2 \cdot \text{QWP})$. The negative and positive values of the QWP angle correspond to the left and right-handedness of the circular polarisation. The condensate PL is depicted on the top row with the black line denoting the major axis oriented at (a-c) 0 , (d-f) -45 , (g-i) 90 , and (j-l) 45 degrees with respect to the cavity plane x -axis (horizontal direction). Adopted from [2]

In contrast to the measurement discussed in the previous Chapter for the symmetric circular condensate, the polarisation of the "linear polarisation island" now is fully defined by the orientation of the optical trap (see Figure 5-2), rather than the inherent to sample position-dependent polarisation splitting. Namely, it follows the short axis of the optical trap. For slightly elliptically polarised excitation around $2P_{th}$, the other linear Stokes component arises in the condensate PL. Notably, their sign is varied for different handedness of the excitation laser. For instance, the S_1 alternation is observed in Figure 5-4(d) and corresponds to the slight rotation of the linear polarisation for the elliptically polarised condensate. The reasons for this rotation will be discussed further.

For the more circularly polarised excitation, the behaviour of the condensate is similar to that of the condensate in the annular trap. The condensate polarisation

for such excitation is defined by the optical orientation effect with the condensate spin adopting the spin of the excitation photons (see the previous Chapter 4).

5.5 All-optical linear polarisation Engineering

5.5.1 Elliptical excitation pattern

To summarize the dependence of the linear polarisation on the orientation of the excitation potential, we perform the incremental stirring of the optical trap with the spatial light modulator. We show that by rotating the excitation profile with the SLM, we can engineer any desired linear polarisation in the condensate. In Figure 5-5(a), we present the measured polarisation components (S_1 , S_2 , S_3) of the condensate PL as a function of the major axis angle, pumped at $P = 1.94P_{th}$. The S_1 and S_2 obey the sine functional dependence (S_1 is shifted by $\pi/2$ with respect to S_2), manifesting the continuous rotation of the condensate spin in the linear polarisation plane. Plotting the experimental points on the Poincare sphere in Figure 5-5(b), we find that all Stokes vectors of the condensate PL lay on the equatorial plane of the sphere and follow a circular trajectory. Note that Stokes vectors of the condensate do not reach 1, meaning the DOP of the condensate is less than unity. We attribute this to the depolarisation inherent to the condensate due to polariton-reservoir interactions described in the previous Chapter.

Figures 5-5(c,d) demonstrate the power dependence for the $S_{1,2}$ Stokes parameters for different alignments of the pump major axis. The linear polarisation rotation is present for the range of studied pump powers starting from $1.2P_{th}$. However, with the increasing pump power, we observe the slight turnabout of the pseudospin, which is evident from the downward trend on the polarisation maps (see Figures Figures 5-5(c,d)). This effect can be attributed to a small amount of residual circular polarisation in the optical pump, which can arise due to the birefringence of optical elements in the *excitation path*. We have already witnessed this effect in Figure 5-4 for the small values of the QWP angle. The polarisation ellipticity can be eliminated by fine-tuning the orientation of the wave plate in the excitation path or utilising the Soleil-Babinet compensator, making the polarisation of the PL perfectly linear

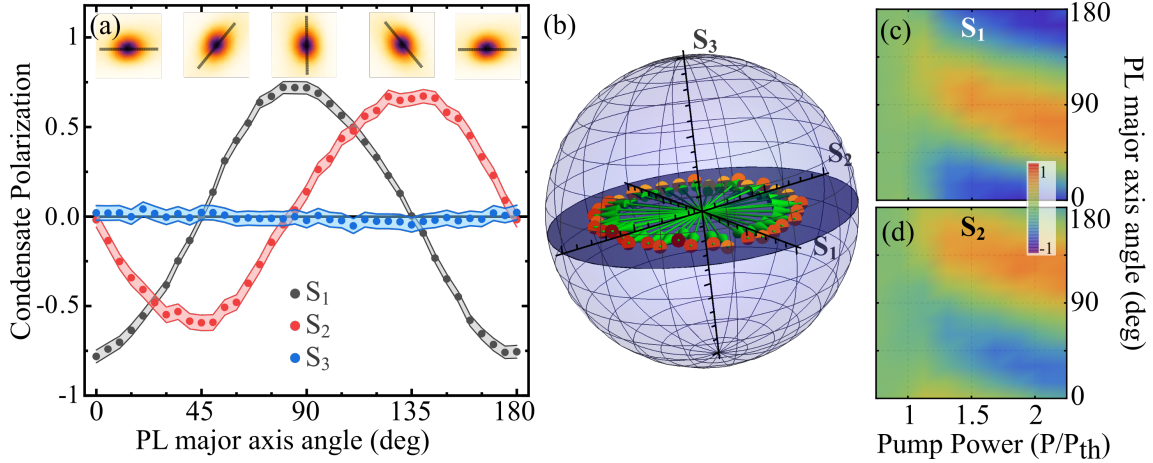


Figure 5-5: (a) Condensate polarisation components (S_1 black, S_2 red, S_3 blue) as a function of the optical trap orientation (PL major axis angle) at pump power $P = 1.94P_{th}$. The yellow-black coloured insets depict the real-space intensity of the condensate, and the black arrow represents the orientation of the PL major axis. (b) polarisation of the condensate for different trap positions plotted on the Poincaré sphere (red points). (c) S_1 and (d) S_2 for varying pump powers and major axis orientation. Adopted from [2]

for all excitation profiles.

5.5.2 8-point excitation pattern

In this section, we show that the shape of the excitation laser pattern is not crucial for the observed effect - the main requirement for the optical trap is to yield an elliptically shaped condensate. The alternative way for the creation of the repulsive potential for polaritons is the utilisation of closely spaced, tightly focused laser spots [85]. It is often used instead of the uniform ring laser patterns [27]. The point excitation creates the confining potential for polaritons, due to the exciton diffusion, with the condensate forming inside of the trap. This method is often more convenient if the fine-tuning of the effective potential shape for polaritons is required.

We create an excitation pattern composed of 8 Gaussian spots forming an elongated confinement potential (see Figure 5-6(b)). The condensate (see Figure 5-6(c)) occupies the elliptical ground state of the optical trap. Then, we rotate the excitation pattern with the SLM (as it was done for the elliptical trap) and detect the

polarisation components of the condensate emission at $P = 2P_{th}$. The rotation of the linear polarisation on a par with the laser pattern is observed, similar to the uniform excitation pattern (Figure 5-5(a)). The slight deviation from the sinusoidal fits in Figure 5-6(a) occurs due to small differences in power and shape of the differently oriented profiles.

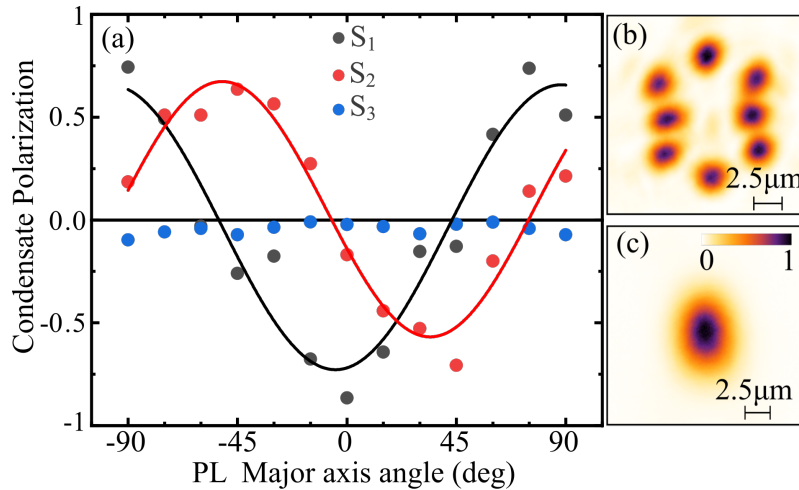


Figure 5-6: (a) Condensate polarisation for different spatial orientations of the 8-Gaussian excitation profile at $P = 2P_{th}$. Red and black curves are the sine fit for the experimental data. (b) Excitation laser intensity profile. (c) Condensate PL. Adopted from [2]

5.6 Compensation for experimental setup optical retardance

For the polarisation data presented in this Chapter, the Author applied a post-processing correction to *eliminate the optical retardance of the detection part* of the experimental setup. The optical retardance is the phase shifts of the orthogonally polarised waves propagating in the birefringent media which leads to the alternation of the polarisation state. The polarisation of the condensate PL changes while travelling from the sample to the polarimeter. This change is happening due to the many reflections from mirrors and due to the propagation of the PL through lenses and cryostat windows (that could be birefringent). In the experiment, this effect manifests itself, for example, when the condensate PL acquires a non-zero

S_3 component when it is diagonally polarised. The raw data for the polarisation measurements without the corrections is presented in Figure 5-7.

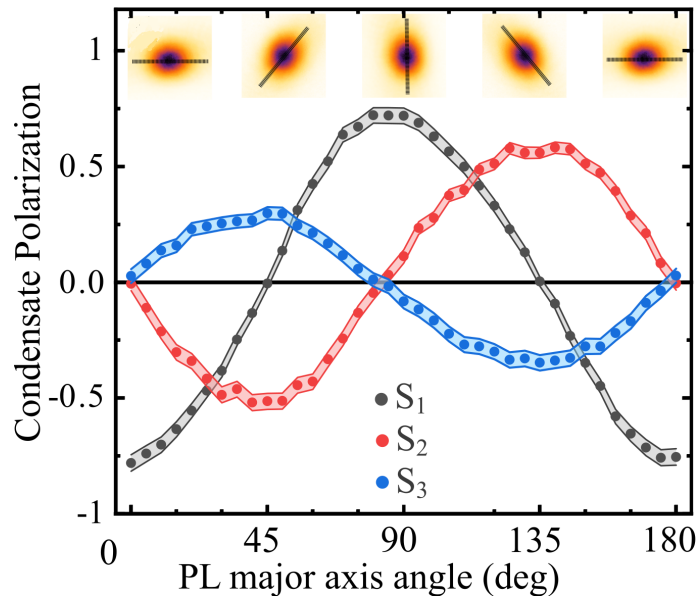


Figure 5-7: The experimental data for the elliptical trap rotation without the correction on the optical retardance of the experimental setup. The figure demonstrates the condensate Stokes components S_1 (black), S_2 (red) and S_3 (blue) as a function of the orientation of the elliptical condensate (x-axis and yellow-to-black insets). The image is adopted from [2].

In order to compensate for this effect, we characterise the retardance of the detection part of the setup using laser light with a known polarisation state. We detect how the laser light polarisation is changed by the optical elements in the detection part of the setup when it is travelling via the same path as the condensate PL. For this, we assume that the setup acts as the retarder plate aligned at some angle θ and having some optical retardance δ . The Mueller matrix for the arbitrarily rotated retarder plate M_{arb} in the laboratory frame reads as

$$M_{arb} = \begin{bmatrix} 1 & 0 & 0 & 0 \\ 0 & \cos^2(2\theta) + \sin^2(2\theta)\cos(\delta) & \cos(2\theta)\sin(2\theta)(1 - \cos(\delta)) & \sin(2\theta)\sin(\delta) \\ 0 & \cos(2\theta)\sin(2\theta)(1 - \cos(\delta)) & \cos^2(2\theta)\cos(\delta) + \sin^2(2\theta) & -\cos(2\theta)\sin(\delta) \\ 0 & \sin(2\theta)\sin(\delta) & \cos(2\theta)\sin(\delta) & \cos(\delta) \end{bmatrix} \quad (5.1)$$

To define the fast and slow axes of this retarder, we use a set of two linear po-

larisers. One of them is used for setting the linear polarisation state; the other is for characterisation of the polarisation after it travels through the detection part of the setup. Illuminating the sample with known linearly polarised laser light of different azimuthal angles (by rotating the first polariser), we define (by rotating the second polariser) the fast and slow axes of the detection part of the setup by identifying two orthogonal linear polarisations which travel through the setup unchanged. We find the angle of the slow axis to be angled at $\theta = \pi/2$ in the laboratory frame. The Mueller matrix M_{exp} for the detection part of the setup is written as

$$M_{exp} = M_{arb}(\theta = \pi/2) = \begin{bmatrix} 1 & 0 & 0 & 0 \\ 0 & 1 & 0 & 0 \\ 0 & 0 & \cos(\delta) & \sin(\delta) \\ 0 & 0 & -\sin(\delta) & \cos(\delta) \end{bmatrix} \quad (5.2)$$

For the Mueller matrix M_{exp} , we find that optical retardance δ can be easily retrieved if the retarder is illuminated with the diagonally polarised light $S_i = (1, 0, 1, 0)^T$. The Stokes vector S_f of the transmitted light is given by $S_f = M_{exp}S_i = (1, 0, \cos(\delta), -\sin(\delta))^T$. Interestingly, the S_2 component of the transmitted light equals $\cos(\delta)$. Measuring the S_2 we find $\delta = 0.155\pi$. Finally, substituting these parameters to Eq. (5.1) yields:

$$M_{exp} = \begin{bmatrix} 1 & 0 & 0 & 0 \\ 0 & 1 & 0 & 0 \\ 0 & 0 & 0.8838 & 0.4679 \\ 0 & 0 & -0.4679 & 0.8838 \end{bmatrix} \quad (5.3)$$

The transformation matrix M_{exp} (Equation (5.3)) is then applied to the experimental Stokes vectors of the condensate PL for the correction of the detrimental polarisation effect of the optical setup. As a result, the raw data in Figure 5-7 transforms to the data presented in Figure 5-5(a). Note that this Mueller transformation only performs the rotation of the Stokes vector on the Poincare sphere while preserving the DOP.

5.7 Theory of a single condensate in an elliptical trap

The appearance of the linear polarisation in elliptically shaped condensates is attributed to the splitting of orthogonal linear polarisations in the experimental sample, which arises due to TE-TM splitting and the elliptical shape of the condensate. TE-TM splitting refers to the splitting of electromagnetic waves into two different polarisation modes, transverse electric (TE) and transverse magnetic (TM), when they propagate through a cavity. This splitting is (angle) k -dependent [13] (see Figure 5-8(a)). So, every spatial orientation of the condensate has a unique distribution of the corresponding in-plane momenta, resulting in a splitting between different linear polarisations (aligned with the major and minor axes of the ellipse). We experimentally measure the splitting between orthogonal linear polarisations to be $20\mu\text{eV}$ (see Figure 5-8(b), Figure 5-8(c) shows the intensity power dependence of two polarisations). Interestingly, the condensate's emission is coming from the polarisation mode, which has a bigger energy.

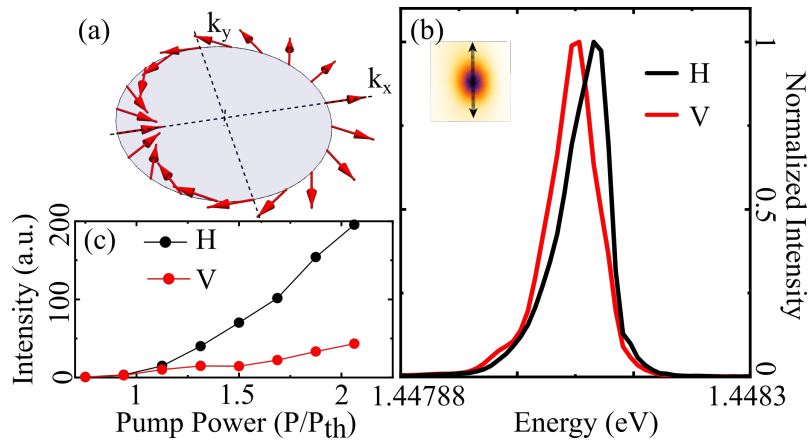


Figure 5-8: (a) Distribution of the in-plane effective magnetic field $\Omega(\mathbf{k})$ (red arrows) in momentum space due to TE-TM splitting given by Eq. (5.5). (b) Horizontal (black) and vertical (red) polarisation resolved the normalized energy spectrum of the condensate emission at $k = 0$ for a vertically elongated trap. Splitting between energy levels is $\approx 20 \mu\text{eV}$. (c) Pump power dependence of the population of H and V polarisation mode for the vertically elongated condensate. The figures are adopted from [2]

Linear model

Dr Helgi Sigurdsson has developed a theoretical model to describe the observed effect more rigorously. At first, he considered the simplest case of non-interacting polaritons where the following Hamiltonian can describe condensate:

$$\hat{H} = \frac{\hbar^2 k^2}{2m} - \hat{\boldsymbol{\sigma}} \cdot \boldsymbol{\Omega} + V(\mathbf{r}) - \frac{i\hbar\Gamma}{2}, \quad (5.4)$$

where m is the effective mass, $\mathbf{k} = (k_x, k_y)$ is the in-plane momentum, Γ^{-1} is the polariton lifetime, $V(\mathbf{r})$ is an asymmetric (elliptical) confining potential and

$$\boldsymbol{\Omega} = \hbar^2 \Delta \begin{pmatrix} k_x^2 - k_y^2 \\ 2k_x k_y \\ 0 \end{pmatrix} \quad (5.5)$$

is the effective magnetic field arising due to TE-TM splitting of strength Δ [73, 108, 161], its distribution in the momentum space is depicted in Figure 5-8(a). Assuming that the laser-induced potential can be approximated by a harmonic oscillator potential $V(\mathbf{r}) = m\omega_x^2 x^2/2 + m\omega_y^2 y^2/2$ that allowed to solve the problem based on the two-dimensional harmonic oscillator modes $|n_x, n_y\rangle = |n_x\rangle \otimes |n_y\rangle$ where $n_{x,y}$ are the potentials quantum numbers. The lowest trap state $|n_x, n_y\rangle = |0, 0\rangle$ can be approximated by the following 2×2 spinor Hamiltonian,

$$\hat{H} \approx \frac{\hbar}{2} \begin{pmatrix} \omega_x + \omega_y - i\Gamma & -m\Delta(\omega_x - \omega_y) \\ -m\Delta(\omega_x - \omega_y) & \omega_x + \omega_y - i\Gamma \end{pmatrix}. \quad (5.6)$$

Solving the eigenvalue problem (see Ref. [2] for the detailed derivation), the energies of two orthogonal linearly polarised modes read as:

$$E_{0,0}^{H,V} = \frac{\hbar}{2} [\omega_x + \omega_y \mp m\Delta(\omega_x - \omega_y)] - \frac{i\hbar\Gamma}{2} \quad (5.7)$$

The splitting of two energies becomes evident from Equation (5.7), and its value corresponds to the one observed experimentally and presented in Figure 5-8(b).

This splitting can be interpreted as an effective in-plane magnetic field acting on

the condensate spin. In general, depending on the condensate orientation, it can be written as follows [2]:

$$\mathbf{\Omega}_{\text{trap}} \simeq -\frac{\hbar m |\Delta| \delta\omega}{2} \begin{pmatrix} \cos(2\theta_{\text{min}}) \\ \sin(2\theta_{\text{min}}) \\ 0 \end{pmatrix}. \quad (5.8)$$

Here, θ_{min} is the angle of the traps' minor axis from the horizontal, and $\delta\omega = |\omega_x - \omega_y|$ is the absolute difference between the trap oscillator frequencies along the major and the minor axes of the condensate. Thus, the direction of the effective magnetic field is controlled by the angle of the elliptical trap, θ_{min} , which consequently rotates the condensate pseudospin in the equatorial plane of the Poincaré sphere. This leads to smooth changes in the $S_{1,2}$ Stokes components of the emitted light as the trap rotates, as shown in Figure 5-5.

The results of the experiments are also reproduced through a mean-field simulation using a generalized Gross-Pitaevskii equation coupled to an excitonic reservoir [2]. These simulations were also made by Dr Helgi Sigurdsson.

5.8 Effect of spatial ellipticity

By changing the trap shape with the SLM, we can engineer the spatial ellipticity of the condensate, i.e. the ratio of its major and minor axes - going from a cylindrically symmetric to an elliptical one. In this experiment, we change the trap *spatial* ellipticity from a vertically elongated trap ($a < b$) to a horizontally elongated one ($a > b$), a and b here denote the major and minor axes, respectively. We observe that the pseudospin of the condensate steadily changes from horizontal to vertical polarisation through a low DOP regime (see Figure 5-9). This measurement has been performed for a spot on the sample where some finite birefringence was present. That is why the low DOP regime is shifted with respect to the symmetric condensate (when ellipticity equals one). Thus, the sample's inherent effective magnetic field due to local birefringence adds up to the effective magnetic field induced by the elliptical trap. They compensate each other at ellipticity 0.9, resulting in a

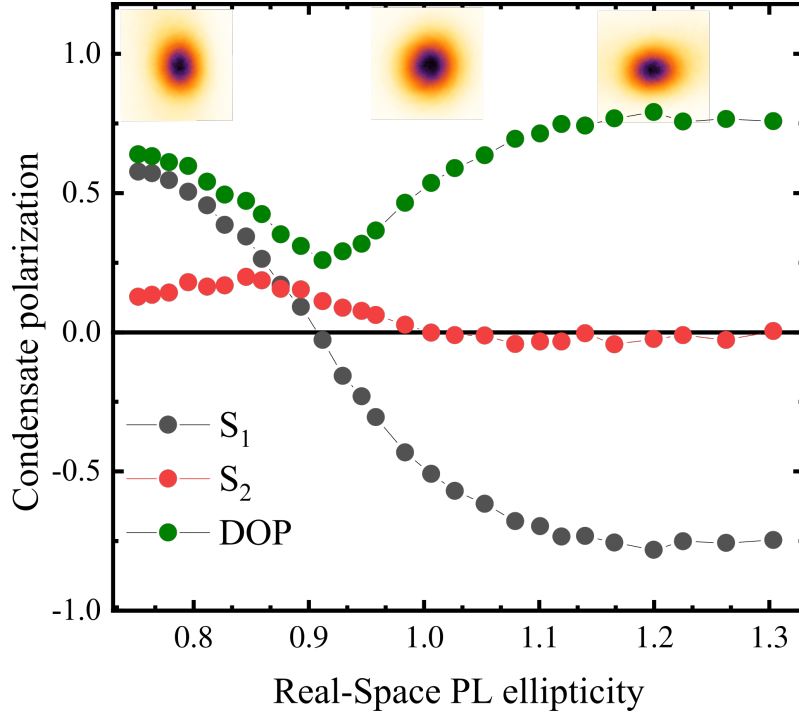


Figure 5-9: S_1 , S_2 and DOP of the condensate PL as a function of the spatial ellipticity (the ratio between the major and minor axes of the condensate real-space intensity distribution).

low integrated DOP. So the net in-plane magnetic field acting to the condensate in this case can be written as follows: $\mathbf{\Omega}_{\text{net}} = \mathbf{\Omega}_{\text{bir}}(\mathbf{r}) + \mathbf{\Omega}_{\text{trap}}$. Thus, by engineering the trap profile, it is possible to compensate for the polarisation pinning effect, which can be detrimental for some experiments (the ones where it is essential to have the spontaneous breaking of spin symmetry).

To sum up, we have achieved control over the linear polarisation of the condensate using a non-resonant elliptical optical trap. We find that the orientation of the confining potential, pump power and spatial ellipticity define the linear polarisation of the condensate.

5.9 Coupled elliptical condensates

The arrays of coupled polariton condensates are very promising for the analogue simulation [26] and modelling of physical systems. Lattices of different geometry have been realised for ballistically propagating condensates [21, 23, 162] and the

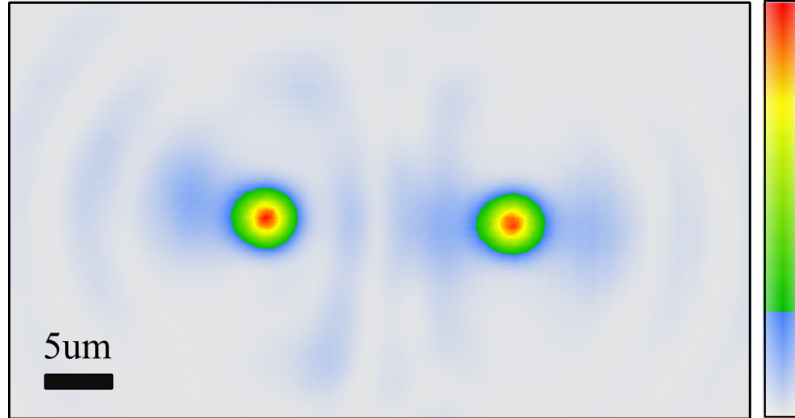


Figure 5-10: Real-space normalised intensity distribution of two coupled elliptical, horizontally elongated condensates. The colour scale corresponds to the normalised intensity (spans from 0 to 1).

ones confined in the etched mesas structures [163, 164] or in the optical traps [31]. Driven by these works, we bring together two condensates in elliptical optical traps (the building block of the future lattice) and study their coupling and polarisation properties.

The two condensates depicted in Figure 5-10 are created with two spatial light modulators. The utilisation of two SLMs allows us to make the traps identical and control the pump power, energy and spatial orientation for both of them separately. We bring two condensates together on the sample and choose individually the pump power for each so that they have the same energy when separated. By changing the tilt on one of the SLMs (the periodic grating imprinted on top of the elliptical trap hologram), it is possible to control the separation distance between the condensates.

To narrow down the study, we investigate only horizontally and vertically elongated condensates even though the SLMs offer the possibility to realise a whole variety of mutual condensate orientations. There are four possible orientations for the studied case - both traps horizontal, both traps vertical, and two variations of the traps being not coaligned. We start with the two former cases. The real-space intensity distribution for two coupled horizontally elongated condensates is presented in Figure 5-10. The interference fringes between the condensates stand for the synchronisation (coupling) between them.

The dependence of the condensate spin on the condensate spatial orientation

described above could potentially allow for the adjustment of couplings between two condensates depending on their mutual orientation. Namely, the spin fine structure of each optical trap can be adjusted through its major axis angle. Moreover, the interaction strength between different condensates changes for different separation distances.

The laser pattern used in the experiments (see Figure 5-1(b)) has a non-uniform intensity that allows polaritons to escape more efficiently along its major axis (see Figure 5-1(b)). This can be evidenced in Figure 5-1(e) as a bigger population of polariton along k_x in k-space. This leads to the stronger coupling between two condensates when their major axes are orientated parallel to the coupling direction and weaker transverse (estimated three times weaker from energy-resolved spatial PL). The difference in the coupling strength is seen by the different visibility in the momentum space of interference fringes (implying synchronisation) shown in the insets of Figs. 5-11(a), (c).

In order to study the spin of coupled condensates, we split the horizontal (H) and vertical (V) polarisation components of the PL with the Wollaston prism. So that we can separately measure them in the real space and calculate a spatial distribution of the $S_1(\mathbf{r})$ component as follows

$$S_1(\mathbf{r}) = \frac{I_H(\mathbf{r}) - I_V(\mathbf{r})}{I_H(\mathbf{r}) + I_V(\mathbf{r})} \quad (5.9)$$

where $I_H(\mathbf{r})$, $I_V(\mathbf{r})$ are the real-space intensities distributions of horizontal and vertical polarisation components, respectively.

While doing the experiments with coupled traps, we noticed that the polarisation of the condensate is not stable from one realisation to another of the condensate. In order to study this peculiar behaviour, we investigate the condensate S_1 component in the single shot regime. The excitation shots have 50 μs duration. The condensate emission is integrated during one shot and S_1 Stokes component is calculated. The examples of obtained real-space S_1 distribution are depicted in Figures 5-11(a-c). We study 100 single realisations of the condensates for each separation distance. The S_1 component is integrated over the region of the most intense emission (number of polaritons) depicted in Figure 5-11(a-c) with the dashed line. As a result, each shot

is characterised by two values of integrated S_1 corresponding to the left and right condensate, respectively. Finally, we merge these values into one graph presented in Figures 5-11(d-g), where the blue and red lines represent the averaged S_1 component for the left and right condensate, respectively.

The recent studies for ballistic [29] and trapped [30] coupled polariton condensates showcased that the coupling in such systems is distance-dependent. In this regard, we investigate the coupling of two elliptical condensates for different separation distances. The values of the separation distance (26.5 μm and 27.5 μm) are chosen to more vividly demonstrate the distinctive polarisation regimes. Interestingly, for strongly coupled horizontally elongated traps separated by 26.5 μm , we observe approximately zero S_1 and DOP (Figure 5-11(d)) for both condensates (blue and red curves, respectively). On the contrary, at a 27.5 μm distance, the S_1 component is significant and stochastically flipping from shot to shot (Figure 5-11(e)) between positive and negative values. So, both condensates simultaneously adopt either vertical or horizontal polarisation. The corresponding real-space S_1 distributions are depicted in Figures 5-11(a) and (b). Moreover, the polarisation of two condensates is almost perfectly correlated (Pearson correlation coefficient $\rho = 0.99$), meaning that they have the same spin and are strongly coupled. On the other hand, the observed random linear polarisation flips suggest the presence of bistability in the system [106] triggered by the spatial coupling mechanism.

For the weakly coupled (vertically elongated) traps (see Figure 5-11(c)), the qualitatively different behaviour is observed. Choosing the same distances, we observe at 26.5 μm strong positive S_1 component in each condensate (Figure 5-11(f)) as it is for a single optical trap (see Figure 5-12(b)). However, at 27.5 μm , we reveal the semi-depolarised behaviour of the system (Figure 5-11(g)). Due to the weaker spatial coupling, the condensates are no longer strongly correlated in their S_1 components with $\rho = 0.5$ and 0.26 for the two studied distances, respectively. Note that the different average S_1 values between the left and the right condensate in Figure 5-11(g) can be attributed to the location-dependent sample birefringence.

The polarisation flipping or zero DOP regimes arise as a consequence of condensates coupling. It is confirmed by the measurement of S_1 component for 100

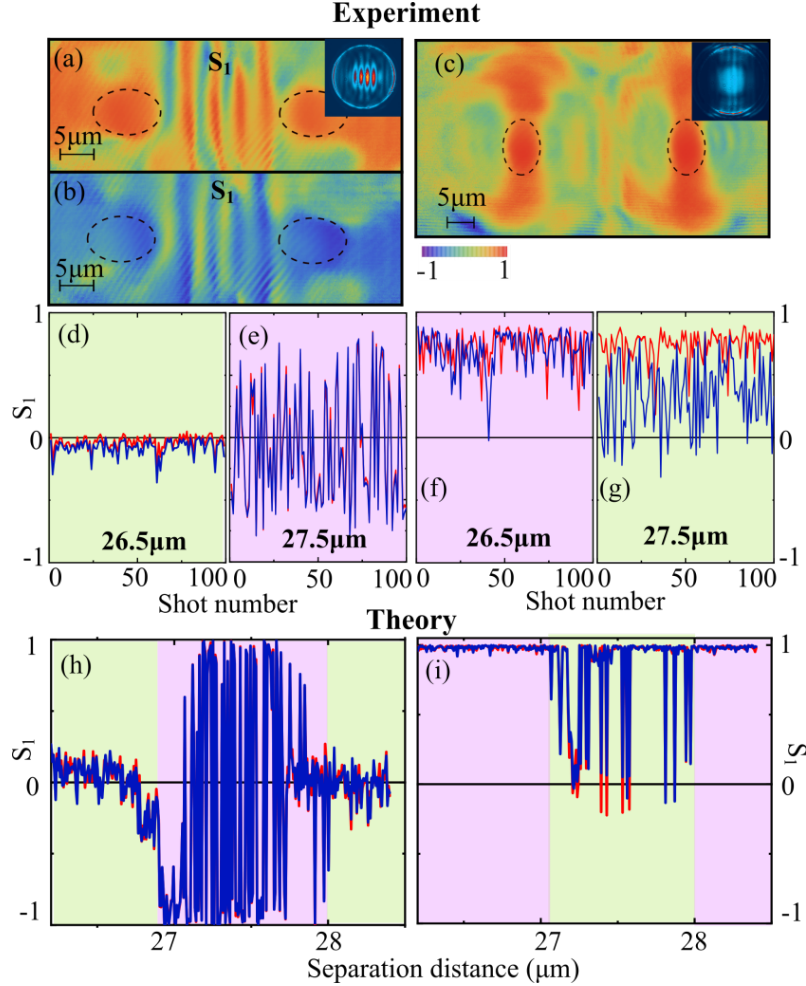


Figure 5-11: Spatially resolved S_1 of coupled condensates oriented horizontally and separated by $27.5 \mu\text{m}$ for two different shots (a,b), showing the formation of either horizontal (a) or vertical polarisation (b) in both condensates. (c) Spatially resolved S_1 of the two coupled condensates orientated vertically at $26.5 \mu\text{m}$. Insets in (a) and (c) depict the corresponding k -space PL. (d,e) 100 time-integrated realisations (shots) of the S_1 for the left (blue) and right (red) condensate in the horizontal-horizontal major axis configuration and (f,g) in the vertical-vertical configuration. The experimental data is taken at $\approx 1.8 P_{th}$. Distance dependence of the S_1 from simulations corresponding to (h) horizontal-horizontal and (i) vertical-vertical major axes configuration. Each data point represents one shot (time-averaged). Green and purple backgrounds in (d)-(i) illustrate regions of similar behaviour between experiment and theory. Adopted from [2].

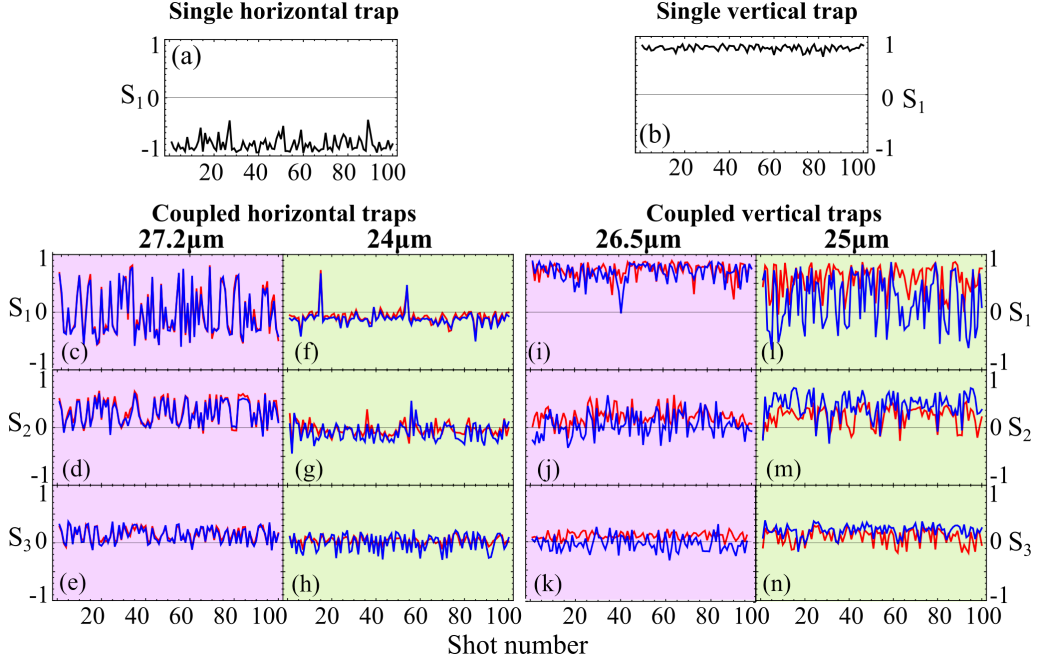


Figure 5-12: 100 realisations of the condensates Stokes components time-integrated in each $50 \mu\text{s}$ excitation shot. (a) and (b) shows S_1 of single horizontally and vertically elongated condensate, respectively. S_1 , S_2 , and S_3 for two coupled condensates with their trap's major axes orientated longitudinally to the coupling direction and separated by $27.2 \mu\text{m}$ (c)-(e) and $24 \mu\text{m}$ (f)-(h), respectively. S_1 , S_2 , and S_3 for two coupled condensates with their trap's major axes orientated vertically and separated by $26.5 \mu\text{m}$ (i)-(k) and $25 \mu\text{m}$ (l)-(n), respectively. Blue and red colours correspond to the right and left condensate, respectively. Green and purple backgrounds depict different coupling regimes.

single realisations of the single condensates (see Figures 5-12(a) and (b)). Note that fluctuation of the S_1 component for the individual condensate is significantly suppressed compared to the coupled condensate. The spin fluctuations in Figure 5-12(a) appear due to noise as well as different polarisation mode competition. It is worth noting that such fluctuations decrease the values of the Stokes components presented in Figures 5-2, 5-5, 5-4, 5-3 since it is averaged over hundreds of condensate realisations.

To get a full picture of the coupled condensates spin, we characterise all polarisation components of the Stokes vector. The results are depicted in Figures 5-12(c-n). Note that the S_1 , S_2 and S_3 are not measured simultaneously but consequently under the same excitation conditions. For the regime of stochastic linear polarisation flipping for two horizontal condensates separated by $27.2 \mu\text{m}$, we observe S_1 hav-

ing the biggest amplitude out of 3 Stokes components (see Figure 5-12(c-e)). This is defined by the orientation of the traps inducing the splitting between H and V. The S_2 has smaller values (less than 0.5) but also flips from shot to shot. On the other hand, the S_3 component stays close to zero, implying that the condensates are linearly polarised. For another separation distance $24 \mu\text{m}$ shown in Figures 5-12(f-h), all Stokes components are close to zero in each condensate realisation. This means that the condensate pseudospin fluctuates rapidly in time within one excitation pulse with a zero mean polarisation, just like it was for a single symmetric trapped condensate described in the previous chapter and Ref. [1]. Note that the Stokes components remain correlated, indicating that the condensates are coupled.

We also plot all polarisation components for two coupled vertically elongated condensates (Figures 5-12(i)-(n)). The weaker coupling of such trap configurations is evidenced through weaker correlations between the left and right condensates. For a distance of $26.5 \mu\text{m}$, both condensates have strong horizontal polarisation. At $25 \mu\text{m}$, the condensates are in a semi-depolarised regime with oscillating S_1 and S_2 from shot to shot.

To sum up, we identified two coupling regimes for two horizontal condensates - stochastic synchronous spin flips from horizontal to vertical polarisation states and zero DOP regimes depending on the separation distance. Similarly, for two vertically oriented condensates, there are also two distinctive regimes - both condensates are horizontally polarised, or both have low DOP. In order to get an insight into the dynamics of the coupled system, we again refer to the simulation kindly made by Dr Helgi Sigurdsson.

5.10 Theory of Coupled condensates

The experimental observations are reproduced through mean-field simulations on time-delay coupled spinor polariton condensates. The 1D GPE equation describes the condensates spinor $\Psi = (\psi_+, \psi_-)^T$ components; the equations are coupled to the rate equations describing the spin-polarised exciton reservoir [133]. The indexes (1) and (2) denote the left and right condensate, respectively.

$$\begin{aligned}
i \frac{d\psi_{\pm}^{(1,2)}}{dt} &= \left[\omega_0 + \alpha |\psi_{\pm}^{(1,2)}|^2 + g X_{\pm}^{(1,2)} + i \frac{R X_{\pm}^{(1,2)} - \Gamma}{2} \right] \psi_{\pm}^{(1,2)} + (\epsilon + i\gamma) \psi_{\mp}^{(1,2)} + \\
&+ J \psi_{\pm}^{(2,1)}(t - \tau) + \mathcal{J} \psi_{\mp}^{(2,1)}(t - \tau), \\
\frac{dX_{\pm}^{(1,2)}}{dt} &= P - \left(\Gamma_R + R |\psi_{\pm}^{(1,2)}|^2 \right) X_{\pm}^{(1,2)} + \Gamma_s (X_{\mp}^{(1,2)} - X_{\pm}^{(1,2)}).
\end{aligned} \tag{5.10}$$

where ω_0 is the condensate intrinsic energy, and most of the other terms had been defined in the previous Chapters. Moreover, coupling between two condensates is also taken into account in this set of equations. The inter-condensate coupling, denoted with $J, \mathcal{J} \in \mathbb{C}$, which is described through time-delay coupled equations of motion [29]. The time delay of the coupling appears due to the finite time of the propagation of polaritons from one trap to the other. Such coupling becomes qualitatively different from evanescent coupling when the propagation time τ of particles between condensates is comparable to their intrinsic frequencies. As it was previously demonstrated in [29], the strength of the coupling J depends on the separation distance d between the condensates,

$$J(d) = J_0 |H_0^{(1)}(k_c d)|, \tag{5.11}$$

where $H_0^{(1)}$ is the zeroth order Hankel function of the first kind, $J_0 \in \mathbb{C}$ quantifies the coupling strength dictated by the overlap of the condensates, and k_c is the wavevector of the polaritons propagating outside the optical trap,

$$k_c = k_c^{(0)} + i \frac{\Gamma m}{2\hbar k_c^{(0)}}. \tag{5.12}$$

From experiment, $k_c^{(0)} \approx 1.35 \mu\text{m}^{-1}$. This value corresponds to the radius of the outer momentum space PL ring shown in Figure 5-1(e). The imaginary term in Eq. (5.12) describes the additional attenuation of polaritons due to their finite lifetime, and m is the polariton effective mass. The coupling between the spins of the two condensates due to the TE-TM splitting is captured with the parameter \mathcal{J} .

The time delay parameter is approximated from the polariton phase velocity, which gives,

$$\tau = \frac{2dm}{\hbar k_c^{(0)}}. \quad (5.13)$$

The results from simulations for both strongly and weakly coupled traps are presented in Figures 5-11(h) and 5-11(i), respectively. Depending on the distance d between the condensates (each data point is one shot using random initial conditions), the periodic appearance of different polarisation dynamics (green and purple backgrounds) is evident. That is similar to the experimental results and the phase-flip transitions recently reported in [29].

For the strongly coupled traps, Figure 5-11(h) indeed shows that—depending on distance—one can retrieve very low time-averaged polarisation. There, the interplay of spin-coupling and ballistic coupling results in chaotic spin dynamics in time. Between 27 μm and 28 μm , a high amplitude random S_1 component builds up from shot to shot due to the condensate spinors suddenly synchronizing. These results are in qualitative agreement with those seen in an experiment in Figs. 5-11(d) and 5-11(e). For the weakly coupled traps, there is a qualitative agreement between theory (Figure 5-11(i)) and experiment (Figures. 5-11(f) and 5-11(g)). This weak coupling there is implemented into the simulation by scaling $J_0 \rightarrow J_0/3$. Now, depending on the separation distance, the strong $S_1 \approx 1$ regimes alter with the regime of semi-depolarised averaged spins (see Figure 5-11(i)). The parameters of the simulation are given in Ref. [2]. Overall, the simulation showcased that the spins of two coupled elliptical condensates are separation distance-dependent. They periodically alter because of the time-delayed coupling. Moreover, simulations showcased that the polarisation regimes depend on the excitation power so that both condensates for larger excitation power can stabilise in the vertical or horizontal polarisation [2]. Therefore, in further investigations, it will be crucial to take into account both power and separation distance dependence.

5.11 Conclusion

To summarise, we have investigated single and coupled optically confined elliptical polariton condensates created by non-resonant excitation. We find that for the linear polarisation of the excitation laser, the condensate polarisation is defined by its shape; namely, the spinor is oriented along the short axis of the condensate ellipse. We demonstrate that by rotating the pump profile with the SLM, we can drive the condensate through all linear polarisation states on the equator of the Poincare sphere. We also found that the pump power and spatial ellipticity of the condensate impact its linear polarisation. Furthermore, we have investigated the dyad of coupled elliptical condensates and identified the dependence of their spin behaviour on the separation distance. We also reveal the regimes of "strong" and "weak" condensate mutual coupling for horizontally and vertically elongated condensates.

Our results could provide one of the missing pieces of the puzzle for creating all-optical spin circuits for spinoptronics applications. Moreover, it paves the way towards coherent light sources with on-demand switchable linear polarisation. In our experiment, the response of the SLM limits the polarisation rotation speed to a few Hertz for a full revolution. However, in the next Chapter, we describe an approach that allows us to reach GHz linear polarisation rotation speed, which is hardly feasible with conventional polarising devices.

Additionally, our results on coupled condensates open up the possibility of studying synchronisation phenomena or chaotic spin dynamics in networks of polariton condensates. This offers new degrees of freedom for condensate lattices - spatially anisotropic coupling strength and polarisation engineering, which could enrich the physics of such systems.

The developed all-optical linear polarisation engineering technique was recently patented in the Russian Federation.

Chapter 6

Driven Spin Precession in Polariton Condensate

The preprint of the study discussed in this Chapter is published in arXiv [4]. The experimental results discussed in this Chapter were obtained by the Author if not stated otherwise. The experimental results on the intensity correlation of the condensate emission were obtained by the Author and Dr Stepan Baryshev together. All experimental Figures have been produced by the Author if not stated otherwise. The utilisation of Figures in this Chapter is granted by the CC BY 4.0. The numerical simulations were carried out by Dr. Helgi Sigurdsson. The Figures containing the simulation results were made by Dr. Helgi Sigurdsson and are also published in the preprint [4]. Their usage in the thesis is granted by CC BY 4.0.

6.1 Introduction

After successfully demonstrating control over the condensate spinor in the previous chapter, the next logical step would be to achieve that control at higher GHz speeds. Previously, the response time of the SLM had hindered the maximum achievable rotation frequency of the condensate spin to just a few Hz. However, the use of an alternative technique for optical pattern rotation in this chapter has enabled us to implement GHz rotation of the linear polarization of the condensate and achieve

driven spin precession for the very first time in polariton condensates.

The spin subjected to the external magnetic field precesses around the direction of an applied field in the phenomenon called Larmor precession. The precession frequency ω_L is proportional to the field magnitude B and reads as $\omega_L = \gamma B$, where γ is the gyromagnetic ratio. This effect has been observed in various magnetic systems [103, 165] and is already utilised for numerous applications. The effects of nuclear or electronic magnetic resonance [165] based on this precession are now actively utilised for commercial applications in medicine, chemistry, biology and material science. On the other hand, the spin precession driven by the optical field [40] in dilute gases and Bose-Einstein condensates is suitable for high-precision magnetometry [166]. Moreover, driven spin precession is a standard tool for quantum computing to manipulate the spin state of the qubits [167]. The oscillating magnetic or optical fields at a specific frequency and amplitude are shown to drive the spin into the required state for the realisation of quantum gates. In this regard, the studies of spin precession are of great importance for possible applications.

The phenomenon of self-induced Larmor precession is established and reported for polariton condensates. It appears in polariton condensates as oscillations in the pseudospin due to the spin-anisotropic interactions of polaritons, which form an effective out-of-plane magnetic field when the spin populations are imbalanced through e.g. elliptically polarised pumping [33, 168]. In Chapter 4, we observed and discussed this effect's signatures in lowering the DOP at high pump power. The recent studies showcased the self-induced Larmor precession effect evidenced in first [6] and second [8] order coherence measurements. Even though the spin coherence time ($\approx 5ns$) [8] in such an experiment is high compared to the polariton lifetime, the polariton-exciton and polariton-polariton interactions decohere the polariton spinor limiting the timescale of its coherent operation. Therefore, extended spin coherence is crucial for future applications of condensate in spin-optonics and quantum computing [48]. One of the approaches of spin coherence prolongation could be an external driving analogously to conventional condensates [40]. However, it has not been studied to date for polariton condensates. The elliptical optical trap described in the previous Chapter acts as an effective in-plane magnetic field for polaritons,

making them adopt a defined spin state; thus, continuously shaping the confining potential should allow us to drive the spin state even at high frequencies. The only problem is the realisation of such fast alternating time-periodic potential.

In this regard, this Chapter concerns the developed technique for the fast trap rotation. The beating note of two frequency-detuned and spatially structured laser beams is used to create a rotating optical trap, which confines and sustains the condensate with particles. Upon condensation, the polariton pseudospin spontaneously aligns itself along the short axis of the trap in the cavity plane [2] and rotates in sync with it. Not only do we achieve controllable rotation of the condensate spin using a rotating optical trap at GHz frequencies, but we reveal a resonant behaviour of this precession. The driven precession becomes amplified when the external driving frequency matches the condensate internal Larmor precession frequency. In fact, the trap acts as a rotating in-plane magnetic field so that the observed phenomena could be considered as a driven-dissipative analogue of the famous Nuclear Magnetic Resonance effect [165]. At resonance, the unprecedented spin coherence time exceeding 170 ns is achieved, which is an order of magnitude longer than the record value [8].

6.2 The quest for the rotating trap realisation

The realisation of the laser beam rotation is quite a challenging problem, and its solution depends on the required stirring speed. The relatively slow rotation can be implemented mechanically by alternating the mirrors, which reflect the laser beam, or rotating the hologram pattern on the SLM. The faster rotation can be achieved with the acousto-optic or electro-optic deflectors. This approach was used, for example, in Ref. [42]. However, the operation speed of such deflectors is limited to a few GHz and hardly allows for tuning the driving frequency. In this regard, we develop an elegant alternative approach for laser pattern modulation based on the beating note of two lasers.

The idea is as follows: to use two frequency-detuned beams and shape each

of them with the SLMs in the form of a ring with the phase winding. We utilise the so-called "perfect vortex" mask [122], and it is the sum of the hologram for Laguerre-Gaussian and the ring pattern (conventionally made with axicon prism). Such configuration allows for the separate tuning of both the radius and orbital angular momentum (OAM) of the created laser pattern. Then we overlap two laser beams on the beamsplitter, and the resultant beating note rotates at a frequency proportional to the lasers frequency difference $f_1 - f_2$ and inversely proportional to their OAMs difference $l_1 - l_2$:

$$f = \frac{\Delta f}{\Delta l} = \frac{f_1 - f_2}{l_1 - l_2}. \quad (6.1)$$

Here, $f_{1,2}$ and $l_{1,2}$ correspond to the linear frequency and OAM of two laser beams, respectively. Note that positive and negative f correspond to counterclockwise and clockwise rotation of the intensity pattern, respectively. The example relevant to the study discussed in this Chapter is presented in Figure 6-1. Here, we suggest creating two "perfect vortex" beams with the same diameter but the opposite topological charge of +1 and -1, respectively. Putting the intensity of one of them to be smaller (here one-fifth with respect to the first one) than the other and interfering them, we get the pattern depicted in the right panel of Figure 6-1, which rotates in time at frequency f . Interestingly, this pattern is practically identical to the one used for controlling the linear polarisation of the condensate (see Figure 5-1(a,b)).

On the experimental setup, we already had two integrated SLMs, so the task was to create two beams at different frequencies detuned by a few hundred MHz or more. The initial approach was to utilise one laser, split its emission into two parts and then shift one's part frequency with the acousto-optic modulator (AOM). The frequency of the laser beam deflected in the first order of AOM is frequency-shifted with respect to incident one by the value of the driving RF wave frequency. It is worth noting that this shift could have positive or negative signs, depending on the incident angle of the laser beam, which is defined by the sign of the projection of the beam k-vector onto the propagation direction of a sound wave. Additionally, the double-path AOM configuration allows doubling this frequency shift. There, the

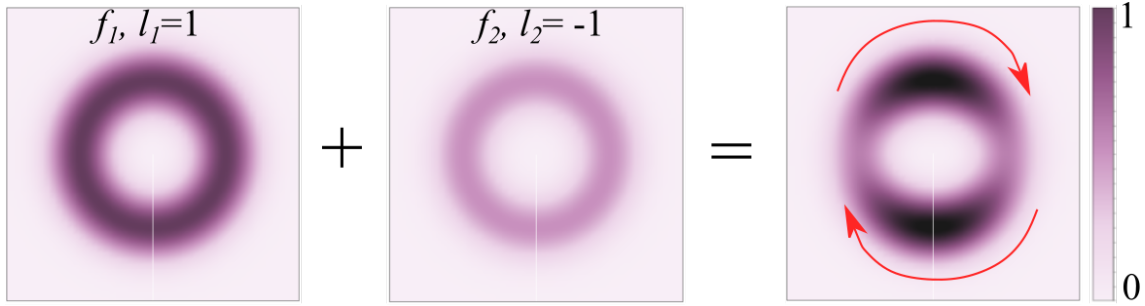


Figure 6-1: The simulated pump laser profiles for the realisation of the rotating excitation pattern for polaritons. The left image corresponds to the pattern created with the "perfect vortex" mask on the SLM and carries the topological charge of $l_1 = 1$ at laser emission frequency f_1 . The middle profile has a similar radius but the opposite OAM $l_2 = -1$ and lower intensity. The resultant beating pattern presented in the right panel is rotating at frequency f and is reminiscent of that used for the previous experiment described in Chapter 5.

modulated beam diffracted in the first order of AOM is reflected back to the device, where it experiences another diffraction in the crystal. The outgoing beam is co-aligned with incident one. To separate them, the QWP with the fast axis oriented at 45 degrees is inserted in the beam path after the AOM (see Figure 6-2 (a)) so that the incoming and outgoing beams have orthogonal linear polarisations. The frequency-shifted (the frequency shift is twice the RF frequency) beam is then routed with PBS to the SLM.

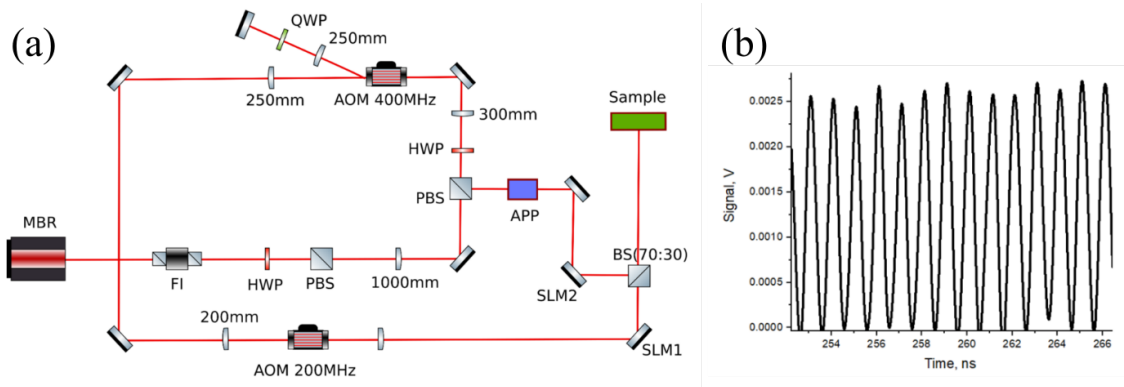


Figure 6-2: (a) Experimental setup for realising the rotating optical pattern with AOMs used for the laser frequency shift. One part of the laser is shifted in a double-path AOM (driving frequency 400 MHz) configuration, the other one with another AOM (driving frequency 200 MHz). Here, the anamorphic prism pair (APP) is used to correct the beam ellipticity induced by AOM. (b) The beating signal at 1 GHz of two beams frequency-shifted with AOMs.

We were able to achieve the 1 GHz frequency difference between two lasers: for

one part of the radiation, we used the double-path configuration described above and an AOM operating at 400 MHz modulation frequency. The other part is frequency-shifted with another AOM (the driving frequency is 200 MHz). The experimental setup schematic is depicted in Figure 6-2(a). The beating note of two beams measured with the photodiode is shown in Figure 6-2(b), manifesting the obtained 1 GHz frequency shift.

The approach with AOMs worked quite well for the realisation of the rotating pattern for polariton condensates. However, we were unable to tune the stirring frequency, as the AOM models we used did not support the driving frequency change option. To achieve the desired stirring frequency higher than 1 GHz and frequency tuning, we had to switch to another experimental setup. Namely, we utilise two Ti:Sapphire lasers, described in Chapter 3 and drive their frequencies separately. Figure 6-3 depicts the excitation part of the experimental setup. Using two lasers, we can fine-tune their frequency independently to realise any desired frequency difference. To stabilise it and compensate for the wavelength drift of two lasers, we lock their frequencies externally with the MOGLABs wavelength meter (wavemeter). This device not only measures the wavelength with high precision but has two inputs and works as a feedback and PID generator to produce a controlling voltage to tune both laser cavities simultaneously. The temporal behaviour of the laser emission wavelength with and without external locking is shown in Figure 6-3. With the stabilisation, the wavelength holds still for the entire experiment duration with a frequency jitter of approximately 10 MHz at 3 minutes timescale.

Two frequency stabilised lasers are then shaped with the two SLMs, overlapped on the beamsplitter and focused on the sample. As a result, the optical pattern is rotating with the frequency f acting as a rotating trap for polaritons.

The mutual coherence of two lasers dictates the stability of the beating frequency and, ergo, the stability of the rotation frequency f of the optical trap. Even though the linewidth of lasers is narrow (less than a few MHz) and the emission frequency of both is stabilised with the wavemeter, the frequency jitter and instant shifts can affect their mutual coherence. The beating signal of the excitation laser detuned by several MHz is presented in Figure 6-4(a). Here, the instant changes in the

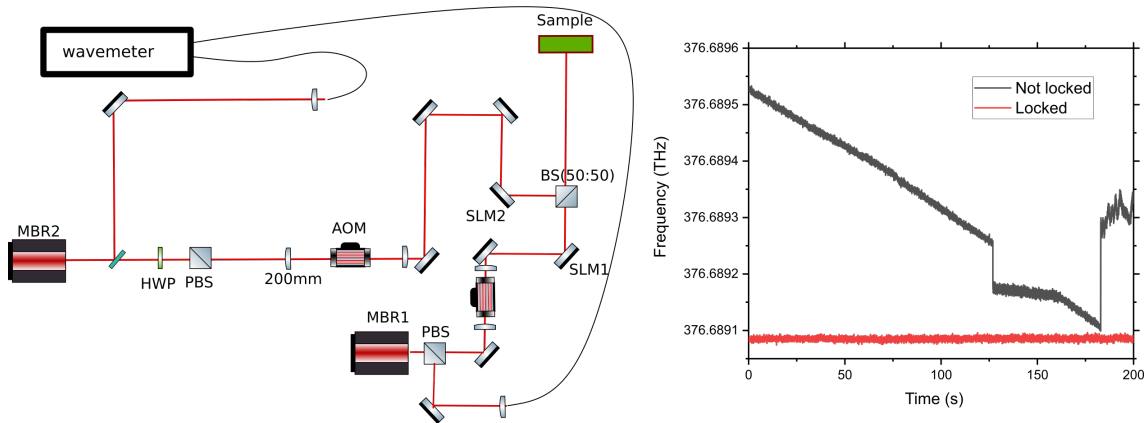


Figure 6-3: Left panel: experimental setup for the realisation of the rotating optical pattern with the beating note of two single-mode lasers (MBR1 and MBR2). The frequency of both lasers is externally stabilised with the wavemeter and PID loop. Right panel: the track of the laser frequency (in THz) versus time (in seconds) when externally stabilised (red line) and not (black line).

beating frequency are evident on the time scale of 40 microseconds. During the measurement time, the periodicity of the oscillations is changed several times. The Fourier transform of the beating signal depicted in Figure 6-4(b) shows that the beating harmonics have a finite width $\Delta\nu$. Consequently, the mutual coherence time over the 40 μs measurement window is calculated as $1/\Delta\nu$ and equals $\approx 2.8\mu\text{s}$. Given that the excitation laser pulses have a width of 2 μs , the optical trap rotation frequency for one realisation of the condensate, on average, stays unchanged.

However, the mutual coherence of two lasers measured over a larger time window is significantly less due to accumulated frequency jitter. In the experiments, we use the HBT setup described in Chapter 3, and one measurement with this apparatus takes us over ten minutes (millions of realisations of the condensate). To characterise the stability of the lasers at such timescale, we use the same HBT intensity correlation setup and overlap two excitation lasers (frequency-detuned by 1 GHz) and measure the $g^{(2)}$ at big time-delays. The results are presented in Figure 6-4(c). The auto-correlation of the beating lasers demonstrates the decay at longer time delays of the HBT interferometer. The decay time here is around (142 ± 8) ns, which is the mutual coherence time of two excitation lasers over the measurement time. Nevertheless, even that does not prevent the intensity correlation measurements since usually GHz rotation speed is required for the experiments, which is

significantly higher than the inverted mutual coherence time.

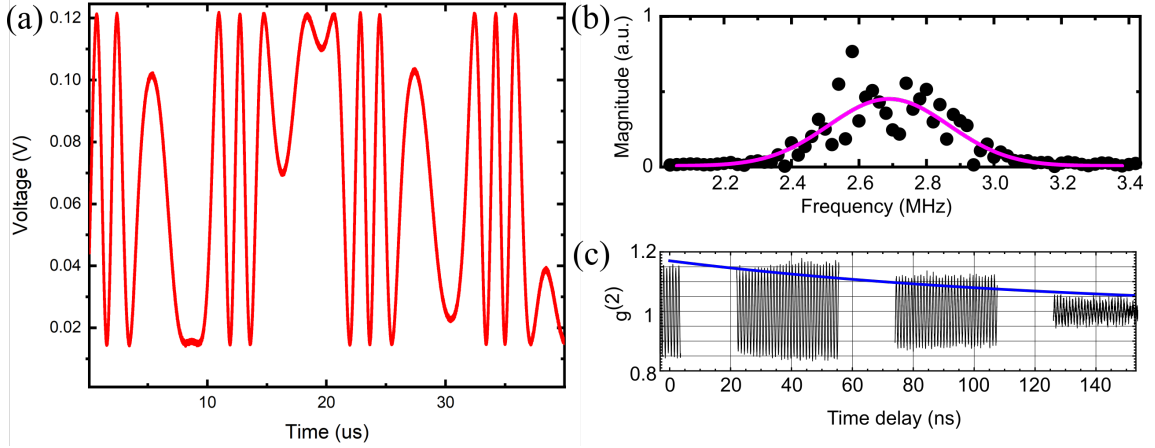


Figure 6-4: (a) The beating note of two single-mode excitation lasers (MBR1 and MBR2) measures in time with photodetector. (b) The spectrum of the beating signal (black points) near the beating frequency, the purple line, is a Gaussian fit. (c) Measured $g^{(2)}$ intensity auto-correlation function for the expanded time delay in the HBT interferometer for two single-mode frequency-detuned lasers. The frequency detuning is 1 GHz. The blue line is an exponential fit.

6.3 Slow MHz polarisation rotation

As shown in the previous Chapter 5, the elliptical confinement potential for the condensate makes it adopt the definite spinor (polarisation) aligned with the short axis of the trap. Thus, by applying the rotation described in the previous section, we can dynamically change (stir) the shape of the trap, which will drag the spinor of the condensate on the equator of the Poincare sphere (see Figure 6-5(a)). The schematic of the excitation part of the setup is depicted in Figure 6-5(a).

First, the stirring frequency is set to a few MHz, and the rotation is counter-clockwise ($l_1 = 1, l_2 = -1$). The counter-clockwise is defined here as if one is looking along the beam. The intrinsic spin dynamics (spin coherence time) of polariton condensate is a few nanoseconds [8], so 5 MHz stirring is adiabatic for the condensate spinor. At 5 MHz, the time-integrated condensate intensity distribution is symmetric and depicted in Figure 6-5(c). The intensities of the two pump lasers are not equal, and their ratio is 1:10. Pump power is set to $2P_{th}$, so the condensate occupies the trap energy ground state [27]. The optical trap diameter on the sample is $10.5 \mu m$

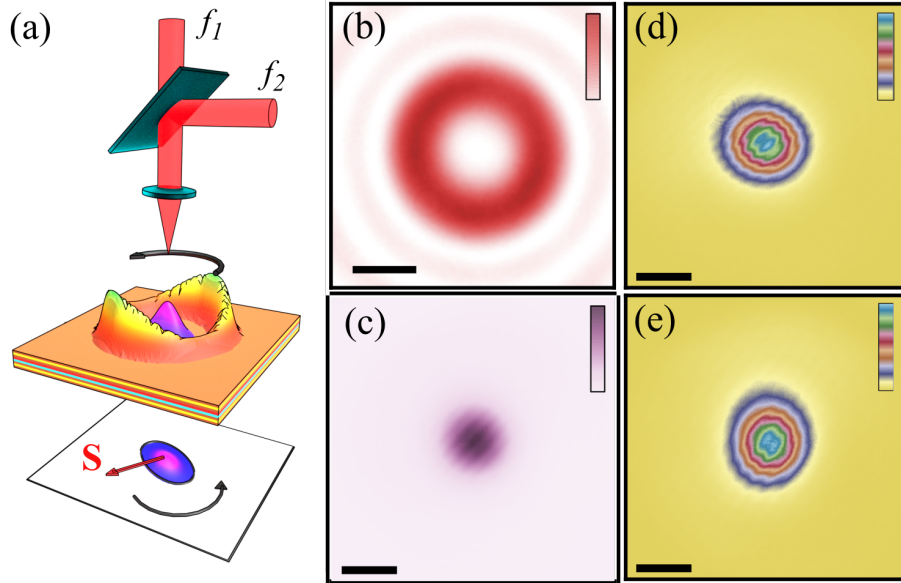


Figure 6-5: (a) The schematic of experimental setup demonstrating two frequency detuned (f_1 and f_2) "perfect vortex" beams ($l_1 = \pm 1$ and $f_2 = \mp 1$) overlapping on the beamsplitter. The resultant rotating non-resonant excitation pattern (coloured in red to yellow gradient) is projected onto the microcavity sample and results in the rotating elliptical polariton condensate (coloured in blue to purple gradient). The bottom of the panel (a) depicts the planar spinor projection of the condensate. (b) Time-integrated intensity profile of the excitation pattern. (c) Time-averaged condensate total intensity distribution. Time-averaged and normalised (d) vertical and (e) horizontal polarisation projections of the condensate. The black scale bar in panels (b-e) corresponds to $5 \mu\text{m}$. Figures are adopted from Ref. [4].

(see Figure 6-5(b)). Note that the integration time of the utilised detection cameras prevents us from resolving the rotation of the trap and condensate; because of that, the excitation and condensate intensity profiles appear symmetric (Figure 6-5(b) and (c) respectively).

However, vertical and horizontal linear polarisation projections of the condensate emission resolved with the Wollaston prism are elliptical even in time-integrated measurements, as shown in Figures 6-5(d), (e). We observe that the vertical projection is horizontally elongated (Figure 6-5(d)), whereas the horizontal one is vertically elongated. It is the evidence that the condensate rotates and, when horizontally aligned, has vertical polarisation and vice versa [2]. The relation between the condensate spatial distribution and its polarisation state allows us to separate different time realisations (spatial position of the ellipse) in the polarisation domain and see an approximate instant condensate profile even with the long exposure time of the

detecting camera.

To resolve the linear polarisation rotation in time, we split the condensate emission in the polarisation domain with polarising beamsplitter (PBS) and detect the intensity of horizontal(H) and vertical(V) components with photo-multiplier tube detectors. The normalised readings from the detectors obtained simultaneously are presented in Figure 6-6 (a,b). Both horizontal (H) and vertical (V) polarisation projections are sinusoidal, however, they are out-of-phase (V has a π phase shift with respect to H). Note that the signal modulation depth is close to 100%, with the signal from both H and V almost reaching zero. This manifests the condensate's high linear polarisation degree and modulation efficiency. Sampling the part of the condensate emission before the polarising beamsplitter, we simultaneously detect the diagonal polarisation component [1]. The phase shift of the diagonal(D) component (see Figure 6-6(c)) is $\frac{\pi}{2}$, which is expected for the linear polarisation rotation in time. The slight asymmetry of polarisation rotation tracks in Figures 6-6(a)-(e) arises due to small polarisation pinning [1, 2, 15] making the condensate spin leaning more towards horizontal polarisation.

Given three linear polarisation projections, we calculate the Stokes components of the characterised light [1]. Normalised S_1 and S_2 of the polariton condensate are depicted in Figures 6-6 (d) and (e), respectively, and also alternate in time. Plotting the experimentally retrieved S_1 and S_2 on the equatorial plane of the Poincare sphere in Figure 6-6(f), we get the circle with a radius of 0.85. Thus, the condensate spinor driven by the stirring continuously travels through all linear polarisation states. Note that the spin makes two revolutions per the trap rotation period.

We note that the width of the circle in Figure 6-6(f) is associated with the noise in the detection scheme, as well as internal condensate spinor dynamics. Under linearly polarised non-resonant excitation due to an effective in-plane magnetic field, the condensate spinor can destabilise and flip instantly between two orthogonal linear polarisations. This effect was discussed in Chapter 3 and led, for example, to the dramatic change in the condensate photon statistics reported in Ref. [8]. The instance of the described flip can be noticed in Figures 6-6(a) and (b) near the $0.4 \mu s$ as a synchronous dip in H and peak in V. However, despite the noise, the achieved

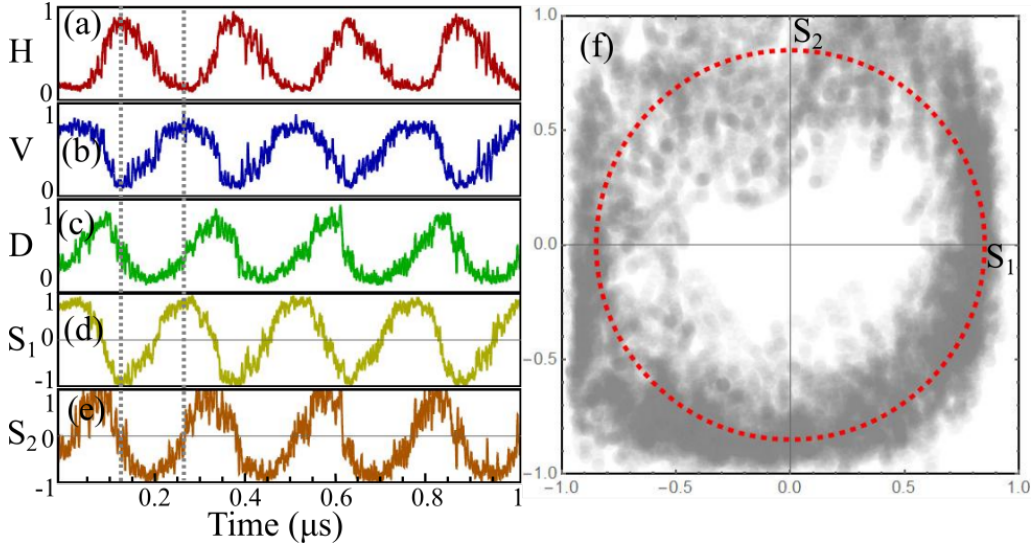


Figure 6-6: Horizontal (a), vertical (b) and diagonal (c) polarisation projections of the condensate emission. The power ratio of excitation lasers is 10%. Time-resolved (d) S_1 and (e) S_2 polarisation components of the condensate emission. (f) The trajectory of the condensate spinor on the equator of the Poincaré sphere. The red dashed line is to guide the eye.

polarisation modulation is stable within the whole excitation laser pulse.

6.4 Control over spin rotation direction

The direction of the trap rotation is dictated by the sign of the f in Equation (6.1), and the positive and negative values correspond to the counter- and clockwise rotations, respectively. Thus, by changing either Δf or Δl , one can control the trap rotation direction as well as the condensate spin defined by the trap orientation.

So, for $\Delta f \approx 5$ MHz, $l_1 = 1, l_2 = -1$, and the resultant time series for the S_1 and S_2 Stokes components of the condensate PL are presented in Figure 6-7(a). Plotting one with respect to another on the equatorial plane of the Poincaré sphere and tracking the time, we can retrieve the handedness (direction) of the rotation. So for the Δf and Δl introduced above, we get, as expected, the anti-clockwise rotation of the condensate pseudo-spin (see Figure 6-7(b)). On the contrary, flipping the OAMs of the interfering beams ($l_1 = -1, l_2 = 1$) at the same frequency detuning $\Delta f \approx 5$ MHz, we receive the clockwise rotation plotted in Figures 6-7(c),(d). These results underpin the control of the condensate spin rotation direction or, alternatively, the

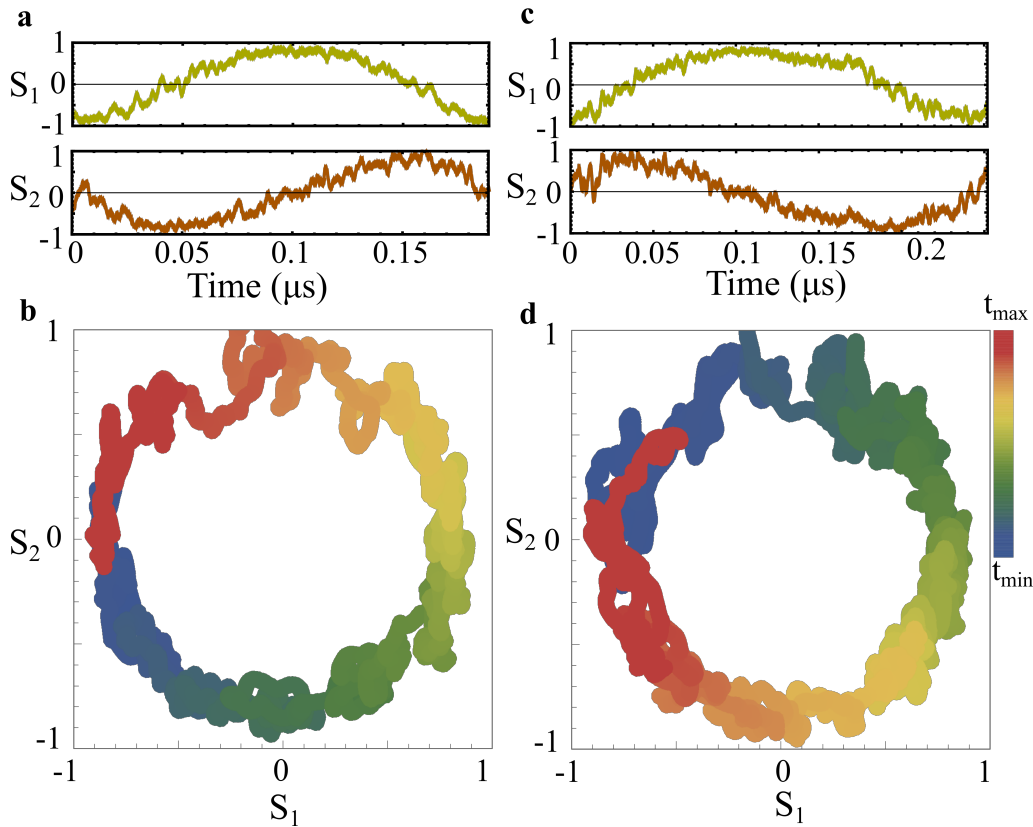


Figure 6-7: (a) Time-resolved S_1 and S_2 polarisation components of the polariton condensate emission versus time. Here, the condensate forms in the rotating trap with the $\Delta f \approx 5$ MHz and $l_1 = 1, l_2 = -1$. (b) The corresponding Stokes vector trajectory on the equator of the Poincare sphere. (c) Time-resolved S_1 and S_2 polarisation components of the condensate emission for the $\Delta f \approx 5$ MHz and $l_1 = -1, l_2 = 1$, and the corresponding trajectory (d) in the linear polarisation plane of the Poincare sphere. The colour scale in panels (b,d) represents the time passing.

linear polarisation of the condensate emission.

6.5 GHz precession and resonance

The temporal response of the detectors and oscilloscope utilised for the time-resolved polarisation measurements do not allow us to investigate the driven spinor precession at higher (GHz) frequencies. The bandwidth of the detection apparatus was limited to ≈ 500 MHz. To overcome this constraint, we put to use the experimental apparatus described in Chapter 3. We employ the Hanbury Brown and Twiss (HBT) interferometer coupled with a time-correlated single photon counting technique (TC-SPC) to measure the cross-correlation function ($g_{H,V}^2$) of the H and V polarisation

components of the cavity emitted light. Similarly to the setup used for time-resolved polarisation measurement, we split the condensate emission in the linear polarisation domain with the PBS and then measure the statistics of their polarisation projection photon coincidence with avalanche photodiodes (APD) and TCSPC technique (see Figure 6-8(a)). Additionally, by applying the HBT interferometer to one of the polarisation components or the whole condensate PL (by taking off the PBS), we characterise respective intensity auto-correlation functions g_H^2 , g_{Total}^2 . This experimental approach allows us to investigate the stirring frequencies up to a few GHz, while grasping the condensate spin coherence properties [8, 169].

For the GHz rotation speed, we increase the ratio of the two excitation laser intensities to be 20% in order to compensate for the exciton decay and the effective smearing of the exciton reservoir. Interestingly, with linearly polarised excitation at $\Delta f = 1GHz$ and $\Delta l=2$, we do not observe the rotation of the condensate spinor at the driving frequency. On the contrary, the spin dynamics resemble the one of the stationary optical trap (see Fig. 6-8(b)) - the instant spin flips described in Chapter 4 result in anti-bunching of H-V intensity cross-correlation function at zero time delay [8].

The behaviour of the condensate spinor is drastically changed when we apply small polarisation ellipticity to the pump lasers by inserting the QWP into the excitation path. For the 8° of the QWP, we observe persistent oscillations of the H-V cross-correlation function (see Figure 6-8(c)). The frequency of these oscillations is twice the external stirring frequency f because spin makes two revolutions for 1 rotation period. The local minimum at zero time delay manifests the anti-correlation of H and V polarisation components, confirming the induced condensate spinor rotation. On the other hand, the auto-correlation function of horizontal polarisation depicted in Figure 6-8(d) possesses a local maximum at zero time delay as well as sine modulation, which is expected for the photon statistics of the light source with rotating polarisation. The overall emitted light intensity auto-correlation function g_2 (Figure 6-8(e)) does not demonstrate any oscillations and is equal to 1. That stands for the absence of condensate intensity modulation as well as for the coherent nature of polariton condensate.

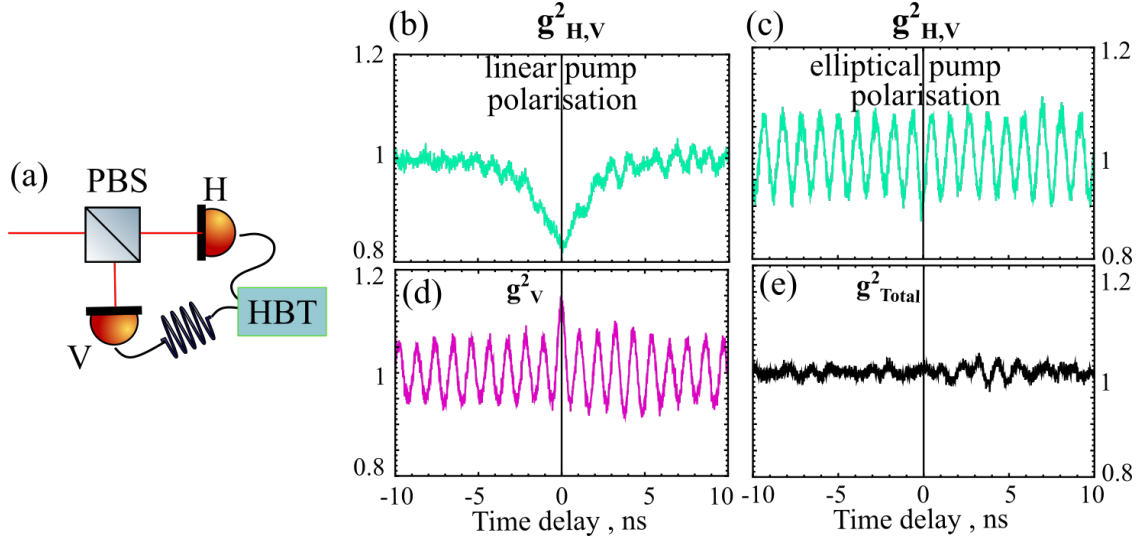


Figure 6-8: (a) The schematic of the detection part of the experimental setup. The condensate emission is split on the polarising beamsplitter (PBS), and the horizontal (H) and vertical (V) polarisation components are correlated in the Hanbury Brown and Twiss (HBT) interferometer either in cross- or auto-correlation configuration. H and V cross-correlation (b) of the condensate excited with linearly polarised pump $f = 0.5$ GHz. (c) $g^2_{H,V}$ of the condensate in the rotating trap with elliptical pump polarisation and corresponding g^2_V (d), and g^2_{Total} (e). Figures are adapted from Ref. [4].

Interestingly, the persistent driven GHz rotation of the condensate spinor appears only for the specific values of pump polarisation ellipticity. Under elliptically polarised excitation spin of the condensate in the optical trap precesses in the effective magnetic field [6, 8]. Moreover, the precession speed is directly proportional to the ellipticity of the optical pump - more circular excitation leads to faster spin oscillations [8]. To reveal the dependence of the induced spin rotation on the polarisation ellipticity, we perform the $g^2_{H,V}$ cross-correlation measurements for different angles of the QWP in the excitation path, starting with zero degree corresponding to the linearly polarised excitation. The resultant correlation maps for $f = 0.5$ GHz and $f = 1$ GHz rotation frequencies are presented in Figures 6-9(a) and (b), respectively. For the ellipticities lower than 5° at $f = 0.5$ GHz in Figure 6-9(a), the condensate behaves as if there is no external stirring [8]. The spinor dynamics is limited by 5 ns and goes from anti-bunching under linear excitation to decaying oscillations for the elliptically polarised pump corresponding to the self-induced Larmor precession. However, in the vicinity of 8° of QWP, the condensate spinor

eventually adopts the external stirring and does not decohere for the whole 30 ns measurement window. This significant increase in spin coherence appears only when the external driving is in resonance with the self-induced Larmor precession. By the spin coherence hereafter, we mean the coherence of the spin precession.

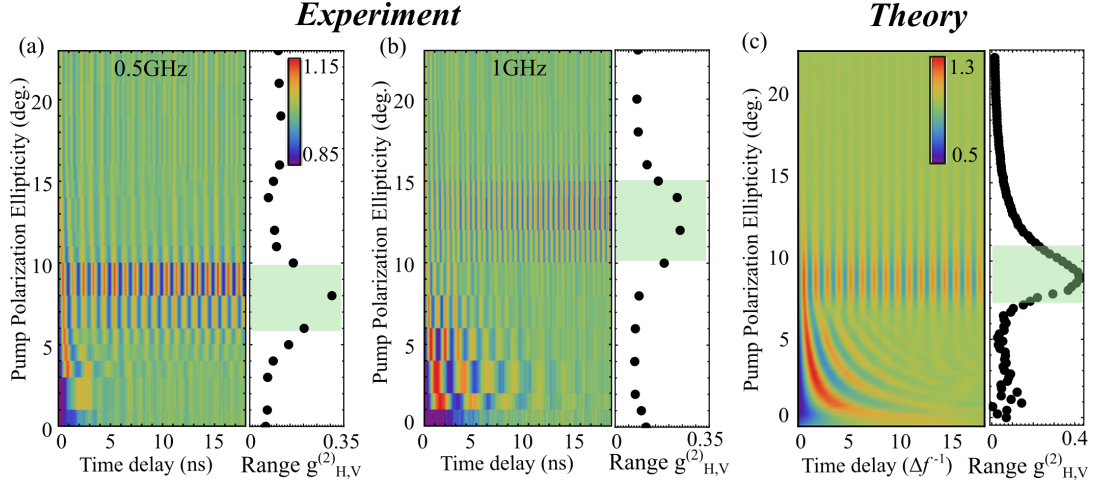


Figure 6-9: Measured H-V cross-correlation maps for (a) $f = 0.5$ GHz and (b) $f = 1$ GHz trap rotation as a function of time-delay and pump polarisation ellipticity. (c) Simulated $g_{H,V}^{(2)}$ of the condensate emission versus the time delay and pump polarisation ellipticity. The black and red point graphs on (a-c) respectively demonstrate the amplitude of the cross-correlation function at 15 ns delay. Figure is adopted from Ref. [4].

Analogously to the experiments with the spin of diluted gases [40], resonant driving of the system leads to the driven precession, which does not decay in time. In the inset of Figure 6-9(a), we plot the amplitude of the H-V cross-correlation in the vicinity of 15 ns (within 2 ns) time delay versus the pump ellipticity. The obtained curve highlights the resonant nature of the observed driven precession, with the resonance appearing near the 8° . Under the same experimental conditions but for the 1GHz stirring, we observe the shift of the resonance (Figure 6-9(b)) to the higher value of the polarisation ellipticity (near 13°). Larger pump ellipticity accelerates the self-induced Larmor precession [8], and the resonance with external rotation is also shifted with respect to the 0.5 GHz rotation.

6.6 Persistence of the precession

We note that the observed intensity oscillations are very stable and persistent, not only in the 30 ns HBT measurement window but also in the expanded observation window. In order to probe the temporal stability of the oscillations at longer time scales, we measure the cross-correlation of the H and V polarisation components at an extended time delay. To do so, we add additional optical delay to one of the correlating signal paths. We incrementally add a few 10-meter optical fibres (each corresponding to 52 ns delay) in one arm of the HBT interferometer and measure the $g_{H,V}^{(2)}$ for the increased time delay. We add up to 31 m (≈ 162 ns delay) of optical fibre, as well as some electronic delay available with the HBT apparatus (so the maximum time delay achieved is ≈ 200 ns). The obtained results are presented in Figure 6-10. Note that the decrease of the $g_{H,V}^{(2)}$ amplitude for each part of the black curve towards bigger delays in Figure 6-10 is the artefact of the experimental apparatus. It can be attributed to the non-linearity of time to amplitude converting electronics of the single photon counting card.

For the comparison, we also plot in the same graph the self-induced Larmor precession of the condensate under elliptically polarised excitation (see the red curve in Figure 6-10). The amplitude of the driven oscillations is dropped twice at approximately 150 ns, even though the precession is still distinguishable up to 200 ns. We fit the envelope of the oscillations presented in Figure 6-10 with the decay exponent ($Ae^{-t/\tau}$), where A is an amplitude of the oscillations at zero time delay, t is time, τ is spin coherence (characteristic decay time of the spin oscillations) time. From the fit, we retrieve the $\tau = (174 \pm 10)$ ns, which is 20 times more [8] than the previously reported value for polariton condensates. Further, we estimate the quality factor Q of the driven precession $Q = \tau\omega/2$, where $\omega = 2f = 1$ GHz is precession frequency, to be 546.

We underline here that the decrease in $g_{H,V}^{(2)}$ at big-time delay appears due to the imperfect mutual stability of two excitation lasers (see Section 6.2). Frequency jitter during the acquisition time results in the effective change of the stirring frequency, which smears the $g_{H,V}^{(2)}$ at a bigger time delay. The measurement of one $g_{H,V}^{(2)}$ curve

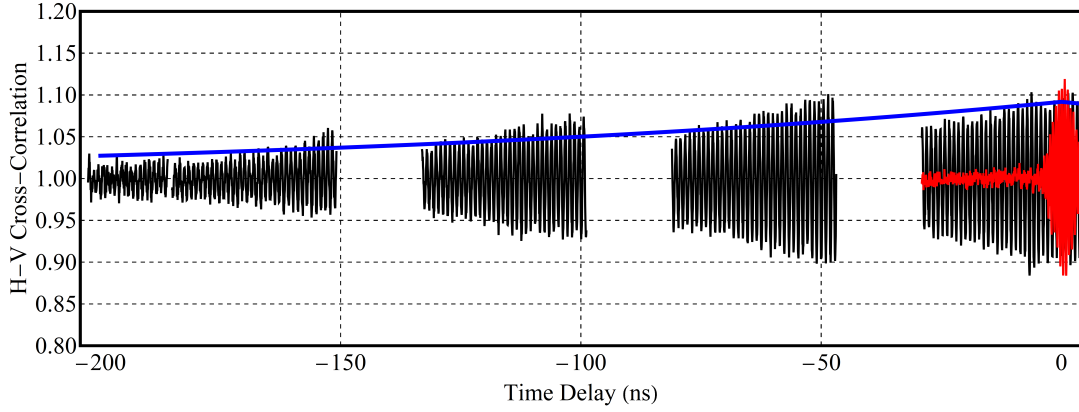


Figure 6-10: The H-V cross-correlation $g_{H,V}^{(2)}$ for the condensate in the rotating optical trap (black curve) and static annular optical trap (red curve). The blank spaces in the black graph appear due to the incremental addition of the optical delay and limited measurement window. The solid blue line is the fit of the experimental data envelope with $Ae^{-t/\tau}$. The figure is adopted from Ref. [4].

takes at least 10 minutes, which implies the integration over 6×10^6 realisations ($2\mu\text{s}$ pulses) of the condensate. We stress that the spin precession in time (but not in the correlation domain) is persistent in the condensate for the whole μs excitation pulse (see 6-6). Using other approaches for laser frequency detuning featuring improved stability could potentially increase the induced spin coherence even more.

6.7 Theory

From the previous Chapter, we know that the elliptical optical trap acts as an effective magnetic field Ω_{trap} for polariton condensate, making its spin align along the short axis of the ellipse. This field is written in Equation 5.8. When the elliptical trap is rotating, the Ω_{trap} is rotating in sync, and its short axis θ_{min} angle is defined by ωt . $\omega = 2\pi f$ is the angular rotation frequency. The alternating effective magnetic field induced by the rotating potential reads as

$$\mathbf{\Omega}_{\text{trap}} = \begin{pmatrix} \Omega_{\parallel} \cos [2\omega t] \\ \Omega_{\parallel} \sin [2\omega t] \\ 0 \end{pmatrix}, \quad (6.2)$$

where Ω_{\parallel} is a constant. The pump polarisation ellipticity results in the formation

of two unequal reservoirs of spin-up and spin-down polaritons. As we have shown in Chapter 3, as it was reported in Refs. [6, 8, 33, 168], it gives rise to the self-induced Larmor precession of the condensate spin around the effective out-of-plane magnetic field. This precession also happens in the equatorial plane of the Poincare sphere. Then, the total effective magnetic field acting on the condensate can be written as

$$\mathbf{\Omega}_{\text{Total}} = \begin{pmatrix} \Omega_{\parallel} \cos [2\omega t] \\ \Omega_{\parallel} \sin [2\omega t] \\ \Omega_{\perp} \end{pmatrix}, \quad (6.3)$$

where Ω_{\perp} is the out-of-plane effective field component proportional to pump ellipticity [8]. When $\Omega_{\perp} = 2\omega$, the trap rotation is in resonance with the self-induced Larmor precession, and the pseudospin starts rotating with renewed stability.

6.8 GPE simulations

The results are well reproduced with the numerical simulations performed (as well as the theory in the previous Section) by Dr. Helgi Sigurdsson. Overall, the numerical simulations help to have an insight into the dynamics of the condensate, which is often not accessible in experiments. From the Author's point of view, simulation results complement the reported effects and benefit the comprehension of the reported study. Moreover, the simulation, when the parameters corresponding to the experiment are chosen, allows investigating and searching for new effects that further could be implemented in the experiment.

The dynamics of the spinor polariton condensate order parameter is modelled through a set of stochastic driven-dissipative Gross-Pitaevskii equations coupled to spin-polarised reservoirs X_{\pm} feeding the two spin components ψ_{\pm} of the trap ground

state condensate [142].

$$i\frac{d\psi_\sigma}{dt} = \left[\alpha|\psi_\sigma|^2 + G \left(X_\sigma + \frac{P_\sigma}{W} \right) + \frac{i}{2} (RX_\sigma - \Gamma) \right] \psi_\sigma + \Omega_\parallel \psi_{-\sigma} e^{-\sigma i 2\omega t} + \theta_\sigma(t), \quad (6.4a)$$

$$\frac{dX_\sigma}{dt} = - (\Gamma_R + R|\psi_\sigma|^2) X_\sigma + \Gamma_s (X_{-\sigma} - X_\sigma) + P_\sigma. \quad (6.4b)$$

Here, $\sigma \in \{+, -\}$ are the two spin indices, Γ_R and Γ_s describe the decay rate and spin relaxation [170] of reservoir excitons. G denotes the same-spin polariton-reservoir interaction strengths. The elliptical trap shape and the TE-TM splitting from the cavity mirrors cause fine-structure splitting in the polariton condensate described by an effective in-plane magnetic field Ω_\parallel along the trap minor axis (see Chapter 5). Consequently, the effective field rotates at a frequency 2ω . The other parameters are described in the previous Chapter and in Chapter 3.

A famous phenomenon corresponding to the model and experiment is *nuclear magnetic resonance* wherein a two-level spin (i.e., a spin 1/2 particle) is subject to a time-dependent magnetic field $\mathbf{B} = (B_x \cos(2\omega t), B_y \sin(2\omega t), B_z)^T$. In our case, the time-dependent in-plane magnetic field corresponds to the oscillating birefringence from our spinning non-axisymmetric trap $B_{x,y} = \hbar\Omega_\parallel/\mu$, where μ is the Bohr magneton. The out-of-plane magnetic field in our experiment comes from the spin-anisotropic interactions between polaritons $B_z = \hbar\Omega_\perp/\mu = \hbar(\Omega_+ - \Omega_-)/\mu$ given by Eq. (6.4a), which is non-zero when the pump beam is elliptically polarised $P_+ \neq P_-$. Notice that if the beam ellipticity is reversed, then the sign of the effective field Ω_\perp flips.

As long as the exciton reservoir lifetime is bigger than polariton one we can write pump terms as $P_+ = P_0(W \cos^2(\theta) + \Gamma_s)/(W + 2\Gamma_s)$ and $P_- = P_0(W \sin^2(\theta) + \Gamma_s)/(W + 2\Gamma_s)$. Here, P_0 is the total power of the pump. The calculated $g_{H,V}^{(2)}(\tau)$ is obtained by replacing the operators a_μ^\dagger and a_μ in Equation (3.8) with ψ_μ^* and ψ_μ obtained by solving the GPE in time.

The simulation results are depicted in Figure 6-9(c) and perfectly match with the experimental findings and reproduce the resonance behaviour of the condensate spin. The simulation parameters in units of ω are as follows: $\Gamma = 100$; $\Omega_\parallel = 0.16$;

$R = 6$; $G = 0.2$; $\alpha = 1$; $W = \Gamma/4$; $\Gamma_R = \Gamma_s = \Gamma/2$; $P_0 = 2.2\Gamma\Gamma_R/R$; $\sqrt{\eta} = 0.01$.

6.9 Conclusion

To sum up, we have demonstrated the GHz rotation of the polariton condensate spinor driven by the external stirring of the non-resonant optical trap. The induced precession features exceptional stability and spin coherence and arises only in resonance with the internal condensate Larmor precession. The observed resonance is reminiscent of the classical nuclear magnetic resonance effect. In our system, the rotating exciton reservoir leads to the effective in-plane magnetic field, and elliptically polarised excitation creates an out-of-plane magnetic field for polaritons. In analogy to classical NMR, the former plays the role of an NMR transverse field, and the latter is a holding field [165]. The effect is also closely related to the optically driven spin precession observed in the dilute atomic gases [40].

Unlike the conventional spin switches implemented in magnets, polaritonics [117], or VCSELs [160], our results show that condensate spin travels through all linear polarisation states on the equator of the Poincare sphere. The short polariton lifetime (≈ 5 ps) permits us to achieve GHz polarisation modulation, which is not feasible for conventional polarisation modulators.

It is worth noting that the approach of the external driving is different to the one already implemented for control of polaritons spin. For example, the ultra-fast spin evolution spanning through various states on the Poincare sphere was realised relying on the Rabi oscillations between upper and lower polariton branches in the study Colas et al. [171]. The difference is the excitation scheme - CW non-resonant time-periodic excitation in our case and pulsed resonant one in Ref. [171]. Furthermore, the mechanisms of the evolution of the spin vary - the resonance of the external drive with the self-induced Larmor precession in our study and Rabi oscillations of two induced cross-polarised populations of polaritons in the linear regime in Ref. [171]. It would be interesting to explore the interplay of the complex polarisation patterns and the time-periodic drive in future research.

A 20-fold increase in spin coherence discussed in this Chapter will potentially

enlarge the time of coherent operations with condensate pseudo-spin. This opens up excellent prospects for novel spinoptronic devices based on polaritons and utilisation of spin degree of freedom for quantum computing [48]. Moreover, the external spin drive can also be applied in the study of the arrays of coupled polariton condensates [32].

All in all, the developed method of optical stirring opens great prospects for possible experiments on polariton condensate in time-periodic potentials. In the next Chapter, we investigate these potentials further and implement the classical "Rotating Bucket" experiment with polariton condensate.

Chapter 7

Vortices in "Rotating Bucket"

Experiment with Polariton

Condensate

The method of the optical trap rotation described in the previous Chapter opens great perspectives for the investigation of polariton condensates in the rotating time-modulated potentials. Furthermore, the versatility of the optical setup coupled with the accessibility of the wide range of the rotating frequencies allowed us, for the first time, to realise the famous "rotating bucket" experiment [41, 44, 172] with polariton condensates. In this Chapter, we will introduce the details about the experiment and developed theory while the study itself is published in the Science Advances journal [3].

The experimental results discussed in this Chapter were obtained by the Author if not stated otherwise. All experimental Figures have been produced by the Author and published in Ref. [3] if not stated otherwise. The utilisation of Figures in this Chapter is granted by the AAAS Author License to Publish Policy. The numerical simulations were carried out by Dr. Stella Harrison and Dr. Helgi Sigurdsson. The Figures containing the simulation results were made by Dr. Stella Harrison and Dr. Helgi Sigurdsson and are also published in Ref. [3]. Their usage in the thesis is granted by AAAS Author License to Publish Policy.

7.1 Introduction

Vortices are objects found in gases, fluids or light that are characterised by the circulation of some physical quantity around their hollow core. Depending on the character of the revolutions, there are quantised or continuous vortices. The simplest example of a continuous vortex would be a vortex of water in the drain of a sink. There, the speed of the rotating water can have any positive value and can be changed continuously by the external force. On the other hand, in the quantised vortices, the speed of the particles, or other characteristic values, can have only a restricted set of values. Vortices are inherent to different systems and widely found in nature ranging from the enormous few thousand kilometres vortices on Jupiter [173] and cyclones in Earth's atmosphere to tiny micrometre-size vortices in superconductors [174], superfluids [43, 44], Bose-Einstein condensates [41, 42] and optical vortices [175]. Vortices have drawn the attention of researchers over the last century, both from fundamental and application points of view. Material vortices can become the building block of quantum information processing [176]. Optical vortices can magnify data transferring capabilities [177] of the optical communication line through the channel multiplexing with an orbital angular momentum. The vortical optical beams can also benefit optical tweezers, allowing efficient manipulation and stirring of nanoobjects [178, 179].

Vortices in conventional fluids appear due to viscosity and carry continuous angular momentum dictated by external forces. On the contrary, superfluids demonstrate remarkable properties which are drastically different from conventional fluids [180]. The absence of viscosity and quantum nature results in the quantisation of the orbital angular momentum in superfluid vortices [43]. The "rotating bucket" experiment [41, 44, 172] is a famous manifestation of this effect.

In this experiment, the superfluid is held in the rotating container, and depending on the stirring frequency, one or more quantised vortices are observed in the bulk of the fluid (see schematic in Figure 7-1(m)). The behaviour of the superfluid can be described by a macroscopic wavefunction $\Psi_s(\mathbf{r}) = A(\mathbf{r})\exp(i\Phi(\mathbf{r}))$, where $A(\mathbf{r})$ is the amplitude of the wavefunction and $\Phi(\mathbf{r})$ is its phase. The velocity [181] of the

superfluid is proportional to the gradient of the phase $v_s = (\hbar/m)\nabla\Phi(\mathbf{r})$, where m is the mass of the particles in the superfluid. Further, directly from the definition of v_s , it follows that

$$\nabla \times v_s = 0, \quad (7.1)$$

the curl of the gradient is zero, meaning that the superfluid is irrotational. In fact, below some critical rotation frequency, the superfluid remains stationary (Landau state). However, when the superfluid is stirred faster, the Landau state becomes unstable, and the vortex appears. The condition (7.1) can be satisfied if the superfluid has lines of normal fluid in bulk with the quantised circulation of the superfluid around this core. The circulation on the closed contour around the vortex core is then given by

$$\oint v_s d\mathbf{r} = \frac{2\pi\hbar}{m}n \quad (7.2)$$

where n is an integer which depends on the rotation speed of the container. So, the faster one rotates the superfluid, the more vortices will appear. Overall, the "rotating bucket experiment" is one of the most significant demonstrations of superfluid state and is often used for the confirmation or refutation of the superfluidity in the system.

The "rotating bucket" experiment was implemented with different isotopes of superfluid Helium [44, 172, 181]. The vortices there were detected by nuclear magnetic resonance and by imaging the trapped electrons (ions) in the vortex core. The vortices photographed by the latter method by E.J. Yarmchuk in 1979 are depicted in Figures 7-1(a-l). The rotation of the reservoir was realised mechanically, and vortices were formed at frequencies less than Hertz. As it was discussed previously, the number of vortices depends on the reservoir rotation speed, and the step-like frequency dependence of the vortex number reported by R. E. Packard in 1972 [182] is presented in Figure 7-1(n). It was realised by the measurement of electrons injected and trapped in the vortex core depending on the rotation frequency.

Quantized vortices were also observed in atomic Bose-Einstein condensates [56]

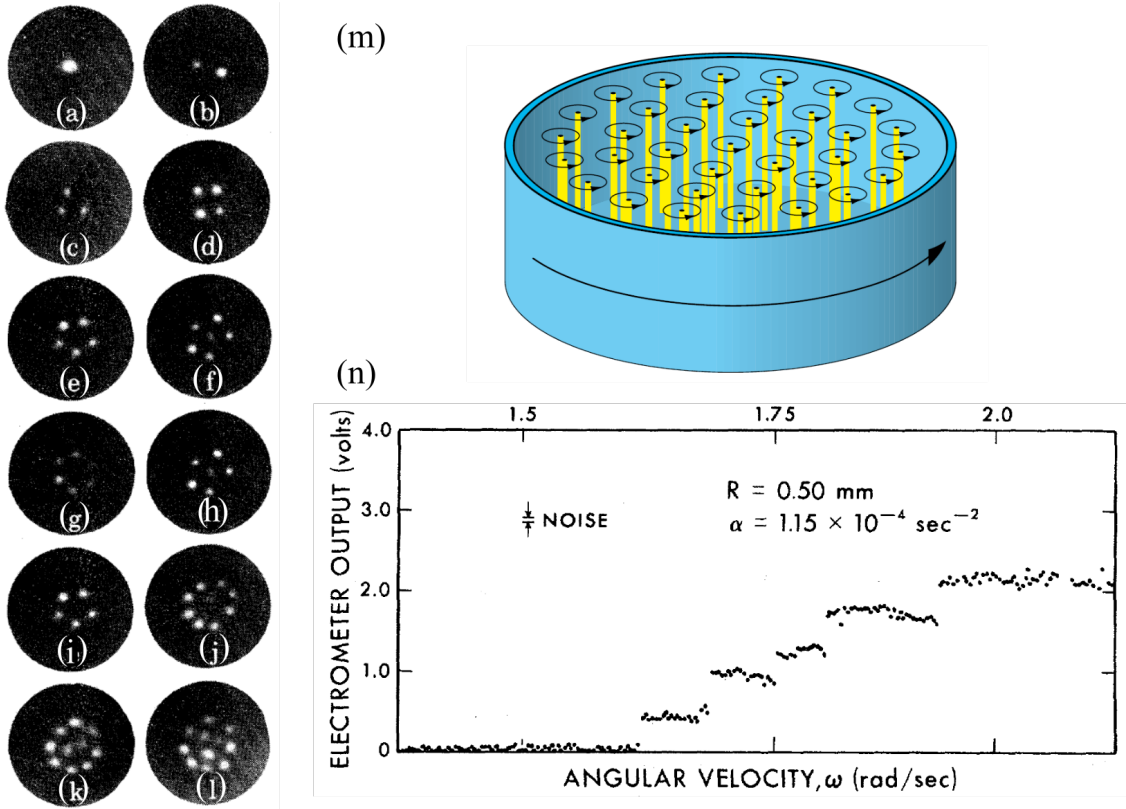


Figure 7-1: (a-l) The photographs of the vortex arrays in the rotating superfluid He II obtained by imaging of the trapped ions. The angular velocities were (a) $0.80S^{-1}$, (b) $0.80s^{-1}$, (c) $0.40s^{-1}$ i, (d) $0.87s^{-1}$, (e) $0.45s^{-1}$ i, (f) $0.47s^{-1}$, (g) $0.47s^{-1}$, (h) $0.45s^{-1}$, (i) $0.86s^{-1}$, (j) $0.55s^{-1}$, (k) $0.58s^{-1}$, and (l) $0.59s^{-1}$. Panels (a-l) are reprinted with permission from [44]. Copyright 1979 by the American Physical Society. (m) Adopted from [181] and shows the schematic of the "rotating bucket" experiment with the superfluid, the yellow lines represent the vortex lines, and the black arrows depict the direction of the reservoir rotation and the vortices circulation. Reprinted panel (n) with permission from [182]. Copyright 1972 by the American Physical Society. The step-like vortex number dependence (measured as an electrometer output) on the angular velocity. R and α correspond to the vessel size and angular acceleration, respectively.

(BEC). The numerous ways of vortex generation were developed there, including direct imprinting [101] and condensate rotation [41]. Similarly to the superfluids, the condensates in the rotating reservoir demonstrated the quantization of angular momentum and growth of vortex number with increasing rotation speed [41]. The stirring of the condensate was performed by the magnetic field [183], optical field [42] or the interplay between spin components of the condensate [184]. The stirring of the laser profile around the BEC (see Figure 7-2 (a)) was shown to result in a vortex nucleation inside the BEC [184]. Below the critical stirring frequency, K.W. Madison and co-authors [184] did not observe the vortex in the condensate (see Figure 7-2(b)). While increasing the rotation higher than 150 Hz, they observed one and then multiple vortices depicted in Figures 7-2(b-g). Interestingly, by increasing the stirring frequency even more, scientists revealed the turbulent condensate pattern followed by the complete depletion of the condensate. Due to the instability of the condensate, they were not able to measure the step-like vortex number frequency dependence. However, theoretically, it is shown that the frequency dependence [185] is qualitatively similar to that of the superfluid Helium (see Figure 7-2(h)). Due to the properties of the BEC, the rotations speed required for the vortex generation is on the order of hundred Hertz, [41], which can be relatively easily realized in the experiment, for example, by the deflection of the stirring laser beam with acousto-optic modulator [184].

Overall, the "rotating bucket" experiment is a classical experiment carried out with the superfluids. In the scope of this thesis, we wanted to recreate the same experiment with polariton condensate. Being the non-equilibrium systems, polariton condensates, though, share a lot of similarities with the material systems described above (superfluids and atomic BEC). Namely,

1. As it was described in Chapter 2, under certain pumping conditions **polaritons are shown to be a superfluid**.
2. In essence, **polariton condensates are Bose-condensates** and have numerous similarities with atomic BECs.
3. Many experimental and theoretical works have demonstrated that polariton

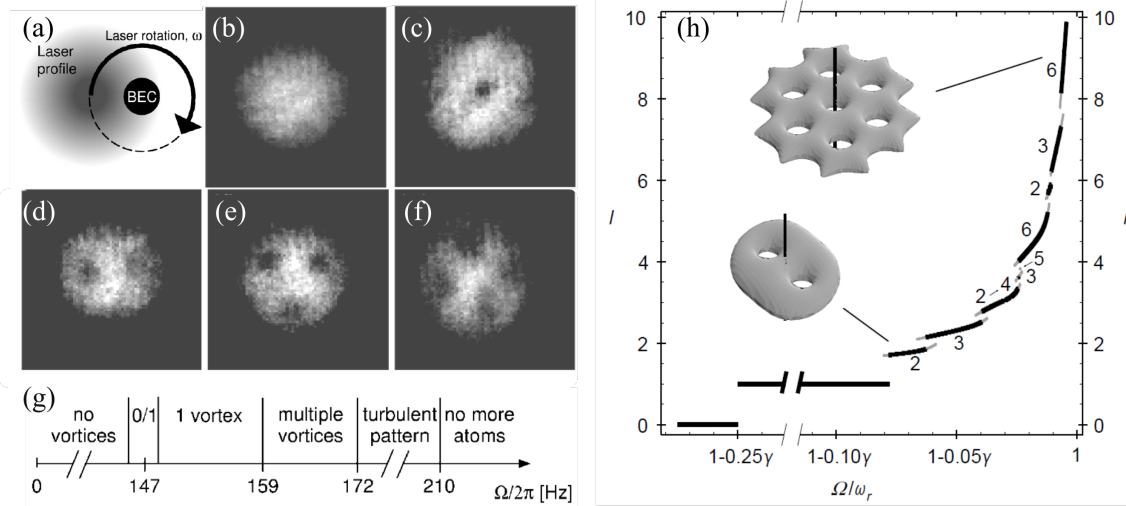


Figure 7-2: (a) The schematic of the vortex generation in BEC setup with stirring laser. The image is reprinted with permission from [101]. Copyright 2011 by the American Physical Society. The panels (b-g) are reprinted with permission from [184]. Copyright 1999 by the American Physical Society. The images of the BEC stirred with the laser beam at (b) 145 Hz, (c) 152 Hz, (d) 169 Hz, (e) 163 Hz, (f) 168 Hz. The black regions in the condensate bulk in (b-f) correspond to vortices. (g) Different regimes of the condensate depending on the rotation frequency. The panel (h) is adopted from [185] and reproduced with permission from Springer Nature. Panel (h) shows the angular momentum per particle l of the rotating condensate versus the angular velocity of stirring. The 3D insets correspond to condensate density distribution.

condensates **can have vortices** (see Chapter 2).

Thus, realising the "rotating bucket" experiment should be feasible for polaritons. However, it has not been implemented experimentally to date, with the scarce theoretical investigations, for instance, Ref. [186]. This is due to short typical polariton timescales (picosecond lifetime and nanosecond coherence time). So, exceptionally high (at least GHz) rotation speed, which is challenging to implement with the existing experimental techniques, is required in order to influence the polariton state. In this thesis, this hurdle is overcome, and stirring of the polariton condensate was realised. The details are described below.

7.2 Experimental setup

To implement the "rotating bucket" for polaritons, we utilise the same experimental setup described in Section 6.2. Figure 7-3 schematically depicts the excitation part of the setup. Similarly to the previous experiment, we apply the perfect vortex mask [122] on both of the SLMs. Both applied masks are identical except for the charge of the vortex imprinted. So we either have optical angular momentum 1 on the SLM_1 and -1 on the SLM_2 or vice versa (see Figure 7-3). For this experiment, the intensities of two excitation lasers are equal in order to create non-uniform exciton reservoir, which will induce the torque to the condensate at high frequencies. The resulting optical patterns from both SLMs are overlapped on the beamsplitter, and their dumbbell-shaped beating pattern rotates with the frequency described in the previous Chapter in Equation (6.1). The photon-exciton detuning is -3.2 meV, and the other details of the experimental setup configuration are described in Chapter 3.

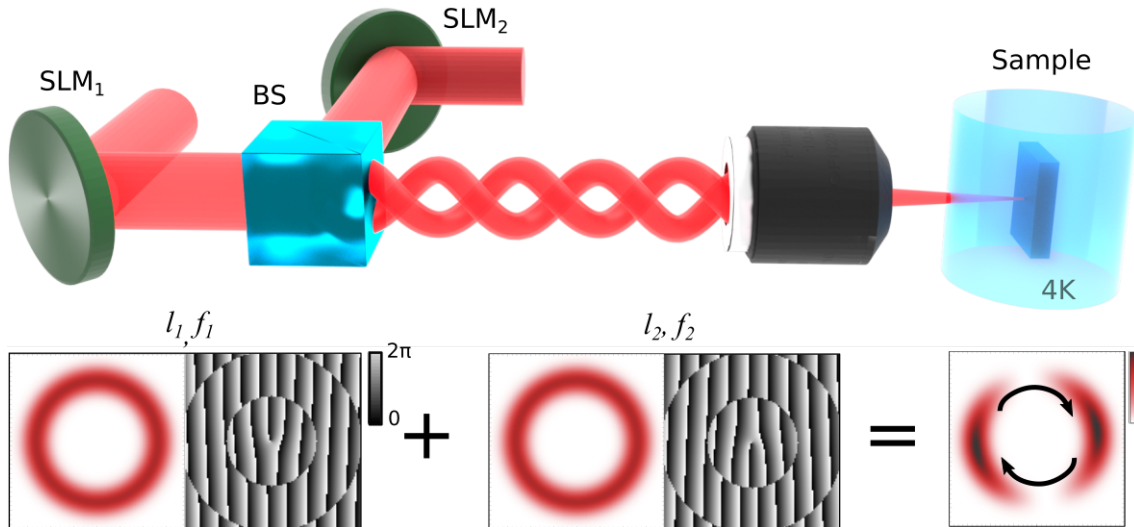


Figure 7-3: The excitation part of the experimental setup. The beating of two modified with the SLMs and frequency-detuned lasers forms the rotating in-time laser pattern utilised as the confining and stirring potential for polaritons. The red-scaled images show the excitation lasers' profiles, and the grayscale images are SLM masks for corresponding pattern generation. The figure is adopted from [3]

The rotating nonresonant laser pattern is projected on the sample and has a diameter of $14 \mu\text{m}$. It acts as a "rotating bucket" for the polaritons, confining and stirring condensate simultaneously. The non-uniform intensity of the laser pattern creates an asymmetric optical trap for polaritons. The asymmetry acts as rough

walls of the reservoir and allows applying the torque to the polariton condensate and stirring it. Nonresonant optical trap [27] feeds the condensate and decreases the overlap of the condensate with the reservoir, minimizing their interaction and increasing the condensate coherence time.

7.3 Vortex observation

The condensate should "feel" the rotation of the trap, so the stirring should be of the order of its coherence time (less than 1 ns for our system [80]). This means that GHz pump rotation frequencies can cover several periods within the coherence time of the condensate, which can result in a deterministic vortex formation of definite OAM. So, we are seeking the vortices appearance in the rotation range of 1 GHz and higher. We set the lasers frequency difference Δf to 4.6GHz and $(l_1, l_2) = (1, -1)$, and pumping power to $P = 1.1P_{\text{th}}$. The laser excitation pattern is thus rotating counterclockwise with $f = 2.3\text{GHz}$. Polaritons condense, and we observe annular condensate intensity distribution with zero intensity in the middle Figure 7-4(a)). Detecting the dispersion of the condensate PL, we find that condensate occupies a single energy state (see Figure 7-4 (b)) corresponding to the first excited mode of the confining potential [28].

To find out if the condensate is in the vortex state, we perform the homodyne interferometry (see Section 3.3.3), overlapping the condensate emission with the reference plane wave laser. The interference pattern depicted in Figure 7-4(c) reveals the fork dislocation, implying the winding of the condensate phase. Reconstructing the phase by the off-axis digital holography (see Section 3.3.4), we retrieve the phase pattern presented in Figure 7-4(d). The phase of the condensate wave function possesses a singularity in the centre corresponding to the minimum intensity distribution. The phase circulates about the singularity, changing linearly from 0 to 2π in a counterclockwise direction corresponding to the quantised vortex with topological charge $l = 1$. Thus, the phase winding of the condensate is co-directed with the rotation direction of the pump, as well as polaritons in the condensate co-rotate with the optical trap.

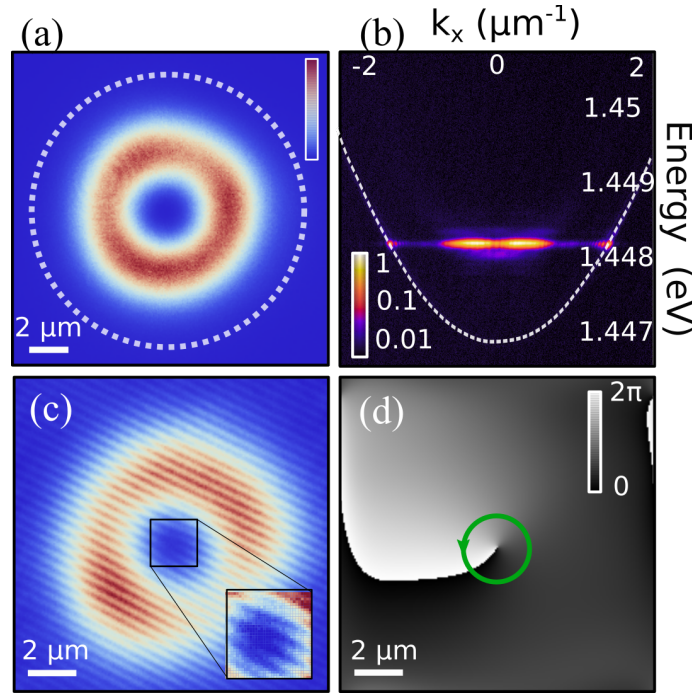


Figure 7-4: (a) Spatial profile (normalised) of the polariton condensate in rotating trap $f=2.3\text{GHz}$ (Δf is 4.6GHz and $(l_1, l_2) = (1, -1)$). The white dashed line represents the circumference of the optical trap. (b) Corresponding normalised dispersion of the condensate emission (in logarithmic colour scale). (c) Interference pattern of the condensate with the plane reference wave revealing the fork-like fringe dislocation (enlarged). (d) Retrieved phase distribution demonstrating phase dislocation and phase winding from 0 to 2π . The scale bar for Figure (c) is depicted in (a). The Figure is adopted from [3].

We note that for the trap with the same diameter but without the rotation (using just one excitation laser) depicted in Figure 7-5(a), we do not observe the formation of the vortex in the condensate. Instead, a dipole or ground state is formed depending on the pump power (see Figure 7-5 (b-d)). This means that we **do not** imprint [89] any OAM to the condensate and the vorticity observed for the rotating trap is dictated by the "mechanical" stirring of the condensate with the laser pattern.

The direction of the trap rotation is governed by the excitation lasers profiles. Namely, following the equation (6.1) it is worth noting that stirring can be inverted by swapping the angular momenta on the SLMs or by changing the frequency detuning sign Δf . To test this relation, we measure the condensate phase for different possible configurations of Δf and Δl . The results are summarised in Figure 7-6, where

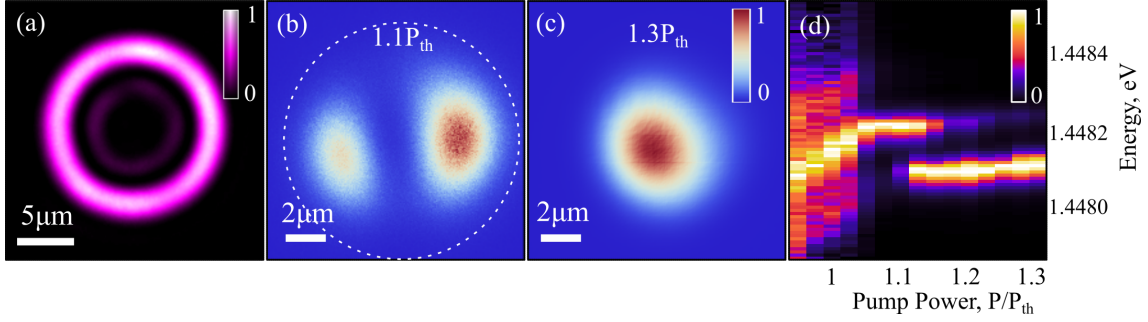


Figure 7-5: (a) Experimental pump profile of one of the excitation lasers. The condensate PL in the stationary optical trap (a) with $14 \mu\text{m}$ diameter at a pump power of (b) $1.1P_{\text{th}}$ and (c) $1.3P_{\text{th}}$. (d) Corresponding energy resolved excitation power dependence of the condensate PL, showing an eventual departure from the excited state into the trap ground state. The white dashed line in (b) schematically depicts the annulus of the laser pump profile.

we show the condensate phase for 4 different cases. The phase profiles presented in Figures 7-6(a,b) correspond to $\Delta l = 2$ and (c,d) to $\Delta l = -2$. Figures 7-6(a,c) shows the positive laser frequency detuning $\Delta f = 4.6 \text{ GHz}$ and Figures 7-6(b,d) depict the negative one $\Delta f = -3.7 \text{ GHz}$. The corresponding four scenarios all result in a polariton fluid co-rotating with the pump pattern with a nearly constant angular phase gradient around the phase singularities (see circular line profiles of the phase in lower panels). So that for the same experimental conditions (pumping power, trap size, etc.), at the same spot on the sample, we can deterministically achieve the condensation in the vortex (Figures 7-6(a,d)) and anti-vortex (Figures 7-6(b,c)) states only by controlling the trap rotation direction.

The repulsive interaction between the "dumbbell" exciton reservoir and polaritons leads to the steady polariton flow when the trap rotates, forming the vortex state with a topological charge dictated by the direction of the stirring.

7.4 Frequency dependence

The frequency dependence of the vortex appearance is an important part of the "rotating bucket" experiment. Analogously to the superfluids [43] and BECs [42] vortex in the polariton condensate appears only above some critical rotation frequency. Setting OAMs of two excitation lasers to have $l_1 = 1$, $l_2 = -1$ and varying their frequency

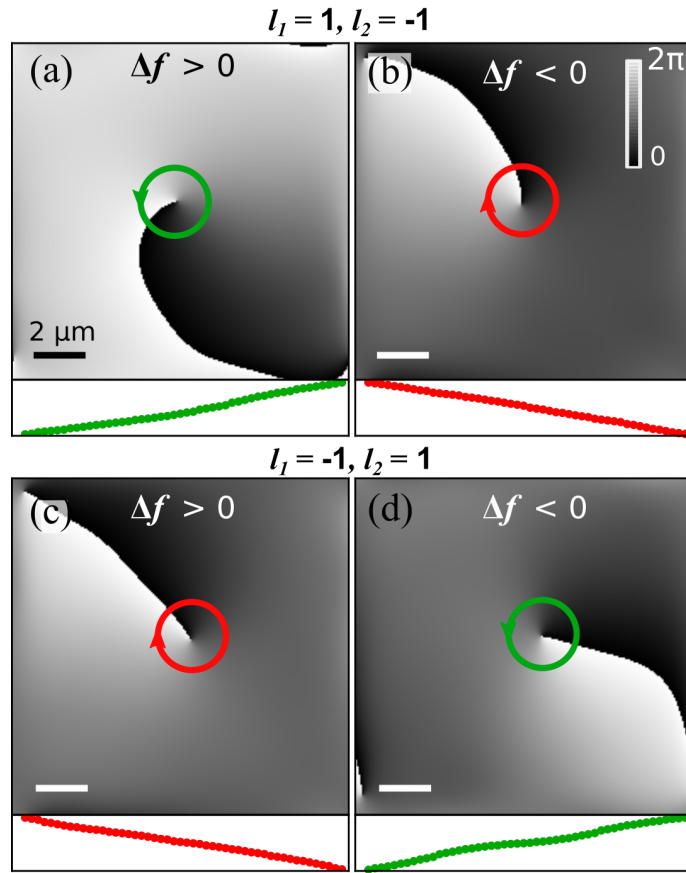


Figure 7-6: Condensate phase distribution for $l_1 = 1$, $l_2 = -1$ of the first and the second excitation lasers respectively and (a) $\Delta f = f_1 - f_2 > 0 = 4.6$ GHz and (b) $\Delta f < 0 = -3.7$ GHz. Rel-space phase of the condensate for $l_1 = -1$, $l_2 = 1$ and (c) $\Delta f = f_1 - f_2 > 0 = 4.6$ GHz and (d) $\Delta f < 0 = -3.7$ GHz. The red and green insets in each panel depict the corresponding circular phase profile taken along the circle with $2.6 \mu\text{m}$ around the phase dislocation. The figure is adopted from [3].

detuning, we find that the vortex appears for the stirring frequencies f above 1 GHz for both clockwise and anticlockwise directions. Below that frequency, the condensate experiences adiabatic rotation of the trap since the rotation period is much bigger than the characteristic timescales of the condensate (coherence time and polariton lifetime). In this case, the condensate is poorly confined. Some part of the condensate under slow rotation forms directly on the pump ring, and some part is inside the trap. The condensate intensity distribution for $f = 50$ MHz is shown in Figure 7-7(a). Note that the uniform level of the condensate population across the trap corresponds to polaritons leaking from the trap. This is additionally confirmed by the high momenta and energy occupied by the condensate (see PL dispersion in

Figure 7-7(b)). In contrast, at $f = 2.5$ GHz, condensate occupies the vortex state at the first excited level of the trap (see Figure 7-7(c,d)). When the rotation velocity is increased even higher to 10 GHz, the vortex disappears, and condensate occupies the Gaussian ground state of the optical trap (see Figure 7-7(e,f)).

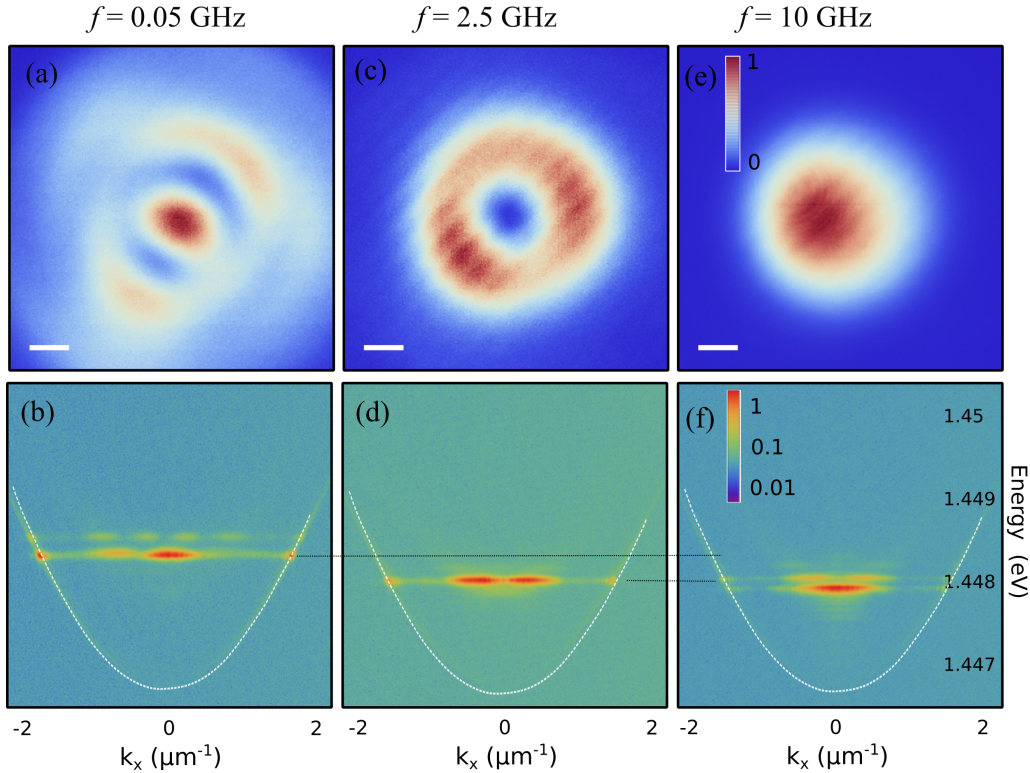


Figure 7-7: Time-integrated condensate intensity profiles (a,c,e) and dispersion (b,d,f), when externally stirred at $f = 0.05$, 2.5 and 10 GHz respectively. The white scale bar in (a-c) corresponds to $2\mu\text{m}$. The white dashed lines in panels (b-f) depict the lower polariton branch dispersion. The black dashed line is to guide the eye and compare the energy of the condensate at different rotations.

For retrieving the frequency dependence, we interfere the condensate PL with itself (displaced and retro-reflected); this method is described in Section 3.3.3. The examples of two studied interference patterns are presented in Figures 7-8 (a-b). Panel (a) corresponds to the $f = -2.5$ GHz; the direct condensate intensity distribution is circled with the green dashed circle while its retro-reflected copy is highlighted with the purple one. Figures 7-8(c-g) depict the condensate phase distributions for different rotation frequencies and corresponding unwrapped phases (black dots) around the dislocation. The red solid line corresponds to the phase distribution of the ideal vortex and depicts the linear phase gradient going from 2π to

zero. Note there the difference between the unwrapped experimental phases and the "ideal" ones. This difference appears due to various reasons. First, overlapping the condensate to itself leads to the interference of two non-flat phase fronts, resulting in phase scrambling. Second, the condensate can simultaneously occupy neighbouring energy states (ground and excited states of the trap), leading to a mixture of phases corresponding to specific energy states. Finally, condensate may not possess the angular momentum and can occupy the ground or dipole state of the optical trap.

To characterise the behaviour of the condensate under different rotation frequencies, we investigated the condensate phase for each 10 μs excitation realisations (single-shots) when it interfered with itself. For each studied rotation frequency and fixed total pump power, we measure 100 interference shots and calculate the number of vortices in this set. In order to take into account different possible phase configurations in the condensate and correctly identify vortices in a big set of experimental data (more than 2000 realisations of the condensate in total), we develop a vortex sorting algorithm. This algorithm consists of the following steps:

1. For each 10 μs shot, we retrieve the phase distribution with the off-axis digital holography.
2. We approximately identify the position of the phase dislocation and retrieve the circular phase profile with $2.6\mu\text{m}$ diameter around it (see black dots in Figures 7-8(c-g)).
3. We transform the phase profile so there is no 2π phase jumps when it goes from the beginning to the end of the profile.
4. We calculate the normalised root mean square error (NRMSE) of the experimental phase profile curve and the theoretical ideal one (solid red lines in Figure 7-8(c-g)). The NRMSE is given by

$$NMRSE = \sqrt{\frac{1}{4} \frac{1}{N} \sum_{n=1}^N [(\cos(\theta_n) - \cos(\theta_{ideal,n}))^2 + (\sin(\theta_n) - \sin(\theta_{ideal,n}))^2]} \quad (7.3)$$

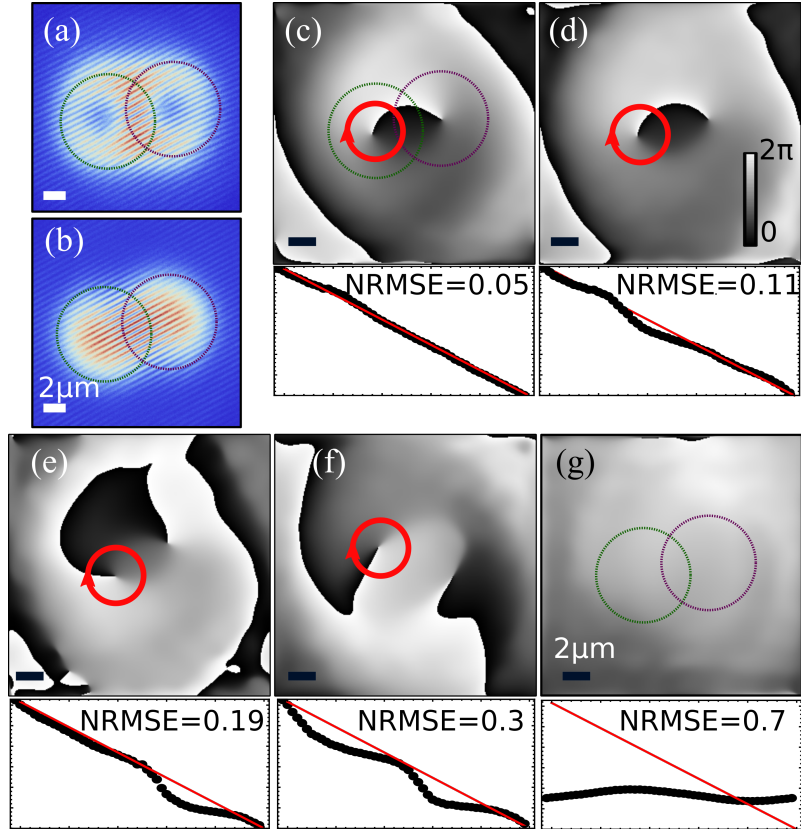


Figure 7-8: Condensate emission (green ring) interfered with the retro-reflected and displaced copy of itself (purple ring) at $f = -2.5$ GHz (a) and $f = -8.2$ GHz (b). The green and purple dashed circles in (a-c) schematically depict the contour of the condensate for direct and retro-reflected copy, respectively. (c-g) Examples of the condensate phase distribution for different realisations with a $10 \mu\text{s}$ excitation pulse width. The bottom panels of (c-g) represent the annular line profile with a $2.6 \mu\text{m}$ diameter around each phase singularity unwound starting from the black-white colour dislocation and compared to the phase profile of a perfect antivortex (red line). In panels ((c) and (d)) $f = -1.5$ GHz, and in ((e) and (f)) $f = -3.8$ GHz, and in (g) $f = -8.2$ GHz. The figure is adopted from [3].

where $\theta_n, \theta_{ideal,n}$ are the corresponding values of the experimental and ideal vortex profiles, respectively. N is the number of points in the experimental unwrapped phase profile, $N = 50$. NRMSE can have values from 0 to 1, with 0 corresponding to the ideal phase profile and 1 to the vortex of different winding.

5. We find that the value of NRMSE strongly depends on the centre position of the circular phase profile. In order to eliminate this dependence, we scan the position of the profile centre and retrieve the set of NRMSE values for the

given phase distribution. Namely, we scan the centre position in the square with the side of $2.6 \mu\text{m}$ corresponding to the 40 by 40 pixels square around the initially chosen profile position. Then, steps 1 - 4 are repeated for each new profile centre position and retrieve an array of 1600 values of NRMSE for the given phase shot.

6. We choose the minimal value over the 1600 NRMSE received at the previous step.
7. We repeat steps 1-6 for the other 99 phase distribution shots for each rotation frequency (100 shots of the phase distribution for each rotation frequency in total).
8. Further, we consider having a vortex (antivortex) only for those shots when the calculated NRMSE value is smaller or equal to 0.2. See, for example, Figure 7-8(e) for typical phase distribution with the extracted value of NRMSE = 0.19 close to the threshold error value. The number of shots fitting this condition allows us to consider the probability of the vortex appearance for different rotation frequencies.
9. The previous steps are performed for every studied stirring frequency and corresponding 100 condensate realisations. The results are then summarised in Figure 7-9. Note that we also multiply the number of vortices in the set by its topological charge in order to make results more vivid.

The vortex appears in the condensate for stirring frequencies from 1 to 4 GHz (see the blue graph in Figure 7-9), so the critical frequency of the vortex formation in the "rotating bucket" experiment with polariton condensate is 1 GHz (for $14\mu\text{m}$ optical trap). Remarkably, the probability of finding the vortex in the condensate at the middle of the range (approximately at 2.5 GHz) is close to 1 for both stirring directions. That allows us to observe the vortex even when condensate PL is integrated over thousands of condensate realisations and underlines the robustness of the developed vortex generation technique.

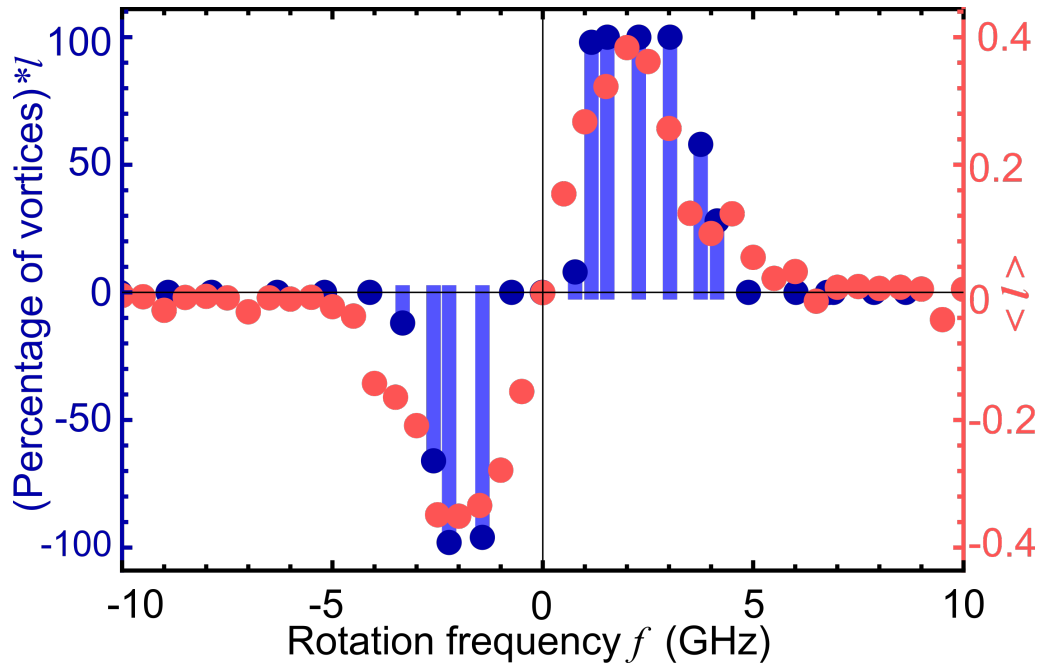


Figure 7-9: Blue points: the number of condensate realisations with vortex out of 100 for each rotation frequency f multiplied by the corresponding topological charge of the vortex $l = \pm 1$. Red points: average angular momentum $\langle l \rangle$ of the condensate over 40 simulation runs. The figure is adopted from [3].

The flipping of the vortex charge with the rotation frequency discussed in Figure 7-6 is also evident in Figure 7-9. For small rotation frequencies, $f \in [-1, 1]$ GHz, due to the finite exciton recombination time, the exciton reservoir induced by the dumbbell-shaped excitation pattern is not sufficiently populated to build a confining repulsive potential for a quantum vortex to form. On the other hand, for big rotation frequencies, $|f|$ higher than 4 GHz, the asymmetry of the exciton reservoir is smeared out, resulting in a cylindrical symmetric trapping potential that does not exert sufficient torque to the condensate for inducing the formation of a quantum vortex state. In other words, the rotation is so fast that the reservoir perturbation does not decay fully for the one rotation period and condensate experiences the uniform trapping potential without any rotation and forms in the ground state of the trap. To understand the physics of the condensate in the rotating trap in more detail, the numerical simulation of the system with the Gross-Pitaevskii equation were performed.

7.5 Numerical simulation of 2D Gross-Pitaevskii equation.

This simulation was carried out by Dr Helgi Sigurdsson from the University of Iceland and Dr Stella Harrison from Southampton University.

The polariton system in the rotating potential is modelled with the generalised Gross-Pitaevskii equation coupled to active and inactive exciton reservoirs $n_{A,I}(\mathbf{r}, t)$ [133]. The polariton condensate is described by macroscopic two-dimensional wave function $\Psi(\mathbf{r}, t)$. The active reservoir excitons undergo bosonic scattering into the condensate, whereas the inactive reservoir excitons does not scatter into it but feed the active reservoir:

$$i\hbar \frac{\partial \Psi}{\partial t} = \left[-\frac{\hbar^2 \nabla^2}{2m} + G(n_A + n_I) + \alpha |\Psi|^2 + \frac{i\hbar}{2}(Rn_A - \gamma) \right] \Psi \quad (7.4)$$

$$\frac{\partial n_A}{\partial t} = -(\Gamma_A + R|\Psi|^2)n_A + Wn_I \quad (7.5)$$

$$\frac{\partial n_I}{\partial t} = -(\Gamma_I + W)n_I + P(\mathbf{r}, t). \quad (7.6)$$

Here, m is the effective polariton mass, $G = 2g|X|^2$ and $\alpha = g|X|^4$ are the polariton-reservoir and polariton-polariton interactions strengths, respectively, where g is the exciton-exciton dipole interaction strength and $|X|^2$ is the exciton Hopfield coefficient. R is the rate of stimulated scattering of polaritons into the condensate from the active reservoir, γ is the polariton decay rate, $\Gamma_{A,I}$ are the active and inactive reservoir exciton decay rates, W is the inactive to active reservoir exciton conversion rate, and $P(\mathbf{r}, t)$ describes the nonresonant rotating pumping profile described as follows:

$$\begin{aligned} P(\mathbf{r}, t) &= \mathcal{P}(r) |e^{i(l_1\theta - \omega_1 t)} + e^{i(l_2\theta - \omega_2 t)}|^2 \\ &= 4\mathcal{P}(r) \cos^2 \left[\frac{(l_1 - l_2)\theta}{2} - \frac{(\omega_1 - \omega_2)t}{2} \right], \end{aligned} \quad (7.7)$$

where $\mathcal{P}(r)$ is the annular intensity profile.

As it was described above, the shape of the exciton reservoir induced potential changes with the rotation frequency, thus affecting the condensate and vortex appearance. To check this, the solution of the Equation 7.6 should be found. It reads as follows:

$$n_I(\mathbf{r}, t) = e^{-(W+\Gamma_I)t} [4\mathcal{P}(r)I(\theta, t) + n_I(\mathbf{r}, 0)] \quad (7.8)$$

where

$$I(\theta, t) = e^{(W+\Gamma_I)\tau} \frac{(W + \Gamma_I) \cos^2(\bar{\theta} - \bar{\omega}\tau) - \bar{\omega} \sin[2(\bar{\theta} - \bar{\omega}\tau)] + \frac{2\bar{\omega}^2}{W+\Gamma_I}}{(W + \Gamma_I)^2 + 4\bar{\omega}^2} \Big|_0^t. \quad (7.9)$$

Here, $\bar{\theta} = (l_1 - l_2)\theta/2$, and $\bar{\omega} = (\omega_1 - \omega_2)/2$.

Thus, in the limit of the slowly rotating trap ($\bar{\omega} - > 0$), we get

$$n_I(\mathbf{r}, t) \Big|_{W+\Gamma_I \gg f} \approx \frac{P(\mathbf{r}, t)}{W + \Gamma_I}. \quad (7.10)$$

So, the inactive exciton reservoir's shape follows the pump's shape. The same argument can be applied to the active reservoir $n_A(\mathbf{r}, t)$ assuming that nonlinear effects are weak and that the decay rate Γ_A of the active reservoir is fast, i.e. $\Gamma_A \gg f', R|\Psi|^2$; then it will also adiabatically follow the dynamics of the inactive reservoir,

$$n_A(\mathbf{r}, t) \Big|_{\Gamma_A \gg f} \approx \frac{W n_I(\mathbf{r}, t)}{\Gamma_A} = \frac{P(\mathbf{r}, t)}{\Gamma_A(1 + \Gamma_I/W)}. \quad (7.11)$$

On the other hand, in the case of very fast rotation, the effective shape of the reservoirs is changing. This corresponds to $W + \Gamma_I \ll f$, an inactive reservoir then becomes cylindrically symmetric and time-independent and does not induce any torque to the condensate.

$$n_I(\mathbf{r}) \Big|_{W+\Gamma_I \ll f} \approx 2\mathcal{P}(r)/(W + \Gamma_I) \quad (7.12)$$

The same applies to the active reservoir.

To sum up, the estimate of the exciton reservoir shape confirms our hypothesis

on its effect on the vortex formation in the condensate under rotation.

The Equations (7.4)-(7.5) are solved numerically. The parameters used in the simulation are inherent to the sample [55]. Namely, $m = 5.3 \times 10^{-5}m_0$ where m_0 is the electron mass, $\gamma = \frac{1}{5.5} \text{ ps}^{-1}$, $g = 1 \mu\text{eV } \mu\text{m}^2$, and $|X|^2 = 0.35$. The remaining parameters are enumerated through fitting to experimental data, giving $R = 0.01 \text{ ps}^{-1}$, and $W = 0.05 \text{ ps}^{-1}$. The $P(\mathbf{r}, t)$ term is similar to the experimental one.

Given these parameters, the annular distribution of the condensate intensity and a phase winding co-directed with the pump rotation are reproduced (see Figure 7-10).

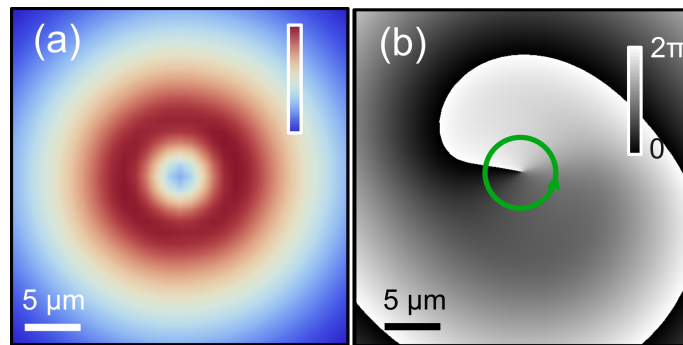


Figure 7-10: Simulated time integrated real-space intensity (a) and instantaneous phase (b) of the condensate at $f = 2 \text{ GHz}$ demonstrating the formation of the quantised vortex after 800 ps of numerical integration. The figure is adopted from [3].

Moreover, the numerical solution of the Gross-Pitaevskii equation (7.4)-(7.5) gives an insight into the exciton reservoir shape at different rotation frequencies. So the snapshots of the exciton reservoir at different stirring retrieved numerically are depicted in Figure 7-11. It is evident from the reservoir snapshots obtained by the simulation that the active reservoir follows the shape of the rotating excitation laser pattern for low frequency (see reservoir distribution at 0 GHz). Increasing the frequency of rotation to 5 GHz, the smearing of the exciton reservoir is observed; the reservoir's shape now favors the confinement of condensate in the vortex state while still inducing the torque to the condensate, making it adopt external rotation.

As it was estimated above, for the higher rotations, the shape of the active reservoir is completely uniform; the numerical results are presented in Figure 7-11

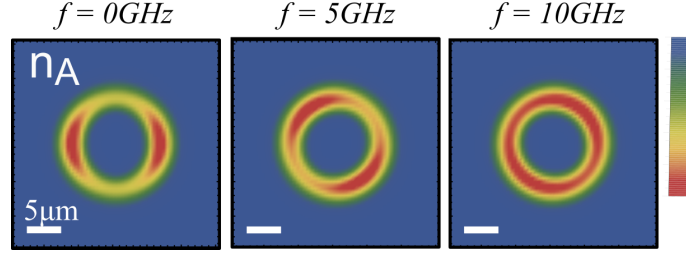


Figure 7-11: The active reservoir distribution snapshots for 0 GHz, 5GHz, and 10 GHz rotation frequency.

for 10 GHz rotation. Such an effective trap for the condensate does not rotate; thus, the vortex in the condensate disappears at higher frequencies.

Moreover, simulations allowed us to directly retrieve the value of the angular momentum acquired by the condensate in the rotating trap. For each rotation frequency in the range from minus to plus 10 GHz, f' , 40 unique realisations of the condensate are calculated, each starting with different random initial conditions. Further, they are integrated in time until they converge to a final state. The expectation value of the OAM in the condensate plotted in Figure 7-9 with red dots is written,

$$\langle l \rangle = \frac{1}{\hbar} \frac{\langle \Psi | \hat{L}_z | \Psi \rangle}{\langle \Psi | \Psi \rangle} \quad (7.13)$$

where \hat{L}_z is the angular momentum operator. Note that the simulated values of the averaged orbital angular momentum qualitatively reproduce the experimental data.

7.6 Why the second vortex does not appear?

So far, we have demonstrated the appearance of the vortex in the condensate above 1 GHz critical rotation frequency and also explained its disappearance at a higher rotation frequency. But why the second vortex does not appear in our system as it does for the superfluids and atomic BEC? We perform a series of excitation power scans to shed light on this question. Namely, we do energy-resolved pump power scans. For this measurement, we detect the condensate PL dispersion, integrate it over the wavevectors, and then stick together the resulting graphs for different pump

power. The results are depicted in Figure 7-12(a-c). Note that below the threshold, polaritons are broadly distributed across several energy branches. As soon as the threshold is achieved, bosonic stimulation occurs, and polaritons populate a specific energy state with clear spectral narrowing and intensity increase.

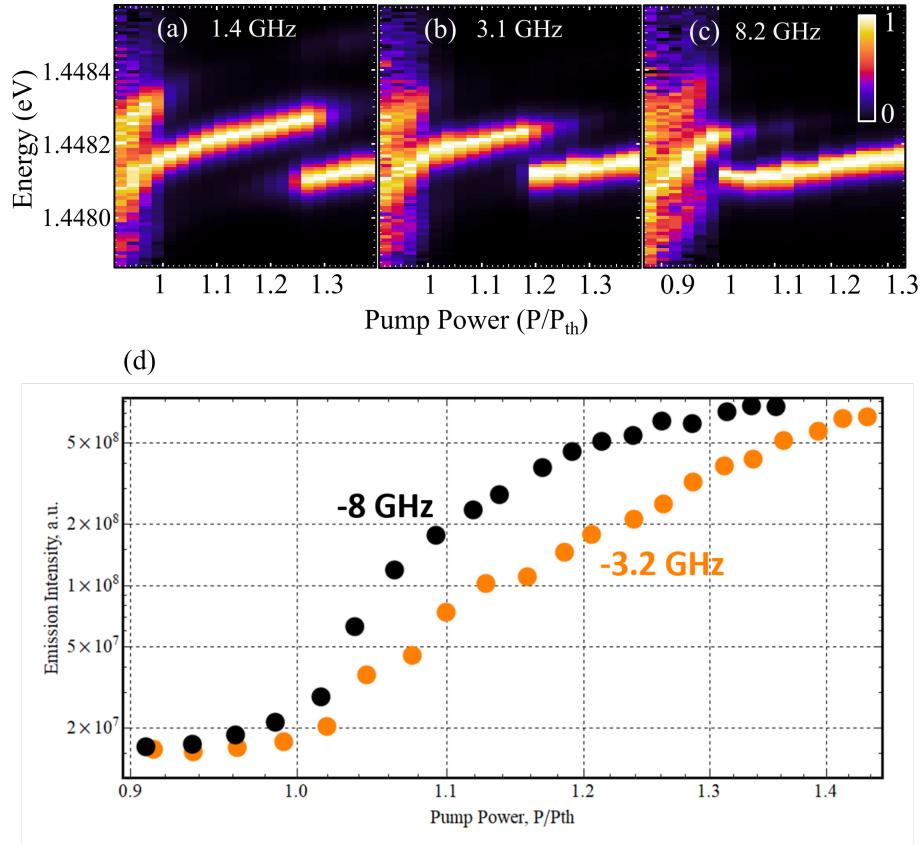


Figure 7-12: Condensate energy spectrum pump power dependence for (a) $f = 1.4$ GHz (b) 3.1 GHz, (c) 8.2 GHz. (d) Intensity power dependence for two values of rotation frequencies demonstrating the different non-linear growth of condensate emission in intensity.

When scanning the pump power, we observe a transition from the excited branch (corresponding to the first excited state of the trap) to a lower energy branch, implying that the condensate vortex eventually destabilises and collapses into the ground state for higher powers and higher rotation frequencies. This dynamics is generally inherent to our sample and was reported in [187]. For $f = 1.4$ GHz above the condensation threshold, the condensate is formed in the first excited state of the trap and contains a vortex (see Figure 7-12 (a)). However, when the power is increased to $1.25P_{th}$, condensate falls to the ground state (with the lower energy)

and does not have the phase singularity inside. The effective potential confining the polaritons changes with the rotation frequency as we described above, leading to the redistribution of condensate energy levels. So that when the trap is rotated faster, the ground state appears earlier at pumping power, and for $f = 3.1$ GHz, the ground state is formed already at $1.2P_{th}$ (see Figure 7-12 (b)). On the contrary, for the $f = 8.2$ GHz depicted in Figure 7-12 (e), the condensate falls to the ground state immediately above the condensation threshold. These findings support the disappearance of the vortex at high rotation frequencies presented above.

For the $14\mu m$ trap, we do not observe the increasing number of vortices in the condensate for bigger rotation frequencies. As shown, the trap configuration and system response at the higher stirring rates do not sustain the first excited state and, consequently, the vortex. The ground state can not support a stable vortex solution due to the minimal required vortex size or healing length. For the same reason, the condensate populating the first excited state could not sustain more than one vortex inside.

7.7 Pump power dependence of the condensate emission

Additionally, we investigate the intensity of the condensate emission versus pump power for different rotation speeds. First, we find that the condensation threshold changes when we alter the rotation frequency. Interestingly, it increases for higher rotation frequencies. The smearing of the exciton reservoir at high rotation frequencies makes the effective area of the exciton reservoir bigger and, ergo, requires higher pump power in order to achieve the critical concentration of polaritons for condensation. On the other hand, for the slow rotations, the critical concentration is achieved within a period of the rotation and effectively acts as a static potential for polaritons.

As we have described above, the higher rotation speed makes the exciton reservoir more uniform, and thus, polaritons are more confined in the optical trap. This leads to a decrease in the polariton leakage from the cavity and, as a result, a larger

concentration of polaritons in the condensate. It is evident from the intensity power dependence curve obtained for two rotation frequencies $f = -3.2$ GHz and -8 GHz depicted in Figure 7-12 (d). Note the sharper non-linear increase of the PL intensity at -8 GHz, indicating the smaller number of losses in this system compared to the slower rotation. To sum up, by altering the stirring frequency, we can engineer the properties of the polariton condensate, namely its emission intensity, energy and phase.

7.8 Bigger rotating traps

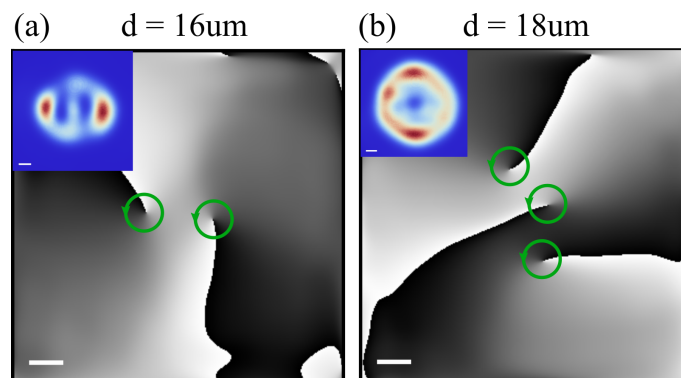


Figure 7-13: (a) The phase profile of the condensate in the rotating trap with $16 \mu\text{m}$ diameter d at $f = 3$ GHz demonstrating two co-rotating vortices in the condensate. (b) The phase profile of the condensate in the rotating trap with $17.5 \mu\text{m}$ diameter d at $f = 3$ GHz demonstrating 3 vortices. The insets in (a) and (b) represent the real-space condensate intensity distribution. The white scale bar corresponds to $2 \mu\text{m}$.

The optical trap of a larger diameter can host a bigger number of states [28]. We increase the diameter of the rotating trap to $d = 15.4 \mu\text{m}$. The condensate now can occupy the trap's second excited state; as a result, we observe two vortices in the condensate for $f = 3$ GHz. As it was for the smaller trap, vortices, in this case, also co-rotate with the rotating potential and appear in the finite range of the stirring frequencies. Increasing the pump ring diameter even further to $17.5 \mu\text{m}$, we observe the state with 3 vortices with the same OAM. However, the energy structure of the condensate at a larger trap size is complicated by the fine energy splitting reported in [7]. This splitting is on the order of the stirring frequency and can

affect the state of the condensate in the rotating trap. However, the investigation of the bigger rotating trap is ongoing in our lab and out of the scope of this thesis. Nevertheless, the possibility of on-demand generation of the co-rotating clusters of vortices is exciting both from the fundamental and application point of view.

7.9 Conclusions

All in all, we have demonstrated an analogue of the "rotating bucket" experiment for exciton-polariton condensates under a nonresonant time-periodic drive. The "rotating bucket" experiment has previously been demonstrated as a means to generate quantised vorticity in superfluids [188] and ultra-cold atoms [41, 42, 189, 190], but its investigation for nonequilibrium quantum fluids has lacked attention. We achieve the rotation by utilising the beating note of two nonresonant, single-mode, frequency-stabilised and controllably detuned lasers which create an optical trap that rotates at GHz frequencies. In the range of rotation frequencies, a quantised vortex with a phase winding co-directed with the trap rotation is formed. By controlling the orbital angular momentum and the frequency detuning of the excitation lasers, we can deterministically drive the vortex phase winding from clockwise to counter-clockwise. Similarly to the conventional superfluid, vortex in polariton condensate appears only above the critical rotation frequency, which, in our case, is 1 GHz. Moreover, the vortex holds in the range of stirring frequencies from 1 to 4 GHz, with a 100 % probability of appearing in the middle of the range. The interesting difference between our dissipative quantum system and conventional superfluids is that the number of vortices does not increase with the bucket rotation speed.

Our results pave the way towards the comparative studies of the polariton condensate on par with other superfluids. For example, in liquid helium, the required rotation frequencies for the generation of quantised vortices are in the sub-Hz range. In atomic condensates, it is in the hundreds of Hz range (see respective panels in Figure 7-14). In contrast, the required rotation frequencies in polariton condensates are 7-8 orders higher and lay in the GHz range (bottom panel of Figure 7-14). In this sense, the large body of studies of BEC of superfluid applied to polaritons in con-

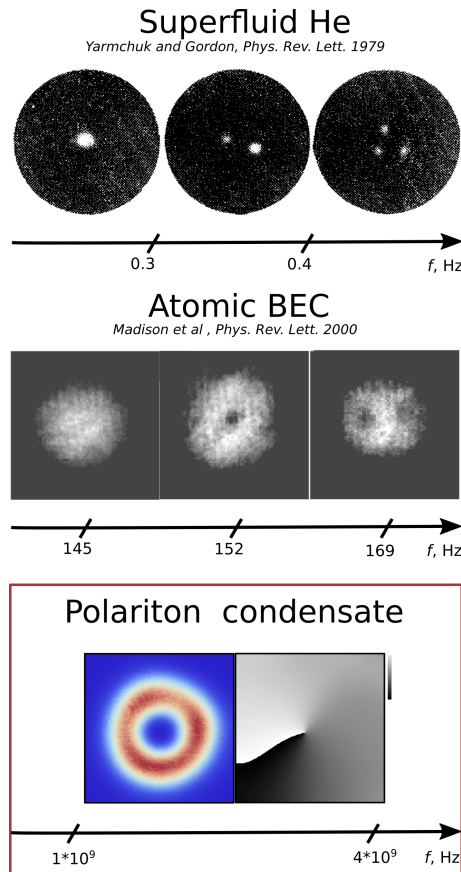


Figure 7-14: "Rotating bucket" experiment in different systems. The top row represents the vortices in the stirred superfluid He alongside the characteristic frequencies of their appearance that are on the order of 1 Hz. The image is adopted from [44]. The middle panel represents the images of the vortices in the rotated BEC; the required rotation frequency is in the order of 100Hz. The images are adopted from [184]. The bottom panel represents the results of the "Rotating bucket" experiment with polariton condensate (Intensity and phase distribution). The characteristic frequencies of the vortex appearance are around 1GHz. The image is adopted from [3].

junction with unique features of polaritons itself could result in numerous intriguing findings.

The investigation of polaritons in rotating potentials has raised a big interest in the polaritonics community. In parallel with our study, another experimental observation of the acquisition of angular momenta by externally stirred condensate has been reported by Y.V.I. Redondo et al [191]. They experimentally investigated the angular momentum of the condensate formed by a similar technique. Interestingly, even though the rotating trap was formed by the combination of Gaussian and Laguerre-Gaussian ($l = 1$) beams (in contrast to our work), Y.V.I. Redondo and col-

leagues observed the rotation of the condensate and vortex formation in the similar GHz frequency range. Moreover, the recent theoretical study [192] comprehensively considers the theory of the vortex formation in the rotating trap and investigates the coupling and formation of the states with different OAM. Another theoretical work [193] from the same group reports on the spin effects of the condensate in the rotating potential.

Our findings demonstrate an unconventional GHz stirring method for the generation of robust polariton condensate vortex states co-rotating with the stirring direction. We also provide evidence that time-periodic driving can fundamentally affect the dynamics of the excited polariton condensate and, thus, the emission properties of the microcavity. Notably, we have shown that the emission intensity and spectral composition of the condensate depend strongly on the pump rotation speed. This opens new perspectives on Floquet engineering [38, 39] in the strong coupling regime and spatiotemporal control of nonlinear fluids of light. With the rapid advancements in creating extended polariton networks [31], our method can be used to engineer vortex arrays with controllable OAM to study the complex interplay of polarisation, OAM in polariton lattices. Moreover, polariton condensates offer an alternative platform for generating a nonlinear structured light. In particular, polariton vortices can be used for various applications ranging from classical [31, 46, 194] and quantum computing [48, 195] to super-resolution imaging [196] and optical manipulation of small objects [197].

Chapter 8

Conclusion and Outlook

Overall, in the scope of this thesis, the all-optical spinor and vorticity control of polariton condensates in the optical traps were realised. Below, the main findings of this work are listed alongside the discussion on their possible applications and further research directions.

The main findings of the thesis can be divided into two parts: obtained for the static optical trap and the rotating one. In turn, two types of static laser patterns to excite polariton condensate were utilised - the annular and elliptical traps. For the annular trap (Chapter 4), we have comprehensively studied the condensate spin properties depending on the pump power, excitation polarisation and trap size. We have confirmed that under circularly polarised excitation, condensate adopts the polarisation of the non-resonant excitation through the process of **optical orientation**. For the linear excitation, the spin of the condensate is **pinned** to the direction of the effective in-plane magnetic field caused by local sample birefringence. However, the pinning regime does not appear immediately after the condensation threshold but at some finite pump power ($\approx 1.2P_{th}$). Before this, the condensate spin is unstable and stochastically flips between different linear polarisation states. This **destabilisation** is governed by the interplay between the pinning field and polariton interactions with the excitonic reservoir. By decreasing the optical trap size, we also find that the region of linear polarisation pinning shrinks until it completely disappeared for the 9 μm trap. At both higher pump power and elliptically polarised

excitation, we have observed the lowering of the condensate degree of polarisation in the integrated measurements. This effect was attributed to the **self-induced Larmor precession** of the pseudo-spin, which had been observed experimentally in Ref. [8]. Overall, this study has demonstrated the peculiarities of the condensate spin properties as well as showcased the variety of approaches for its manipulation: with the non-resonant excitation power, polarisation and optical trap size.

Even though the control of the elliptical and circular polarisation was achieved for the annular trap, the linear polarisation of the emission was pre-defined by the condensate position of the sample and could not be tuned. We have overcome this hurdle using the elliptical non-resonant excitation profile (as shown Chapter 5). Sharing similar properties with the annular condensate for the elliptical and circular excitation polarisation, the elliptical shape of the condensate has allowed us to **establish the control also over the linear polarisation** of the emission. We have found that the cavity's inherent TE-TM splitting, along with the prolonged shape of the condensate, splits the orthogonal linear polarisation states, making the condensate adopt the defined spinor projection co-directed with the short axis of the condensate ellipse. This effect allowed us to overcome the internal birefringence of the sample and drive the condensate to the desired spin state by rotating the excitation profile. Thus, as a result of the two works mentioned above, we have gained control over both linear and circular polarisation projections of the condensate emission. As discussed in the bulk of the thesis, beyond the fundamental interest, these findings can be applied to the realisation of polariton-based spinoptronic devices [37]. Another promising avenue is utilising the spin degree of freedom in the extended networks of polariton condensates. We have made a first step in this direction by investigating the coupled elliptical condensates at different mutual orientations and separation distances. We have found several distinct spin interaction regimes - destabilised and flipping ones and demonstrated that the **coupling between two elliptical condensates** can be changed by their mutual orientation. The logical next step would be the investigations of chains [198, 199] and lattices of interacting ellipses or symmetric condensates. It is worth noting that all studies mentioned above were carried out for the trap ground state. The utilisation of the

bigger pumping profiles will allow for the investigation of the spin structure of the condensates in the excited states of the confining potential and could reveal new phenomena and non-trivial polarisation patterns.

In the second part of this thesis, a developed **experimental approach for the rotation of an optical trap for polaritons** at the GHz rate (see Chapter 6) have been described. It was achieved by virtue of a beating note of two single-mode frequency detuned lasers shaped with the SLM into a "perfect vortex". The developed approach allows us to create a laser pattern rotating at an arbitrary frequency in the desired direction. Tuning intensities of two excitation lasers, we realised the excitation profile similar to the one used for the condensate linear polarisation control. As a result, we were able to optically drive the spin and stir it on the equator of the Poincare sphere. Interestingly, we find the resonance characteristics of the optically driven spin precession at GHz rotation frequencies. The driven precession coherence is prolonged only when in resonance with the internal condensate self-induced Larmor precession. This effect is **a quantum fluidic analogue of the famous Nuclear Magnetic resonance effect and optical driving of the BEC spin**. We also find that **spin coherence time** of the condensate when in the resonance is **increased by at least 20 times** with respect to previous reports [8]. Building the bridges between different branches of modern physics, this finding can be utilised for the precise and coherent control of spin in future quantum computing [48, 167] applications of polaritons. Furthermore, the optically driven spin precession can be applied to studying the arrays of interacting condensates to investigate the effect of the rotating spin on the neighbouring condensates. The stirring technique could also allow the realisation of the complex skyrmion and meron topological structures in polariton condensates [200].

Increasing the trap size and setting the two excitation laser intensities to be equal, we were able **to realise the famous "Rotating Bucket" experiment with a polariton condensate** (see Chapter 7). The formation of the vortices in the rotating reservoir is the distinctive feature of the superfluids. We have found that analogous to the superfluid He [44] and BEC [41], the vortex in the condensate forms above the critical stirring frequency (1GHz). We reveal that the polariton

vortex co-rotates with the optical trap and exists only in the narrow range of stirring frequencies **from 1 to 4 GHz**. This finding opens a route for the comparative studies of polariton condensates with other superfluid systems as well as the research of the superfluidity in polariton condensate itself [97]. Moreover, tailoring time-periodic potential for polaritons could open a new branch of the research on Floquet engineering [38] in such systems. The on-demand vorticity control could benefit the realisation of an analogue simulator [31] and quantum bits [48] based on circular currents and vortices. We have already looked into the bigger rotating optical traps and observed the co-rotating vortex clusters of two and three vortices. The realisation of an even bigger optical trap or stirring of the unbound condensate could potentially allow the creation of bigger clusters and investigate the turbulent polariton flow [87, 95] in rotating polariton fluid.

This brings this thesis to an end. However, the polariton investigations are ongoing. The physics of such system is very rich, and numerous investigations and outstanding results are yet to come!

Bibliography

- [1] I. Gnusov, H. Sigurdsson, S. Baryshev, T. Ermatov, A. Askitopoulos, and P. G. Lagoudakis, “Optical orientation, polarization pinning, and depolarization dynamics in optically confined polariton condensates,” *Phys. Rev. B*, vol. 102, p. 125419, Sep 2020.
- [2] I. Gnusov, H. Sigurdsson, J. Töpfer, S. Baryshev, S. Alyatkin, and P. Lagoudakis, “All-optical linear-polarization engineering in single and coupled exciton-polariton condensates,” *Phys. Rev. Applied*, vol. 16, p. 034014, Sep 2021.
- [3] I. Gnusov, S. Harrison, S. Alyatkin, K. Sitnik, J. Töpfer, H. Sigurdsson, and P. Lagoudakis, “Quantum vortex formation in the "rotating bucket" experiment with polariton condensates,” *Science Advances*, vol. 9, no. 4, p. eadd1299, 2023.
- [4] I. Gnusov, S. Baryshev, H. Sigurdsson, K. Sitnik, J. Töpfer, S. Alyatkin, and P. G. Lagoudakis, “Optically driven spin precession in polariton condensates,” *preprint arXiv 2305.03782*, 2023.
- [5] I. Gnusov, H. Sigurdsson, S. Baryshev, A. Askitopoulos, and P. G. Lagoudakis, “Pseudo-spin destabilization in optically confined exciton-polariton condensates,” in *Frontiers in Optics / Laser Science*, p. FTu2D.4, Optica Publishing Group, 2020.
- [6] H. Sigurdsson, I. Gnusov, S. Alyatkin, L. Pickup, N. A. Gippius, P. G. Lagoudakis, and A. Askitopoulos, “Persistent self-induced larmor precession evidenced through periodic revivals of coherence,” *Phys. Rev. Lett.*, vol. 129, p. 155301, Oct 2022.
- [7] K. A. Sitnik, S. Alyatkin, J. D. Töpfer, I. Gnusov, T. Cookson, H. Sigurdsson, and P. G. Lagoudakis, “Spontaneous formation of time-periodic vortex cluster in nonlinear fluids of light,” *Phys. Rev. Lett.*, vol. 128, p. 237402, Jun 2022.
- [8] S. Baryshev, A. Zasedatelev, H. Sigurdsson, I. Gnusov, J. D. Töpfer, A. Askitopoulos, and P. G. Lagoudakis, “Engineering photon statistics in a spinor polariton condensate,” *Phys. Rev. Lett.*, vol. 128, p. 087402, Feb 2022.
- [9] T. Ermatov, R. E. Noskov, A. A. Machnev, I. Gnusov, V. Atkin, E. N. Lazareva, S. V. German, S. S. Kosolobov, T. S. Zatsepin, O. V. Sergeeva, J. S. Skibina, P. Ginzburg, V. V. Tuchin, P. G. Lagoudakis, and D. A. Gorin,

- “Multispectral sensing of biological liquids with hollow-core microstructured optical fibres,” *Light: Science and Applications*, vol. 9, Oct. 2020.
- [10] T. Ermatov, I. Gnusov, J. Skibina, R. E. Noskov, and D. Gorin, “Noncontact characterization of microstructured optical fibers coating in real time,” *Optics Letters*, vol. 46, p. 4793, Sept. 2021.
- [11] M. J. Allen, V. C. Tung, and R. B. Kaner, “Honeycomb carbon: A review of graphene,” *Chemical Reviews*, vol. 110, pp. 132–145, July 2009.
- [12] J. K. Patra, G. Das, L. F. Fraceto, E. V. R. Campos, M. del Pilar Rodriguez-Torres, L. S. Acosta-Torres, L. A. Diaz-Torres, R. Grillo, M. K. Swamy, S. Sharma, S. Habtemariam, and H.-S. Shin, “Nano based drug delivery systems: recent developments and future prospects,” *Journal of Nanobiotechnology*, vol. 16, Sept. 2018.
- [13] A. Kavokin, J. J. Baumberg, G. Malpuech, and F. P. Laussy, *Microcavities*. OUP Oxford, Dec. 2007.
- [14] J. Plumhof, T. Stöferle, L. Mai, U. Scherf, and R. Mahrt, “Room-temperature Bose-Einstein condensation of cavity exciton-polaritons in a polymer,” *Nature materials*, vol. 13, 12 2013.
- [15] J. Kasprzak, M. Richard, S. Kundermann, A. Baas, P. Jeambrun, J. M. J. Keeling, F. M. Marchetti, M. H. Szymańska, R. André, J. L. Staehli, V. Savona, P. B. Littlewood, B. Deveaud, and L. S. Dang, “Bose-Einstein condensation of exciton polaritons,” *Nature*, vol. 443, pp. 409–14, Sept. 2006.
- [16] K. G. Lagoudakis, M. Wouters, M. Richard, A. Baas, I. Carusotto, R. André, L. S. Dang, and B. Deveaud-Plédran, “Quantized vortices in an exciton-polariton condensate,” *Nature Physics*, vol. 4, pp. 706–710, Aug. 2008.
- [17] A. Amo, J. Lefrère, S. Pigeon, C. Adrados, C. Ciuti, I. Carusotto, R. Houdré, E. Giacobino, and A. Bramati, “Superfluidity of polaritons in semiconductor microcavities,” *Nature Physics*, vol. 5, pp. 805–810, Sept. 2009.
- [18] M. Sich, D. N. Krizhanovskii, M. S. Skolnick, A. V. Gorbach, R. Hartley, D. V. Skryabin, E. A. Cerda-Méndez, K. Biermann, R. Hey, and P. V. Santos, “Observation of bright polariton solitons in a semiconductor microcavity,” *Nature Photonics*, vol. 6, pp. 50–55, Nov. 2011.
- [19] T. Byrnes, N. Y. Kim, and Y. Yamamoto, “Exciton-polariton condensates,” *Nature Physics*, vol. 10, pp. 803–813, Oct. 2014.
- [20] H. Deng, H. Haug, and Y. Yamamoto, “Exciton-polariton Bose-Einstein condensation,” *Rev. Mod. Phys.*, vol. 82, pp. 1489–1537, May 2010.
- [21] S. Alyatkin, H. Sigurdsson, A. Askitopoulos, J. D. Töpfer, and P. G. Lagoudakis, “Quantum fluids of light in all-optical scatterer lattices,” *Nature Communications*, vol. 12, Sept. 2021.

- [22] S. Alyatkin, J. D. Töpfer, A. Askitopoulos, H. Sigurdsson, and P. G. Lagoudakis, “Optical control of couplings in polariton condensate lattices,” *Phys. Rev. Lett.*, vol. 124, p. 207402, May 2020.
- [23] R. Tao, K. Peng, L. Haeberlé, Q. Li, D. Jin, G. R. Fleming, S. Kéna-Cohen, X. Zhang, and W. Bao, “Halide perovskites enable polaritonic XY spin hamiltonian at room temperature,” *Nature Materials*, vol. 21, pp. 761–766, June 2022.
- [24] T. H. Harder, O. A. Egorov, J. Beierlein, P. Gagel, J. Michl, M. Emmerling, C. Schneider, U. Peschel, S. Höfling, and S. Klembt, “Exciton-polaritons in flatland: Controlling flatband properties in a Lieb lattice,” *Phys. Rev. B*, vol. 102, p. 121302, Sep 2020.
- [25] I. Buluta and F. Nori, “Quantum simulators,” *Science*, vol. 326, pp. 108–111, Oct. 2009.
- [26] N. G. Berloff, M. Silva, K. Kalinin, A. Askitopoulos, J. D. Töpfer, P. Cilibrizzi, W. Langbein, and P. G. Lagoudakis, “Realizing the classical XY hamiltonian in polariton simulators,” *Nature Materials*, vol. 16, pp. 1120–1126, Sept. 2017.
- [27] A. Askitopoulos, H. Ohadi, A. V. Kavokin, Z. Hatzopoulos, P. G. Savvidis, and P. G. Lagoudakis, “Polariton condensation in an optically induced two-dimensional potential,” *Physical Review B*, vol. 88, p. 041308, July 2013.
- [28] A. Askitopoulos, T. C. H. Liew, H. Ohadi, Z. Hatzopoulos, P. G. Savvidis, and P. G. Lagoudakis, “Robust platform for engineering pure-quantum-state transitions in polariton condensates,” *Phys. Rev. B*, vol. 92, p. 035305, Jul 2015.
- [29] J. Töpfer, H. Sigurdsson, L. Pickup, and P. Lagoudakis, “Time-delay polaritonics,” *Communications Physics*, vol. 3, p. 2, 01 2020.
- [30] S. L. Harrison, H. Sigurdsson, and P. G. Lagoudakis, “Synchronization in optically trapped polariton stuart-landau networks,” *Phys. Rev. B*, vol. 101, p. 155402, Apr 2020.
- [31] S. Alyatkin, C. Milian, Y. V. Kartashov, K. A. Sitnik, J. D. Topfer, H. Sigurdsson, and P. G. Lagoudakis, “All-optical artificial vortex matter in quantum fluids of light,” 2022.
- [32] H. Ohadi, A. J. Ramsay, H. Sigurdsson, Y. del Valle-Inclan Redondo, S. I. Tsintzos, Z. Hatzopoulos, T. C. H. Liew, I. A. Shelykh, Y. G. Rubo, P. G. Savvidis, and J. J. Baumberg, “Spin order and phase transitions in chains of polariton condensates,” *Phys. Rev. Lett.*, vol. 119, p. 067401, Aug 2017.
- [33] I. Shelykh, G. Malpuech, K. V. Kavokin, A. V. Kavokin, and P. Bigenwald, “Spin dynamics of interacting exciton polaritons in microcavities,” *Phys. Rev. B*, vol. 70, p. 115301, Sep 2004.

- [34] M. Klaas, O. A. Egorov, T. C. H. Liew, A. Nalitov, V. Marković, H. Suchomel, T. H. Harder, S. Betzold, E. A. Ostrovskaya, A. Kavokin, S. Klembt, S. Höfling, and C. Schneider, “Nonresonant spin selection methods and polarization control in exciton-polariton condensates,” *Phys. Rev. B*, vol. 99, p. 115303, Mar 2019.
- [35] K. G. Lagoudakis, T. Ostatnický, A. V. Kavokin, Y. G. Rubo, R. André, and B. Deveaud-Plédran, “Observation of half-quantum vortices in an exciton-polariton condensate,” *Science*, vol. 326, pp. 974–976, Nov. 2009.
- [36] Y. Redondo, H. Sigurdsson, H. Ohadi, I. Shelykh, Y. Rubo, Z. Hatzopoulos, P. Savvidis, and J. Baumberg, “Observation of inversion, hysteresis, and collapse of spin in optically trapped polariton condensates,” *Physical Review B*, vol. 99, 04 2019.
- [37] T. Liew, I. Shelykh, and G. Malpuech, “Polaritonic devices,” *Physica E: Low-dimensional Systems and Nanostructures*, vol. 43, no. 9, pp. 1543 – 1568, 2011.
- [38] C. Weitenberg and J. Simonet, “Tailoring quantum gases by Floquet engineering,” *Nature Physics*, vol. 17, pp. 1342–1348, Aug. 2021.
- [39] T. Oka and S. Kitamura, “Floquet engineering of quantum materials,” *Annual Review of Condensed Matter Physics*, vol. 10, no. 1, pp. 387–408, 2019.
- [40] W. E. Bell and A. L. Bloom, “Optically driven spin precession,” *Phys. Rev. Lett.*, vol. 6, pp. 280–281, Mar 1961.
- [41] A. L. Fetter, “Rotating trapped Bose-Einstein condensates,” *Rev. Mod. Phys.*, vol. 81, pp. 647–691, May 2009.
- [42] K. W. Madison, F. Chevy, W. Wohlleben, and J. Dalibard, “Vortex formation in a stirred Bose-Einstein condensate,” *Phys. Rev. Lett.*, vol. 84, pp. 806–809, Jan 2000.
- [43] G. A. Williams, “Vortices and superfluidity,” *Endeavour*, vol. 16, no. 3, pp. 102–109, 1992.
- [44] E. J. Yarmchuk, M. J. V. Gordon, and R. E. Packard, “Observation of stationary vortex arrays in rotating superfluid helium,” *Phys. Rev. Lett.*, vol. 43, pp. 214–217, Jul 1979.
- [45] K. G. Lagoudakis, F. Manni, B. Pietka, M. Wouters, T. C. H. Liew, V. Savona, A. V. Kavokin, R. André, and B. Deveaud-Plédran, “Probing the dynamics of spontaneous quantum vortices in polariton superfluids,” *Phys. Rev. Lett.*, vol. 106, p. 115301, Mar 2011.
- [46] X. Ma and S. Schumacher, “Vortex-vortex control in exciton-polariton condensates,” *Phys. Rev. B*, vol. 95, p. 235301, Jun 2017.

- [47] L. Dominici, R. Carretero-González, A. Gianfrate, J. Cuevas-Maraver, A. S. Rodrigues, D. J. Frantzeskakis, G. Lerario, D. Ballarini, M. D. Giorgi, G. Gigli, P. G. Kevrekidis, and D. Sanvitto, “Interactions and scattering of quantum vortices in a polariton fluid,” *Nature Communications*, vol. 9, Apr. 2018.
- [48] A. Kavokin, T. C. H. Liew, C. Schneider, P. G. Lagoudakis, S. Klembt, and S. Hoefling, “Polariton condensates for classical and quantum computing,” *Nature Reviews Physics*, vol. 4, pp. 435–451, Apr. 2022.
- [49] B. Saleh and M. Teich, *Fundamentals of photonics, 2nd Edition*. Wiley-Interscience, 2007.
- [50] C. Kittel, *Introduction to Solid State physics*. Nauka, 1979.
- [51] J. Frenkel, “On the transformation of light into heat in solids. i,” *Phys. Rev.*, vol. 37, pp. 17–44, Jan 1931.
- [52] T. Yagafarov, D. Sannikov, A. Zasedatelev, K. Georgiou, A. Baranikov, O. Kyriienko, I. Shelykh, L. Gai, Z. Shen, D. Lidzey, and P. Lagoudakis, “Mechanisms of blueshifts in organic polariton condensates,” *Communications Physics*, vol. 3, p. 18, 01 2020.
- [53] G. H. Wannier, “The structure of electronic excitation levels in insulating crystals,” *Phys. Rev.*, vol. 52, pp. 191–197, Aug 1937.
- [54] E. Hanamura and H. Haug, “Condensation effects of excitons,” *Physics Reports*, vol. 33, pp. 209–284, Oct. 1977.
- [55] P. Cilibrizzi, A. Askitopoulos, M. Silva, F. Bastiman, E. Clarke, J. M. Zajac, W. Langbein, and P. G. Lagoudakis, “Polariton condensation in a strain-compensated planar microcavity with InGaAs quantum wells,” *Applied Physics Letters*, vol. 105, p. 191118, Nov. 2014.
- [56] M. H. Anderson, J. R. Ensher, M. R. Matthews, C. E. Wieman, and E. A. Cornell, “Observation of Bose-Einstein condensation in a dilute atomic vapor,” *Science*, vol. 269, pp. 198–201, July 1995.
- [57] K. B. Davis, M. O. Mewes, M. R. Andrews, N. J. van Druten, D. S. Durfee, D. M. Kurn, and W. Ketterle, “Bose-Einstein condensation in a gas of sodium atoms,” *Phys. Rev. Lett.*, vol. 75, pp. 3969–3973, Nov 1995.
- [58] N. D. Mermin and H. Wagner, “Absence of ferromagnetism or antiferromagnetism in one- or two-dimensional isotropic heisenberg models,” *Phys. Rev. Lett.*, vol. 17, pp. 1133–1136, Nov 1966.
- [59] V. Bagnato and D. Kleppner, “Bose - einstein condensation in low-dimensional traps,” *Phys. Rev. A*, vol. 44, pp. 7439–7441, Dec 1991.
- [60] H.-J. Miesner, D. M. Stamper-Kurn, M. R. Andrews, D. S. Durfee, S. Inouye, and W. Ketterle, “Bosonic stimulation in the formation of a Bose-Einstein condensate,” *Science*, vol. 279, pp. 1005–1007, Feb. 1998.

- [61] P. G. Savvidis, J. J. Baumberg, R. M. Stevenson, M. S. Skolnick, D. M. Whittaker, and J. S. Roberts, “Angle-Resonant Stimulated Polariton Amplifier,” *Physical Review Letters*, vol. 84, pp. 1547–1550, Feb. 2000.
- [62] C. Ciuti, P. Schwendimann, B. Deveaud, and A. Quattropani, “Theory of the angle-resonant polariton amplifier,” *Phys. Rev. B*, vol. 62, pp. R4825–R4828, Aug 2000.
- [63] R. M. Stevenson, V. N. Astratov, M. S. Skolnick, D. M. Whittaker, M. Emam-Ismaïl, A. I. Tartakovskii, P. G. Savvidis, J. J. Baumberg, and J. S. Roberts, “Continuous wave observation of massive polariton redistribution by stimulated scattering in semiconductor microcavities,” *Phys. Rev. Lett.*, vol. 85, pp. 3680–3683, Oct 2000.
- [64] H. Deng, G. Weihs, C. Santori, J. Bloch, and Y. Yamamoto, “Condensation of semiconductor microcavity exciton polaritons,” *Science*, vol. 298, pp. 199–202, Oct. 2002.
- [65] S. Christopoulos, G. B. H. von Högersthal, A. J. D. Grundy, P. G. Lagoudakis, A. V. Kavokin, J. J. Baumberg, G. Christmann, R. Butté, E. Feltin, J.-F. Carlin, and N. Grandjean, “Room-temperature polariton lasing in semiconductor microcavities,” *Phys. Rev. Lett.*, vol. 98, p. 126405, Mar 2007.
- [66] F. Li, L. Orosz, O. Kamoun, S. Bouchoule, C. Brimont, P. Disseix, T. Guillet, X. Lafosse, M. Leroux, J. Leymarie, M. Mexis, M. Mihailovic, G. Patriarche, F. Réveret, D. Solnyshkov, J. Zuniga-Perez, and G. Malpuech, “From excitonic to photonic polariton condensate in a ZnO-based microcavity,” *Phys. Rev. Lett.*, vol. 110, p. 196406, May 2013.
- [67] F. Tassone, C. Piermarocchi, V. Savona, A. Quattropani, and P. Schwendimann, “Bottleneck effects in the relaxation and photoluminescence of microcavity polaritons,” *Phys. Rev. B*, vol. 56, pp. 7554–7563, Sep 1997.
- [68] Y. Sun, P. Wen, Y. Yoon, G. Liu, M. Steger, L. N. Pfeiffer, K. West, D. W. Snoke, and K. A. Nelson, “Bose-Einstein condensation of long-lifetime polaritons in thermal equilibrium,” *Phys. Rev. Lett.*, vol. 118, p. 016602, Jan 2017.
- [69] R. Balili, V. Hartwell, D. Snoke, L. Pfeiffer, and K. West, “Bose-Einstein Condensation of Microcavity Polaritons in a Trap,” *Science*, vol. 316, pp. 1007–1010, May 2007.
- [70] R. B. Balili, D. W. Snoke, L. Pfeiffer, and K. West, “Actively tuned and spatially trapped polaritons,” *Applied Physics Letters*, vol. 88, Jan. 2006.
- [71] A. Das, P. Bhattacharya, J. Heo, A. Banerjee, and W. Guo, “Polariton bose-einstein condensate at room temperature in an al(ga)n nanowire-dielectric microcavity with a spatial potential trap,” *Proceedings of the National Academy of Sciences*, vol. 110, pp. 2735–2740, Feb. 2013.

- [72] D. Bajoni, P. Senellart, E. Wertz, I. Sagnes, A. Miard, A. Lemaître, and J. Bloch, “Polariton laser using single micropillar GaAs–GaAlAs semiconductor cavities,” *Phys. Rev. Lett.*, vol. 100, p. 047401, Jan 2008.
- [73] M. Maragkou, A. J. D. Grundy, E. Wertz, A. Lemaître, I. Sagnes, P. Senellart, J. Bloch, and P. G. Lagoudakis, “Spontaneous nonground state polariton condensation in pillar microcavities,” *Phys. Rev. B*, vol. 81, p. 081307, Feb 2010.
- [74] L. Ferrier, E. Wertz, R. Johne, D. D. Solnyshkov, P. Senellart, I. Sagnes, A. Lemaître, G. Malpuech, and J. Bloch, “Interactions in confined polariton condensates,” *Phys. Rev. Lett.*, vol. 106, p. 126401, Mar 2011.
- [75] E. Wertz, L. Ferrier, D. D. Solnyshkov, R. Johne, D. Sanvitto, A. Lemaître, I. Sagnes, R. Grousson, A. V. Kavokin, P. Senellart, G. Malpuech, and J. Bloch, “Spontaneous formation and optical manipulation of extended polariton condensates,” *Nature Physics*, vol. 6, pp. 860–864, Aug. 2010.
- [76] T. Gao, P. S. Eldridge, T. C. H. Liew, S. I. Tsintzos, G. Stavriniadis, G. Deligeorgis, Z. Hatzopoulos, and P. G. Savvidis, “Polariton condensate transistor switch,” *Phys. Rev. B*, vol. 85, p. 235102, Jun 2012.
- [77] G. Tosi, G. Christmann, N. G. Berloff, P. Tsotsis, T. Gao, Z. Hatzopoulos, P. G. Savvidis, and J. J. Baumberg, “Sculpting oscillators with light within a nonlinear quantum fluid,” *Nature Physics*, vol. 8, pp. 190–194, Mar 2012.
- [78] P. Cristofolini, A. Dreismann, G. Christmann, G. Franchetti, N. G. Berloff, P. Tsotsis, Z. Hatzopoulos, P. G. Savvidis, and J. J. Baumberg, “Optical superfluid phase transitions and trapping of polariton condensates,” *Phys. Rev. Lett.*, vol. 110, p. 186403, May 2013.
- [79] S. Harrison, H. Sigurdsson, S. Alyatkin, J. Töpfer, and P. Lagoudakis, “Solving the max-3-cut problem with coherent networks,” *Phys. Rev. Appl.*, vol. 17, p. 024063, Feb 2022.
- [80] A. Askitopoulos, L. Pickup, S. Alyatkin, A. Zasedatelev, K. G. Lagoudakis, W. Langbein, and P. G. Lagoudakis, “Giant increase of temporal coherence in optically trapped polariton condensate,” 2019.
- [81] M. Richard, J. Kasprzak, R. Romestain, R. André, and L. S. Dang, “Spontaneous coherent phase transition of polaritons in cdte microcavities,” *Phys. Rev. Lett.*, vol. 94, p. 187401, May 2005.
- [82] E. Wertz, L. Ferrier, D. D. Solnyshkov, P. Senellart, D. Bajoni, A. Miard, A. Lemaître, G. Malpuech, and J. Bloch, “Spontaneous formation of a polariton condensate in a planar GaAs microcavity,” *Applied Physics Letters*, vol. 95, Aug. 2009.
- [83] M. Wouters, I. Carusotto, and C. Ciuti, “Spatial and spectral shape of inhomogeneous nonequilibrium exciton-polariton condensates,” *Phys. Rev. B*, vol. 77, p. 115340, Mar 2008.

- [84] M. Wouters, T. C. H. Liew, and V. Savona, “Energy relaxation in one-dimensional polariton condensates,” *Phys. Rev. B*, vol. 82, p. 245315, Dec 2010.
- [85] R. Dall, M. D. Fraser, A. S. Desyatnikov, G. Li, S. Brodbeck, M. Kamp, C. Schneider, S. Höfling, and E. A. Ostrovskaya, “Creation of orbital angular momentum states with chiral polaritonic lenses,” *Phys. Rev. Lett.*, vol. 113, p. 200404, Nov 2014.
- [86] G. Roumpos, M. D. Fraser, A. Löffler, S. Höfling, A. Forchel, and Y. Yamamoto, “Single vortex–antivortex pair in an exciton-polariton condensate,” *Nature Physics*, vol. 7, pp. 129–133, Nov. 2010.
- [87] G. Nardin, G. Grosso, Y. Léger, B. Pietka, F. Morier-Genoud, and B. Deveaud-Plédran, “Hydrodynamic nucleation of quantized vortex pairs in a polariton quantum fluid,” *Nature Physics*, vol. 7, pp. 635–641, Apr. 2011.
- [88] D. Sanvitto, S. Pigeon, A. Amo, D. Ballarini, M. D. Giorgi, I. Carusotto, R. Hivet, F. Pisanello, V. G. Sala, P. S. S. Guimaraes, R. Houdré, E. Giacobino, C. Ciuti, A. Bramati, and G. Gigli, “All-optical control of the quantum flow of a polariton condensate,” *Nature Photonics*, vol. 5, pp. 610–614, Sept. 2011.
- [89] M.-S. Kwon, B. Y. Oh, S.-H. Gong, J.-H. Kim, H. K. Kang, S. Kang, J. D. Song, H. Choi, and Y.-H. Cho, “Direct transfer of light’s orbital angular momentum onto a nonresonantly excited polariton superfluid,” *Phys. Rev. Lett.*, vol. 122, p. 045302, Jan 2019.
- [90] X. Ma, Y. V. Kartashov, T. Gao, L. Torner, and S. Schumacher, “Spiraling vortices in exciton-polariton condensates,” *Phys. Rev. B*, vol. 102, p. 045309, Jul 2020.
- [91] X. Ma, B. Berger, M. Aßmann, R. Driben, T. Meier, C. Schneider, S. Höfling, and S. Schumacher, “Realization of all-optical vortex switching in exciton-polariton condensates,” *Nature Communications*, vol. 11, Feb. 2020.
- [92] F. Manni, Y. Léger, Y. Rubo, R. André, and B. Deveaud, “Hyperbolic spin vortices and textures in exciton–polariton condensates,” *Nature Communications*, vol. 4, Oct. 2013.
- [93] G. Tosi, G. Christmann, N. Berloff, P. Tsotsis, T. Gao, Z. Hatzopoulos, P. Savvidis, and J. Baumberg, “Geometrically locked vortex lattices in semiconductor quantum fluids,” *Nature Communications*, vol. 3, Jan. 2012.
- [94] T. Gao, O. A. Egorov, E. Estrecho, K. Winkler, M. Kamp, C. Schneider, S. Höfling, A. G. Truscott, and E. A. Ostrovskaya, “Controlled ordering of topological charges in an exciton-polariton chain,” *Phys. Rev. Lett.*, vol. 121, p. 225302, Nov 2018.

- [95] R. Panico, P. Comaron, M. Matuszewski, A. S. Lanotte, D. Trypogeorgos, G. Gigli, M. D. Giorgi, V. Ardizzone, D. Sanvitto, and D. Ballarini, “Onset of vortex clustering and inverse energy cascade in dissipative quantum fluids,” *Nature Photonics*, vol. 17, pp. 451–456, Mar. 2023.
- [96] R. Hivet, E. Cancellieri, T. Boulier, D. Ballarini, D. Sanvitto, F. M. Marchetti, M. H. Szymańska, C. Ciuti, E. Giacobino, and A. Bramati, “Interaction-shaped vortex-antivortex lattices in polariton fluids,” *Phys. Rev. B*, vol. 89, p. 134501, Apr 2014.
- [97] J. Keeling and N. G. Berloff, “Going with the flow,” *Nature*, vol. 457, pp. 273–274, Jan. 2009.
- [98] G. Lerario, A. Fieramosca, F. Barachati, D. Ballarini, K. S. Daskalakis, L. Dominici, M. D. Giorgi, S. A. Maier, G. Gigli, S. Kéna-Cohen, and D. Sanvitto, “Room-temperature superfluidity in a polariton condensate,” *Nature Physics*, vol. 13, pp. 837–841, June 2017.
- [99] D. Sanvitto, F. M. Marchetti, M. H. Szymańska, G. Tosi, M. Baudisch, F. P. Laussy, D. N. Krizhanovskii, M. S. Skolnick, L. Marrucci, A. Lemaître, J. Bloch, C. Tejedor, and L. Viña, “Persistent currents and quantized vortices in a polariton superfluid,” *Nature Physics*, vol. 6, pp. 527–533, May 2010.
- [100] S. Utsunomiya, L. Tian, G. Roumpos, C. W. Lai, N. Kumada, T. Fujisawa, M. Kuwata-Gonokami, A. Löffler, S. Höfling, A. Forchel, and Y. Yamamoto, “Observation of bogoliubov excitations in exciton-polariton condensates,” *Nature Physics*, vol. 4, pp. 700–705, Aug. 2008.
- [101] J. F. S. Brachmann, W. S. Bakr, J. Gillen, A. Peng, and M. Greiner, “Inducing vortices in a Bose-Einstein condensate using holographically produced light beams,” *Opt. Express*, vol. 19, pp. 12984–12991, Jul 2011.
- [102] K. V. Kavokin, I. A. Shelykh, A. V. Kavokin, G. Malpuech, and P. Bigenwald, “Quantum theory of spin dynamics of exciton-polaritons in microcavities,” *Phys. Rev. Lett.*, vol. 92, p. 017401, Jan 2004.
- [103] M. H. Levitt, *Spin dynamics: basics of nuclear magnetic resonance*. Chichester, UK: John Wiley & Sons, Dec. 2013.
- [104] I. A. Shelykh, A. V. Kavokin, Y. G. Rubo, T. C. H. Liew, and G. Malpuech, “Polariton polarization-sensitive phenomena in planar semiconductor microcavities,” *Semiconductor Science and Technology*, vol. 25, p. 013001, Dec. 2009.
- [105] L. Pickup, K. Kalinin, A. Askitopoulos, Z. Hatzopoulos, P. Savvidis, N. Berloff, and P. Lagoudakis, “Optical Bistability under Nonresonant Excitation in Spinor Polariton Condensates,” *Physical Review Letters*, vol. 120, p. 225301, May 2018.
- [106] H. Sigurdsson, “Hysteresis in linearly polarized nonresonantly driven exciton-polariton condensates,” *Physical Review Research*, vol. 2, p. 023323, Jun 2020.

- [107] T. K. Paraíso, M. Wouters, Y. Léger, F. Morier-Genoud, and B. Deveaud-Plédran, “Multistability of a coherent spin ensemble in a semiconductor microcavity,” *Nature Materials*, vol. 9, no. 8, pp. 655–660, 2010.
- [108] C. Leyder, M. Romanelli, J. P. Karr, E. Giacobino, T. C. H. Liew, M. M. Glazov, A. V. Kavokin, G. Malpuech, and A. Bramati, “Observation of the optical spin Hall effect,” *Nature Physics*, vol. 3, pp. 628–631, Sept. 2007.
- [109] R. Hivet, H. Flayac, D. D. Solnyshkov, D. Tanese, T. Boulier, D. Andreoli, E. Giacobino, J. Bloch, A. Bramati, G. Malpuech, and A. Amo, “Half-solitons in a polariton quantum fluid behave like magnetic monopoles,” *Nature Physics*, vol. 8, no. 10, pp. 724–728, 2012.
- [110] M. Sich, L. E. Tapia-Rodriguez, H. Sigurdsson, P. M. Walker, E. Clarke, I. A. Shelykh, B. Royall, E. S. Sedov, A. V. Kavokin, D. V. Skryabin, M. S. Skolnick, and D. N. Krizhanovskii, “Spin domains in one-dimensional conservative polariton solitons,” *ACS Photonics*, vol. 5, no. 12, pp. 5095–5102, 2018.
- [111] S. Dufferwiel, F. Li, E. Cancellieri, L. Giriunas, A. A. P. Trichet, D. M. Whittaker, P. M. Walker, F. Fras, E. Clarke, J. M. Smith, M. S. Skolnick, and D. N. Krizhanovskii, “Spin textures of exciton-polaritons in a tunable microcavity with large TE-TM splitting,” *Phys. Rev. Lett.*, vol. 115, p. 246401, Dec 2015.
- [112] S. Donati, L. Dominici, G. Dagvadorj, D. Ballarini, M. De Giorgi, A. Bramati, G. Gigli, Y. G. Rubo, M. H. Szymańska, and D. Sanvitto, “Twist of generalized skyrmions and spin vortices in a polariton superfluid,” *Proceedings of the National Academy of Sciences*, vol. 113, no. 52, pp. 14926–14931, 2016.
- [113] E. Kammann, T. C. H. Liew, H. Ohadi, P. Cilibrizzi, P. Tsotsis, Z. Hatzopoulos, P. G. Savvidis, A. V. Kavokin, and P. G. Lagoudakis, “Nonlinear Optical Spin Hall Effect and Long-Range Spin Transport in Polariton Lasers,” *Physical Review Letters*, vol. 109, p. 036404, July 2012.
- [114] P. Cilibrizzi, H. Sigurdsson, T. C. H. Liew, H. Ohadi, S. Wilkinson, A. Askitopoulos, I. A. Shelykh, and P. G. Lagoudakis, “Polariton spin whirls,” *Physical Review B*, vol. 92, p. 155308, Oct. 2015.
- [115] P. Cilibrizzi, H. Sigurdsson, T. C. H. Liew, H. Ohadi, A. Askitopoulos, S. Brodbeck, C. Schneider, I. A. Shelykh, S. Höfling, J. Ruostekoski, and P. Lagoudakis, “Half-skyrmion spin textures in polariton microcavities,” *Physical Review B*, vol. 94, p. 045315, July 2016.
- [116] I. Shelykh, K. V. Kavokin, A. V. Kavokin, G. Malpuech, P. Bigenwald, H. Deng, G. Weihs, and Y. Yamamoto, “Semiconductor microcavity as a spin-dependent optoelectronic device,” *Phys. Rev. B*, vol. 70, p. 035320, Jul 2004.
- [117] A. Amo, T. C. H. Liew, C. Adrados, R. Houdré, E. Giacobino, A. V. Kavokin, and A. Bramati, “Exciton-polariton spin switches,” *Nature Photonics*, vol. 4, no. 6, pp. 361–366, 2010.

- [118] R. Cerna, Y. Léger, T. K. Paraiso, M. Wouters, F. Morier-Genoud, M. T. Portella-Oberli, and B. Deveaud, “Ultrafast tristable spin memory of a coherent polariton gas,” *Nature Communications*, vol. 4, p. 2008, Jun 2013.
- [119] T. Gao, C. Antón, T. C. H. Liew, M. D. Martín, Z. Hatzopoulos, L. Viña, P. S. Eldridge, and P. G. Savvidis, “Spin selective filtering of polariton condensate flow,” *Applied Physics Letters*, vol. 107, no. 1, p. 011106, 2015.
- [120] M. Pasienski and B. DeMarco, “A high-accuracy algorithm for designing arbitrary holographic atom traps,” *Opt. Express*, vol. 16, pp. 2176–2190, Feb 2008.
- [121] R. W. Gerchberg and W. O. Saxton, “Practical algorithm for determination of phase from image and diffraction plane pictures,” *OPTIK*, vol. 35, no. 2, pp. 237–&, 1972.
- [122] M. Chen, M. Mazilu, Y. Arita, E. M. Wright, and K. Dholakia, “Dynamics of microparticles trapped in a perfect vortex beam,” *Optics Letters*, vol. 38, p. 4919, Nov. 2013.
- [123] E. A. Cerda-Méndez, D. N. Krizhanovskii, K. Biermann, R. Hey, M. S. Skolnick, and P. V. Santos, “Wavefunction of polariton condensates in a tunable acoustic lattice,” *New Journal of Physics*, vol. 14, p. 075011, July 2012.
- [124] J. V. T. Buller, R. E. Balderas-Navarro, K. Biermann, E. A. Cerda-Méndez, and P. V. Santos, “Exciton-polariton gap soliton dynamics in moving acoustic square lattices,” *Phys. Rev. B*, vol. 94, p. 125432, Sep 2016.
- [125] R. Houdré, J. L. Gibernon, P. Pellandini, R. P. Stanley, U. Oesterle, C. Weisbuch, J. O’Gorman, B. Roycroft, and M. Ilegems, “Saturation of the strong-coupling regime in a semiconductor microcavity: Free-carrier bleaching of cavity polaritons,” *Phys. Rev. B*, vol. 52, pp. 7810–7813, Sep 1995.
- [126] J. M. Zajac, E. Clarke, and W. Langbein, “Suppression of cross-hatched polariton disorder in GaAs/AlAs microcavities by strain compensation,” *Applied Physics Letters*, vol. 101, p. 041114, July 2012.
- [127] E. Hecht, *Optics, 5th Edition*. Pearson, Adelphi University, 2016.
- [128] J. W. Cooley and J. W. Tukey, “An algorithm for the machine calculation of complex fourier series,” *Mathematics of Computation*, vol. 19, no. 90, pp. 297–301, 1965.
- [129] J. Kasprzak, M. Richard, A. Baas, B. Deveaud, R. André, J.-P. Poizat, and L. S. Dang, “Second-order time correlations within a polariton Bose-Einstein condensate in a cdte microcavity,” *Phys. Rev. Lett.*, vol. 100, p. 067402, Feb 2008.
- [130] S. Kim, B. Zhang, Z. Wang, J. Fischer, S. Brodbeck, M. Kamp, C. Schneider, S. Höfling, and H. Deng, “Coherent polariton laser,” *Phys. Rev. X*, vol. 6, p. 011026, Mar 2016.

- [131] G. S. Landsberg., *Optics[in Russian]*. Fizmatlit, Moscow, 2006.
- [132] W. Shurcliff, *Polarized light: production and use*. Harvard University press, 1962.
- [133] M. Wouters and I. Carusotto, “Excitations in a Nonequilibrium Bose-Einstein Condensate of Exciton Polaritons,” *Phys. Rev. Lett.*, vol. 99, p. 140402, Oct. 2007. Publisher: American Physical Society.
- [134] A. Dreismann, H. Ohadi, Y. del Valle-Inclan Redondo, R. Balili, Y. G. Rubo, S. I. Tsintzos, G. Deligeorgis, Z. Hatzopoulos, P. G. Savvidis, and J. J. Baumberg, “A sub-femtojoule electrical spin-switch based on optically trapped polariton condensates,” *Nature Materials*, vol. 15, no. 10, pp. 1074–1078, 2016.
- [135] H. Ohadi, A. Dreismann, Y. Rubo, F. Pinsker, Y. del Valle-Inclan Redondo, S. Tsintzos, Z. Hatzopoulos, P. Savvidis, and J. Baumberg, “Spontaneous Spin Bifurcations and Ferromagnetic Phase Transitions in a Spinor Exciton-Polariton Condensate,” *Physical Review X*, vol. 5, p. 031002, July 2015.
- [136] I. A. Shelykh, Y. G. Rubo, G. Malpuech, D. D. Solnyshkov, and A. Kavokin, “Polarization and propagation of polariton condensates,” *Phys. Rev. Lett.*, vol. 97, p. 066402, Aug 2006.
- [137] J. J. Baumberg, A. V. Kavokin, S. Christopoulos, A. J. D. Grundy, R. Butté, G. Christmann, D. D. Solnyshkov, G. Malpuech, G. Baldassarri Höger von Högersthal, E. Feltin, J.-F. Carlin, and N. Grandjean, “Spontaneous Polarization Buildup in a Room-Temperature Polariton Laser,” *Physical Review Letters*, vol. 101, p. 136409, Sept. 2008.
- [138] H. Ohadi, E. Kammann, T. C. H. Liew, K. G. Lagoudakis, A. V. Kavokin, and P. G. Lagoudakis, “Spontaneous Symmetry Breaking in a Polariton and Photon Laser,” *Physical Review Letters*, vol. 109, no. 1, p. 016404, 2012.
- [139] E. del Valle, D. Sanvitto, A. Amo, F. P. Laussy, R. André, C. Tejedor, and L. Viña, “Dynamics of the formation and decay of coherence in a polariton condensate,” *Physical Review Letters*, vol. 103, Aug. 2009.
- [140] Ł. Kłopotowski, M. Martín, A. Amo, L. Viña, I. Shelykh, M. Glazov, G. Malpuech, A. Kavokin, and R. André, “Optical anisotropy and pinning of the linear polarization of light in semiconductor microcavities,” *Solid State Communications*, vol. 139, no. 10, pp. 511 – 515, 2006.
- [141] J. Kasprzak, R. André, L. S. Dang, I. A. Shelykh, A. V. Kavokin, Y. G. Rubo, K. V. Kavokin, and G. Malpuech, “Build up and pinning of linear polarization in the Bose condensates of exciton polaritons,” *Physical Review B*, vol. 75, p. 045326, Jan. 2007.
- [142] D. Read, T. C. H. Liew, Y. G. Rubo, and A. V. Kavokin, “Stochastic polarization formation in exciton-polariton Bose-Einstein condensates,” *Phys. Rev. B*, vol. 80, p. 195309, Nov 2009.

- [143] J.-i. Inoue, T. Brandes, and A. Shimizu, “Renormalized bosonic interaction of excitons,” *Phys. Rev. B*, vol. 61, pp. 2863–2873, Jan 2000.
- [144] M. Vladimirova, S. Cronenberger, D. Scalbert, K. V. Kavokin, A. Miard, A. Lemaître, J. Bloch, D. Solnyshkov, G. Malpuech, and A. V. Kavokin, “Polariton-polariton interaction constants in microcavities,” *Physical Review B*, vol. 82, p. 075301, Aug. 2010.
- [145] P. G. Lagoudakis, P. G. Savvidis, J. J. Baumberg, D. M. Whittaker, P. R. Eastham, M. S. Skolnick, and J. S. Roberts, “Stimulated spin dynamics of polaritons in semiconductor microcavities,” *Physical Review B*, vol. 65, p. 161310, Apr. 2002.
- [146] Y. d. V.-I. Redondo, H. Ohadi, Y. G. Rubo, O. Beer, A. J. Ramsay, S. I. Tsintzos, Z. Hatzopoulos, P. G. Savvidis, and J. J. Baumberg, “Stochastic spin flips in polariton condensates: nonlinear tuning from GHz to sub-Hz,” *New Journal of Physics*, vol. 20, p. 075008, July 2018. Publisher: IOP Publishing.
- [147] I. Carusotto and C. Ciuti, “Quantum fluids of light,” *Rev. Mod. Phys.*, vol. 85, pp. 299–366, Feb 2013.
- [148] K. G. Lagoudakis, B. Pietka, M. Wouters, R. André, and B. Deveaud-Plédran, “Coherent oscillations in an exciton-polariton josephson junction,” *Phys. Rev. Lett.*, vol. 105, p. 120403, Sep 2010.
- [149] G. Li, T. C. H. Liew, O. A. Egorov, and E. A. Ostrovskaya, “Incoherent excitation and switching of spin states in exciton-polariton condensates,” *Phys. Rev. B*, vol. 92, p. 064304, Aug 2015.
- [150] P. Renucci, T. Amand, X. Marie, P. Senellart, J. Bloch, B. Sermage, and K. V. Kavokin, “Microcavity polariton spin quantum beats without a magnetic field: A manifestation of coulomb exchange in dense and polarized polariton systems,” *Phys. Rev. B*, vol. 72, p. 075317, Aug 2005.
- [151] I. I. Ryzhov, V. O. Kozlov, N. S. Kuznetsov, I. Y. Chestnov, A. V. Kavokin, A. Tzimis, Z. Hatzopoulos, P. G. Savvidis, G. G. Kozlov, and V. S. Zapasskii, “Spin noise signatures of the self-induced larmor precession,” *Phys. Rev. Res.*, vol. 2, p. 022064, Jun 2020.
- [152] D. Ballarini, D. Caputo, C. S. Muñoz, M. De Giorgi, L. Dominici, M. H. Szymańska, K. West, L. N. Pfeiffer, G. Gigli, F. P. Laussy, and D. Sanvitto, “Macroscopic two-dimensional polariton condensates,” *Phys. Rev. Lett.*, vol. 118, p. 215301, May 2017.
- [153] C. P. Dietrich, A. Steude, L. TROPF, M. Schubert, N. M. Kronenberg, K. Ostermann, S. Höfling, and M. C. Gather, “An exciton-polariton laser based on biologically produced fluorescent protein,” *Science Advances*, vol. 2, no. 8, 2016.

- [154] B. Gayral, J. M. Gérard, B. Legrand, E. Costard, and V. Thierry-Mieg, “Optical study of GaAs/AlAs pillar microcavities with elliptical cross section,” *Applied Physics Letters*, vol. 72, no. 12, pp. 1421–1423, 1998.
- [155] S. Gerhardt, M. Deppisch, S. Betzold, T. H. Harder, T. C. H. Liew, A. Predojević, S. Höfling, and C. Schneider, “Polarization-dependent light-matter coupling and highly indistinguishable resonant fluorescence photons from quantum dot-micropillar cavities with elliptical cross section,” *Physical Review B*, vol. 100, p. 115305, Sep 2019.
- [156] A. Daraei, D. Sanvitto, J. A. Timpson, A. M. Fox, D. M. Whittaker, M. S. Skolnick, P. S. S. Guimarães, H. Vinck, A. Tahraoui, P. W. Fry, S. L. Liew, and M. Hopkinson, “Control of polarization and mode mapping of small volume high Q micropillars,” *Journal of Applied Physics*, vol. 102, no. 4, p. 043105, 2007.
- [157] J. M. Ostermann and R. Michalzik, *Polarization Control of VCSELs*, pp. 147–179. Berlin, Heidelberg: Springer Berlin Heidelberg, 2013.
- [158] L. Xiang, X. Zhang, J. Zhang, Y. Huang, W. Hofmann, Y. Ning, and L. Wang, “Vcsel mode and polarization control by an elliptic dielectric mode filter,” *Appl. Opt.*, vol. 57, pp. 8467–8471, Oct 2018.
- [159] T. Pusch, E. La Tona, M. Lindemann, N. C. Gerhardt, M. R. Hofmann, and R. Michalzik, “Monolithic vertical-cavity surface-emitting laser with thermally tunable birefringence,” *Applied Physics Letters*, vol. 110, no. 15, p. 151106, 2017.
- [160] M. Lindemann, G. Xu, T. Pusch, R. Michalzik, M. Hofmann, I. Žutić, and N. Gerhardt, “Ultrafast spin-lasers,” *Nature*, vol. 568, pp. 1–4, 04 2019.
- [161] A. Kavokin, G. Malpuech, and M. Glazov, “Optical spin Hall effect,” *Phys. Rev. Lett.*, vol. 95, p. 136601, Sep 2005.
- [162] J. D. Töpfer, I. Chatzopoulos, H. Sigurdsson, T. Cookson, Y. G. Rubo, and P. G. Lagoudakis, “Engineering spatial coherence in lattices of polariton condensates,” *Optica*, vol. 8, pp. 106–113, Jan 2021.
- [163] C. E. Whittaker, E. Cancellieri, P. M. Walker, D. R. Gulevich, H. Schomeerus, D. Vaitiekus, B. Royall, D. M. Whittaker, E. Clarke, I. V. Iorsh, I. A. Shelykh, M. S. Skolnick, and D. N. Krizhanovskii, “Exciton polaritons in a two-dimensional Lieb lattice with spin-orbit coupling,” *Phys. Rev. Lett.*, vol. 120, p. 097401, Mar 2018.
- [164] F. Scafirimuto, D. Urbonas, M. A. Becker, U. Scherf, R. F. Mahrt, and T. Stöferle, “Tunable exciton–polariton condensation in a two-dimensional Lieb lattice at room temperature,” *Communications Physics*, vol. 4, Mar. 2021.
- [165] I. I. Rabi, J. R. Zacharias, S. Millman, and P. Kusch, “A new method of measuring nuclear magnetic moment,” *Phys. Rev.*, vol. 53, pp. 318–318, Feb 1938.

- [166] I. K. Kominis, T. W. Kornack, J. C. Allred, and M. V. Romalis, “A subfemtotesla multichannel atomic magnetometer,” *Nature*, vol. 422, pp. 596–599, Apr. 2003.
- [167] G. D. Fuchs, V. V. Dobrovitski, D. M. Toyli, F. J. Heremans, and D. D. Awschalom, “Gigahertz dynamics of a strongly driven single quantum spin,” *Science*, vol. 326, no. 5959, pp. 1520–1522, 2009.
- [168] D. N. Krizhanovskii, D. Sanvitto, I. A. Shelykh, M. M. Glazov, G. Malpuech, D. D. Solnyshkov, A. Kavokin, S. Ceccarelli, M. S. Skolnick, and J. S. Roberts, “Rotation of the plane of polarization of light in a semiconductor microcavity,” *Phys. Rev. B*, vol. 73, p. 073303, Feb 2006.
- [169] F. P. Laussy, I. A. Shelykh, G. Malpuech, and A. Kavokin, “Effects of Bose-Einstein condensation of exciton polaritons in microcavities on the polarization of emitted light,” *Phys. Rev. B*, vol. 73, p. 035315, Jan 2006.
- [170] M. Z. Maialle, E. A. de Andrada e Silva, and L. J. Sham, “Exciton spin dynamics in quantum wells,” *Phys. Rev. B*, vol. 47, pp. 15776–15788, Jun 1993.
- [171] D. Colas, L. Dominici, S. Donati, A. A. Pervishko, T. C. Liew, I. A. Shelykh, D. Ballarini, M. de Giorgi, A. Bramati, G. Gigli, E. del Valle, F. P. Laussy, A. V. Kavokin, and D. Sanvitto, “Polarization shaping of poincaré beams by polariton oscillations,” *Light: Science & Applications*, vol. 4, pp. e350–e350, Nov. 2015.
- [172] E. L. Andronikashvili and Y. G. Mamaladze, “Quantization of macroscopic motions and hydrodynamics of rotating helium ii,” *Rev. Mod. Phys.*, vol. 38, pp. 567–625, Oct 1966.
- [173] S. J. Bolton, S. M. Levin, T. Guillot, C. Li, Y. Kaspi, G. Orton, M. H. Wong, F. Oyafuso, M. Allison, J. Arballo, S. Atreya, H. N. Becker, J. Bloxham, S. T. Brown, L. N. Fletcher, E. Galanti, S. Gulkis, M. Janssen, A. Ingersoll, J. L. Lunine, S. Misra, P. Steffes, D. Stevenson, J. H. Waite, R. K. Yadav, and Z. Zhang, “Microwave observations reveal the deep extent and structure of Jupiter’s atmospheric vortices,” *Science*, vol. 374, pp. 968+, NOV 19 2021.
- [174] G. Blatter, M. V. Feigel’man, V. B. Geshkenbein, A. I. Larkin, and V. M. Vinokur, “Vortices in high-temperature superconductors,” *Rev. Mod. Phys.*, vol. 66, pp. 1125–1388, Oct 1994.
- [175] Y. Shen, X. Wang, Z. Xie, C. Min, X. Fu, Q. Liu, M. Gong, and X. Yuan, “Optical vortices 30 years on: OAM manipulation from topological charge to multiple singularities,” *Light: Science & Applications*, vol. 8, Oct. 2019.
- [176] T. Golod, A. Iovan, and V. M. Krasnov, “Single Abrikosov vortices as quantized information bits,” *Nature Communications*, vol. 6, Oct. 2015.

- [177] N. Bozinovic, Y. Yue, Y. Ren, M. Tur, P. Kristensen, H. Huang, A. E. Willner, and S. Ramachandran, “Terabit-scale orbital angular momentum mode division multiplexing in fibers,” *Science*, vol. 340, pp. 1545–1548, June 2013.
- [178] L. Paterson, M. P. MacDonald, J. Arlt, W. Sibbett, P. E. Bryant, and K. Dhollakia, “Controlled rotation of optically trapped microscopic particles,” *Science*, vol. 292, pp. 912–914, May 2001.
- [179] M. V. Berry, “Optical vortices evolving from helicoidal integer and fractional phase steps,” *Journal of Optics A: Pure and Applied Optics*, vol. 6, pp. 259–268, jan 2004.
- [180] P. Kapitza, “Viscosity of liquid helium below the λ -point,” *Nature*, vol. 141, pp. 74–74, Jan. 1938.
- [181] O. V. Lounasmaa and E. Thuneberg, “Vortices in rotating superfluid ^3He ,” *Proceedings of the National Academy of Sciences*, vol. 96, pp. 7760–7767, July 1999.
- [182] R. E. Packard and T. M. Sanders, “Observations on single vortex lines in rotating superfluid helium,” *Phys. Rev. A*, vol. 6, pp. 799–807, Aug 1972.
- [183] E. Hodby, G. Hechenblaikner, S. A. Hopkins, O. M. Maragò, and C. J. Foot, “Vortex nucleation in Bose-Einstein condensates in an oblate, purely magnetic potential,” *Phys. Rev. Lett.*, vol. 88, p. 010405, Dec 2001.
- [184] M. R. Matthews, B. P. Anderson, P. C. Haljan, D. S. Hall, C. E. Wieman, and E. A. Cornell, “Vortices in a Bose-Einstein condensate,” *Phys. Rev. Lett.*, vol. 83, pp. 2498–2501, Sep 1999.
- [185] D. A. Butts and D. S. Rokhsar, “Predicted signatures of rotating bose-einstein condensates,” *Nature*, vol. 397, pp. 327–329, Jan. 1999.
- [186] Y. V. Kartashov and D. A. Zezyulin, “Rotating patterns in polariton condensates in ring-shaped potentials under a bichromatic pump,” *Opt. Lett.*, vol. 44, pp. 4805–4808, Oct 2019.
- [187] J. D. Töpfer, H. Sigurdsson, S. Alyatkin, and P. G. Lagoudakis, “Lotka-volterra population dynamics in coherent and tunable oscillators of trapped polariton condensates,” *Phys. Rev. B*, vol. 102, p. 195428, Nov 2020.
- [188] R. J. Donnelly, *Quantized vortices in helium II*, vol. 2. Cambridge: Cambridge University Press, 1991.
- [189] J. R. Abo-Shaeer, C. Raman, J. M. Vogels, and W. Ketterle, “Observation of vortex lattices in Bose-Einstein condensates,” *Science*, vol. 292, no. 5516, pp. 476–479, 2001.
- [190] P. Engels, I. Coddington, P. C. Haljan, V. Schweikhard, and E. A. Cornell, “Observation of long-lived vortex aggregates in rapidly rotating Bose-Einstein condensates,” *Phys. Rev. Lett.*, vol. 90, p. 170405, May 2003.

- [191] Y. del Valle-Inclan Redondo, C. Schneider, S. Klemmt, S. Höfling, S. Tarucha, and M. D. Fraser, “Optically driven rotation of exciton–polariton condensates,” *Nano Letters*, vol. 23, pp. 4564–4571, May 2023.
- [192] A. V. Yulin, I. A. Shelykh, E. S. Sedov, and A. V. Kavokin, “Vorticity of polariton condensates in rotating traps,” 2023.
- [193] A. V. Yulin, I. A. Shelykh, E. S. Sedov, and A. V. Kavokin, “Spin resonance induced by a mechanical rotation of a polariton condensate,” 2022.
- [194] H. Sigurdsson, O. A. Egorov, X. Ma, I. A. Shelykh, and T. C. H. Liew, “Information processing with topologically protected vortex memories in exciton-polariton condensates,” *Phys. Rev. B*, vol. 90, p. 014504, Jul 2014.
- [195] Y. Xue, I. Chestnov, E. Sedov, E. Kiktenko, A. K. Fedorov, S. Schumacher, X. Ma, and A. Kavokin, “Split-ring polariton condensates as macroscopic two-level quantum systems,” *Phys. Rev. Research*, vol. 3, p. 013099, Jan 2021.
- [196] G. Vicidomini, P. Bianchini, and A. Diaspro, “STED super-resolved microscopy,” *Nature Methods*, vol. 15, pp. 173–182, Jan. 2018.
- [197] M. Padgett and R. Bowman, “Tweezers with a twist,” *Nature Photonics*, vol. 5, pp. 343–348, May 2011.
- [198] S. Mandal, R. Banerjee, E. A. Ostrovskaya, and T. C. H. Liew, “Nonreciprocal transport of exciton polaritons in a non-hermitian chain,” *Phys. Rev. Lett.*, vol. 125, p. 123902, Sep 2020.
- [199] S. Mandal, R. Banerjee, and T. C. H. Liew, “From the topological spin-hall effect to the non-hermitian skin effect in an elliptical micropillar chain,” *ACS Photonics*, vol. 9, pp. 527–539, Jan. 2022.
- [200] A. V. Yulin, A. V. Nalitov, and I. A. Shelykh, “Spinning polariton vortices with magnetic field,” *Phys. Rev. B*, vol. 101, p. 104308, Mar 2020.